Synthesis of naphthalene diimide structures for application in polymer solar cells

by

Jonas Mattiasson Bjuggren

Thesis
Submitted to Flinders University
for the degree of

Doctor of Philosophy
College of Science and Engineering
2nd August 2019

The good thing about science is that it's true whether or not you believe in it.

— Neil deGrasse Tyson

Dedicated to the youth climate movement.

Table of Contents

Abstract

The field of organic photovoltaics (OPV) has made tremendous progress during the 21st century with efficiencies now exceeding 15% for single-junction polymer solar cell (PSC) devices. These efficiencies are highly promising, with the technology set-up to participate in the solar boom that is predicted to constitute a major contribution to the phasing out fossil fuels. Given the urgency to reduce greenhouse gas (GHG) emissions it is imperative that the research conducted is focused toward the commercialisation of PSC. However, complex synthesis routes involving highly toxic chemicals, widespread use of chlorinated processing solvents, and the utilisation of laboratory scale processing methods could delay commercialisation. These methods were necessary to develop a deeper understanding of PSCs, taking the research field from efficiencies of <1% in its infancy to where it is today, but are now counterintuitive for further development of this potentially very green technology. Therefore, further research efforts are needed on green synthesis, environmentally friendly processing, and scalable fabrication to drive the commercialisation of PSC.

This thesis is devoted to the development of n-type naphthalene diimide (NDI) based compounds for use in PSC. Three different material categories were investigated in this thesis work; with i) small molecule non-fullerene acceptors (NFA) presented in Chapter 4, ii) NDI-bithiophene based acceptor polymers introduced in Chapter 5, and iii) cathode interface layers (CIL) discussed in Chapter 6 & 7. Particular attention was given to the green and facile synthesis routes of materials with elevated solubilities in non-chlorinated, greener solvents that are compatible with scalable manufacturing methods.

A number of different NDI based n-type materials were successfully synthesised, ranging from small molecules to polymers. These include series of small molecule NFAs, acceptor polymers, and CILs with variations in crystal forming ability for enhanced morphology control, side chain length along with number for increased solubility in greener solvents, and linker unit as well as pendant side-group moiety for increased doping, respectively.

The small molecule NFAs of varying crystal forming ability, employed in active layer blends in inverted device structures, were found to yield low power conversion efficiencies (PCE) with trade-offs possibly occurring between favourable morphology and the presence of charge carrier pathways. These materials could potetntially fit niche applications, e.g. semitransparent PSCs.

For the acceptor polymers octyldodecyl (OD) side chains were found to yield higher PCEs than their hexyldecyl (HD) counterparts. Moreover, partial substitution of bithiophene in the N2200 polymer backbone yielded high PCEs with tuneable solubilities in greener processing solvents. The novel polymer P(NDI2OD-14T2) achieved PCEs of 4.68% and 4.06% for spin coated (SC) and blade coated (BC) all-polymer devices, respectively.

Significant improvements in PCEs were observed when employing PNDIT10N as a CIL. New record PCEs were achieved for two out of three donor polymers in inverted devices with polymer:fullerene bulk heterojunction (BHJ) layers. This was attributed to a significant reduction of the ITO work function and the formation of an interfacial dipole at the ITO-CIL interface. Moreover, an ultra-thin layer of the CIL experienced a good stability under varied storage conditions.

CILs with a variety of linkers and either tertiary amine or quaternary amine bearing pendant side-groups were studied. Significant reductions of the ITO work function were observed for all CILs. Preliminary results reveal the benzene linker with quaternary amine to experience the highest PCE. Moreover, this polymer also experiences a more suitable absorbance at lower wavelength regions and suitable solubilities for orthogonal solvent processing in inverted PSCs.

Declaration

I certify that this thesis does not incorporate without acknowledgment any material previously submitted for a degree or diploma in any university; and that to the best of my knowledge and belief it does not contain any material previously published or written by another person except where due reference is made in the text.

Signed:...................

Date:

Acknowledgements

The past four years have been an amazing experience with so many memories that I will cherish for the rest of my life. My PhD journey has seen many challenges, and because of this I have grown both as a researcher as well as on a personal level, it has truly been an invaluable experience. With that said, I would like to take this opportunity to express my sincere gratitude to the people that have aided me on this crazy journey that took me, both physically, from Europe to Australia, and mentally to where I am today.

Firstly, I would like to thank my primary supervisor Prof. Mats Andersson for making my PhD experience the very best possible. I have worked with Mats ever since I started my Master's back in Sweden and it has been an absolute honor to have had his support and guidance throughout this time. I'm grateful for it all; the long scientific discussions, the visits in the laboratory to check I'm doing oaky, the constant encouragement to challenge myself, and so much more. But I'm especially grateful for him letting me follow my own path, make mistakes, letting me grow into the role of a researcher.

I would also like to extend my gratitude to my co-supervisor Prof. David Lewis for taking me on halfway through my PhD, after the transfer from UniSA to Flinders. Your support, and that of your group, has turned what would otherwise have been a tough time into a joyful experience.

To all the post-docs that I have worked: Renee Kroon, Desta Gedefaw, Anirudh Sharma, Sait Elmas, and Martyn Jevric. I wouldn't have been able to do this without! You have graciously shared your knowledge about organic synthesis, device fabrication, electrochemistry, and writing. Apart from science I have also learned quite a few dirty jokes along the way!

To the rest of my colleagues, you have really brightened my PhD and we have shared so many memories, ranging from office-yoga to spotting doppelgangers at scientific conferences and moving labs or just sharing a good time. To Rajni Garg, Caroline Pan, and Petri Murto; thank you for being the perfect combinations of serious and silly.

A big thank you to all my family and friends that have supported me during this long journey by distracting me with non-science activities (and not asking to often when I'll finish). I've been appreciating every moment at the beach, in the snow, at bbqs, visiting summer houses, etc. I love you all, never stop being amazing people!

Finally, I would like to thank my best friend and my partner, Jessie, for being a pillar of support. I love you with all my heart!

List of figures

List of tables

List of schemes

Abbreviations and acronyms

AcOH	acetic acid
AM1.5	air mass 1.5
BC	blade coating
CB	chlorobenzene
CN	1-chloronaphthalene
CT	charge transfer
CV	cyclic voltammetry
E_g	band gap
ETL	electron transporting layer
FF	fill factor
GHG	greenhouse gases
HOMO	highest occupied molecular orbital
HTL	hole transporting layer
IEA	international energy agency
J_{sc}	short-circuit current
LUMO	lowest unoccupied molecular orbital
MRC	mini roll coater
$\bar{M}_n$	number-average molecular weight
$\bar{M}_w$	weight-average molecular weight
NDI	naphthalene diimide
NFA	non-fullerene acceptors
NMR	nuclear magnetic resonance spectroscopy
NTCDA	1,4,5,8-naphthalene tetracarboxylic dianhydride
o-DCB	1,2-dichlorobenzene
OPV	organic photovoltaic
P3HT	poly(3-hexylthiophene)
P4VP	poly(4-vinylpyridine)
PA	poly(acetylene)
$PC_{61}BM$	[6,6]-Phenyl-C61-butyric acid methyl ester
$PC_{71}BM$	[6,6]-Phenyl-C71-butyric acid methyl ester

PCE	power conversion efficiency
PDI	perylene diimide
PEDOT:PSS	poly(3,4-ethylenedioxythiophene):poly(styrenesulfonic acid)
PEI	poly(ethylenimine)
PEIE	poly(ethylenimine ethoxylated)
PTCDA	perylene tetracarboxylic dianhydride
PV	photovoltaics
RBF	round-bottom flask
SC	spin coating
STA	simultaneous thermal analyser
SWV	squarewave voltammetry
TA	thermal annealing
TGA	thermal gravimetric analysis
TQ1	poly[2,3-bis-(3-octyloxyphenyl)quinoxaline-5,8-diyl- alt -thiophene-2,5-diyl]
THF	tetrahydrofuran
UPS	ultraviolet photoelectron spectroscopy
UV/vis	ultraviolet-visible
UV/vis/NIR	ultraviolet-visible near infrared
V_{oc}	open-circuit voltage
ZnO	zinc oxide
Đ	polydispersity index

Synthesised compounds:

AsNDI
2-(2-dimethoxyphenyl)-7-octyl-benzo[lmn][3,8]phenanthroline-1,3,6,8(2*H*,7*H*)-tetrone

DANDI
2,7-bis[3-(dimethylamino)propyl]-benzo[lmn][3,8]phenanthroline-1,3,6,8(2*H*,7*H*)-tetrone

DEHNDI
2,7-bis(2-ethylhexyl)benzo[lmn][3,8]phenanthroline-1,3,6,8(2*H*,7*H*)-tetrone

DHDNDI
2,6-dibromo-1,4,5,8-tetracarboxylic-*N,N'*-bis(2-hexyldecyl)diimide

diBrDANDI
dibromo-2,7-bis[3-(dimethylamino)propyl]benzo[lmn][3,8]phenanthroline-1,3,6,8(2*H*,7*H*)-tetrone

diBrNTCDA
2,6-dibromonaphthalene-1,4,5,8-tetracarboxylic dianhydride

DODNDI
2,6-dibromo-1,4,5,8-tetracarboxylic-*N,N'*-bis(2-octyldodecyl)diimide

DOBNDI
2,7-bis(2-octyloxyphenyl)benzo[lmn][3,8]phenanthroline-1,3,6,8(2*H*,7*H*)-tetrone

DONDI
N,N'-bis(octyl)-1,4,5,8-naphthalenetetracarboxylic diimide

P(NDI3N-T)
polymers   poly[*N,N'*-bis(3-dimethylaminopropyl)naphthalene-1,4,5,8-bis(dicarboximide)-2,6-diyl]-alt-2,5-thiophene)

P(NDI3N-P)
poly[*N,N'*-bis(3-dimethylaminopropyl)naphthalene-1,4,5,8-bis(dicarboximide)-2,6-diyl]-alt-1,4-benzene)

P(NDI3N-F8)
poly[*N,N'*-bis(3-dimethylaminopropyl)naphthalene-1,4,5,8-bis(dicarboximide)-2,6-diyl]-alt-2,7-(9,9'-dihexylfluorene))

P(NDI3N-T-Br)
poly[(*N,N'*-bis(3-(*N,N*-dimethyl)-*N*-ethylammonium)propyl)naphthalene-1,4,5,8-bis(dicarboximide)-2,6-diyl)-alt-2,5-thiophene)]dibromide

P(NDI3N-P-Br)
poly[(*N,N'*-bis(3-(*N,N*-dimethyl)-*N*-ethylammonium)propyl)naphthalene-1,4,5,8-bis(dicarboximide)-2,6-diyl)-alt-1,4-benzene)]dibromide

P(NDI3N-F8-Br)
poly[(*N,N'*-bis(3-(*N,N*-dimethyl)-*N*-ethylammonium)propyl)naphthalene-1,4,5,8-bis(dicarboximide)-2,6-diyl)-alt-2,7-(9,9'-dihexylfluorene))]dibromide

N2200
poly[[*N,N'*-bis(2-octyldodecyl)-naphthalene-1,4,5,8-bis(dicarboximide)-2,6-diyl]-alt-5,5'-(2,2'-bithiophene)]

N2300
poly[[*N,N'*-bis(2-hexyldecyl)-naphthalene-1,4,5,8-bis(dicarboximide)-2,6-diyl]-alt-5,5'-(2,2'-bithiophene)]

Chapter 1. Motivation

1.1 Transition toward renewables

The current situation on global warming with rising emissions of greenhouse gases (GHG), despitesigns of it slowing down, is quite dire. Regardless, fossil fuels continue to dominate the global energy market. According to communication from the international energy agency (IEA), in the form of their annual report, the World Energy Outlook 2017, the goals set in the Paris Agreement will not be reached with the current emissions trajectory.[1] However, projected emissions of GHG for the year 2040 have been readjusted by a staggering 600 million tonnes below the levels predicted in 2016 years report.[2] This is a good indication of improvement, but the 2040 levels are still predicted at 35.7 giga tonnes GHG emissions or ∼50% over the level required to reach the 2 °C goal, as agreed on in the Paris Agreement to mitigate the threat of climate change[3]. This high estimate can partly be explained by the predicted 30% increase in energy usage for 2040 above 2016 levels. Further, 1.5 °C as well as 2 °C sustainable development scenarios were presented in the World Energy Outlook 2017.[1] These scenarios explore the possible developments for limiting the global warming to a mean temperature of 2 °C and 1.5 °C above pre-industrial levels. The main points include the quick rollout of energy efficiency targets as well as the immediate decline in coal use and a massive shift towards low carbon sources, e.g. renewables, reaching a 40% share of the global energy market by 2040. This increased market share will likely be met by photovoltaics (PV) as well as by wind power. The abundance of these sources (Figure 1.1) with 23 000 terawatt years/year (TWy/y) for solar and 75-130 TWy/y for wind power is nothing short of astonishing in comparison to the most abundant finite resource, coal, with a total recoverable energy equivalent to 830 TWy.
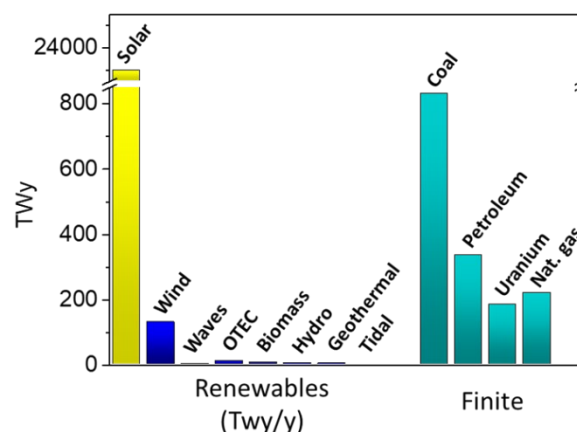
Figure 1.1: Yearly energy available from renewable sources with world energy reserves for finite resources shown as comparison.[4]

In 2014, the addition of new power capacity was nearing 50% renewables, with solar PV being the fastest growing, followed by wind power, compared to the 2010 levels.[5] At the current rate, ~74 GW of solar power is predicted to be installed between 2017 to 2040 accounting for about 40% of the renewable

capacity added, closely followed by wind power at ~50 GW.[1] It is quite clear that the global trend heavily favours renewables and especially solar power over the coming decades.

1.1.1 Solar boom in Australia

The trend toward renewables, although strong worldwide, is perhaps even more evident in Australia with rooftop solar installations soaring over the last couple of years. South Australia has led this transition, which started in the early 2000's. After reaching the self-imposed goal of 33% renewables in the electricity mix prior to 2025, the goal has now been reassessed leading to an even higher ambition of 50% renewables by 2025.[6] In 2014 South Australia was the state with the highest penetration of rooftop solar with 26.1% of household having a solar PV system. Since then Queensland has surpassed this, with over 30% of households owning a solar PV system.[7] Overall, Australia has had an amazing growth in capacity for rooftop solar from 23 MW in 2008 to over 4300 MW in 2016 with over 1,000,000 installations taking place in 2015-2016.[8] At current adoption rate, Australia could reach as high as 52% renewables in the electricity mix by 2030.[9] This fast transition toward renewables and especially solar PV not just in Australia, but also worldwide, is remarkable. However, further efforts are needed to mitigate the damage of climate change; this creates strong incentives to improve this relatively young technology.

1.1.2 Photovoltaics

The photovoltaic effect, the creation of voltage and electric current upon irradiance and the basic working principle for all solar cells, was discovered in 1839 by French physicist Edmond Becquerel.[10] Over 100 years would pass before the accidental discovery at Bell Laboratories in 1953 that doped silicon is photoactive. This milestone was shortly followed by the first silicon based *p-n* junction solar cell in 1954.[11] Fast progress was seen in the early days with efficiencies of over 10% reached within 18 months.[12] Nevertheless, the high costs of these early cells deterred from wider commercialisation outside of their use within non-cost sensitive specialised industries, e.g. space exploration. However, the oil embargoes of the 70's sparked new interest in the field, starting a new era of rapid development with the first modern silicon cell being introduced in 1976.[13] The development has since continued with new types of solar cells being introduced over the years. These are classified into three different generations based on the maturity of the photoactive material:

- 1st generation solar cells. This class is often referred to as traditional or conventional cells. They are made of crystalline silicon, including both mono- and multicrystalline solar cells.

- 2nd generation solar cells. This generation of thin film solar cells have somewhat lower efficiencies, but instead provide the possibility of bendable, lightweight devices. The photoactive material composition ranges from copper indium gallium selenide over cadmium telluride to amorphous Si.
- 3rd generation solar cells. The latest generation includes i) the multijunction cells, ii) dye-sensitised solar cells, iii) an array of hybrid cells, and iv) organic photovoltaics (OPV).[14] These tend to either offer high theoretical efficiencies or moderate efficiencies at a very low cost.

1.1.2.1 Organic and hybrid photovoltaic systems

In OPV devices, solar cells, semiconducting conjugated polymers or organic small molecules are utilised for light absorption, charge carrier generation, and charge transport. These include small molecule solar cells and polymer solar cells (PSCs). In a broader context, solar cells utilising organic materials for charge carrier generation, charge transport or charge collection would also encompass systems such as dye-sensitised solar cells, quantum dot solar cells, and perovskite solar cells.

Dye-sensitised solar cells (DSSC) consists of five main components; a transparent substrate, a set of electrodes, a dye, a semiconducting film onto which the dye is adsorbed, and an electrolyte with a redox mediator.[15] In DSSC the processes of charge generation and charge transport are decoupled with charge generation occurring in the dye, or sensitiser, and charge transport taking place in the semiconducting film and electrolyte.[16] Upon absorption of a photon an electron-hole pair is generated with the electron being transported through the semiconducting material and the hole transferred to the electrolyte remediator. These are connected via an external circuit, thus, forming a current.

Analogous to the DSSCs, there exists the quantum-dot solar cells (QDSC). These operate in the same manner, with the sensitiser, i.e. quantum-dot, absorbing the light and generating charge carriers, which are then selectively transported through semiconductor and electrolyte, to form a current.[17] Record efficiencies for QDSCs are currently sitting at over 12%.[18]

Perovskite solar cells utilise a metal-halide perovskite absorber, commonly a hybrid organic-inorganic lead or tin halide, that is sandwiched between p- and n-type selective contacts, forming a so-called p-i-n planar heterojunction. If the perovskite layer formation is aided by a metal oxide it is instead called a meso structured device.[19] Unlike the dye-sensitised solar cells, the metal-halide perovskite does not only act as an absorber but is also solely responsible for charge carrier generation, as well as functioning as both hole and electron conductor.[20] Perovskite solar cells have experienced the most rapid growth with efficiencies reaching well over 20%.

Lastly, in small molecule solar cells the light absorption and charge carrier generation occurs in the active layer, with charges then transported through active layer and interface layers to finally be collected at the electrodes, that are connected by an external circuit. The active layer consists of two organic small molecules that are processed in either a planar or a finely intermixed bulk-hetero junction

(BHJ) architecture.[21] Small molecule solar cell active layers are either deposited via thermal evaporation under vacuum (~10^{-5} mbar) or solution processed,[22] with the latter being the preferred method due to the simplicity in upscaling through roll-to-roll processes. Small molecule solar cells have reached record efficiencies of close to 10% for single-junction devices.[23]

1.1.2.2 Polymer Solar Cells

This thesis will focus on PSCs, which is a sub-class of OPVs. This 3rd generation solar cell combines low cost, stemming from the use of abundant materials with low temperature solution processing, short energy pay-back times (EPBT), and green processing. Another advantage is the potential for upscaling via roll-to-roll processing, i.e. printing, on flexible low-cost transparent substrates. Further, EPBTs as low as one day have been estimated.[24] Considering the transition away from fossil fuels toward renewables, this attribute should be considered of high value. The EPBT for inorganic counterparts are, unlike the PSC, measured in years instead of days.[25] The advantages are aplenty but the technology has not yet matured. The efficiency, lifetime and processing of PSCs pose major challenges for a successful commercialisation of the technology.

1.2 Aim

As stated above, there are many incentives to further develop polymer solar cells. It is one of few emerging technologies that can achieve major improvements to the current electricity market and contribute to a decrease in GHG emissions. This thesis will focus on the development of new materials based on naphthalene diimide (NDI) cores for use in polymer solar cells. The work is based around the premise that new materials developed should be suitable for upscaling. Interface materials, small molecule acceptors, and polymer acceptors have been synthesised. Short and green synthesis routes have been premiered when possible, as well as the use of inexpensive materials. Green processing has been the second priority throughout the work.

The work in this thesis is conducted with the aim to both explore new and improve on existing NDI based compounds for use in PSCs. These compounds can be applied in a range of applications, each with their own challenges. Thus, the work was divided into a series of research questions specific to each investigated application. The research questions, presented below, with associated hypotheses are studied in the respective thesis chapters.

Research question 1: Can small molecule NDI based acceptor-blends be used as the electron transporting material?

Hypotheses:

- Side-group engineering can modify the crystallinity and miscibility.
- Multicomponent blends can tune morphology.

Research question 2: Is it possible to increase the solubility of N2200 derivatives in environmentally friendly solvents while retaining good power conversion efficiency?

Hypotheses:

- Side-group engineering can greatly modify the polymers solubility.
- The introduction of additional stereo-centres via the ternary co-polymer approach can alter the solution properties while the film properties are retained.

Research question 3: Can NDI based polymers work well as interface materials when processed from environmentally friendly solvents and are they compatible with a facile synthesis route?

Hypotheses:

- The low-lying HOMO level of an NDI based polymer provides a hole blocking ability to the interface layer increasing the efficiency.
- The strong n-type character contributes to an efficient doping and good conductivity.
- Polymer design can provide solvent orthogonal abilities to the material.

1.3 References

(1)   World Energy Outlook 2017; International Energy Agency: **2017**.

(2)   World Energy Outlook 2016; International Energy Agency: **2016**.

(3)   Summary of the Paris Agreement. https://bigpicture.unfccc.int/#content-the-paris-agreemen (accessed 30th July).

(4)   Marc Perez, R. P., A Fundamental Look At Supply Side Energy Reserves For The Planet.   *Nat. Gas* **2015**, 2, 215.

 (5)   Energy and Climate Change; Internation Energy Agency: **2017**; p 200.

(6)   THE AUSTRALIAN RENEWABLE ENERGY RACE: WHICH STATES ARE WINNING OR LOSING?; Climate Council of Australia: **2014**.

(7)   SOLAR REPORT; Australian Energy Council: **2017**.

(8)   SOUTH AUSTRALIAN FUEL AND TECHNOLOGY REPORT; Australian Energy Market Operator: **2017**.

(9)   CLEAN & RELIABLE POWER: ROADMAP TO A RENEWABLE FUTURE; Climate Council of Australia: **2018**.

(10)   Becquerel, A. E., Recherches sur les Effets de la Radiation Chimique de la Lumiere Solaire au Moyen des Courants Clectriques. *Comptes Rendus de L´Academie des Sciences* **1839**, 9.

(11)   Chapin, D. M., Fuller, C. S., Pearson, G. L., A New Silicon p-n Junction Photocell for Converting Solar Radiation into Electrical Power. *J. Appl. Phys.* **1954**, 25, 676-677.

(12)   Green, M. A., The Path to 25% Silicon Solar Cell Efficiency: History of Silicon Cell Evolution. *Progress in Photovoltaics: Research and Applications* **2009**, 17, 183-189.

(13)   Green, M. A., Silicon Photovoltaic Modules: a Brief History of the first 50 Years. *Progress in Photovoltaics: Research and Applications* **2005**, 13, 447-455.

(14)   Kippelen, B.; Brédas, J.-L., Organic Photovoltaics. *Energy Environ. Sci.* **2009**, 2, 251-261.

(15)   Nazeeruddin, M. K.; Baranoff, E.; Grätzel, M., Dye-sensitized solar cells: A brief overview. *Sol. Energy* **2011**, 85, 1172-1178.

(16)   Grätzel, M., Dye-sensitized solar cells. *J. Photochem. Photobiol., C* **2003**, 4, 145-153.

(17)   Pan, Z.; Rao, H.; Mora-Seró, I.; Bisquert, J.; Zhong, X., Quantum dot-sensitized solar cells. *Chem. Soc. Rev.* **2018**, 47, 7659-7702.

(18)   Du, Z.; Artemyev, M.; Wang, J.; Tang, J., Performance Improvement Strategies for Quantum Dot-sensitized Solar Cells: a Review. *J. Mater. Chem. A* **2019**, 7, 2464-2489.

(19)   Stranks, S. D.; Nayak, P. K.; Zhang, W.; Stergiopoulos, T.; Snaith, H. J., Formation of Thin Films of Organic–Inorganic Perovskites for High-Efficiency Solar Cells. *Angew. Chem., Int. Ed.* **2015**, 54, 3240-3248.

(20)   Stranks, S. D.; Snaith, H. J., Metal-halide perovskites for photovoltaic and light-emitting devices. *Nat. Nanotechnol.* **2015**, 10, 391.

(21)   Li, Y., Organic Solar Cells Based on Small Molecules. In Organic Optoelectronics **2015**.

(22)   Hoppe, H.; Sariciftci, N. S., Organic Solar Cells: An overview. *J. Mater. Res.* **2004**, 19, 1924-1945.

(23)   Bin, H.; Yang, Y.; Zhang, Z.-G.; Ye, L.; Ghasemi, M.; Chen, S.; Zhang, Y.; Zhang, C.; Sun, C.; Xue, L.; Yang, C.; Ade, H.; Li, Y., 9.73% Efficiency Nonfullerene All Organic Small Molecule Solar Cells with Absorption-Complementary Donor and Acceptor. *J. Am. Chem. Soc.* **2017**, 139, 5085-5094.

(24)   Espinosa, N.; Hösel, M.; Angmo, D.; Krebs, F. C., Solar Cells with One-day Energy Payback for the Factories of the Future. *Energy Environ. Sci.* **2012**, 5, 5117-5132.

(25)   Laboratory, N. R. E. Energy Payback: Clean Energy from PV; **2004**.

Chapter 2. Polymer solar cells (PSC)

2.1 Overview

In this chapter, a literature review is presented to provide the reader with a clear overview of the history of the research field of polymer solar cells, as well as a good insight into the high-performance materials and device architectures. The different material categories with donors, acceptors and interface materials and their primary functions are introduced. The development of device architectures is discussed with emphasis on the bulk-hetero junction layer structure. Further, active layer morphology and its effect on the performance of the solar cells is discussed in detail. The wide range of processing techniques available are introduced to the reader, providing a clear distinction between small scale laboratory techniques and scalable fabrication methods. Lastly, the stability and its clear connection to commercialisation is discussed, showcasing the different degradation pathways. Firstly though, the reader will be familiarised with the working principle of a solar cell as well as introduced to the important Shockley-Queisser limit that designates the maximum theoretical efficiency of a single-junction cell.

2.2 Working principle of polymer solar cells

In PSCs, unlike their inorganic counterparts, free charge carriers cannot be formed directly due to the relative permittivity, i.e. the decrease in an electric field in a material relative to vacuum, being too low. The working mechanism (illustrated in Figure 2.1) is commonly divided into a six step process[1]: i) Absorption of a photon resulting in the excitation of an electron from the HOMO to the LUMO, leading to the consequent formation of an exciton, an electron-hole bound pair, upon irradiation. ii) Diffusion of the exciton toward the donor:acceptor interface. iii) Transformation of excitons into weakly bound charge transfer (CT) states, iv) dissolution of CT states to free charge carriers, e.g. electron and hole, attributable to the strong electric field present at this interface. v) Transportation of charge carriers through the active layer toward respective electrode, driven by the built-in bias originating from the work function (WF) difference between said electrodes. vi) Collection / recombination of the free charge carriers at the electrodes resulting in an electric current.

Solar cells are characterised by the following parameters, which are crucial for the device performance (characteristics): The short circuit current density (J_{sc}), the open circuit voltage (V_{oc}), and the fill factor (FF).

The J_{sc} is defined as the maximum current at short circuit conditions and is typically given in mA cm^{-2} to exclude variations due to cell area. Figure 2.2 illustrates how the J_{sc} is derived from a J-V curve. Further, the J_{sc} is dependent on the absorption, reflectance, spectrum of incident light, charge generation and transport.

The V_{oc} is the maximum voltage that can be extracted from a device under zero current conditions. The V_{oc} is highly dependent on the LUMO$_{Acceptor}$ – HOMO$_{Donor}$ offset with a range of additional loss mechanisms playing an important role. Materials employed in the photoactive layer of OPVs characteristically have a E_g of 1.7-2.1 eV with a V_{oc} of ~1.0 V. This indicates losses of close to 50%,[2] which can be related to the microstructure, donor:acceptor interface area, energetic disorder, and CT states.[3]
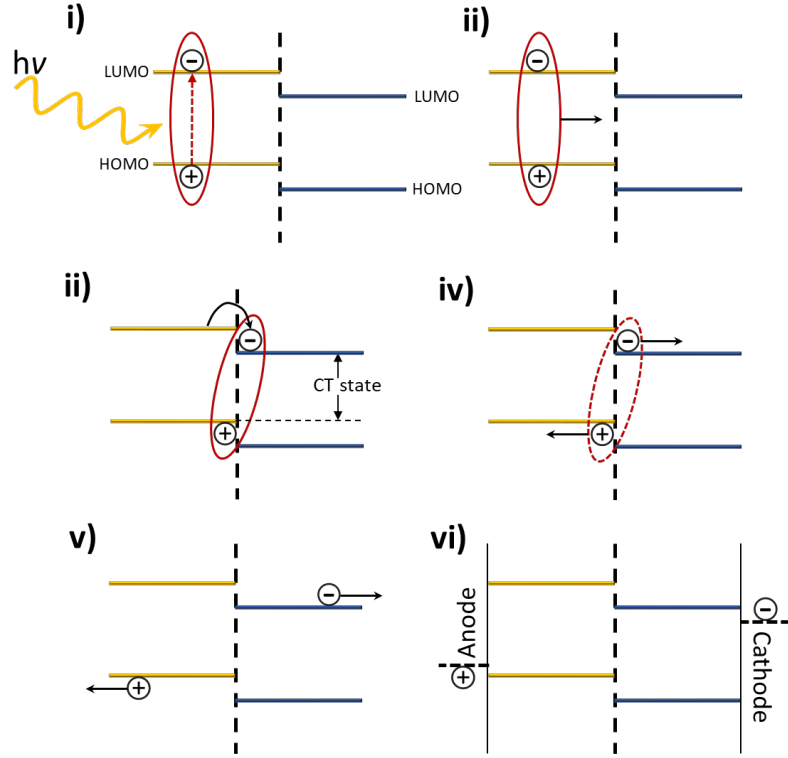
Figure 2.1: Illustration of: i) Absorption of a photon and formation of an exciton. ii) Exciton diffusion toward donar:acceptor interface with iii) consequent formation of a CT state. iv) Formation of free charge carriers (i.e. electron and hole). v) Charge carrier transport through the active layer followed by vi) collection at their respective electrodes.

The fill factor (FF) is defined as the ratio between the real maximum power output (P_{max}) and theoretical maximum power output, where P_{max} is the area formed at the maximum power point (Figure 2.2).

$$FF = \frac{P_{max}}{J_{sc}*V_{oc}} = \frac{J_{mp}*V_{mp}}{J_{sc}*V_{oc}}$$ (eq. 2.1)

Thus, the FF is a measure of how ideal, or how close to a square the shape, the J-V curve is, as illustrated in Figure 2.2.

The efficiency of a solar cell, defined as the ratio between the obtained maximum power output and the power input of the incident light (P_{in}), is referred to as the power conversion efficiency (PCE) and is expressed as:

$$PCE = \frac{P_{max}}{P_{in}} = \frac{FF*J_{sc}*V_{oc}}{P_{in}}$$ (eq. 2.2)

11
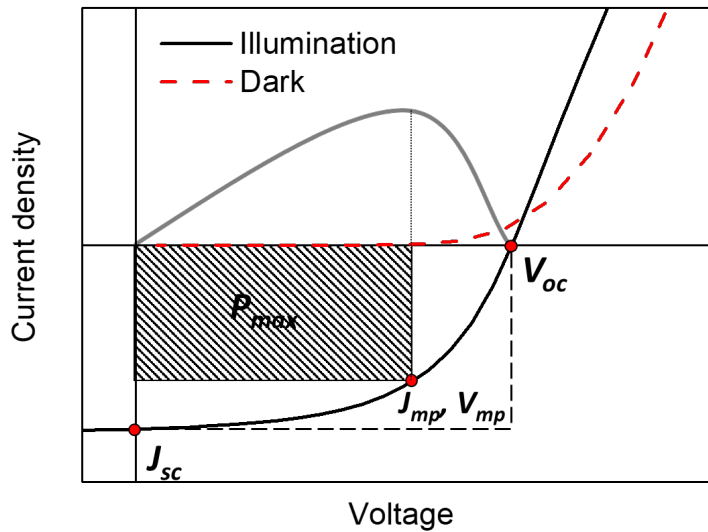
Figure 2.2: Example *J-V* curve and dark curve for PTB7-Th:PC$_{71}$BM active layer polymer solar cell for illustration of J$_{sc}$, V$_{oc}$, and *P$_{max}$* (*J$_{mp}$* * *V$_{mp}$*).

2.2.1 Performance - Shockley-Queisser limit

Evaluation of the performance of solar cells, including PSCs, is normally conducted with a solar simulator operating at the standard air mass 1.5 (AM1.5) Global solar irradiance output, illuminating the device through the bottom electrode. The AM1.5 Global with the ASTM International Standard developed by the American Society for Testing and Materials is designed for flat plate modules, defining one-sun as a solar radiance of 100 mW cm^{-2}.

The absorption within the solar spectrum of the photoactive layer, defines the theoretical upper efficiency limit introduced in 1960 by William Shockley and Hans J. Queisser (Figure 2.3).[4] This theoretical maximum efficiency for a single-junction solar cell is deduced from the energy gap at only radiative recombination. For PSCs this would be the band gap (a more correct term would be energy gap, however, this thesis will follow the convention used for the wider area of OPV in the use of band gap) of the active layer components. A maximum efficiency of ~33% is reached for a band gap of 1.34 eV (wavelength of ~925 nm), with high efficiencies in a range between ~1-1.5 eV. A trade-off is observed between the band gap and the cumulative photon flux (Figure 2.3). A large band gap is tied to a large V$_{oc}$ for which the device experiences a small J$_{sc}$ due to the low cumulative photon flux, the opposite being true for a high cumulative photon flux. Thus, the optimal PCE is found to be a compromise between voltage and current.
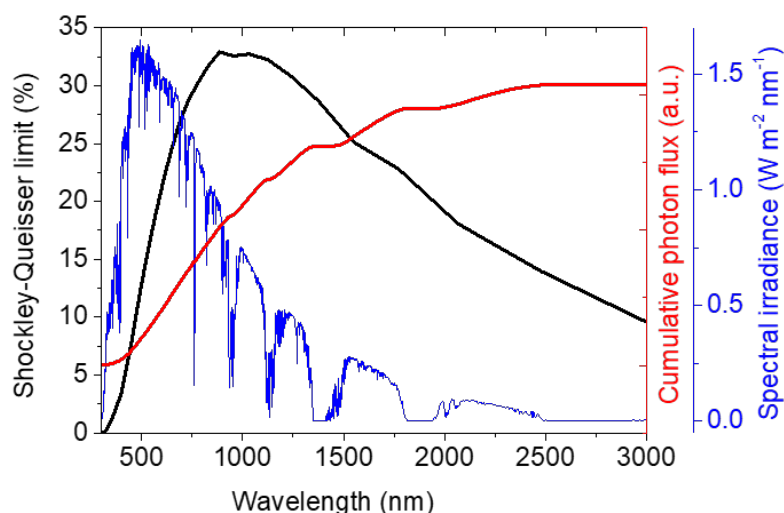
Figure 2.3: Schematic representation of the overlay of the AM1.5 Global spectral irradiance spectrum and the theoretical upper efficiency, Shockley-Queisser, limit of a solar cell.[5]

2.3 Introduction to materials

There are two versions of PSCs based on the active layer components (donor and acceptor): i) polymer-small molecule and ii) all-polymer. Historically an electron rich conjugated polymer (donor) is paired with an electron deficient small molecule (acceptor). This is no longer the norm. A large number of polymer acceptors emerged during the 2000's, sparking interest in the all-polymer active layers. Further, the same time period has seen an increase in the use of organic interface materials.

2.3.1 Conjugated polymers

In 1977 Alan J. Heeger, Alan MacDiarmid and Hideki Shirakawa demonstrated the increased conductivity of polyacetylene (PA) through doping with iodine[6], a discovery for which they later received the Noble Prize in Chemistry. This formed the foundation for research on conjugated polymers and can be regarded as the starting point for the field of OPV. The electrical properties of conjugated polymers arise from the delocalisation of π-electrons along the single-double bond alternating polymer backbone.

In detail, carbon atoms have four valence electrons in the 2p and 2s orbitals. Carbon atoms with a double bond are hybridised, showing a different symmetry, with three electrons in the sp^2 orbitals forming σ-bonds, single bonds, with one electron in the p_z orbital for the π-bond, the double bond. Electrons in the p_z orbital experience delocalisation for extended systems of alternating single and double bonds, as the integrity of the chemical structure is kept intact by the σ-bonds.[7] This allows for the electrons in the π-bond to undergo electronic transitions, giving rise to semiconductor properties. Molecular weight, inter-chain hopping, and π-π stacking hence affect the conductivity.

13

One of the reasons semiconducting conjugated polymers have attracted attention from within a number of different research fields, is the ease of which they can be modified. Put simply, the polymers can be divided in to two components, backbone and side-groups. The conjugated backbone determines the electronic properties, e.g. E_g and HOMO/LUMO levels, while the side-groups affect thermal transitions, aggregation, and solubility. Both backbone and side-groups tend to heavily influence the crystallinity of these polymers. The effect of crystallinity on PCE is not obvious. Increased crystallinity contributes to good hole transport capabilities, but there are highly amorphous polymers showing good efficiencies. Zhang *et al*. proposed miscibility as an additional design criterion to crystallinity.[8] Miscibility, rather than looking at the individual components, evaluates the donor-acceptor blend as a whole. Thus, making it another important criterion to consider for PSCs of long lifetimes and high efficiency.[9] From the text above, it is evident that the properties of conjugated polymers can have a substantial effect on overall performance. It is therefore of utmost importance to develop an understanding of how structural changes affect these properties, and in turn the PCE of PSCs.

2.3.1.1 Band Gap

For polymers the band gap (E_g), or energy gap, is affected by a number of parameters. These include molecular weight, bond length alternation, torsion angle, aromatic resonance energy, substituents, and intermolecular interactions.[10] Efficient strategies have been developed for tuning of the E_g of polymeric semiconductors. These strategies include i) altering the quinoid-aromatic ground state equilibrium, ii) the introduction of electron withdrawing/donating substituents, iii) the so-called push-pull approach of alternating D-A units as well as iv) the co-planarity approach. These strategies are explored further in following sections.

The quinoid form of polymers based on aromatic structures is less energetically stable than the aromatic form due to the breaking of aromaticity, thus, resulting in a narrower band gap.[11-12] This narrowing results from a shift in equilibrium toward the quinoid mesomeric structures, causing the alternating bond length difference to decrease, as is illustrated in Figure 2.4. A low Eg of 1 eV was achieved by Bredas *et al.* for the polymer polyisothianphthene (PITN) in 1985, by pushing the equilibrium toward the quinoid form.[13] In this example the larger resonance energy of the benzene compared to the thiophene moiety alters the equilibrium of the polymer backbone to favour the quinoid form.
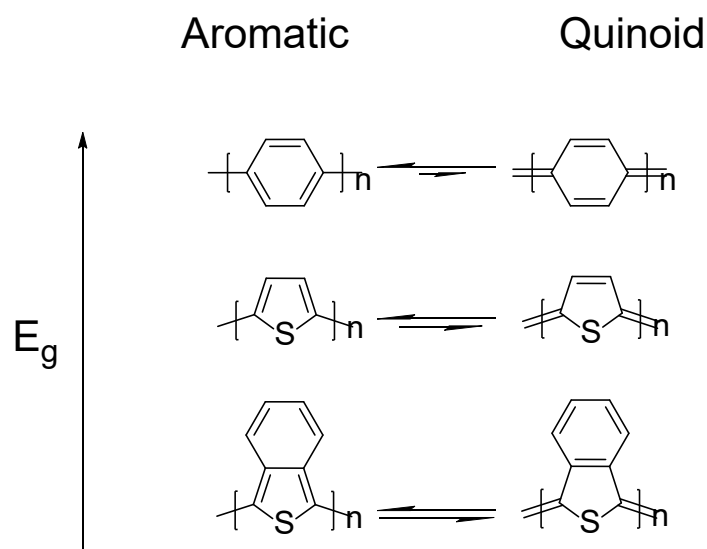
Aromatic   Quinoid

Figure 2.4: Illustration of the equilibrium between aromatic (left) and quinoid (right) character for poly(paraphenylene) (PPP), poly(thiophene) (PT) and poly(isothianaphthene) (PITN), shown in respective order with quinoid character increasing from top to bottom.

Bredas and Heeger showed in 1993 that the incorporation of electron-withdrawing/donating substituents in the polymer backbone can also be an effective strategy for bandgap modification.[14] There is a tendency for electron-donating groups to up-lift the energy levels, showing a larger rise in HOMO level than LUMO level. The opposite is true for electron-withdrawing groups with a downshift of the energy levels, showing a larger decline in LUMO level than HOMO level. An effective utilisation of this strategy is the fluorination[15-17] of many donor polymers for narrower E_g.

The push-pull strategy affects the E_g via two processes, with a shift toward the quinoid mesomeric structure as well as hybridisation of the donor and acceptor molecular orbitals. Alternating donor units and acceptor units of the polymer backbone facilitate an electron push-pull effect causing internal charge transfer (ICT) and delocalisation. This increases the double bond character in between the monomer units and shortens the bond length, i.e. decreasing the alternating bond length difference, for a narrower band gap.[10] Concomitantly, hybridisation of the molecular orbitals of donor and acceptor units will form new HOMO and LUMO levels for the polymer[18-19], as illustrated in Figure 2.5. Additionally, the optical absorption of the polymer is red shifted (lower E_g), which is typically desired for high PCE materials.[20] Thus, push-pull is the most widely applied approach for band gap tuning/modification.[21-22]

15
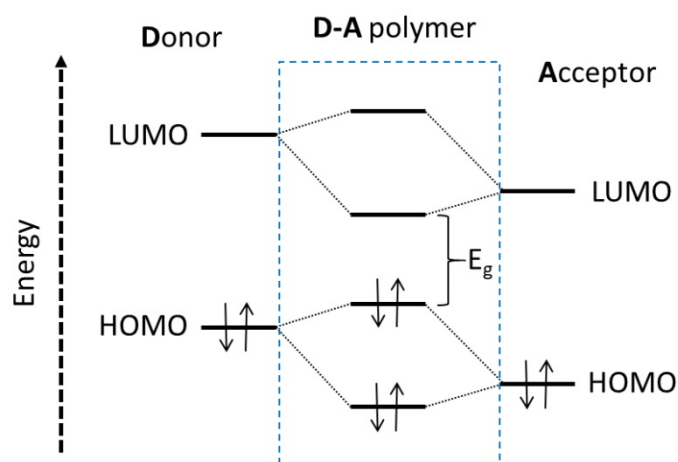
Figure 2.5: Illustration of hybridisation of molecular orbitals for a D-A polymer.

The delocalisation of electrons via induced π-π stacking also results in a narrower band gap.[23] Lowering the torsion angle, i.e. increasing co-planarity, decreases the steric hindrance for efficient packing, inducing π-π stacking in the solid state. Further, substituents can have both positive and negative effects on the co-planarity, either enhancing supramolecular ordering or disrupting it via steric hindrance. Enhancing the supramolecular ordering, i.e. crystallinity, affects not only the E_g but also charge carrier transport and morphology, which is further discussed in coming sections.

2.3.1.2 Morpology

Disregarding the electrochemical properties, morphology is the single most important parameter for high efficiency PSCs. There are two pathways to influencing the morphology; synthetic (modification of chemical structure) and processing procedure/device engineering (altering of processing conditions/device architecture). This section focuses on the synthetic pathway and the parameters that can be tuned with this approach. These include:

- Crystallinity / π-π stacking
- Solubility
- Stability
- Photon absorption

of which the latter two are highly dependent on the polymer backbone/small molecule core unit. Crystallinity and solubility on the other hand are easily tuned without affecting the fundamental properties that are tightly connected to the polymeric backbone/molecular core. Therefore, modifications are focused on these properties, exploring synthesis options of NDI based materials.

For crystallinity, a trade-off is observed between efficient charge separation (smaller crystals domains) and good charge transport (larger crystal domains) in thin films. As a result, tuning of the crystallinity,

with its indirect connection to blend morphology, has proven an effective strategy to boost PCE. Matching of crystallinity for donor and acceptor materials has contributed to enhanced morphologies and also high PCEs.[24-25] The crystallinity is modified via backbone/core unit or side-group engineering. Introduction of disorder, due to steric hindrance through side-group engineering of branched alkyl chains, reduces crystallinity and increases domain spacing. In a study conducted by You *et al.*, it was observed that the alkyl branching point directly influences the domain spacing, showing shorter distances the further out from the backbone the branching point is situated.[26] For polymers, the crystallinity is additionally affected by the overlap of π-orbitals in the conjugated backbone. Thus, introduction of irregularities reducing this overlap can decrease the crystallinity. This was observed in a study by Li *et al.* where the crystallinity of N2200 was fine-tuned via the substitution of bithiophene for thiophene in the conjugated backbone.[27]

In addition to crystallinity, the morphology in thin films is to a high degree affected by the solubility of both donor and acceptor polymers/small molecules in the processing solvent. High performance polymers possess narrow E_g with high mobilities and large absorption coefficients. These materials typically consist of large aromatic, flat and often rigid backbones with large intermolecular interactions, leading to low solubilities. Solubilising alkyl substituents are added to improve processing conditions and enable high molecular weights. Generally, highly soluble polymers are desirable. However, negative effects have been observed when the solubilising substituents become too large, affecting charge carrier transport, phase separation, and charge carrier recombination.[28] Further, the torsion angles determine the flatness of the polymer, affecting the solubility. Lower angles (flatter) induces stronger packing while higher angles (twisted) prevents packing.

2.3.1.3 Molecular Weight

The performance of OPV devices is also highly dependent on the molecular weight of the polymer components. The molecular weight has been found to influence the charge carrier mobility, solubility, crystallinity, morphology, thermal stability and miscibility in multi component blends. In general, a trade-off is observed between charge carrier mobility and thermal stability (high molecular weight) and solubility (low molecular weight) with crystallinity and miscibility dependent largely on chemical structure. Characterisation of polymer molecular weights is therefore of utmost importance for PSC applications.

Polymer molecular weight determination is based on the average weight and the associated weight distribution width. There are two common ways of presenting the molecular weight. These are the number-average molecular weight ($\bar{M}_n$) and the weight-average molecular weight ($\bar{M}_w$),[29] with $\bar{M}_n$ defined as the sum of weights of individual polymer chains divided by the number of chains in the sample:

$$\bar{M}_n = \frac{\Sigma_i N_i M_i}{\Sigma_i N_i} \tag{3.1}$$

and N_i being the number of polymer chains of mass M_i. Similarly, M_w is defined as:

$$\bar{M}_w = \sum W_i M_i = \frac{\Sigma_i N_i M_i^2}{\Sigma_i N_i M_i}$$
(3.2)

where W_i is the weight fraction.

Another important measure is the polydispersity index ($Đ_M$). This is a measure of the homogeneity of the population, defined as the ratio between $\bar{M}_w$ and $\bar{M}_n$:

$$Đ_M = \frac{\bar{M}_w}{\bar{M}_n}$$
(3.3)

Poly(3-hexylthiophene) (P3HT) is perhaps the most studied conjugated polymer and Ma *et al*. concluded that a mixture of a ratio of 1:4 for high/low molecular weight polymer yielded the best performance in a polymer: fullerene system.[30] This is due to combination of superior charge carrier transport of the high molecular weight component and the excellent crystallinity of the lower molecular weight segments.[30] Thus, a controlled molecular weight is in this case desired over a high molecular weight. Another study by Kang *et al*. showed that poly[(2,5-bis(2-hexyldecyloxy)phenylene)-alt-(5,6-difluoro-4,7-di(thiophen-2-yl)benzo[c][1,2,5]thiadiazole)] (PPDT2FBT) yielded better PCEs with increasing molecular weight, from low to medium to high, when paired with poly[[N,N′-bis(2-octyldodecyl)-napthalene-1,4,5,8-bis(dicarboximide)-2,6-diyl]-alt-5,5′-(2,2′-bithiophene)] (N2200).[31] This is due to an increased π-π stacking and excellent aggregation property. These studies highlight that there is not a single solution for all systems, but rather that an evaluation should be made on a case-by-case basis.

2.3.2 Small Molecules
Small molecules behave quite differently compared to polymers, with respect to solubility, crystallinity and band gap. Unlike polymers, which are populations of segments with varying molecular weight, small molecules have a highly defined structure with no batch-to-batch variability. This has a negative impact on the charge transport capabilities of small molecules; they simply lack the "highways" provided by the polymer backbone. Thus, small molecules are highly reliant on finely tuned crystal domains for efficient charge carrier transport as well as charge carrier generation.

2.4 Donors

The chemical structure of the first conjugated polymer, PA,[32] was extremely simple in its conjugation (Figure 2.6). Since then the structures have progressively become more complex with extended conjugation as well as the inclusion of intricately designed side-groups. During the 00's the second generation donor polymer poly(3-hexylthiophene) (P3HT) dominated the field.[33] The third generation has since taken over, with the last decade seeing a strong growth of polymer donor materials. This, the

latest generation, include materials such as poly[4,8-bis(5-(2-ethylhexyl)thiophen-2-yl)benzo[1,2-b;4,5-b']dithiophene-2,6-diyl-alt-(4-(2-ethylhexyl)-3-fluorothieno[3,4-b]thiophene-)-2-carboxylate-2-6-diyl)] (PTB7-Th), the first donor in a PSC exceeding a PCE of 10%.[34-35] This polymer is based on the popular benzodithiophene building block used in a number donor polymers.[36] poly[(thiophene)-alt-(6,7-difluoro-2-(2-hexyldecyloxy)quinoxaline)] (PTQ10), published by Sun *et al.*, is another prominent example. This polymer was synthesised in an overall yield of 87.4% in a short two-step synthesis route from commercially available materials.[37]

The year 2018 experienced a large increase in record PCEs for single-junction PSCs including the first device to reach a PCE of over 14%. This device had an active layer consisting of PBDB-T-2Cl:IT-4F (D:A) showing a very high PCE of 14.4%.[38] However, this new record efficiency was rapidly eclipsed by Zheng *et al.* achieving a highest PCE of 14.57% for the donor polymer PBDB-T-2Cl, based on a chlorinated BDT building block and coupled with a BDD unit, when paired with IT-4F.[39] This record did not last long either. Yuan *et al.* recently reported a new NFA absorbing in the near infra-red called Y6 that when paired with the commercial polymer PM6 achieved a highest PCE of 15.7%.[40] Fine tuning of the NFA Y6 (BTP-4F) via the substitution of the fluorine atoms with chlorine atoms led to the newly formed BTP-4Cl acceptor achieving a new record PCE of 16.5%, when paired with donor polymer PBDB-T-2F.[41]
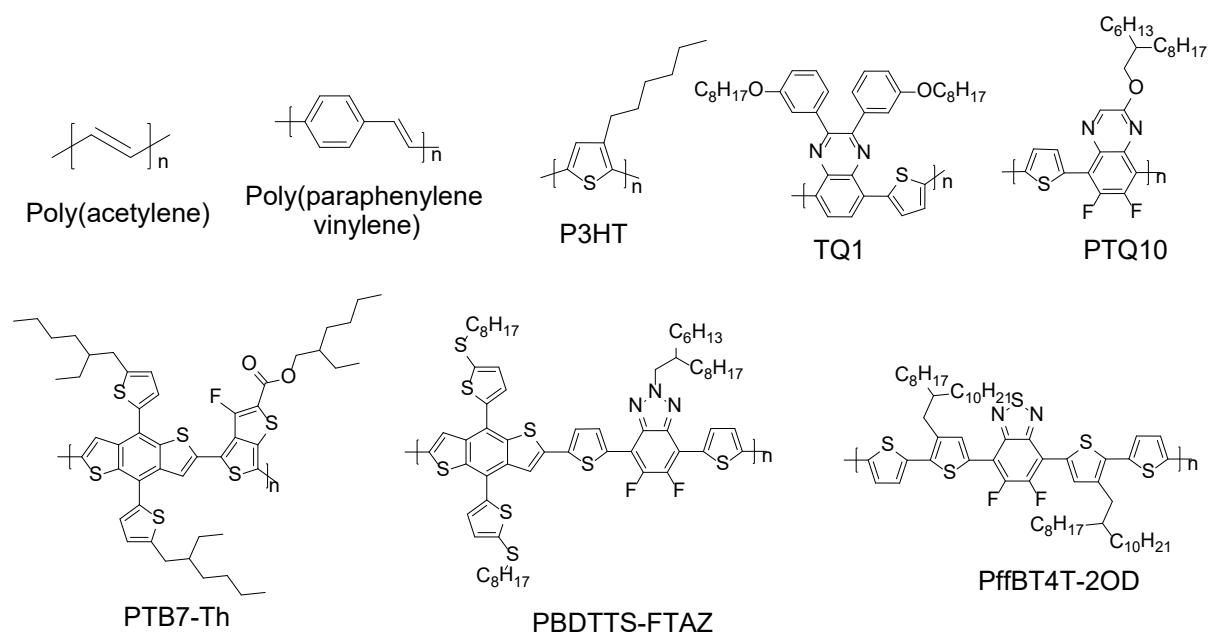
Figure 2.6: Chemical structures of an array of conjugated polymer donors.

2.5 Acceptors

2.5.1 Fullerenes

In 1996, Sir Harold W. Kroto, Richard E. Smalley and Robert F. Curl, Jr. were awarded the Nobel prize for their discovery of fullerene, also referred to as buckminsterfullerene, in the 80's.[42]. Fullerene

derivatives as acceptor materials have dominated the PSC research for the past two decades. The compounds have in general attracted major attention for their usage in PSCs but none more than the derivatives $PC_{61}BM$ (Figure 2.7) and $PC_{71}BM$ which was discovered in the 90's.[43-44]

These fullerene derivatives have advantages of high electron affinity and ultrafast charge transfer capability.[45-46] The isotropy of the football-like sp^2 hybridised carbon structure provides additional advantages over the typically anisotropic non-fullerene acceptors (NFAs) that tend to rely on charge transfer via intermolecular hopping. The compounds do however suffer from a high lying LUMO level compared to many other acceptors, and the optical absorption in the visible region is low[47]. This results in low open-circuit voltages for PSCs with polymer:PCBM blends. The thermal stability of fullerene containing devices is low, phase separation with large scale crystallisation tend to occur at elevated temperatures limiting annealing and operating temperatures.[48] This strong crystallisation tends to have extensive negative impact on the PCE. Despite the many drawbacks of the fullerenes $PC_{71}BM$ was used as the acceptor in the first PSC to reach over 10% PCE.[49]
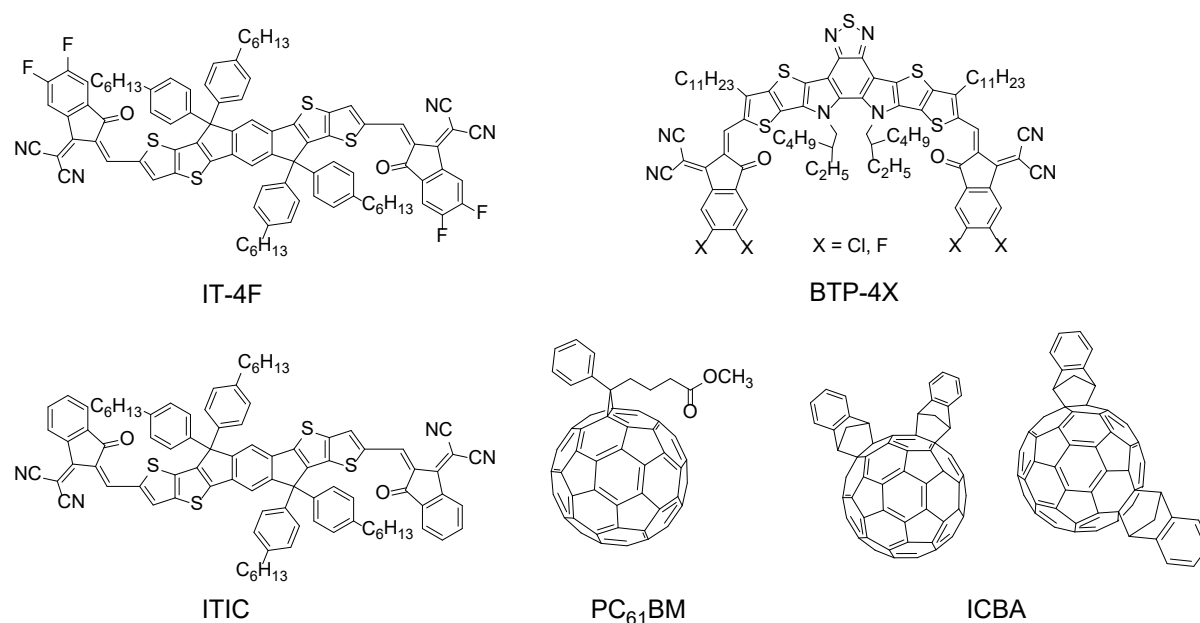
Figure 2.7: Small molecule acceptors with ITIC, $PC_{61}BM$, and ICBA from left to right with the latter shown as a mixture of regioisomers.

2.5.2 Small molecule non-fullerene acceptors (NFA)

The development pace of NFAs has picked up substantially during the last 5 years with over 100 new materials published, with PCEs having surpassed fullerenes as well as acceptor polymers. The first NFA was a perylene diimide (PDI) compound processed via vacuum deposition in a planar bilayer heterojunction OPV cell, published in 1986 by C. W. Tang.[50] PDI compounds have remained popular, despite the early introduction, due to their excellent electron mobilities, absorption coefficients, and high stability.[51-52]

The success of the IDT based IEIC[53] and ITIC[54] compounds has greatly contributed to the widespread application of the acceptor-donor-acceptor (A-D-A) unit configuration. In this configuration, a donor core is flanked by two acceptor moieties creating a so called push-pull system for extended conjugation as well as enabling facile tuning of the chemical structure.[55] These advantages have led to a large number of published A-D-A NFA structures based on a wide variety of building blocks. The current record PCE device contains the NFA IT-4F,[38, 56] based on the popular IDT block.

2.5.3 Polymer acceptors

The number of acceptor compounds has lagged behind the rest of the OPV research field. A likely cause for this could be the dominance of fullerenes all through the 2000's. The situation has been particularly severe for polymers with the NDI-thiophene based polymer N2200[57] being the only widely used material up until a few years ago. The highest PCEs reached for this material is 10.12% by Li *et al.* and 10.1% by Fan *et al.*[58-59] The high PCE achieved by Li *et al.* originated from the use of a ternary blend, utilising Förster Resonance Energy transfer (FRET), achieving low recombination, and thus, a high fill factor. The energy transfer mechanism of FRET was first demonstrated successfully in all-PSCs by Fan *et al.*,[60] where the energy transfer from a low mobility to high mobility donor was responsible for elevated efficiencies. However, the current record for all-polymer solar cells was achieved by Yao *et al.* with the acceptor polymer PFBDT-IDTIC and donor polymer PM6, reaching a highest PCE of 10.3%.[61]

Derivatives of N2200 have been developed and synthesised in efforts to improve the photovoltaic performance. Strategies include side chain engineering, the substitution of thiophene for other donor segments as well as the inclusion of a second donor component in terpolymer synthesis.[27, 62-66] The latter strategy has so far been the most successful, with efficiencies exceeding 9% in all-polymer solar cells for acceptor PNDI-T10 (Figure 2.8). In this case the crystallinity was tuned via the incorporation of 0.1 eq. of thiophene (0.9 eq. bithiophene) in the polymer backbone, leading to high PCE for a ternary blend with the inclusion of the third component providing complementary absorption.[67]

Further, non-NDI based acceptor polymers are uncommon, showing low efficiencies. Li *et al.* developed the acceptor polymer PDPP2TzT (Figure 2.8), based on diketopyrrolopyrrole-isoindigo units, showing a high V_{oc} of 1.07 V with moderate PCE of 4.2% in all-PSCs (donor PBDTTS-FTAZ).[68] P-BNBP-fBT synthesised by Long *et al.* does instead utilise a bridged bipyridine unit, this polymer reached a PCE of 3.38%.[69] In addition NDI containing acceptor polymers such as PNDI-RDN[70] and PNNT[71] have shown moderate PCEs.

PDI based acceptor polymers is the only larger branch that has come close to rivalling the dominance of the N2200 derivatives. Guo *et al.* achieved a highest PCE of 8.59% for the PDI based polymer NDP-V (Figure 2.8) when paired with PTB7-Th.[72] The backbone was stiffened via chemical modification, leading to a favourable molecular packing and improved morphology for a record PCE. High PCEs

were also reached for a series of PDI polymers with varying alkyl chain length with PDI-V-C7 achieving a highest PCE of 7.44%.[73] Overall, the number of published acceptor polymers still remain low. Thus, the efficiencies of all-polymer solar cells are limited, and unless further efforts are taken within material development, the discrepancies of this material group are likely to persist.
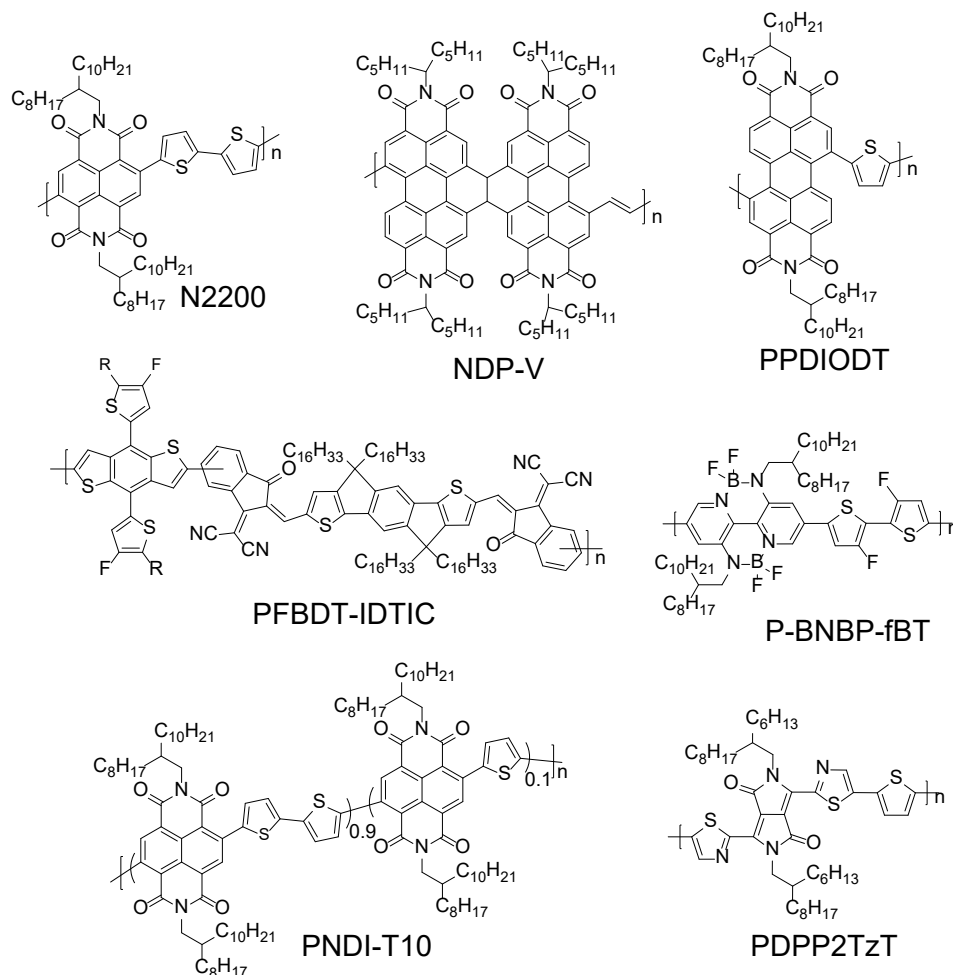
Figure 2.8: Chemical structures of acceptor polymers.

2.6 Interface materials

Interface layers are incorporated in polymer solar cells as a means to increase the PCE, in addition to strategies involving the active layer or the electrodes. Interface layers can consist of a wide array of different materials; p-type, n-type, inorganic, organic, hybrid, conducting, semiconducting, and even non-conducting materials are used. They tend to be divided into categories based on their primary function in regard to the charge selectivity: i) electron transporting layer (ETL), ii) hole transporting layer (HTL), iii) electron blocking layer, and iv) hole blocking layer. Though, there are a number of additional functions these materials fill: [74-75]

- Surface modification
- Tuning of energy levels/electrode work functions (WF)

- Optical spacer
- Protective layer

Modification of the surface energy is especially important in cases of orthogonal solvent processing, where the surface energy determines the wetting and deposition conditions of the layer on top. Contrary, the interface material should also interact with any underlying layer favourably to facilitate the formation of a uniform film as well as complete coverage. For the use of hydrophobic PEDOT:PSS in inverted devices surfactants have been used to facilitate film formation on the more hydrophobic active layer.[76-77] Furthermore, surface modification also include physical features such as surface roughness and topography. These affect sequentially deposited layers and any defects or larger variations are often translated through the solution processed layers of the device.

Charge selectivity is achieved through the careful selection of materials with matching Fermi levels and energy levels. In an ideal case the HOMO level of the HTL aligns with the quasi-Fermi level of holes ($E_{f,h}$) in the BHJ layer, for efficient charge extraction with minimal resistance, while LUMO sits above the quasi-Fermi level of electrons ($E_{f,e}$), as to block electrons and minimise V_{oc} losses, Figure 2.9.[78-79] Inversely for an ideal ETL, that is, LUMO aligned with $E_{f,e}$ and HOMO below $E_{f,h}$.

Tuning of the work function, in the case of pendant amine groups, is related the free electron pair on the nitrogen atom forming an interfacial dipole with the electrode (often ITO).[80] According to a recent study performed by Lee *et al*. the introduction of electric dipole layers (EDLs) assists in efficient charge extraction from the active layer by shifting the vacuum levels at the metal-semiconductor interfaces, resulting in a larger built-in electric field and a decrease in geminate recombination.[74]
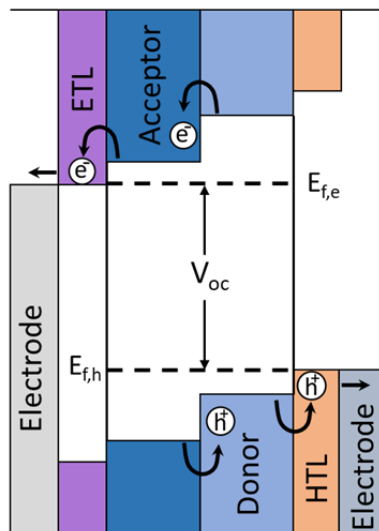
Figure 2.9: Schematic representation of the energy levels and charge carrier transport in a device incorporating both an ETL (with hole blocking ability) and an HTL (with electron blocking ability).

2.6.1 Metals and metal oxides

Inorganic interface layers often consist of metal oxides, e.g. titanium oxide (TiO_2), molybdenum oxide (MoO_x), wolfram oxide (WO_3),[81] with the n-type ETL zinc oxide (ZnO) being one of the most common materials. Other inorganic ETLs include cesium carbonate (Cs_2CO_3) and lithium fluoride (LiF). These inorganic materials are typically processed via thermal evaporation methods, or alternatively via sol gel solution processing with post annealing at elevated temperatures.[79, 82-83] One exception is the ambient temperature solution processed nanoparticle ink of ZnO, which was successfully demonstrated in high performance devices, without post annealing.[84]

2.6.2 Organic interface materials

Of the organic materials it is instead the polymer poly(3,4-ethylenedioxythiophene):poly(styrenesulfonic acid) (PEDOT:PSS) with its unique properties, including charge carrier capability, that has been favoured (Figure 2.10). A range of PEDOT:PSS inks for use in OPVs are commercially available. These inks are typically tailored for a specific application in the device and may incorporate performance enhancing components like silver nanowires. Thus, PEDOT:PSS is commonly used as either ETL, HTL, or electrode in combination with other supporting layers of interface materials or inorganic electrodes, e.g. silver mesh.[85] The hygroscopic character of PEDOT:PSS can create issues with the stability, hence thermal annealing is conducted in certain cases to lower the water content and reach optimal efficiency.[86-87] Further, the PSS unit is acidic and the polymer has been observed to affect the long term stability of adjacent layers.

The modification of the ITO work function has been demonstrated with non-conducting polymers that contain pendant amine groups such as poly(4-vinylpyridine) P4VP and polyethylenimine (PEI).[88-89] These interlayers effectively work as insulators at any thickness above the threshold for tunnelling, thus, the thickness control is of utmost importance. The advantage of these materials is that they can be solution processed from green solvents in orthogonal device fabrication and that they are inexpensive bulk polymers relative to the more complex semiconducting polymers.

The amine containing p-type material poly[(9,9-bis(3'-(N,N-dimethylamino)propyl)-2,7-fluorene)-alt-2,7-(9,9–dioctylfluorene)] (PFN) was one of the first semiconducting polymers employed by Huang *et al.* in PSCs as ETL for a conventional device architecture.[90] The same group later published a study on NDI-fluorene based conjugated polymers (PNDIT-F3N and PNDIT-F3N-Br) for which the impact of tertiary versus quaternary amine, in this case with bromine counter ion, on conductivity was investigated.[91] Interestingly, the conductivity showed a photo response for the tertiary amine containing material, increasing under light. Comparatively the quaternary amine instead experienced constant conductivity at high levels. This difference could be attributed to the doping mechanism for which the tertiary amine shows a photo response while the quaternary amine is constantly doped.[92]
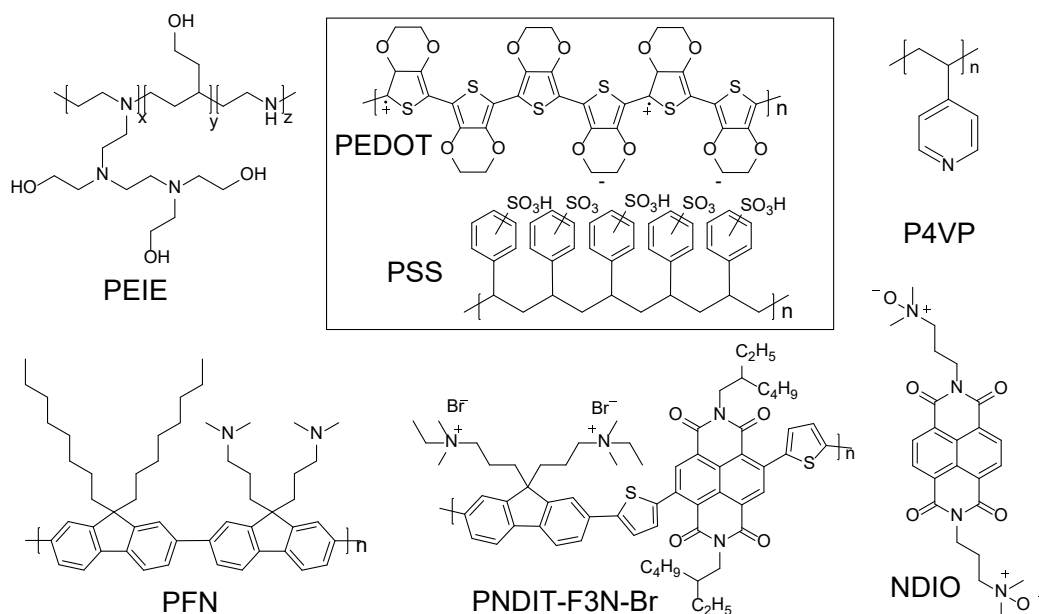
Figure 2.10: Chemical structure of organic interface layers.

Zwitterionic small molecules NDIO and PDINO have also been used successfully in PSCs as well as perovskite solar cells.[93-94] These materials both contain an *n*-oxide pendant group, providing a good solubility in green solvents, e.g. water and alcohol, as well as a free electron pair available for WF modification, via the formation of an interfacial dipole.

2.7 Device structures

2.7.1 Single layer solar cell

The first organic solar cells utilised a single layer structure, a homojunction. These solar cells consisted of an active organic material sandwiched between two metal electrodes. This type of device structure showed extremely low efficiencies, for which the explanation can be found in the mechanism for charge carrier formation. The Frenkel excitons, created upon light absorption, require more energy than a homojunction can provide in order to dissociate, hence the charge carrier generation is extremely low [95].

2.7.2 Bilayer planar hetero-junction

Bilayer OPVs were introduced during the 80's and the first bilayer planar heterojunction solar cell in the 90's.[95] The active material in a bilayer planar heterojunction consists of a donor and an acceptor. These are consecutively deposited onto a substrate by evaporation resulting in a flat interfacial surface and small surface area. Efficiencies are still relatively low, ~1%, for this type of solar cell, which is a large improvement compared to the homojunction. The explanation for the low efficiencies can again be related to the formation of charge carriers. The exciton diffusion length limits the number of excitons reaching the donor-acceptor interface and hence the charge carrier formation as well as efficiency. [95-96]

2.7.3 Bulk heterojunction

The bulk heterojunction concept, demonstrated by Heeger *et al.* in 1995[4], has been almost exclusively used since its introduction in the field[44]. The donor and acceptor materials are intermixed in bulk heterojunction solar cells forming an interpenetrating phase separated network with a large interfacial surface area, see Figure 2.11c.[96] The exciton diffusion length (1-10 nm)[97] would in the ideal case be half the length of the thickest donor – acceptor domains in the active layer, providing all excitons a chance to diffuse to the nearest interface to dissociate.[98-99]

Manufacturing methods in use today create an interspersed material where conduction partly occurs through hopping between acceptor – acceptor/donor – donor domains. If continuous domains could be achieved they would prevent hopping, and as a result, the recombination of excitons. Morphology control is critical for parameters, such as domain size and interfacial surface area, that directly affect the efficiency of bulk heterojunction solar cells.[95]
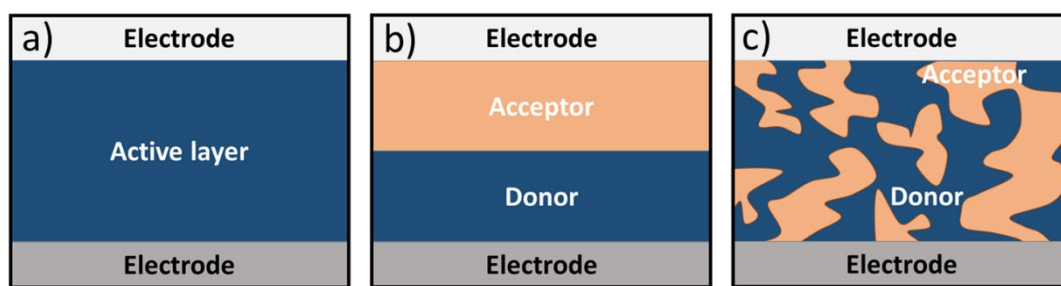
Figure 2.11: a) Single layer solar cell, b) bilayer planar heterojunction, and c) bulk heterojunction solar cell.

2.7.4 Ternary blends

Three component BHJ systems, i.e. ternary blends, with either $D:A_1:A_2$ or $D_1:D_2:A$ configurations are interesting alternatives to the normal two component BHJ active layer or tandem PSCs. These systems utilise some of the benefits of the latter without suffering from the complex processing associated with tandem cells.[100] Potential advantages of ternary blends include enhanced light absorption, efficient charge extraction, increased open circuit voltage and suppression of trap-assisted recombination.[101] Additionally, the nature of a three component system also contributes to good morphology control and increased thermal stability[102].

The BHJ morphologies of ternary blends can be divided into four categories based on where the third component is located. These categories are i) parallel, ii) at the interfaces, iii) embedded and iv) in an alloy (Figure 2.12). For the first three cases charge transfer can take place either through parallel or cascade (Figure 2.12e). However, in the case where an alloy is formed the components are electronically coupled and a new charge transfer state is created, however, the materials retain their individual light absorption.[101]
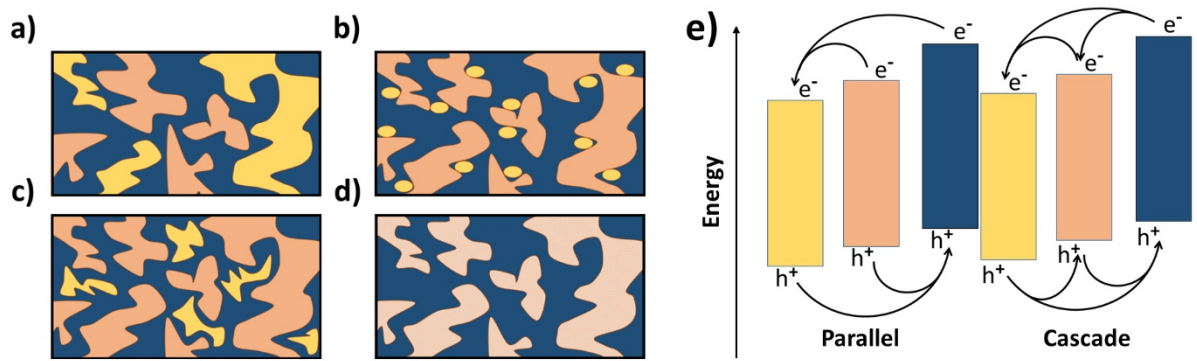
Figure 2.12: Schematic of the bulk heterojunction morphology in ternary blend solar cells, showing the third component in either: a) parallel, b) at the interface, c) embedded or d) alloy. e) Illustration of the parallel and cascade charge transfer mechanisms present in ternary blend PSCs.

2.7.5 Device architectures

The conventional device architecture, typically utilises ITO and PEDOT:PSS[85] as anode and hole-transport layer, respectively (Figure 2.13a). However, this architecture typically suffers from ITO degradation due to the aforementioned acidic and hygroscopic properties of the widely used interface material PEDOT:PSS. Further, the use of unstable low work function metals, e.g. calcium and aluminium, for top electrode applications contribute to low stability.[103] The inverted device architecture was introduced in response to these issues (Figure 2.13b), effectively avoiding the use of low work function electrodes as well as the degradation susceptible ITO-PEDOT:PSS interface. While the PEDOT:PSS is made redundant at the cathode, leading to the inclusion of ZnO as cathode interface layer,[82] the low work function electrodes are instead replaced by the much more stable Ag as anode. This architecture contributes to a better stability than that experienced by the conventional architecture.
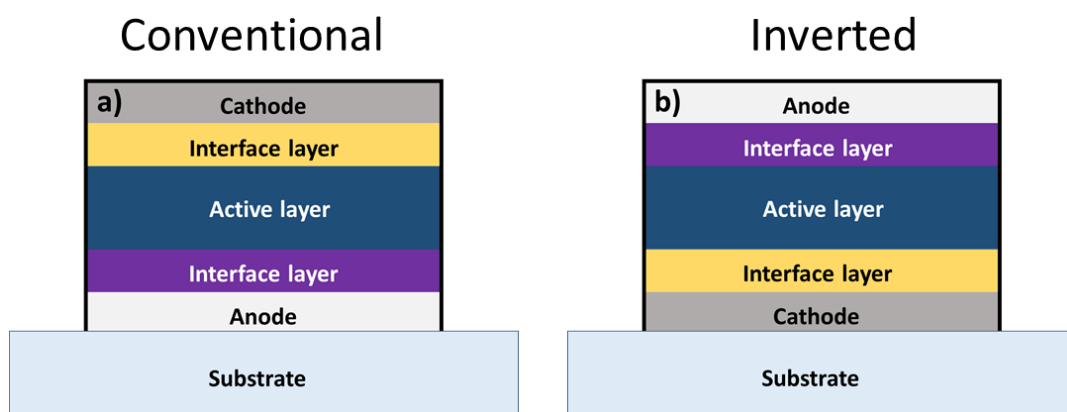
Figure 2.13: Schematic of a) conventional and b) inverted device architecture.

2.8 Morphology

Active layer blend morphology is crucial for the performance of PSCs. Optimal morphologies for a bulk heterojunction (BHJ) active layer consist of tightly interspersed donor-acceptor domains with spacing equal to or shorter than half the exciton diffusion lengths, allowing maximum charge carrier dissociation. Concomitantly, these domains should provide continuous networks for efficient charge transport of the charge carriers through the active layer blend, thereby avoiding build-up of space charges.[104-105] Further, the domain purity affects the electric field strength at the donor-acceptor interface with high domain purities contributing to an efficient exciton dissociation via the formation of a stronger electric field. Contrarily, in a homogenous active layer blend the donor-acceptor interface is absent and no electric field is formed, resulting in a non-functioning device. Thus, the morphology is of utmost importance in improving the photophysical properties, maximising exciton dissociation, and reducing charge carrier recombination as well as improving fill factor.

There are several widely adopted strategies for modification of the active layer blend morphology. These include, but are not limited to; i) chemical modification of active layer materials to induce/reduce π-π stacking or crystallinity, ii) matching of the active layer components, e.g. surface energies, for altering of domain size and domain purity via improved miscibility,[106] iii) the use of high boiling point additives for a prolonged drying process during which the swelled polymer chain configuration can relax,[107-108] iv) gelling of the active layer blend upon processing to lock-in the morphology during deposition, either via chemical modification or solvent choice[109-110].

2.9 Processing

PSCs is an emerging technology and the research field is still quite young. This is reflected in the processing, where the small-scale laboratory technique of spin coating dominates. Further, the active layer, to date has almost solely been processed from chlorinated solvents of high toxicity and large environmental impact, with a few noteworthy exceptions[111-113]. Thus, the processing of laboratory devices deviate extensively from the green solvent printing required for upscaling.[114-115] There are however a number of roll-to-roll compatible techniques that have been applied for the manufacture of flexible solar cells:[116]

- Slot-die printing[117]
- Screen printing[118]
- Spray-coating[119]
- Inkjet printing[120]
- Knife-over-edge coating[121]

These processing techniques do not only supply roll-to-roll compatibility. A strong correlation with low cost potential is also present due to minimal material waste and cheap substrates, combined with low

labour intensity. In addition to these processing techniques, blade coating (commonly referred to as doctor blading) has emerged as a popular technique for manufacturing of large lab scale devices on the square-centimetre scale. Although similar to knife-over-edge coating (moving substrate), blade coating (moving blade) is not fully roll-to-roll compatible. However, blade coating could be considered a bridging technique between the laboratory scale devices and large-scale solar cells.[122-123] A complementary technique to the above mentioned processes is the arguably underutilised, lamination processing.[124-126] Unlike the fully sequential deposition methods, for which each layer is deposited on top of the previous, this technique involves the sandwiching of two layers or layer stacks under elevated temperature and pressure. Bergqvist et al, using the lamination technique with the active layer as an adhesive, demonstrated a fully printed solar cell with a PET / PEDOT:PSS / Active layer / PEI / PEDOT:PSS / PET device architecture.[127] Although, the PCE is low at 2.6% it is still a noteworthy achievement with solution processed flexible solar cells from a scalable manufacturing procedure using only low cost materials. This device architecture could avoid a secondary encapsulation step, otherwise necessary for minimising the degradation and extending the device lifetime, if the encapsulation material/barrier foil can be incorporated into lamination process or incorporated in the substrate.

Although, the areas of the laboratory scale devices are typically measured in square-millimetres, a number of groups have published devices with areas exceeding 10 cm^2.[84, 128-131] Of note, in the work by Gu *et al*. a maximum PCE of 5.1% was reached for slot-die coated devices manufactured in a continues roll-to-roll process.[129] This is the current record PCE for continuous roll-to-roll processing and the first device to exceed the important barrier of 5% efficiency.[132-138] This is a significant increase compared to previous work on continuous roll-to-roll processed devices, which has shown efficiencies averaging 2-3%, highlighting the rapid progress within the field. These results, highlighting progress of PSCs with large device areas, are not to be confused with large area active layer deposition, for which PCEs of over 9% has been achieved with slot-die coating for device areas of 0.1 cm^2.[139]

Apart from the major challenge of translating morphologies from laboratory scale processing in rigid substrates to roll-to-roll compatible processes on flexible substrates there are additional obstacles that need to be addressed. These include the adoption of new deposition methods for electrodes, e.g. printing of silver inks,[114] the switch to polymeric electrodes, and delamination due to poor thermomechanical matching in flexible devices[103]. The thermal stability of the substrates should also be considered with regard to annealing of the active layer, for which the substrate potentially limits annealing temperatures.

2.9.1 Solvents & nanoparticle inks

As mentioned previously, the use of chlorinated solvents, e.g. *o*-DCB, is not compatible with large scale roll-to-roll processing. Consequently, a shift toward less harmful solvents such as *o*-xylene, anisole, 2-methyltetrahydrofuran, and short chain alcohols are necessary to facilitate commercialisation.[115] A second option for a greener processing is the fabrication of water dispersed nanoparticle inks. These inks are prepared from either the mini-emulsion[140] or the precipitation method[141], with the active layer

components mixed in the nanoparticles. Fabrication of the inks typically requires use of organic solvents, however, the solvent can potentially be reused, forming a circular closed system.[142]

2.9.2 Solvent additives & post processing

Controlling the morphology is of utmost importance for achieving high efficiencies. Apart from material engineering, strategies for morphology control include the use of additives during processing[143] and/or post processing annealing step(s). The inclusion of a small volume percentage of solvent additives such as diiodooctane (DIO)[144] and 1-chloronaphthalene (CN)[145] can greatly improve the morphology. In the case of polymer-fullerene BHJ, Fontana *et al*. investigated the mechanism of different solvent additives, showing that low vapour-pressure additives, e.g. DIO, works as a swelling agent or plasticiser while higher vapour-pressure additives are more likely to influence the morphology by increasing crystallinity of the polymers.[146] These solvent additives have proved so effective that they have become common-practice in high performing PSCs. The second strategy, post-processing annealing include thermal annealing,[147] and solvent annealing.[108] In thermal annealing, the active layer/cell is exposed to elevated temperatures, often close to the glass transition temperature (T_g) where the polymer softens, allowing the polymer chains to relax and reorient.[148-151] Solvent annealing is either performed by exposing the active layer to solvent vapours or in a separate processing step in which a solvent is deposited on top of the active layer. In the first case a good solvent is typically used, and the annealing process works similarly to thermal annealing, allowing the polymer chains time to reorient themselves. For the latter case, the solvents range from non-solvents to good solvents, producing effects such as accumulation of one species at the top electrode.

2.10 Stability

Achieving a good stability of a PSC module under a range of varying working conditions is of utmost importance for successful commercialisation of this emerging technology. The lifetime of devices, or modules, is affected by a number of degradation mechanisms, ranging from photo oxidative to purely mechanical pathways:

- Photochemical
- Thermal
- Oxidative
- Morphological
- Mechanical

Harsh operating conditions including elevated operating temperatures or high humidity could result in an increased occurrence of stresses, drastically reducing the lifetime. Flexible substrates used for printed devices pose additional difficulties compared to rigid glass substrates, e.g. detachment in between layers due to stretching caused by handling or a mismatch in thermomechanical properties. These are

detrimental to the lifetime of PSCs.[152] Further, processing in ambient conditions could also lead to enhanced degradation caused by the presence of oxygen containing species or water. This can be specifically prominent during irradiation with the onset of photo-induced degradation. Several strategies to improve the lifetime has been developed, targeting different degradation pathways.

The pathways resulting in morphological change of the active layer have been thoroughly studied due to the strong relation to the performance. Strategies for improved morphological stability include chemical modification (e.g. side-group engineering), vitrification through introduction of a third component (i.e. formation of a ternary glass)[102, 153], and crosslinking of the active layer components[154-156].

Although many studies of the separate layers or components have been carried out there are only a few which evaluate a full module. [103] Angmo *et al*. published a one year study on full device modules in 2014 in which they identified engineering problems as the major causes of degradation for their first generation modules.[157] These issues were rectified in their second generation modules, featuring a thicker encapsulation sheet as well as a wider adhesive joint at the edges. These module edges were specifically pointed out as weak zones to stress due to the higher penetration rate of water and oxygen in the adhesive compared to the encapsulation sheet. Similar conclusions were drawn by Rivaton *et al*. in regards to the importance of encapsulation and the penetration of oxidative species.[158] It must be noted that both studies used an encapsulation sheet incorporating a UV light blocker with a cut off at the edge of the visible spectra. The mechanical stability of PSC modules were investigated by Finn III *et al.* for which the edges were concluded to be an initiating point for crack propagation during high torsion.[159] Their study further revealed bending to cause crazing of the encapsulation layer. Thus, the few published studies appear to agree that the largest improvements in stability will be achieved through the engineering and specifically encapsulation of the polymer solar cell modules in conjunction with careful selection of active layer blend.

Stability of PSCs has greatly improved during the last decade with record devices now operating over thousands of hours.[157, 160] However, a discrepancy exists between these record devices and the majority of active layer OPV materials. This is painstakingly clear for some of the high performing materials, possessing lifetimes counted in minutes under ambient conditions. Design of more robust materials, in regard to both morphological as well as photochemical degradation, is sorely needed to reach the target of a device with a PCE of 10% and a lifetime of 10 years. In addition to material development, engineering solutions for efficient encapsulation are needed for further improvements of operating lifetimes.

2.11 References

(1)   Sariciftci, N. S.; Smilowitz, L.; Heeger, A. J.; Wudl, F., Photoinduced Electron Transfer from a Conducting Polymer to Buckminsterfullerene. *Science* **1992**, 258, 1474-1476.

(2)   Perez, M. D.; Borek, C.; Forrest, S. R.; Thompson, M. E., Molecular and Morphological Influences on the Open Circuit Voltages of Organic Photovoltaic Devices. *J. Am. Chem. Soc.* **2009**, 131, 9281-9286.

(3)   Elumalai, N. K.; Uddin, A., Open circuit voltage of organic solar cells: an in-depth review. *Energy Environ. Sci.* **2016**, 9, 391-410.

(4)   Shockley, W.; Quessier, H. J., Detailed Balance Limit of Efficiency of p-n Junction Solar Cells. *J. Appl. Phys.* **1961**, 32, 510-519.

(5)   Rühle, S., Tabulated Values of the Shockley–Queisser Limit for Single Junction Solar Cells. *Sol. Energy* **2016**, 130, 139-147.

(6)   Shirakawa, H.; Louis, E. J.; MacDiarmid, A. G.; Chiang, C. K.; Heeger, A. J., Synthesis of electrically conducting organic polymers: halogen derivatives of polyacetylene, (CH). *J. Chem. Soc., Chem. Commun.* **1977**, 578-580.

(7)   Brabec, C. J.; Dyakonov, V.; Parisi, J.; Sariciftci, N. S., Organic Photovoltaics: Concepts and Realization. Springer, Berlin, Heidelberg: **2003**.

(8)   Zhang, C.; Langner, S.; Mumyatov, A. V.; Anokhin, D. V.; Min, J.; Perea, J. D.; Gerasimov, K. L.; Osvet, A.; Ivanov, D. A.; Troshin, P.; Li, N.; Brabec, C. J., Understanding the Correlation and Balance between the Miscibility and Optoelectronic Properties of Polymer–Fullerene Solar Cells. *J. Mater. Chem. A* **2017**, 5, 17570-17579.

(9)   Li, N.; Perea, J. D.; Kassar, T.; Richter, M.; Heumueller, T.; Matt, G. J.; Hou, Y.; Guldal, N. S.; Chen, H.; Chen, S.; Langner, S.; Berlinghof, M.; Unruh, T.; Brabec, C. J., Abnormal Strong Burn-in Degradation of Highly Efficient Polymer Solar Cells Caused by Spinodal Donor-Acceptor Demixing. *Nat Commun* **2017**, 8, 14541.

(10)   Kroon, R.; Lenes, M.; Hummelen, J. C.; Blom, P. W. M.; de Boer, B., Small Bandgap Polymers for Organic Solar Cells (Polymer Material Development in the Last 5 Years). *Polym. Rev.* **2008**, 48, 531-582.

(11)   Brédas, J. L., Relationship between Band Gap and Bond Length Alternation in Organic Conjugated Polymers. *The Journal of Chemical Physics* **1985**, 82, 3808-3811.

(12)   Schleyer, P. v. R., Introduction: Aromaticity. *Chem. Rev.* **2001**, 101, 1115-1118.

(13)   Wudl, F.; Kobayashi, M.; Heeger, A. J., Poly(isothianaphthene). *The Journal of Organic Chemistry* **1984**, 49, 3382-3384.

(14)   Brédas, J. L.; Heeger, A. J., Influence of donor and acceptor substituents on the electronic characteristics of poly(paraphenylene vinylene) and poly(paraphenylene). *Chem. Phys. Lett.* **1994**, 217, 507-512.

(15)   Zhou, H.; Yang, L.; Stuart, A. C.; Price, S. C.; Liu, S.; You, W., Development of Fluorinated Benzothiadiazole as a Structural Unit for a Polymer Solar Cell of 7 % Efficiency. *Angew. Chem., Int.* **2011**, 50, 2995-2998.

(16)   Albrecht, S.; Janietz, S.; Schindler, W.; Frisch, J.; Kurpiers, J.; Kniepert, J.; Inal, S.; Pingel, P.; Fostiropoulos, K.; Koch, N.; Neher, D., Fluorinated Copolymer PCPDTBT with Enhanced Open-Circuit Voltage and Reduced Recombination for Highly Efficient Polymer Solar Cells. *J. Am. Chem. Soc.* **2012**, 134, 14932-14944.

(17)   Stuart, A. C.; Tumbleston, J. R.; Zhou, H.; Li, W.; Liu, S.; Ade, H.; You, W., Fluorine Substituents Reduce Charge Recombination and Drive Structure and Morphology Development in Polymer Solar Cells. *J. Am. Chem. Soc.* **2013**, 135, 1806-1815.

(18)   Kitamura, C.; Tanaka, S.; Yamashita, Y., Design of Narrow-Bandgap Polymers. Syntheses and Properties of Monomers and Polymers Containing Aromatic-Donor and o-Quinoid-Acceptor Units. *Chem. Mater.* **1996**, 8, 570-578.

(19)   Brocks, G.; Tol, A., Small Band Gap Semiconducting Polymers Made from Dye Molecules: Polysquaraines. *The Journal of Physical Chemistry* **1996**, 100, 1838-1846.

(20)   Li, Y., Molecular Design of Photovoltaic Materials for Polymer Solar Cells: Toward Suitable Electronic Energy Levels and Broad Absorption. *Acc. Chem. Res.* **2012**, 45, 723-733.

(21)   Wang, M.; Hu, X.; Liu, P.; Li, W.; Gong, X.; Huang, F.; Cao, Y., Donor–Acceptor Conjugated Polymer Based on Naphtho[1,2-c:5,6-c]bis[1,2,5]thiadiazole for High-Performance Polymer Solar Cells. *J. Am. Chem. Soc.* **2011**, 133, 9638-9641.

(22)   Scharber, M. C.; Mühlbacher, D.; Koppe, M.; Denk, P.; Waldauf, C.; Heeger, A. J.; Brabec, C. J., Design Rules for Donors in Bulk-Heterojunction Solar Cells—Towards 10 % Energy-Conversion Efficiency. *Adv. Mater.* **2006**, 18, 789-794.

(23)   Hutchison, G. R.; Ratner, M. A.; Marks, T. J., Intermolecular Charge Transfer between Heterocyclic Oligomers. Effects of Heteroatom and Molecular Packing on Hopping Transport in Organic Semiconductors. *J. Am. Chem. Soc.* **2005**, 127, 16866-16881.

(24)   Shi, S.; Yuan, J.; Ding, G.; Ford, M.; Lu, K.; Shi, G.; Sun, J.; Ling, X.; Li, Y.; Ma, W., Improved All-Polymer Solar Cell Performance by Using Matched Polymer Acceptor. *Adv. Funct. Mater.* **2016**, 26, 5669-5678.

(25)   Feng, S.; Liu, C.; Xu, X.; Liu, X.; Zhang, L.; Nian, Y.; Cao, Y.; Chen, J., Siloxane-Terminated Side Chain Engineering of Acceptor Polymers Leading to Over 7% Power Conversion Efficiencies in All-Polymer Solar Cells. *ACS Macro Lett.* **2017**, 6, 1310-1314.

(26)   You, H.; Kim, D.; Cho, H.-H.; Lee, C.; Chong, S.; Ahn, N. Y.; Seo, M.; Kim, J.; Kim, F. S.; Kim, B. J., Shift of the Branching Point of the Side-Chain in Naphthalenediimide (NDI)-Based Polymer for Enhanced Electron Mobility and All-Polymer Solar Cell Performance. *Adv. Funct. Mater.* **2018**, 28, 1803613.

(27)   Li, Z.; Xu, X.; Zhang, W.; Meng, X.; Ma, W.; Yartsev, A.; Inganäs, O.; Andersson, M. R.; Janssen, R. A. J.; Wang, E., High Performance All-Polymer Solar Cells by Synergistic Effects of Fine-Tuned Crystallinity and Solvent Annealing. *J. Am. Chem. Soc.* **2016**, 138, 10935-10944.

(28)   Duan, C.; Willems, R. E. M.; van Franeker, J. J.; Bruijnaers, B. J.; Wienk, M. M.; Janssen, R. A. J., Effect of Side Chain Length on the Charge Transport, Morphology, and Photovoltaic Performance of Conjugated Polymers in Bulk Heterojunction Solar Cells. *J. Mater. Chem. A* **2016**, 4, 1855-1866.

(29)   Köhler, A.; Bässler, H., Electronic Processes in Organic Semiconductors: An Introduction. 1 ed.; *Wiley-VCH Verlag GmbH*: **2015**.

(30)   Ma, W.; Kim, J. Y.; Lee, K.; Heeger, A. J., Effect of the Molecular Weight of Poly(3-hexylthiophene) on the Morphology and Performance of Polymer Bulk Heterojunction Solar Cells. *Macromol. Rapid Commun.* **2007**, 28, 1776-1780.

(31)   Kang, H.; Uddin, M. A.; Lee, C.; Kim, K.-H.; Nguyen, T. L.; Lee, W.; Li, Y.; Wang, C.; Woo, H. Y.; Kim, B. J., Determining the Role of Polymer Molecular Weight for High-Performance All-Polymer Solar Cells: Its Effect on Polymer Aggregation and Phase Separation. *J. Am. Chem. Soc.* **2015**, 137, 2359-2365.

(32)   Weinberger, B. R.; Akhtar, M.; Gau, S. C., Polyacetylene Photovoltaic Devices. *Synth. Met.* **1982**, 4, 187-197.

(33)   Dang, M. T.; Hirsch, L.; Wantz, G., P3HT:PCBM, Best Seller in Polymer Photovoltaic Research. *Adv. Mater.* **2011**, 23, 3597-3602.

(34)   Liao, S. H.; Jhuo, H. J.; Cheng, Y. S.; Chen, S. A., Fullerene Derivative-doped Zinc Oxide Nanofilm as the Cathode of Inverted Polymer Solar Cells with Low-bandgap Polymer (PTB7-Th) for High Performance. **2013**, 25, 4766-71.

(35)   Chen, J.-D.; Cui, C.; Li, Y.-Q.; Zhou, L.; Ou, Q.-D.; Li, C.; Li, Y.; Tang, J.-X., Single-Junction Polymer Solar Cells Exceeding 10% Power Conversion Efficiency. *Adv. Mater.* **2015**, 27, 1035-1041.

(36)   Zhang, S.; Ye, L.; Hou, J., Breaking the 10% Efficiency Barrier in Organic Photovoltaics: Morphology and Device Optimization of Well-Known PBDTTT Polymers. *Adv. Energy Mater.* **2016**, 6, 1502529.

(37)   Sun, C.; Pan, F.; Bin, H.; Zhang, J.; Xue, L.; Qiu, B.; Wei, Z.; Zhang, Z. G.; Li, Y., A Low Cost and High Performance Polymer Donor Material for Polymer Solar Cells. *Nat. Commun.* **2018**, 9, 743.

(38)   Zhang, S.; Qin, Y.; Zhu, J.; Hou, J., Over 14% Efficiency in Polymer Solar Cells Enabled by a Chlorinated Polymer Donor. *Adv. Mater.* **2018**, 30, 1800868.

(39)   Zheng, Z.; Hu, Q.; Zhang, S.; Zhang, D.; Wang, J.; Xie, S.; Wang, R.; Qin, Y.; Li, W.; Hong, L.; Liang, N.; Liu, F.; Zhang, Y.; Wei, Z.; Tang, Z.; Russell, T. P.; Hou, J.; Zhou, H., A Highly Efficient Non-Fullerene Organic Solar Cell with a Fill Factor over 0.80 Enabled by a Fine-Tuned Hole-Transporting Layer. *Adv. Mater.* **2018**, 30, 1801801.

(40)   Yuan, J.; Zhang, Y.; Zhou, L.; Zhang, G.; Yip, H.-L.; Lau, T.-K.; Lu, X.; Zhu, C.; Peng, H.; Johnson, P. A.; Leclerc, M.; Cao, Y.; Ulanski, J.; Li, Y.; Zou, Y., Single-Junction Organic Solar Cell with over 15% Efficiency Using Fused-Ring Acceptor with Electron-Deficient Core. *Joule* **2019**.

(41)   Cui, Y.; Yao, H.; Zhang, J.; Zhang, T.; Wang, Y.; Hong, L.; Xian, K.; Xu, B.; Zhang, S.; Peng, J.; Wei, Z.; Gao, F.; Hou, J., Over 16% efficiency organic photovoltaic cells enabled by a chlorinated acceptor with increased open-circuit voltages. *Nat. Commun.* **2019**, 10, 2515.

(42)   Kroto, S. H. W.; Walton, D. R. M., Fullerene. In Encyclopædia Britannica., Encyclopædia Britannica Inc.: Encyclopædia Britannica Online, **2015**.

(43)   Hummelen, J. C.; Knight, B. W.; LePeq, F.; Wudl, F.; Yao, J.; Wilkins, C. L., Preparation and Characterization of Fulleroid and Methanofullerene Derivatives. *The Journal of Organic Chemistry* **1995**, 60, 532-538.

(44)   Dennler, G.; Scharber, M. C.; Brabec, C. J., Polymer-Fullerene Bulk-Heterojunction Solar Cells. *Adv. Mater.* **2009**, 21, 1323-1338.

(45)   He, Z.; Wu, H.; Cao, Y., Recent Advances in Polymer Solar Cells: Realization of High Device Performance by Incorporating Water/Alcohol-Soluble Conjugated Polymers as Electrode Buffer Layer. *Adv. Mater.* **2014**, 26, 1006-1024.

(46)   Zhang, F.; Bijleveld, J.; Perzon, E.; Tvingstedt, K.; Barrau, S.; Inganas, O.; Andersson, M. R., High Photovoltage Achieved in Low Band Gap Polymer Solar Cells by Adjusting Energy Levels of a Polymer with the LUMOs of Fullerene Derivatives. *J. Mater. Chem.* **2008**, 18, 5468-5474.

(47)   Mikroyannidis, J. A.; Kabanakis, A. N.; Sharma, S. S.; Sharma, G. D., A Simple and Effective Modification of PCBM for Use as an Electron Acceptor in Efficient Bulk Heterojunction Solar Cells. *Adv. Funct. Mater.* **2011**, 21, 746-755.

(48)   Günes, S.; Neugebauer, H.; Sariciftci, N. S., Conjugated Polymer-Based Organic Solar Cells. *Chem. Rev.* **2007**, 107, 1324-1338.

(49)   Liao, S. H.; Jhuo, H. J.; Yeh, P. N.; Cheng, Y. S.; Li, Y. L.; Lee, Y. H.; Sharma, S.; Chen, S. A., Single Junction Inverted Polymer Solar Cell Reaching Power Conversion Efficiency 10.31% by Employing Dual-doped Zinc Oxide Nano-film as Cathode Interlayer. *Sci. Rep.* **2014**, 4, 6813.

(50)   Tang, C. W., Two-layer Organic Photovoltaic Cell. *Appl. Phys. Lett.* **1986**, 48, 183-185.

(51)   Zhan, X.; Facchetti, A.; Barlow, S.; Marks, T. J.; Ratner, M. A.; Wasielewski, M. R.; Marder, S. R., Rylene and Related Diimides for Organic Electronics. *Adv. Mater.* **2011**, 23, 268-284.

(52)   Li, C.; Liu, M.; Pschirer, N. G.; Baumgarten, M.; Müllen, K., Polyphenylene-Based Materials for Organic Photovoltaics.   *Chem. Rev.* **2010**, 110, 6817-6855.

(53)   Lin, Y.; Zhang, Z.-G.; Bai, H.; Wang, J.; Yao, Y.; Li, Y.; Zhu, D.; Zhan, X., High-Performance Fullerene-free Polymer Solar Cells with 6.31% Efficiency. *Energy Environ. Sci.* **2015**, 8, 610-616.

(54)   Lin, Y.; Wang, J.; Zhang, Z. G.; Bai, H.; Li, Y.; Zhu, D.; Zhan, X., An Electron Acceptor Challenging Fullerenes for Efficient Polymer Solar Cells. *Adv. Mater.* **2015**, 27, 1170-4.

(55)   Zhang, G.; Zhao, J.; Chow, P. C. Y.; Jiang, K.; Zhang, J.; Zhu, Z.; Zhang, J.; Huang, F.; Yan, H., Nonfullerene Acceptor Molecules for Bulk Heterojunction Organic Solar Cells. *Chem. Rev.* **2018**, 118, 3447-3507.

(56)   Zhao, W.; Li, S.; Yao, H.; Zhang, S.; Zhang, Y.; Yang, B.; Hou, J., Molecular Optimization Enables over 13% Efficiency in Organic Solar Cells. *J. Chem. Soc., Chem.* **2017**; 139, 7148-7151.

(57)   Chen, Z.; Zheng, Y.; Yan, H.; Facchetti, A., Naphthalenedicarboximide- vs Perylenedicarboximide-Based Copolymers. Synthesis and Semiconducting Properties in Bottom-Gate N-Channel Organic Transistors. *J. Chem. Soc., Chem.* **2009**, 131, 8-9.

(58)   Li, Z.; Ying, L.; Xie, R.; Zhu, P.; Li, N.; Zhong, W.; Huang, F.; Cao, Y., Designing Ternary Blend All-polymer Solar Cells with an Efficiency of Over 10% and a Fill Factor of 78%. *Nano Energy* **2018**, 51, 434-441.

(59)   Fan, B.; Ying, L.; Zhu, P.; Pan, F.; Liu, F.; Chen, J.; Huang, F.; Cao, Y., All-Polymer Solar Cells Based on a Conjugated Polymer Containing Siloxane-Functionalized Side Chains with Efficiency over 10%. *Adv. Mater.* **2017**, 29, 1703906.

(60)   Fan, B.; Zhu, P.; Xin, J.; Li, N.; Ying, L.; Zhong, W.; Li, Z.; Ma, W.; Huang, F.; Cao, Y., High-Performance Thick-Film All-Polymer Solar Cells Created Via Ternary Blending of a Novel Wide-Bandgap Electron-Donating Copolymer. *Adv. Energy Mater.* **2018**, 8.

(61)   Yao, H.; Bai, F.; Hu, H.; Arunagiri, L.; Zhang, J.; Chen, Y.; Yu, H.; Chen, S.; Liu, T.; Lai, J. Y. L.; Zou, Y.; Ade, H.; Yan, H., Efficient All-Polymer Solar Cells based on a New Polymer Acceptor Achieving 10.3% Power Conversion Efficiency. *ACS Energy Lett.* **2019**, 417-422.

(62)   Lee, W.; Lee, C.; Yu, H.; Kim, D.-J.; Wang, C.; Woo, H. Y.; Oh, J. H.; Kim, B. J., Side Chain Optimization of Naphthalenediimide–Bithiophene-Based Polymers to Enhance the Electron Mobility and the Performance in All-Polymer Solar Cells. *Adv. Funct. Mater.* **2016**, 26, 1543-1553.

(63)   Suraru, S.-L.; Würthner, F., Strategies for the Synthesis of Functional Naphthalene Diimides. *Angewandte Chemie International Edition* **2014**, 53, 7428-7448.

(64)   Earmme, T.; Hwang, Y.-J.; Murari, N. M.; Subramaniyan, S.; Jenekhe, S. A., All-Polymer Solar Cells with 3.3% Efficiency Based on Naphthalene Diimide-Selenophene Copolymer Acceptor. *J. Am. Chem. Soc.* **2013**, 135, 14960-14963.

(65)   Liu, F.; Li, H.; Wu, Y.; Gu, C.; Fu, H., Naphthalene Diimide and Benzothiadiazole Copolymer Acceptor for All-polymer Solar Cells with Improved Open-circuit Voltage and Morphology. *RSC Adv.* **2015**, 5, 92151-92158.

(66)   Benten, H.; Nishida, T.; Mori, D.; Xu, H.; Ohkita, H.; Ito, S., High-performance Ternary Blend All-polymer Solar Cells with Complementary Absorption Bands from Visible to Near-infrared Wavelengths. *Energy Environ. Sci.* **2016**, 9, 135-140.

(67)   Li, Z.; Xu, X.; Zhang, W.; Meng, X.; Genene, Z.; Ma, W.; Mammo, W.; Yartsev, A.; Andersson, M. R.; Janssen, R. A. J.; Wang, E., 9.0% Power Conversion Efficiency from Ternary All-polymer Solar Cells. *Energy Environ. Sci.* **2017**, 10, 2212-2221.

(68)   Li, Z.; Xu, X.; Zhang, W.; Genene, Z.; Mammo, W.; Yartsev, A.; Andersson, M. R.; Janssen, R. A. J.; Wang, E., High-photovoltage All-polymer Solar Cells Based on a Diketopyrrolopyrrole–isoindigo Acceptor Polymer. *J. Mater. Chem. A* **2017**, 5, 11693-11700.

(69)   Long, X.; Ding, Z.; Dou, C.; Zhang, J.; Liu, J.; Wang, L., Polymer Acceptor Based on Double B<--N Bridged Bipyridine (BNBP) Unit for High-Efficiency All-Polymer Solar Cells. *Adv. Mater.* **2016**, 28, 6504-8.

(70)   Xie, R.; Chen, Z.; Liu, Y.; Wang, Z.; Chen, Z.; Ying, L.; Huang, F.; Cao, Y., Cross-conjugated n-type Polymer Acceptors for Efficient All-polymer Solar Cells. *Chem. Commun.* **2018**, 54, 2204-2207.

(71)   Fang, Y.; Jin, H.; Raynor, A.; Wang, X.; Shaw, P. E.; Kopidakis, N.; McNeill, C. R.; Burn, P. L., Application of an A-A'-A-Containing Acceptor Polymer in Sequentially Deposited All-Polymer Solar Cells. *ACS Appl. Mater. Interfaces* **2018**, 10, 24046-24054.

(72)   Guo, Y.; Li, Y.; Awartani, O.; Han, H.; Zhao, J.; Ade, H.; Yan, H.; Zhao, D., Improved Performance of All-Polymer Solar Cells Enabled by Naphthodiperylenetetraimide-Based Polymer Acceptor. *Adv. Mater.* **2017**, 29, 1700309.

(73)   Guo, Y.; Li, Y.; Awartani, O.; Han, H.; Zhang, G.; Ade, H.; Yan, H.; Zhao, D., Side-chain engineering of perylenediimide-vinylene polymer acceptors for high-performance all-polymer solar cells. *Mater. Chem. Front.* **2017**, 1, 1362-1368.

(74)   Lee, J.-H.; Jeong, S. Y.; Kim, G.; Park, B.; Kim, J.; Kee, S.; Kim, B.; Lee, K., Reinforcing the Built-In Field for Efficient Charge Collection in Polymer Solar Cells. *Adv. Funct. Mater.* **2018**, 28.

(75)   Steim, R.; Kogler, F. R.; Brabec, C. J., Interface Materials for Organic Solar Cells. *J. Mater. Chem.* **2010**, 20.

(76)   Voigt, M. M.; Mackenzie, R. C. I.; Yau, C. P.; Atienzar, P.; Dane, J.; Keivanidis, P. E.; Bradley, D. D. C.; Nelson, J., Gravure printing for three subsequent solar cell layers of inverted structures on flexible substrates. *Sol. Energy Mater. Sol. Cells* **2011**, 95, 731-734.

(77)   Lim, F. J.; Ananthanarayanan, K.; Luther, J.; Ho, G. W., Influence of a novel fluorosurfactant modified PEDOT:PSS hole transport layer on the performance of inverted organic solar cells. *J. Mater. Chem.* **2012**, 22, 25057-25064.

(78)   Bisquert, J.; Garcia-Belmonte, G., On Voltage, Photovoltage, and Photocurrent in Bulk Heterojunction Organic Solar Cells. *The Journal of Physical Chemistry Letters* **2011**, 2, 1950-1964.

(79)   Chueh, C.-C.; Li, C.-Z.; Jen, A. K. Y., Recent Progress and Perspective in Solution-Processed Interfacial Materials for Efficient and Stable Polymer and Organometal Perovskite Solar Cells. *Energy Environ. Sci.* **2015**, 8, 1160-1189.

(80)   van Reenen, S.; Kouijzer, S.; Janssen, R. A. J.; Wienk, M. M.; Kemerink, M., Origin of Work Function Modification by Ionic and Amine-Based Interface Layers. *Adv. Mater. Interfaces* **2014**, 1, 1400189.

(81)   Hung, L. S.; Tang, C. W.; Mason, M. G., Enhanced Electron Injection in Organic Electroluminescence Devices using an Al/LiF Electrode. *Appl. Phys. Lett.* **1997**, 70, 152-154.

(82)   Sun, Y.; Seo, J. H.; Takacs, C. J.; Seifter, J.; Heeger, A. J., Inverted Polymer Solar Cells Integrated with a Low-Temperature-Annealed Sol-Gel-Derived ZnO Film as an Electron Transport Layer. *Adv. Mater.* **2011**, 23, 1679-1683.

(83)   Sharma, A.; George, Z.; Bennett, T.; Lewis, D. A.; Metha, G. F.; Andersson, G. G.; Andersson, M. R., Stability of Polymer Interlayer Modified ITO Electrodes for Organic Solar Cells. *Aust. J. Chem.* **2016**, 69, 735-740.

(84)   Li, M.; Gao, K.; Wan, X.; Zhang, Q.; Kan, B.; Xia, R.; Liu, F.; Yang, X.; Feng, H.; Ni, W.; Wang, Y.; Peng, J.; Zhang, H.; Liang, Z.; Yip, H.-L.; Peng, X.; Cao, Y.; Chen, Y., Solution-Processed Organic Tandem Solar Cells with Power Conversion Efficiencies >12%. *Nat. Photonics* **2016**, 11, 85-90.

(85)   Scott, J. C.; Carter, S. A.; Karg, S.; Angelopoulos, M., Polymeric anodes for organic light-emitting diodes. Synthetic Metals **1997**, 85, 1197-1200.

(86)   Kawano, K.; Pacios, R.; Poplavskyy, D.; Nelson, J.; Bradley, D. D. C.; Durrant, J. R., Degradation of Organic Solar Cells due to Air Exposure. *Sol. Energy Mater. Sol. Cells* **2006**, 90, 3520-3530.

(87)   de Jong, M. P.; van Ijzendoorn, L. J.; de Voigt, M. J. A., Stability of the Interface between Indium-tin-oxide and Poly(3,4-ethylenedioxythiophene)/poly(styrenesulfonate) in Polymer Light-emitting Diodes. *Appl. Phys. Lett.* **2000**, 77, 2255-2257.

(88)   Sharma, A.; Kroon, R.; Lewis, D. A.; Andersson, G. G.; Andersson, M. R., Poly(4-vinylpyridine): A New Interface Layer for Organic Solar Cells. *ACS Appl. Mater. Interfaces* **2017**, 9, 10929-10936.

(89)   Zhang, Y.; Chen, L.; Hu, X.; Zhang, L.; Chen, Y., Low Work-function Poly(3,4-ethylenedioxylenethiophene): Poly(styrene sulfonate) as Electron-transport Layer for High-efficient and Stable Polymer Solar Cells. *Sci. Rep.* **2015**, 5, 12839.

(90)   Huang, F.; Wu, H.; Wang, D.; Yang, W.; Cao, Y., Novel Electroluminescent Conjugated Polyelectrolytes Based on Polyfluorene. *Chem. Mater.* **2004**, 16, 708-716.

(91)   Wu, Z.; Sun, C.; Dong, S.; Jiang, X.-F.; Wu, S.; Wu, H.; Yip, H.-L.; Huang, F.; Cao, Y., n-Type Water/Alcohol-Soluble Naphthalene Diimide-Based Conjugated Polymers for High-Performance Polymer Solar Cells. *J. Am. Chem. Soc.* **2016**, 138, 2004-2013.

(92)   Nian, L.; Zhang, W.; Zhu, N.; Liu, L.; Xie, Z.; Wu, H.; Wurthner, F.; Ma, Y., Photoconductive Cathode Interlayer for Highly Efficient Inverted Polymer Solar Cells. *J. Am. Chem. Soc.* **2015**, 137, 6995-6998.

(93)   Zhang, Z.-G.; Qi, B.; Jin, Z.; Chi, D.; Qi, Z.; Li, Y.; Wang, J., Perylene Diimides: a Thickness-insensitive Cathode Interlayer for High Performance Polymer Solar Cells. *Energy Environ. Sci.* **2014**, 7, 1966-1973.

(94)   Zhao, K.; Ye, L.; Zhao, W.; Zhang, S.; Yao, H.; Xu, B.; Sun, M.; Hou, J., Enhanced Efficiency of Polymer Photovoltaic Cells via the Incorporation of a Water-soluble Naphthalene Diimide Derivative as a Cathode Interlayer. *J. Mater. Chem. C* **2015**, 3, 9565-9571.

(95)   T. McLeskey JR, J., Device Architectures in Organic Photovoltaics. *Turk. J. Phys.* **2014**, 38, 516-525.

(96)   Brabec, C. J., Sariciftci, N. S. and Hummelen, J. C. , Plastic Solar Cells. *Adv. Funct. Mater.* **2001**, 11, 15-26.

(97)   Blom, P. W. M.; Mihailetchi, V. D.; Koster, L. J. A.; Markov, D. E., Device Physics of Polymer:Fullerene Bulk Heterojunction Solar Cells. *Adv. Mater.* **2007**, 19, 1551-1566.

(98)   Yu, G.; Gao, J.; Hummelen, J. C.; Wudl, F.; Heeger, A. J., Polymer Photovoltaic Cells: Enhanced Efficiencies via a Network of Internal Donor-Acceptor Heterojunctions. *Science* **1995**, 270, 1789-1791.

(99)   Halls, J. J. M.; Walsh, C. A.; Greenham, N. C.; Marseglia, E. A.; Friend, R. H.; Moratti, S. C.; Holmes, A. B., Efficient photodiodes from interpenetrating polymer networks. *Nature* **1995**, 376, 498.

(100)   Ameri, T.; Khoram, P.; Min, J.; Brabec, C. J., Organic Ternary Solar Cells: A Review. *Adv. Mater.* **2013**, 25, 4245-4266.

(101)   Lu, L.; Kelly, M. A.; You, W.; Yu, L., Status and Prospects for Ternary Organic Photovoltaics. *Nat. Photonics* **2015**, 9, 491.

(102)   Kim, T.; Choi, J.; Kim, H. J.; Lee, W.; Kim, B. J., Comparative Study of Thermal Stability, Morphology, and Performance of All-Polymer, Fullerene–Polymer, and Ternary Blend Solar Cells Based on the Same Polymer Donor. *Macromolecules* **2017**, 50, 6861-6871.

(103)   Jørgensen, M.; Norrman, K.; Gevorgyan, S. A.; Tromholt, T.; Andreasen, B.; Krebs, F. C., Stability of Polymer Solar Cells. *Adv. Mater.* **2012**, 24, 580-612.

(104)   Watkins, P. K.; Walker, A. B.; Verschoor, G. L. B., Dynamical Monte Carlo Modelling of Organic Solar Cells: The Dependence of Internal Quantum Efficiency on Morphology. *Nano Lett.* **2005**, 5, 1814-1818.

(105)   McNeill, C. R., Morphology of All-polymer Solar Cells. *Energy Environ. Sci.* **2012**, 5, 5653-5667.

(106)   Tumbleston, J. R.; Yang, L.; You, W.; Ade, H., Morphology Linked to Miscibility in Highly Amorphous Semi-conducting Polymer/fullerene Blends. *Polymer* **2014**, 55, 4884-4889.

(107)   Liao, H.-C.; Ho, C.-C.; Chang, C.-Y.; Jao, M.-H.; Darling, S. B.; Su, W.-F., Additives for Morphology Control in High-efficiency Organic Solar Cells. *Mater. Today* **2013**, 16, 326-336.

(108)   Liu, X.; Huettner, S.; Rong, Z.; Sommer, M.; Friend, R. H., Solvent Additive Control of Morphology and Crystallization in Semiconducting Polymer Blends. *Adv. Mater.* **2012**, 24, 669-74.

(109)   Yao, H.; Li, Y.; Hu, H.; Chow, P. C. Y.; Chen, S.; Zhao, J.; Li, Z.; Carpenter, J. H.; Lai, J. Y. L.; Yang, G.; Liu, Y.; Lin, H.; Ade, H.; Yan, H., A Facile Method to Fine-Tune Polymer Aggregation Properties and Blend Morphology of Polymer Solar Cells Using Donor Polymers with Randomly Distributed Alkyl Chains. *Adv. Energy Mater.* **2018**, 8, 1701895.

(110)   Liu, Y.; Zhao, J.; Li, Z.; Mu, C.; Ma, W.; Hu, H.; Jiang, K.; Lin, H.; Ade, H.; Yan, H., Aggregation and morphology control enables multiple cases of high-efficiency polymer solar cells. *Nat. Commun.* **2014**, 5, 5293.

(111)   Bazan, G. C., Over 9% Efficiency Achieved for All-polymer Solar Cells Processed by a Green Solvent. *Sci. China: Chem.* **2017**, 60, 1109-1110.

(112)   Zhao, W.; Ye, L.; Zhang, S.; Sun, M.; Hou, J., A Universal Halogen-free Solvent System for Highly Efficient Polymer Solar Cells. *J. Mater. Chem. A* **2015**, 3, 12723-12729.

(113)   Sprau, C.; Buss, F.; Wagner, M.; Landerer, D.; Koppitz, M.; Schulz, A.; Bahro, D.; Schabel, W.; Scharfer, P.; Colsmann, A., Highly Efficient Polymer Solar Cells Cast from Non-halogenated Xylene/anisaldehyde Solution. *Energy Environ. Sci.* **2015**, 8, 2744-2752.

(114)   Søndergaard, R.; Hösel, M.; Angmo, D.; Larsen-Olsen, T. T.; Krebs, F. C., Roll-to-roll Fabrication of Polymer Solar Cells. *Mater. Today* **2012**, 15, 36-49.

(115)   Zhang, S.; Ye, L.; Zhang, H.; Hou, J., Green-solvent-processable Organic Solar Cells. *Mater. Today* **2016**, 19, 533-543.

(116)   Krebs, F. C., Fabrication and processing of polymer solar cells: A Review of Printing and Coating Techniques. *Sol. Energy Mater. Sol. Cells* **2009**, 93, 394-412.

(117)   Zimmermann, B.; Schleiermacher, H. F.; Niggemann, M.; Würfel, U., ITO-free Flexible Inverted Organic Solar Cell Modules with High Fill Factor Prepared by Slot Die Coating. *Sol. Energy Mater. Sol. Cells* **2011**, 95, 1587-1589.

(118)   Krebs, F. C.; Jørgensen, M.; Norrman, K.; Hagemann, O.; Alstrup, J.; Nielsen, T. D.; Fyenbo, J.; Larsen, K.; Kristensen, J., A Complete Process for Production of Flexible Large Area Polymer Solar Cells Entirely using Screen Printing—First Public Demonstration. *Sol. Energy Mater. Sol. Cells* **2009**, 93, 422-441.

(119)   Susanna, G.; Salamandra, L.; Brown, T. M.; Di Carlo, A.; Brunetti, F.; Reale, A., Airbrush Spray-coating of Polymer Bulk-heterojunction Solar Cells. *Sol. Energy Mater. Sol. Cells* **2011**, 95, 1775-1778.

(120)   Angmo, D.; Larsen-Olsen, T. T.; Jørgensen, M.; Søndergaard, R. R.; Krebs, F. C., Roll-to-Roll Inkjet Printing and Photonic Sintering of Electrodes for ITO Free Polymer Solar Cell Modules and Facile Product Integration. *Adv. Energy Mater.* **2013**, 3, 172-175.

(121)   Krebs, F. C., Polymer Solar Cell Modules Prepared using Roll-to-roll Methods: Knife-over-edge Coating, Slot-die Coating and Screen Printing. *Sol. Energy Mater. Sol. Cells* **2009**, 93, 465-475.

(122)   Lin, Y.; Dong, S.; Li, Z.; Zheng, W.; Yang, J.; Liu, A.; Cai, W.; Liu, F.; Jiang, Y.; Russell, T. P.; Huang, F.; Wang, E.; Hou, L., Energy-effectively Printed All-polymer Solar Cells Exceeding 8.61% Efficiency. *Nano Energy* **2018**, 46, 428-435.

(123)   Sankaran, S.; Glaser, K.; Gärtner, S.; Rödlmeier, T.; Sudau, K.; Hernandez-Sosa, G.; Colsmann, A., Fabrication of Polymer Solar Cells from Organic Nanoparticle Dispersions by Doctor Blading or Ink-jet Printing. *Org. Electron.* **2016**, 28, 118-122.

(124)   Bailey, B. A.; Reese, M. O.; Olson, D. C.; Shaheen, S. E.; Kopidakis, N., Air-processed Organic Photovoltaic Devices Fabricated with Hot Press Lamination. *Org. Electron.* **2011**, 12, 108-112.

(125)   Sharma, A.; Ionescu, M.; Andersson, G. G.; Lewis, D. A., Role of Zinc Oxide Thickness on the Photovoltaic Performance of Laminated Organic Bulk-heterojunction Solar Cells. *Sol. Energy Mater. Sol. Cells* **2013**, 115, 64-70.

(126)   Huang, J.; Li, G.; Yang, Y., A Semi-transparent Plastic Solar Cell Fabricated by a Lamination Process. *Adv. Mater.* **2008**, 20, 415-419.

(127)   Bergqvist, J.; Österberg, T.; Melianas, A.; Ever Aguirre, L.; Tang, Z.; Cai, W.; Ma, Z.; Kemerink, M.; Gedefaw, D.; Andersson, M. R.; Inganäs, O., Asymmetric photocurrent extraction in semitransparent laminated flexible organic solar cells. *Flexible Electron.* **2018**, 2.

(128)   Zhang, J.; Zhao, Y.; Fang, J.; Yuan, L.; Xia, B.; Wang, G.; Wang, Z.; Zhang, Y.; Ma, W.; Yan, W.; Su, W.; Wei, Z., Enhancing Performance of Large-Area Organic Solar Cells with Thick Film via Ternary Strategy. Small **2017**, 13 .

(129)   Gu, X.; Zhou, Y.; Gu, K.; Kurosawa, T.; Guo, Y.; Li, Y.; Lin, H.; Schroeder, B. C.; Yan, H.; Molina-Lopez, F.; Tassone, C. J.; Wang, C.; Mannsfeld, S. C. B.; Yan, H.; Zhao, D.; Toney, M. F.; Bao, Z., Roll-to-Roll Printed Large-Area All-Polymer Solar Cells with 5% Efficiency Based on a Low Crystallinity Conjugated Polymer Blend. *Adv. Energy Mater.* **2017**, 7.

(130).   Park, S.-Y.; Kang, Y.-J.; Lee, S.; Kim, D.-G.; Kim, J.-K.; Kim, J. H.; Kang, J.-W., Spray-coated Organic Solar Cells with Large-area of 12.25 cm2. *Sol. Energy Mater. Sol. Cells* **2011**, 95, 852-855.

(131)   Lungenschmied, C.; Dennler, G.; Neugebauer, H.; Sariciftci, S. N.; Glatthaar, M.; Meyer, T.; Meyer, A., Flexible, Long-lived, Large-area, Organic Solar Cells. *Sol. Energy Mater. Sol. Cells* **2007**, 91, 379-384.

(132)   Schrödner, M.; Sensfuss, S.; Schache, H.; Schultheis, K.; Welzel, T.; Heinemann, K.; Milker, R.; Marten, J.; Blankenburg, L., Reel-to-reel Wet Coating by Variation of Solvents and Compounds of Photoactive Inks for Polymer Solar Cell Production *Sol. Energy Mater. Sol. Cells* **2012**, 107, 283-291.

(133)   Helgesen, M.; Carlé, J. E.; dos Reis Benatto, G. A.; Søndergaard, R. R.; Jørgensen, M.; Bundgaard, E.; Krebs, F. C., Making Ends Meet: Flow Synthesis as the Answer to Reproducible High-Performance Conjugated Polymers on the Scale that Roll-to-Roll Processing Demands.   *Adv. Energy Mater.* **2015**, 5, 1401996.

(134)   Krebs, F. C.; Espinosa, N.; Hösel, M.; Søndergaard, R. R.; Jørgensen, M., 25th Anniversary Article: Rise to Power - OPV-Based Solar Parks. *Adv. Mater.* **2014**, 26, 29-39.

(135)   Liu, K.; Larsen-Olsen, T. T.; Lin, Y.; Beliatis, M.; Bundgaard, E.; Jørgensen, M.; Krebs, F. C.; Zhan, X., Roll-coating Fabrication of Flexible Organic Solar Cells: Comparison of Fullerene and Fullerene-free Systems. *J. Mater. Chem. A* **2016**, 4, 1044-1051.

(136)   Huang, Y.-C.; Cha, H.-C.; Chen, C.-Y.; Tsao, C.-S., Morphological Control and Performance Improvement of Organic Photovoltaic Layer of Roll-to-roll Coated Polymer Solar Cells. *Sol. Energy Mater. Sol. Cells* **2016**, 150, 10-18.

(137)   Vak, D.; Weerasinghe, H.; Ramamurthy, J.; Subbiah, J.; Brown, M.; Jones, D. J., Reverse Gravure Coating for Roll-to-roll Production of Organic Photovoltaics. *Sol. Energy Mater. Sol. Cells* **2016**, 149, 154-161.

(138)   Yan, F.; Noble, J.; Peltola, J.; Wicks, S.; Balasubramanian, S., Semitransparent OPV Modules Pass Environmental Chamber Test Requirements. *Sol. Energy Mater. Sol. Cells* **2013**, 114, 214-218.

(139)   Zhong, W.; Hu, Q.; Jiang, Y.; Li, Y.; Chen, T. L.; Ying, L.; Liu, F.; Wang, C.; Liu, Y.; Huang, F.; Cao, Y.; Russell, T. P., In Situ Structure Characterization in Slot-Die-Printed All-Polymer Solar Cells with Efficiency Over 9%. *Sol. RRL* **2019**, 3, 1900032.

(140)   Landfester, K.; Montenegro, R.; Scherf, U.; Güntner, R.; Asawapirom, U.; Patil, S.; Neher, D.; Kietzke, T., Semiconducting Polymer Nanospheres in Aqueous Dispersion Prepared by a Miniemulsion Process. *Adv. Mater.* **2002**, 14 (9), 651-655.

(141)   Surfactant Free P3HT / PCBM Nanoparticles for Organic Photovoltaics (OPV). *AIP Conference Proceedings* **2011**, 1415, 120-123.

(142)   Pan, X.; Sharma, A.; Gedefaw, D.; Kroon, R.; Diaz de Zerio, A.; Holmes, N. P.; Kilcoyne, A. L. D.; Barr, M. G.; Fahy, A.; Marks, M.; Zhou, X.; Belcher, W.; Dastoor, P. C.; Andersson, M. R., Environmentally Friendly Preparation of Nanoparticles for Organic Photovoltaics. *Org. Electron.* **2018**, 59, 432-440.

(143)   Kim, J. H.; Song, C. E.; Kang, I. N.; Shin, W. S.; Hwang, D. H., A Highly Crystalline Low Band-gap Polymer Consisting of Perylene and Diketopyrrolopyrrole for Organic Photovoltaic Cells. *Chem. Commun.* **2013**, 49, 3248-50.

(144)   Rogers, J. T.; Schmidt, K.; Toney, M. F.; Kramer, E. J.; Bazan, G. C., Structural Order in Bulk Heterojunction Films Prepared with Solvent Additives. *Adv. Mater.* **2011**, 23, 2284-8.

(145)   Hoven, C. V.; Dang, X. D.; Coffin, R. C.; Peet, J.; Nguyen, T. Q.; Bazan, G. C., Improved Performance of Polymer Bulk Heterojunction Solar Cells through the Reduction of Phase Separation via Solvent Additives. *Adv. Mater.* **2010**, 22, E63-6.

(146)   Fontana, M. T.; Kang, H.; Yee, P. Y.; Fan, Z.; Hawks, S. A.; Schelhas, L. T.; Subramaniyan, S.; Hwang, Y.-J.; Jenekhe, S. A.; Tolbert, S. H.; Schwartz, B. J., Low-Vapor-Pressure Solvent Additives Function as Polymer Swelling Agents in Bulk Heterojunction Organic Photovoltaics. *The Journal of Physical Chemistry* C **2018**, 122, 16574-16588.

(147)   Verploegen, E.; Mondal, R.; Bettinger, C. J.; Sok, S.; Toney, M. F.; Bao, Z., Effects of Thermal Annealing Upon the Morphology of Polymer-Fullerene Blends. *Adv. Funct. Mater.* **2010**, 20, 3519-3529.

(148)   Singh, A.; Dey, A.; Iyer, P. K., Influence of Molar Mass Ratio, Annealing Temperature and Cathode Buffer Layer on Power Conversion Efficiency of P3HT:PC71BM based Organic Bulk Heterojunction Solar Cell. *Org. Electron.* **2017**, 51, 428-434.

(149)   Watts, B.; Belcher, W. J.; Thomsen, L.; Ade, H.; Dastoor, P. C., A Quantitative Study of PCBM Diffusion during Annealing of P3HT:PCBM Blend Films. *Macromolecules* **2009**, 42, 8392-8397.

(150)   Xia, Y.; Musumeci, C.; Bergqvist, J.; Ma, W.; Gao, F.; Tang, Z.; Bai, S.; Jin, Y.; Zhu, C.; Kroon, R.; Wang, C.; Andersson, M. R.; Hou, L.; Inganäs, O.; Wang, E., Inverted All-polymer Solar Cells Based on a Quinoxaline–thiophene/Naphthalene-diimide Polymer Blend Improved by Annealing. *J. Mater. Chem. A* **2016**, 4, 3835-3843.

(151)   Nature of the Glass Transition and the Glassy State. *The Journal of Chemical Physics* **1958**, 28, 373-383.

(152)   Savagatrup, S.; Printz, A. D.; O'Connor, T. F.; Zaretski, A. V.; Rodriquez, D.; Sawyer, E. J.; Rajan, K. M.; Acosta, R. I.; Root, S. E.; Lipomi, D. J., Mechanical degradation and stability of organic solar cells: molecular and microstructural determinants. *Energy Environ. Sci.* **2015**, 8, 55-80.

(153)   de Zerio, A. D.; Müller, C., Glass Forming Acceptor Alloys for Highly Efficient and Thermally Stable Ternary Organic Solar Cells. *Adv. Energy Mater.* **2018**, 8, 1702741.

(154)   Derue, L.; Lecourtier, C.; Gorisse, T.; Hirsch, L.; Dautel, O.; Wantz, G., A Solvent Additive to Enhance the Efficiency and the Thermal Stability of Polymer:fullerene Solar Cells. *RSC Adv.* **2015**, 5, 3840-3843.

(155)   Rumer, J. W.; McCulloch, I., Organic photovoltaics: Crosslinking for Optimal Morphology and Stability. *Mater. Today* **2015**, 18, 425-435.

(156)   Miyanishi, S.; Tajima, K.; Hashimoto, K., Morphological Stabilization of Polymer Photovoltaic Cells by Using Cross-Linkable Poly(3-(5-hexenyl)thiophene). *Macromolecules* **2009**, 42, 1610-1618.

(157)   Angmo, D.; Sommeling, P. M.; Gupta, R.; Hösel, M.; Gevorgyan, S. A.; Kroon, J. M.; Kulkarni, G. U.; Krebs, F. C., Outdoor Operational Stability of Indium-Free Flexible Polymer Solar Modules Over 1 Year Studied in India, Holland, and Denmark. *Adv. Eng. Mater.* **2014**, 16, 976-987.

(158)   Rivaton, A.; Tournebize, A.; Gaume, J.; Bussière, P.-O.; Gardette, J.-L.; Therias, S., Photostability of Organic Materials used in Polymer Solar Cells. *Polymer International* **2014**, 63, 1335-1345.

(159)   Finn, M.; Martens, C. J.; Zaretski, A. V.; Roth, B.; Søndergaard, R. R.; Krebs, F. C.; Lipomi, D. J., Mechanical Stability of Roll-to-roll Printed Solar Cells under Cyclic Bending and Torsion. *Sol. Energy Mater. Sol. Cells* **2018**, 174, 7-15.

(160)   Du, X.; Heumueller, T.; Gruber, W.; Classen, A.; Unruh, T.; Li, N.; Brabec, C. J., Efficient Polymer Solar Cells Based on Non-fullerene Acceptors with Potential Device Lifetime Approaching 10 Years. *Joule* **2019**, 3, 215-226.

Chapter 3 – Research Methodology

3.1 Overview

This chapter presents the research methodology, forming the rationale for the individual research projects presented within this thesis. The chapter is divided into four parts starting with an introduction to molecular design followed by the rationale for the three individual projects (small molecule NFAs, polymeric acceptors, and cathode interface materials), including a short synthesis segment, the device fabrication is then briefly introduced, with the characterisation techniques applied presented in the last section.

3.2 Introduction

Upscaling and subsequent commercialisation must be prioritised. This brings challenges that need more emphasis by the wider community,[1] including:

- Roll-to-roll processing (large scale)
  - Switch to greener /non-toxic solvents
  - Deposition on flexible substrate
  - Ambient atmosphere processing conditions
- Stability / Lifetime
- Green chemistry (synthesis)
- Cost restrictions

The challenges of roll-to-roll processing are important to take into account during the development of new materials. Transitioning from small-scale rigid devices to large-scale flexible devices require drastic changes in the processing condition. Thus, high PCE materials for small-scale applications are not guaranteed to provide respectively high efficiencies when applied in large-scale processes. In regards to the upscaling of polymer solar cells, Fredrik C. Krebs stated that the process should; i) be free of toxic solvents and chemicals, ii) provide a low environmental impact product with iii) a high degree of recyclability for successful commercialisation.[2]

Chlorinated, harmful solvents are the preferred option for small-scale devices due to their excellent properties and ability to yield high PCE solar cells. Thus far, a majority of high-performance devices have had the active layer processed from chlorobenzene (CB). The use of greener or more environmentally friendly solvents, in particular water and short chain alcohols, is a requirement that cannot be ignored as the research field progresses toward large scale printing in open environments.

The aim of the project presented in this thesis is to design and synthesise new naphthalene diimide (NDI) based compounds for applications in polymer solar cells (PSCs). These NDI compounds include three different material categories:

- Small molecule non-fullerene acceptors (NFA)
- Polymeric acceptors
- Cathode interface materials

with each category bringing its own set of challenges. The goal is to develop materials that accelerate the transition toward large scale processing enabling the commercialisation step. This can be achieved through the development of a set of design parameters, specific to each category, which addresses one or more of above stated challenges.

3.3 Molecular Design

Design and development of new materials is considered a tedious process for which a number of design parameters must be taken into account. These parameters differ for the materials in the active layer and for materials employed as interface layers. They even differ for small molecules and polymers of similar core structures. This is due to the unique properties of polymers, originating from the varying chain lengths and restricted mobility of the repeating units. For interface layers, a single material, or sequentially deposited materials are used, somewhat simplifying this design process. On the other hand, active layer materials must work well in blends, where minor changes can be detrimental to the overall performance due to changes in morphology. Design of both these material types will be discussed in detail in the following sections.

3.4 Design Strategy

Dominance of fullerene acceptors has led to a situation where NFAs at the current time, are underdeveloped compared to the broader OPV materials research field. Organic interface materials, e.g. conjugated polymers or polyelectrolytes, could also be considered underdeveloped, with research efforts only having intensified in the last few years. Regarding cathode interface layers (CIL), the organic materials have often been developed for use in conjunction with inorganic materials, complementing or improving their properties, e.g. reducing work functions. Commercially available 1,4,5,8-naphthalene tetracarboxylic dianhydride (NTCDA) was chosen as a building block for both interface materials and acceptor materials due to its outstanding acceptor properties as well as synthesis opportunities. NTCDA is also relatively inexpensive and can be converted to a wide range of NDI based small molecules/polymers via short step, facile synthesis routes, as illustrated in Figure 3.1.
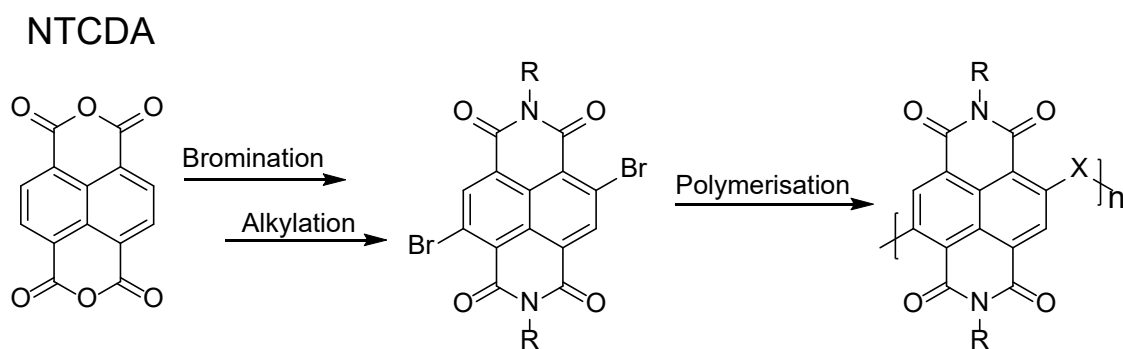
Figure 3.1: Representation of the facile synthesis route of 1,4,5,8-naphthalene tetracarboxylic dianhydride (NTCDA) to naphthalene diimide (NDI) monomers. These monomers are then polymerised in catalysed cross coupling reactions.

This thesis presents the development of new NDI containing materials for polymer solar cell applications, with focus on materials suitable for upscaling and, in particular, on materials that can be printed from green solvents. Certain attention is also given to the synthesis procedures for which greener and more efficient routes are favoured.

3.4.1 Small molecule acceptors for active layer blends

Design criteria were established for the development of new NDI containing small molecule NFAs in solution processed PSCs. These were formulated to answer the research question posed in Chapter 1:

- ***Can small molecule NDI based acceptor-blends be used as the electron transporting material?***

For the small molecule acceptors the focus was to develop NDI based acceptor materials with good crystallinity control from relatively inexpensive materials via high atom economy synthesis. Careful consideration of starting materials could reduce both cost as well as reaction steps required to achieve the target compounds. One way to achieve this is to create a range of materials with varying crystallinity, based on a commercially available core structure.

The building block, NTCDA, can be converted in facile synthesis procedures in as few as one-step reaction routes to a wide array of NDI structures, including dimers.[3] Further, it is a commercially available material and has been well studied with applications in a number of research fields.[4] Within OPVs, Yao *et al*. published the NDI based dimer BiNDI that utilises a vinyl linker and branched alkyl side-groups for crystallinity control.[5] In this study it was concluded that the addition of the solvent additive 1,8-diiodooctane (DIO) facilitated the growth of fibrillary crystals, leading to a highest PCE of 2.41%. In another study by Rundel *et al*. three star-shaped NDI trimers with triarylamine cores were paired with PTB7-Th showing a highest PCE of 2.8%.[6] In this study the star-shaped NFAs were found to contribute to domain sizes smaller than 100 nm. Interestingly, DIO was also found to reduce the device performance at even very low concentrations (0.2 %).

A range of NDI based NFA structures were explored for use in acceptor blends. These structures are modified to incorporate side-groups of varying size and steric hindrance, to produce variations in packing and crystallinity. Modifications were conducted solely on the imide positions, utilising the following classes of side-groups; straight alkyl chain, branched alkyl chain, aromatic, and asymmetric (combination), see Figure 3.2.
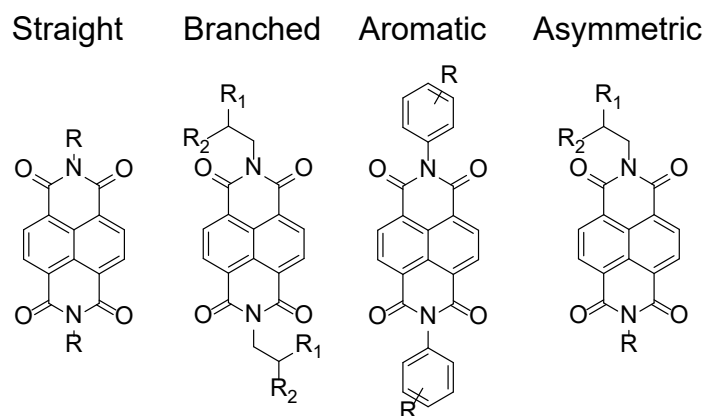
Figure 3.2: Illustration of small molecule acceptors with straight alkyl, branched alkyl, aromatic, and asymmetric (combination) side-groups.

These classes contain a wide variety of structures fitting the prerequisite for reaction, that is the presence of, or facile conversion to, a primary amine. However, the extremely flat core could prove difficult to fine tune in such a manner that the crystallinity is disrupted as the charge carrier transport is retained. Another drawback of these materials is the optical properties with low absorption coefficients and absorbance in the low wavelength, or high energy, region with low photon flux. Hence, the donor polymer will be the major contributor to the active layer absorption. The amorphous polymer TQ1 was chosen as the donor component for evaluation of new acceptor molecules and blends. This polymer has suitable cost profile and a facile synthesis route making it a good candidate for this application[7]. However, it must be noted that TQ1 is an amorphous polymer, meaning that its miscibility with NDI acceptors showing a higher crystallinity, is likely far from optimal.

These small molecule NDI based structures could also be used in multicomponent (e.g. ternary) active layer blends, controlling the crystallinity not only via synthetic side-group design but also through the optimisation of blend ratios.[8] Multi component blends were explored due to previous successes of ternary blends within the field for fine tuning of the active layer properties.[9] Typically, a third component with complementary absorption is introduced to a well-studied system, extending the light absorption of the active layer. Ternary blends have also been known to improve charge extraction, increase V_{oc}, and suppress charge recombination, as discussed in section *2.7.4 Ternary blends*, Chapter 2. However, ternary blend systems tend to require tedious optimisation of blend ratios. This could prove an issue when scanning multiple small molecule acceptors for their suitability. It should also be noted that successful studies of ternary blends in a D:A_1:A_2 configuration, with the acceptors being small molecules, have almost solely been reported for fullerenes.[8] One of the exceptions is a study by Baran *et al*. where the two acceptors IDTBR and IDFBR were paired with PTB7-Th to reach a PCE of 11%.[10] They concluded that the beneficial morphology obtained was locked in by vitrification of the acceptor blend. Studies of ternary blends/multi-component BHJ systems with NFAs is therefore required to progress this area of research and would be of great benefit to the wider community.

3.4.2 Polymeric Acceptors

Design criteria were established for the development of new acceptor polymers, based on the widely used N2200 polymer. These were formulated to answer the second research question posed in Chapter 1:

- ***Is it possible to increase the solubility of N2200 derivatives in environmentally friendly solvents while retaining good power conversion efficiency?***

Development of new polymer acceptors focused on two criteria; i) crystallinity control and ii) increased solubility in non-chlorinated solvents for a greener and less toxic processing. Side-group engineering as well as alteration to the steric hindrance related to free movements around stereo-centres were explored as possible strategies for development of new polymer structures. These methods could contribute to a reduced aggregation in solution with a retained control over crystallinity.

These structures were based on an NDI-thiophene backbone, similar to the widely used N2200[11] upon which many derivatives have been synthesised. The co-planarity of the N2200 backbone induces π-π stacking, crystallisation in the solid state. Polymer crystallinity can be tuned by introduction of irregularities in the backbone, lowering the overlap of the aromatic core and in turn reducing the π-π stacking.[12] Irregularity can also be introduced in the side-groups for similar effect[13], although, not as pronounced. Preferential disturbance of the packing in dissolved state, i.e. increased torsion angles in solution, could further increase solubility without compromising charge carrier transport. Lastly, the solubility can be altered through the inclusion of longer or more numerous alkyl chains.

Based on above statements, two separate strategies, which can be employed either separately or in tandem, were developed for both crystallinity control as well as for solubility control of NDI based acceptor polymers:

- Side-group engineering (NDI)
- Side-group engineering (BT)

Through introduction of solubilising large/bulky side-groups next to stereo-centres in the polymer backbone the torsion angle can be increased, thus, limiting π-π stacking and aggregation. Through fine tuning, these substituents could possibly observe an optimal packing behaviour with the polymer experiencing twisting, i.e. large torsion angles, in solution but retain good enough π-π stacking in the solid phase. The widespread use of push-pull polymer structures has seen NDI monomers paired with bithiophene (BT) compounds. BT contains a stereo-centre and the 3,3' positions are able to be functionalised with a range of side-groups in few reaction steps, depending on starting material (T or BT). Introduction of somewhat bulky groups in these 3,3' positions would affect the torsion angle, thus reducing aggregation and/or packing. This mechanism could be further optimised with a solubilising group limiting the twisting to the dissolved state, illustrated in Figure 3.3.
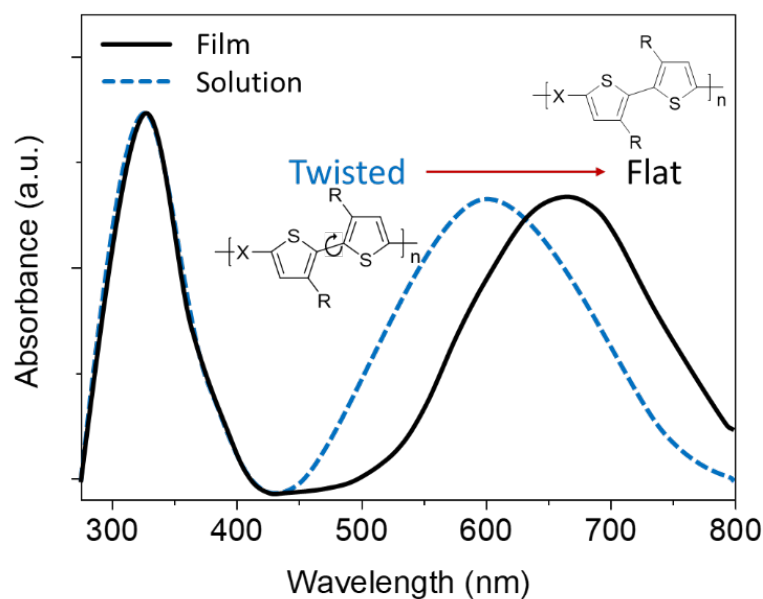
Figure 3.3: Illustration of the optical response for a copolymer that is twisted in solution and flat in solid state (bathochromic shift) due to the steric hindrance in the 3,3'-functionalised-2,2'-bithiophene unit.

Regularity in the polymer backbone allows for maximum overlap, π-π stacking. Thus, the crystallinity can be tuned through the introduction of a third component, forming a random copolymer that disturbs the regularity. However, this method can also affect the energy levels and so the third component should preferably be a close match to either the donor or the acceptor unit in the existing polymer structure. Xu *et al* conducted a random copolymer study with positive results, showing improvements in light absorption as well as a fine tuned aggregation behaviour for BDT, BT, and DPP based terpolymer.[14] Additionally, lowering of the regioregularity to introduce disorder is possible for polymers containing asymmetric building blocks. This was investigated by Woo *et al.* for P3HT, for which a lower regioregularity was found to contribute to a higher thermal stability of the P3HT-PC$_{61}$BM BHJ layer, despite the polymer experiencing a lower crystallinity.[15] The increased thermal stability was instead attributed to the suppression of excessive fullerene crystal growth via the formation of voids in the HT-TH (head to tail – tail to head) polymer segments. Further, studies by Huo *et al.* and Yao *et al.* highlighted the positive effects of varying the side-group lengths for the same core structures in a single random copolymer.[16-17] This strategy avoids the cumbersome synthesis of odd-numbered alkyl side-groups, providing fine tuning opportunities of optical, electronic and morphological properties otherwise not available.

3.4.3 Cathode Interface Materials

Design criteria were established for the development of new cathode interface materials, with the main emphasis on polymers and polyelectrolytes. These were formulated to answer the third and final research question posed in Chapter 1:

- ***Can NDI based polymers work well as interface materials when processed from environmentally friendly solvents and are they compatible with a facile synthesis route?***

The design of new cathode interface materials was focused on the green processing and work function modification. Due to the nature of CILs, they are always employed via orthogonal processing. That is, in a conventional device, the interface material is deposited on top of the active layer. Conversely, in an inverted device the active layer is deposited on top of the interface material. Thus, solubility and wetting play an important role for film formation and a well-maintained layer structure during processing. This is especially important for interface layers that are often processed as ultra-thin layers in the range of 2-20 nm.

Tertiary and quaternary amines, imidazoles, pyridines and *N*-oxides are commonly applied for work function modification of the electrodes. These functional groups contain a free electron pair that can coordinate to many of the commonly used electrodes, resulting in the consequent formation of interfacial dipoles, modifying the work functions (Figure 3.4).[18] The pendant side-groups can be modified with ease for attachment of functional groups with free electron pairs, in order to tailor electrode work functions. Additionally, these pendant side-groups contribute to an increased solubility in highly polar, green solvents such as water and short chain alcohols. In the case of tertiary amines, protonation can greatly enhance this effect with the addition of a minor amount of acid.[19] Quaternary amines and *N*-oxides possess an inherently high solubilising effect in aforementioned solvents due to their ionic character.

These functional groups have also been shown to participate in the doping mechanism of acceptor compounds. It is theorised that one electron from the free electron pair of a functional group is donated into the acceptor core. This mechanism was proposed for Buckminsterfullerene (C60) and a number of amine compounds under illumination by Ghosh *et al*. in 1993. This doping has a positive effect on the conductivity for CILs, affecting the charge carrier transport and consequently also raising the PCE.[19] For example, Wu *et al*. concluded that the fluorene/NDI based CILs PNDIT-F3N (tertiary amine) and PNDIT-F3N-Br (quaternary amine with Br counter ion) experienced elevated conductivities due to intramolecular doping.[20] Further, it was shown that PNDIT-F3N underwent photo-doping while PNDIT-F3N-Br was inherently doped even under darkness. High PCEs of approximately 8% were achieved for devices incorporating these CILs at thicknesses of ~100 nm.
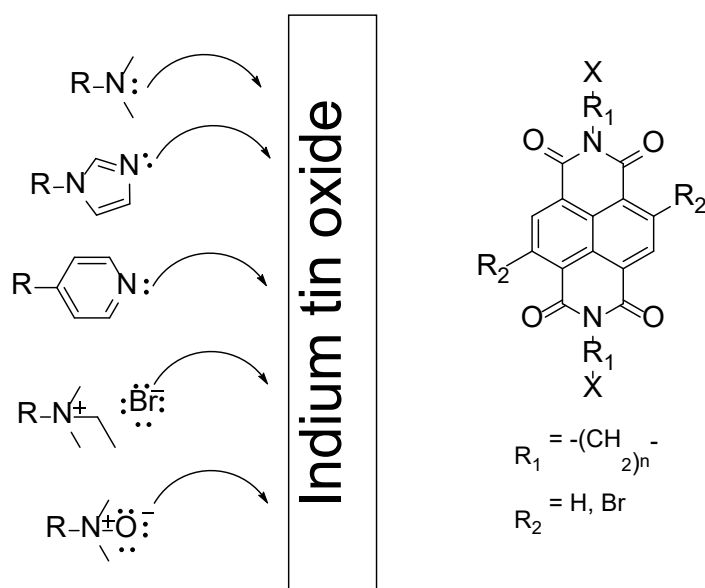
Figure 3.4: Left: Illustration of the formation of an interfacial dipole due to interaction between the free electron pairs and the electrode material indium tin oxide (ITO). Right: Chemical structure of NDI small molecule/monomer.

The strong acceptor character and low-lying HOMOs of NDI derivatives endows these materials with hole blocking properties. This property should ideally be retained for a high PCE material and therefore care must be taken that the co-polymerisation does not result in a HOMO level too close to the vacuum level. This can be achieved through the careful selection of the donor material for the D-A type co-polymers, with stronger donors shifting the HOMO closer toward the vacuum level. As discussed earlier, thiophene and/or bithiophene are commonly paired with NDI structures in acceptor polymers, making these weak donors a good starting point.

3.4.4 Synthesis

The aim is to minimise the use of toxic chemicals, keeping the synthesis procedures as environmentally friendly as possible. However, the main focus is the development of PSC materials, and so, there are other criteria that need to be considered including i) synthesis complexity, ii) cost of starting materials, and iii) maturity of the procedure.

Semiconducting polymers are commonly synthesised through carbon-carbon (C-C) bond forming, cross coupling reactions utilising palladium catalysts. Stille and Suzuki are two such cross coupling reactions, which both follow similar mechanisms with oxidative addition, transmetallation, and reductive elimination steps (Figure 3.5a). These reactions are highly efficient and are the most widely applied for the synthesis of conjugated polymers, however, they are reliant on stannylated (Stille) and boronated (Suzuki) monomers. The tin containing stannyl compounds used in Stille couplings are highly toxic.[21] While the boronic acid/ester compounds are much less toxic, they still require additional reaction steps

to form, adding to the complexity of this procedure. Direct arylation polymerisation (DAP) is not reliant on these compounds but does instead utilise the activation of a C-H bond in a transition metal catalytic cycle for the formation of C-C bonds (Figure 3.5b). DAP therefore, effectively eliminates the use of additional stannylation or boronation of the monomers.[22-23]
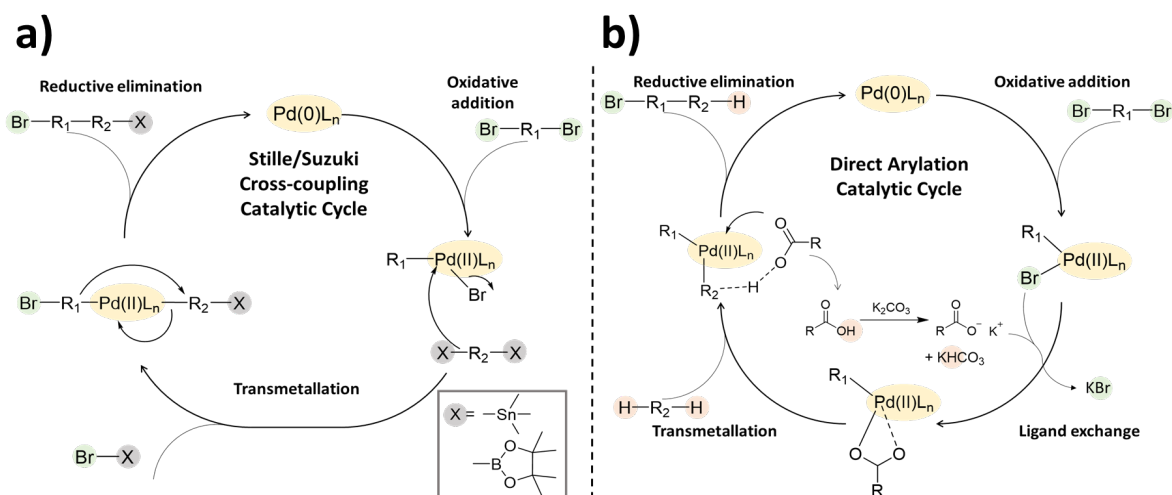
Figure 3.5: Schematic representation of a typical a) Stille/Suzuki cross coupling catalytic cycle and b) direct arylation catalytic cycle.[24]

The area of DAP has experienced rapid progress, with certain reactions showing results on-par with or even superior to the traditional Stille and Suzuki cross coupling reactions.[22] NDI based co-polymers have been synthesised via DAP with promising results for a number of N2200 derivatives.[25-27] The coupling reactions are ordered according to DAP > Suzuki coupling > Stille coupling with regards to environmentally friendliness. However, the well-established Stille and Suzuki couplings present good starting points for novel materials with opportunity to alter the procedure if the developed materials are promising.

Small molecules, including monomers, are evaluated in a similar manner based on the complexity and the environmental friendliness of the procedure, with established synthesis routes taking precedence for novel compounds. Small molecule NDI compounds are synthesised in an alkylation procedure where NTCDA is reacted with a primary amine to form the diimide. This reaction is typically conducted at elevated temperatures in dimethyl formamide (DMF) or in some cases water. NDI based monomers are on the other hand, typically synthesised in a two-step procedure, starting with bromination of the naphthalene ring which is then consecutively followed by the alkylation step and formation of the imide. These steps are usually conducted in oleum and acetic acid respectively,[3] providing scope for improvement. Baumgartner *et al*. studied the conversion of NTCDA to NDI for straight alkyl chain side-groups, achieving quantitative yields in water at elevated temperature and pressure.[28] A third strategy for the alkylation was proposed by Tambara *et al*., utilising a microwave assisted synthesis procedure in dimethylformamide (DMF) for the formation of asymmetric NDI compounds.[29]

3.5 Device Fabrication

The device fabrication is an extremely important aspect of the PhD project outlined in this thesis as well as to the PSC research field as a whole. A short summary of device fabrication, including the three deposition techniques (spin coating, blade coating, and slot-die coating) used in this thesis, is presented below.

Fabrication of polymer solar cells involves the cleaning of substrates, deposition of interface layers, active layer and electrodes. Inorganic materials, which mainly constitute the electrodes, are typically thermally evaporated under high vacuum or deposited from nanoparticle solutions. The organic active layer in PSCs is instead solution processed. This is the case for all polymeric materials in organic electrodes and interface layers as well, with small molecules also heavily relying on solution processing. It should however be noted that small molecule OSCs tend to rely on evaporation of the active layer. Two major techniques are utilised in this thesis for solution processing of the varying NDI structures, spin coating and slot-die coating.

Spin coating, the most well studied coating technique in the area of PSCs, will primarily be used for the scanning of new materials/material combinations. Due to the facile nature of the technique, spin coating is expected to contribute to the realisation of high efficiencies, thus, allowing for the exploration of the upper boundaries for optimised devices. However, it is a small-scale laboratory technique that is non-scalable. Potential for upscaling will instead be investigated through blade coating as well as slot-die coating, which is a fully scalable printing technique, on a Mini Roll Coater (Figure 3.6).

Figure 3.6: Mini-Roll coater for slot-die coating with 1) rotating/heated drum, 2) slot-die coating head, 3) syringe pump, and 4) rotation and temperature controls. In operation, a flexible substrate is attached to the rotating drum and the slot-die coating head is lowered to allow formation of a meniscus between substrate and head.

3.5.1 Spin Coating

Spin coating is a small-scale serial technique that has been well studied for deposition of solution processed layer in PSCs as well as for the wider OPV research field. The technique is based on the deposition of a solution onto a substrate prior to/upon spinning of said substrate. This spinning creates angular velocity, spreading the solution over the substrate and ejecting part of the solution.[30] Thus, a thin film is simultaneously created and dried on the substrate. The film thickness is related to the rotational speed and viscosity of the solution,[2] which is in turn affected by the concentration. Further, the film formation process, which also determines morphology and topography, is dependent on solvent volatility, diffusivity, concentration and molecular weight of solutes.[2] This makes spin coating a highly reliable technique with low batch-to-batch variation.

3.5.2 Blade coating

Blade coating is laboratory scale deposition technique that utilises a static blade to coat thin films. Blade coating, unlike the roll-to-roll compatible technique knife-over-edge coating, operates on a single static substrate. During operation the solution/ink is deposited in front of the blade, which then is drawn over the substrate leaving a wet thin film. The blade typically operates at micrometre distances from the substrate at varying speeds (1-100 mm s^{-1}).[2] Contrary to spin coating, waste can be minimised with only small losses occurring during the solution processing. Film formation in blade coating is dependent on concentration (viscosity), temperature of solution, speed of the blade, and the distance substrate-blade (i.e. the volume deposited).[31] It should be noted that film formation via blade coating is relatively slow. The technique is therefore not suitable for solutions/materials with high tendencies to gel/crystallise under the film forming conditions.[2]

3.5.3 Slot-die Coating

Slot-die coating is a one-dimensional printing technique that utilises a static coating head with a shim, or meniscus guide, to coat on flexible substrates, e.g. PET films. This printing technique is used for smaller laboratory scale equipment (Figure 3.6), in which case a spinning drum typically carries the substrate, and can also be used for large scale roll-to-roll processing. During the coating procedure a wet film is formed from the deposited solution. This film is dried either in the ambient atmosphere, in a separate drying step, e.g. an oven, or in the case of laboratory scale the drum carrying the substrate is typically heated. Slot-die coating utilises all the material deposited, creating minimal amounts of waste.[2] As such, the thickness (*d*) is easily controlled by varying material concentration (*c*), drum rotation speed (*S*), and flow rate (*f*), as seen below:

$$d_{wet} = \frac{f}{S\,w} \qquad\qquad (3.4)$$

and

$$d_{dry} = \frac{f}{S\,w}\,\frac{c}{\rho} \qquad\qquad (3.5)$$

where d_{dry} is the thickness of the formed film, w is the meniscus guide width, and ρ is the density of the dried coating in g cm^{-3}.[2] The drying conditions are varied via solvent choices and additives as well as by the temperature and time of the drying step. Morphology of the BHJ layer is affected by the drying conditions, thus, this step is essential for printing high PCE PSCs.

3.6 Characterisation Techniques

A variety of characterisation techniques were used during the course of this project. Both individual components and blends, as well as full devices were analysed. These categories each required a different set of analysis techniques, for which detailed summaries are found below.

3.6.1 Ultraviolet-visible Spectroscopy

Ultraviolet-visible (UV/vis) spectroscopy, or absorption spectroscopy, is a technique that measures the light absorption, or electron transitions from ground state to excited state, of compounds. The spectrophotometer measures the intensity of light passing through the sample in relation to the light intensity prior to entering the sample. This gives the transmittance, i.e. light intensity ratio, which is recalculated to absorbance. Note that light scattering can interfere with these measurements, altering the appearance of the spectra with a scattering tail, extending beyond the materials natural absorption. As such care must be taken to not misinterpret the spectra, e.g. assigning the scattering tail as the optical absorption onset.

This technique is commonly used within the field of OPVs for determination of the optical band gap (E_g^{opt}) for both donor and acceptor compounds. The onset for absorption in a UV/vis spectrum will reveal $E_{g,opt}$ since the minimum energy needed to excite an electron is equal to the band gap. Good solar cell materials will have an E_g^{opt} of around 1-2 eV and show absorption over a large part of the solar spectrum.[32-33] In this project UV/vis spectroscopy will mainly be used for determination of the compounds absorption spectra, and in turn, the band gap as a first evaluation of possible material combinations. Additionally, the technique will be applied for transmittance measurements of CILs to determine to what degree these will hinder photons from reaching the active layer.

3.6.2 Photoluminescence Spectroscopy

In photoluminescence (PL) spectroscopy the sample, either in solution or as thin film, is illuminated with light of energy exceeding that of the band gap, thereby causing excitation and the formation of an exciton. For fluorescing materials, excited electrons then undergo non-radiative radiation to relaxed excited state (S_1) prior to returning to the ground state (S_0) in an emissive relaxation process, i.e. the release of excess energy in the form of a photon.[34] This photon, that possesses energy equal to or less than the band gap of the material, is detected and an emission spectrum formed. PL spectrums of conjugated polymers show emission peaks due to the presence of delocalised electrons in the polymer backbone.

For PSCs PL spectroscopy is typically used to measure the exciton dissociation, also referred to as quenching, by comparing emission strength for pure material (donor or acceptor) and donor-acceptor combinations.[35] The strong electron affinity of acceptor compounds results in the transfer of excited electrons from the donor LUMO to the acceptor LUMO, i.e. exciton dissociation. This process quenches the emission of the fluorescing material and has long been considered to be a prerequisite for efficient PSCs. However, an increase in PL quenching does not always translate in to higher PCEs, with the two typically being decoupled.

Charge carrier generation, and in turn J_{sc}, is highly dependent on the exciton dissociation. Thus, PL spectroscopy will mainly be used to probe the compatibility between new donor-acceptor combinations by measuring the quenching efficiency. This is typically done by loading a polymer donor thin film with a small amount of an acceptor compound.

3.6.3 Nuclear Magnetic Resonance

Nuclear magnetic resonance spectroscopy (NMR) is a technique commonly used for the characterisation of organic compounds. NMR will be applied for characterisation of monomers and polymers, as well as any intermediates in the longer reaction sequences. It is a method that can identify and provide information about magnetically distinct atoms. Elements that possess a sutiable spin, of which the most common are hydrogen and carbon, can be detected. In the case of hydrogen, also referred to as proton NMR, information can be extracted about the surrounding environment. That is, the atom or functional group on which the proton is located as well as the number of and distance to protons in close proximity [36].

In a modern NMR an electromagnetic radio frequency pulse is emitted which, according to Heisenberg's uncertainty principle, includes all frequencies. This pulse will therefore contain the specific frequencies for all the nuclei. Nuclei will absorb at energy at these specific frequencies and then re-emit electromagnetic radiation that is detected by the instrument. The signal is reported as chemical shift in relation to the universal reference tetramethylsilane (TMS) [36].

Chemical shifts of protons are affected by the neighbouring atoms or groups through shielding/de-shielding and coupling. Shielding occurs when nearby atoms counter the applied magnetic field and thus, de-shielding occurs when they reinforce it. Coupling takes place between protons and is an effect of the distribution of spin states of nearby protons. Together, these phenomena create a unique signal for each chemically different proton.[36]

NMR is a quick and easy method for confirming molecular structure of organic compounds containing carbon and hydrogen. ^{1}H-NMR will be used for routine analysis of organic materials throughout this project.

3.6.4 Thermogravimetric Analysis

Organic solar cell materials need high thermal stability in order to aovid degradation at elevated working temperatures (85 ºC)[37]. Thermogravimetric analysis (TGA) is a technique that measures the change in mass during a temperature ramp. This gives information about physical phenomena and second-order phase transitions such as vaporisation and sublimation. TGA will hence be used to measure thermal stability for the solar cell materials.

In the case of amine containing compounds, the solubility in highly polar solvents can be increased by protonation with a weak acid. Thus, TGA can be utilised to measure the temperature range over which the acid leaves the material as well as the degree of protonation or possible presence of water. This water will either be unbound or exist as a hydrate, which is more likely for the quaternary amines with associated counter ions.

3.6.5 Matrix-Assisted Laser Desorption/Ionisation – Time of Flight

Matrix-assisted laser desorption/ionisation – time of flight (MALDI-TOF) is a common technique that pairs soft ionisation with mass spectrometry. This combination allows for analysis of large organic molecules and polymers. In MALDI-TOF the analyte is typically mixed with a matrix and then deposited on a metal plate as a solution. The matrix then crystallises as the solvent evaporates leaving the analyte embedded in the crystals. The sample is then irradiated with UV-laser causing ablation and desorption of both analyte and matrix. This is the first function of the matrix, the second is to ionise the analyte which is then accelerated by an electric field upon which it enters the drift space. The drift space is a fixed distant over which the travel time of the analyte is measured giving the mass to charge ratio, m/z.

MALDI-TOF is a very quick technique and extremely useful for confirming target compounds. In some instances, it can also be used for measuring the molecular weights of larger molecules such as polymers, for which it was applied in this work.

3.6.6 Neutral Impact Collision Ion Scattering Spectroscopy

Polymer solar cells contain organic layers with thicknesses in the nanometre range, limiting thickness measurements to a select few techniques. One of these include low energy ion scattering technique called neutral impact collision ion scattering spectroscopy (NICISS). NICISS has a high resolution at ~3 Å, providing a depth profile of the elemental composition of up to 300 Å.[38] Thus, this is a perfect technique for measuring ultrathin organic interface layers. These layers typically range from a few to about 15 nm.

NICISS employs helium ion projectiles (He^+) with kinetic energies of ~3 keV (for 300 Å detection depths) that are neutralised at the surface to detect depth profiles of elements.[38] Scattered projectiles are detected at a deflection angle of 168°. Post neutralisation at the surface, the projectiles lose energy due to either back scattering events or small angle scattering events. This energy loss can then be related to

the element causing the backscattering event and the depth at which it occurred. Simply put, projectiles backscattered from heavier elements will lose less energy than those backscattered from lighter elements in addition to losing more energy the deeper the projectiles traverse.

3.6.7 Atomic Force Microscopy
The BHJ layer morphology is crucial for achieving high PCE solar cells. Atomic force microscopy (AFM) run in tapping mode will mainly be used to study the topography of the active layer but can also be used to investigate of the topography of interface layers. In AFM tapping mode a very fine tip is attached to an oscillating cantilever which scans the surface of a sample. Interactions between the tip and the surface will register as deviations of the oscillating pattern of the cantilever. These deviations are monitored with a laser as the surface is scanned and then transferred in to a three-dimensional topography map.

3.6.8 Electrochemistry
Electrochemistry will be used routinely for determination of HOMO and LUMO energy levels of conjugated polymers as well as small molecules throughout this project. In electrochemistry a potential is applied, and the electron flow is measured for the working electrode contra the reference electrode. This electron flow, or current, is measured with any redox event, such as oxidation and reduction potentials, contributing to the signal. HOMO and LUMO can be correlated to the first oxidation potential (ejection of electrons) and first reduction potential (injection of electrons) respectively. These potentials are then related to the vacuum level according to $E_{HOMO} = -(E_{ox} + 5.13)$ and $E_{LUMO} = -(E_{red} + 5.13)$ to give the energy levels.[39-41] To enable internal comparisons all potentials are reported against the ferrocene/ferrocenium (Fc/Fc$^+$) redox couple.

Two major techniques will be applied for the electrochemical measurements, square-wave voltammetry (SWV) and cyclic voltammetry (CV). SWV is a form of linear potential sweep with a high sensitivity. CV is one of the most widely used methods for energy level determination in conjugated semiconducting polymers. In this method, the potential of the working electrode is ramped linearly between two potential points, i.e. cycled. It is common practice to determine the redox potentials based on the maximum peak position for SWV and based on the peak onset for CV.

3.6.9 High Temperature Gel-Permeation Chromatography
Molecular weight determination of conjugated polymers is will be conducted using gel-permeation chromatography (GPC) with tetrahydrofuran (THF) at ambient temperatures or high temperature gel-permeation chromatography (HT-GPC) with 1,2,4-trichlorobenzene for polymers of low solubility. HT-GPC is a form of size-exclusion chromatography (SEC), meaning that the size of the analytes will be a determining factor of the speed at which they travel through the column. In this case, the stationary phase consists of cross-linked porous polystyrene in the form of beads that have been tightly packed and the mobile phase of hot 1,2,4-trichlorobenzene. The separation mechanism of the analytes is based

on their diffusion and level of penetration of the porous polystyrene. Shorter polymer segments further penetrate the polystyrene, travelling a longer distance, extending their elution time. The elution time of the polymer analyte is set in relation to that of a polystyrene (PS) standard of known molecular weight. Thus, the molecular weight, $\bar{M}_n$, $\bar{M}_w$, and $Đ_M$, is determined relative to this PS standard.[42]

3.6.10 Differential Scanning Calorimetry

Morphology control, in which phase transitions play a big part, is essential for solar cell efficiency. Differential scanning calorimetry (DSC) is a technique that can be used to monitor phase transitions and chemical reactions. The technique measures the heat flow required for a constant temperature ramp (increase/decrease) of sample and reference. Thus, phase transitions or chemical reactions that occur in the sample will alter the heat flow required for a constant temperature ramp. These processes are hence detected as exothermic/endothermic peaks, indicating for example crystallisation or melting.[43] In this project DSC will be used for determination of crystallisation temperatures of novel small molecule NFAs. The flat NDI compounds described earlier are prone to crystallisation, therefore it is of utmost importance for thermal annealing to investigate their crystallisation temperatures.

3.6.11 Ultraviolet Photoelectron Spectroscopy

The work function of electrodes and electrode-interface layer combinations play an important role in device engineering. Work function alignment contributes to efficient charge extraction, leading to high currents and PCE. In ultraviolet photoelectron spectroscopy (UPS) the sample is irradiated with ultraviolet light, causing the emission of photoelectrons from the valence band. These photoelectrons are detected, and the work function is determined from the difference between fermi level and vacuum level. UPS is a highly surface sensitive technique with penetration depths of ~1-3 nm, thus, it is heavily influenced by adsorbed contaminants or variations in the surface composition.

3.6.12 Direct Sample Analysis – Time of Flight

Direct Sample Analysis-Time of Flight (DSA-TOF) is a high-resolution mass spectrometry technique, i.e. capable of recording masses with a precision of < 5 ppm.[44] The analyte can either be injected directly or deposited from a solution on metal gauze. Inside the analysis chamber a nitrogen gas stream is subjected to a corona needle, forming reagent ions, and then passed across the sample for ionisation and vaporisation of analytes with sufficient volatility. These compounds enter the mass spectrometer for mass determination. This instrument also allows for the introduction of an internal calibration solution.

DSA-TOF is a very quick technique that can provide accurate mass, however, unlike MALDI-TOF the mass range is quite narrow, with masses counted in hundreds of Da to a couple of thousand Da.

3.6.13 Profilometry

The thickness of active layer films, typically ~100 nm, plays a crucial role in light absorption. In this project, stylus profilometry will be used for thickness measurements of active layer films as well as for thicker CIL layer films. Stylus profilometry is a contact technique (i.e. the probe is in contact with the

sample) that traces the topography of the surface. This technique has a resolution in the nanometre range both vertically and horizontally. Thickness measurements of organic films are conducted by measuring the height difference between a fabricated scratch and the intact film.

3.6.14 Solar Cell Efficiency

In this project, the efficiency of manufactured solar cell devices will be routinely measured. This is the most straightforward, fundamental analysis for solar cells with standardised testing protocols developed. These include the air mass 1.5 spectrum (AM1.5) Global for terrestrial cells, one-sun illumination (i.e. 100 mW cm^{-2}), cell temperatures of 25 °C, and the utilisation of a four-point probe to avoid contact resistance. This requires a setup consisting of a solar simulator, a current-voltage source, a temperature control unit, and a four-point probe, with the latter two commonly found only at certified testing facilities.

3.7 References

(1)   Po, R.; Bernardi, A.; Calabrese, A.; Carbonera, C.; Corso, G.; Pellegrino, A., From Lab to Fab: How Must the Polymer Solar Cell Materials Design Change? - An Industrial Perspective. *Energy Environ. Sci.* **2014**, 7, 925-943.

(2)   Krebs, F. C., Fabrication and Processing of Polymer Solar Cells: A Review of Printing and Coating Techniques. *Sol. Energy Mater. Sol. Cells* **2009**, 93, 394-412.

(3)   Suraru, S.-L.; Würthner, F., Strategies for the Synthesis of Functional Naphthalene Diimides. *Angew. Chem., Int.* **2014**, 53, 7428-7448.

(4)   Al Kobaisi, M.; Bhosale, S. V.; Latham, K.; Raynor, A. M.; Bhosale, S. V., Functional Naphthalene Diimides: Synthesis, Properties, and Applications. *Chem. Rev.* **2016**, 116, 11685-11796.

(5)   Liu, Y.; Zhang, L.; Lee, H.; Wang, H.-W.; Santala, A.; Liu, F.; Diao, Y.; Briseno, A. L.; Russell, T. P., NDI-Based Small Molecule as Promising Nonfullerene Acceptor for Solution-Processed Organic Photovoltaics. *Adv. Energy Mater.* **2015**, 5, 1500195.

(6)   Rundel, K.; Maniam, S.; Deshmukh, K.; Gann, E.; Prasad, S. K. K.; Hodgkiss, J. M.; Langford, S. J.; McNeill, C. R., Naphthalene Diimide-based Small Molecule Acceptors for Organic Solar Cells. *J. Mater. Chem. A* **2017**, 5, 12266-12277.

(7)   Wang, E.; Hou, L.; Wang, Z.; Hellström, S.; Zhang, F.; Inganäs, O.; Andersson, M. R., An Easily Synthesized Blue Polymer for High-Performance Polymer Solar Cells. *Adv. Mater.* **2010**, 22, 5240-5244.

(8)   de Zerio, A. D.; Müller, C., Glass Forming Acceptor Alloys for Highly Efficient and Thermally Stable Ternary Organic Solar Cells. *Adv. Energy Mater.* **2018**.

(9)   Li, H.; Lu, K.; Wei, Z., Polymer/Small Molecule/Fullerene Based Ternary Solar Cells. *Adv. Energy Mater.* **2017**, 7, 1602540.

(10)   Baran, D.; Ashraf, R. S.; Hanifi, D. A.; Abdelsamie, M.; Gasparini, N.; Rohr, J. A.; Holliday, S.; Wadsworth, A.; Lockett, S.; Neophytou, M.; Emmott, C. J.; Nelson, J.; Brabec, C. J.; Amassian, A.; Salleo, A.; Kirchartz, T.; Durrant, J. R.; McCulloch, I., Reducing the Efficiency-stability-cost Gap of Organic Photovoltaics with Highly Efficient and Stable Small Molecule Acceptor Ternary Solar Cells. *Nat. Mater.* **2017**, 16, 363-369.

(11)   Chen, Z.; Zheng, Y.; Yan, H.; Facchetti, A., Naphthalenedicarboximide- vs Perylenedicarboximide-Based Copolymers. Synthesis and Semiconducting Properties in Bottom-Gate N-Channel Organic Transistors. *J. Am. Chem. Soc.* **2009**, 131, 8-9.

(12)   Li, Z.; Xu, X.; Zhang, W.; Meng, X.; Ma, W.; Yartsev, A.; Inganäs, O.; Andersson, M. R.; Janssen, R. A. J.; Wang, E., High Performance All-Polymer Solar Cells by Synergistic Effects of Fine-Tuned Crystallinity and Solvent Annealing. *J. Am. Chem. Soc.* **2016**, 138, 10935-10944.

(13)   Lee, C.; Kang, H.; Lee, W.; Kim, T.; Kim, K.-H.; Woo, H. Y.; Wang, C.; Kim, B. J., High-Performance All-Polymer Solar Cells Via Side-Chain Engineering of the Polymer Acceptor: The Importance of the Polymer Packing Structure and the Nanoscale Blend Morphology. *Adv. Mater.* **2015**, 27, 2466-2471.

(14)   Xu, X.-p.; Zhang, G.-j.; Zhao, Y.-z.; Liu, J.; Li, Y.; Peng, Q., Highly Efficient Random Terpolymers for Photovoltaic Applications with Enhanced Absorption and Molecular Aggregation. *Chin. J. Polym. Sci.* **2017**, 35, 249-260.

(15)   Woo, C. H.; Thompson, B. C.; Kim, B. J.; Toney, M. F.; Fréchet, J. M. J., The Influence of Poly(3-hexylthiophene) Regioregularity on Fullerene-Composite Solar Cell Performance. Journal of the American Chemical Society **2008**, 130 , 16324-16329.

(16)   Yao, H.; Li, Y.; Hu, H.; Chow, P. C. Y.; Chen, S.; Zhao, J.; Li, Z.; Carpenter, J. H.; Lai, J. Y. L.; Yang, G.; Liu, Y.; Lin, H.; Ade, H.; Yan, H., A Facile Method to Fine-Tune Polymer Aggregation Properties and Blend Morphology of Polymer Solar Cells Using Donor Polymers with Randomly Distributed Alkyl Chains. *Adv. Energy Mater.* **2018**, 8.

(17)   Huo, L.; Xue, X.; Liu, T.; Xiong, W.; Qi, F.; Fan, B.; Xie, D.; Liu, F.; Yang, C.; Sun, Y., Subtle Side-Chain Engineering of Random Terpolymers for High-Performance Organic Solar Cells. *Chem. Mater.* **2018**, 30, 3294-3300.

(18)   van Reenen, S.; Kouijzer, S.; Janssen, R. A. J.; Wienk, M. M.; Kemerink, M., Origin of Work Function Modification by Ionic and Amine-Based Interface Layers. *Adv. Mater. Interfaces* **2014**, 1, 1400189.

(19)   Hu, Z.; Zhang, K.; Huang, F.; Cao, Y., Water/alcohol Soluble Conjugated Polymers for the Interface Engineering of Highly Efficient Polymer Light-emitting Diodes and Polymer Solar Cells. *Chem. Commun.* **2015**, 51, 5572-5585.

(20)   Wu, Z.; Sun, C.; Dong, S.; Jiang, X.-F.; Wu, S.; Wu, H.; Yip, H.-L.; Huang, F.; Cao, Y., n-Type Water/Alcohol-Soluble Naphthalene Diimide-Based Conjugated Polymers for High-Performance Polymer Solar Cells. *J. Am. Chem. Soc.* **2016**, 138, 2004-2013.

(21)   Espinet, P.; Echavarren, A. M., The Mechanisms of the Stille Reaction. *Angew. Chem., Int.* **2004**, 43, 4704-4734.

(22)   Bohra, H.; Wang, M., Direct C–H arylation: a "Greener" Approach towards Facile Synthesis of Organic Semiconducting Molecules and Polymers. *J. Mater. Chem. A* **2017**, 5, 11550-11571.

(23)   Kai, W.; Mingfeng, W., Direct Arylation Polymerization: A Green, Streamlining Synthetic Approach to π - conjugated Polymers. *Curr. Org. Chem.* **2013**, 17, 999-1012.

(24)   Gobalasingham, N. S.; Thompson, B. C., Direct Arylation Polymerization: A Guide to Optimal Conditions for Effective Conjugated Polymers. *Prog. Polym. Sci.* **2018**, 83, 135-201.

(25)   Matsidik, R.; Luzio, A.; Hameury, S.; Komber, H.; McNeill, C. R.; Caironi, M.; Sommer, M., Effects of PNDIT2 End Groups on Aggregation, Thin Film Structure, Alignment and Electron Transport in Field-effect Transistors. *J. Mater. Chem. C* **2016**, 4, 10371-10380.

(26)   Matsidik, R.; Komber, H.; Sommer, M., Rational Use of Aromatic Solvents for Direct Arylation Polycondensation: C–H Reactivity versus Solvent Quality. *ACS Macro Lett.* **2015**, 4, 1346-1350.

(27)   Sharma, S.; Soni, R.; Kurungot, S.; Asha, S. K., Naphthalene Diimide Copolymers by Direct Arylation Polycondensation as Highly Stable Supercapacitor Electrode Materials. *Macromolecules* **2018**, 51, 954-965.

(28)   Baumgartner, B.; Svirkova, A.; Bintinger, J.; Hametner, C.; Marchetti-Deschmann, M.; Unterlass, M. M., Green and Highly Efficient Synthesis of Perylene and Naphthalene Bisimides in Nothing but Water. *Chem. Commun.* **2017**, 53, 1229-1232.

(29)   Tambara, K.; Ponnuswamy, N.; Hennrich, G.; Pantoş, G. D., Microwave-Assisted Synthesis of Naphthalenemonoimides and N-Desymmetrized Naphthalenediimides. *The Journal of Organic Chemistry* **2011**, 76, 3338-3347.

(30)   Norrman, K.; Ghanbari-Siahkali, A.; Larsen, N. B., 6 Studies of Spin-coated Polymer Films. *Annu. Rep. Prog. Chem., Sect. C: Phys. Chem.* **2005**, 101, 174-201.

(31)   Brabec, C. J.; Durrant, J. R., Solution-Processed Organic Solar Cells. *MRS Bull.* **2008**, 33, 670-675.

(32)   Kroon, R.; Lenes, M.; Hummelen, J. C.; Blom, P. W. M.; de Boer, B., Small Bandgap Polymers for Organic Solar Cells (Polymer Material Development in the Last 5 Years). *Polym. Rev.* **2008**, 48, 531-582.

(33)   Dong, X.; Deng, Y.; Tian, H.; Xie, Z.; Geng, Y.; Wang, F., Isoindigo-based Low Bandgap Conjugated Polymer for o-xylene Processed Efficient Polymer Solar Cells with Thick Active Layers. *J. Mater. Chem. A* **2015**, 3, 19928-19935.

(34)   Lakowicz, J. R., Principles of Fluorescence Spectrocscopy. 3rd ed.; *Springer Science*: **2006**.

(35)   Mirzov, O.; Scheblykin, I. G., Photoluminescence Spectra of a Conjugated Polymer: from Films and Solutions to Single Molecules. *Phys. Chem. Chem. Phys.* **2006**, 8, 5569-5576.

(36)   Pavia, D. L.; Lampman, G. M.; Kriz, G. S.; Vyvyan, J. A., Introduction to Spectroscopy. 4th ed.; United States of America, **2009**.

(37)   E1171-15, A., Standard Test Methods for Photovoltaic Modules in Cyclic Temperature and Humidity Environments. In ASTM International, **2015**.

(38)   Andersson, G.; Ridings, C., Ion Scattering Studies of Molecular Structure at Liquid Surfaces with Applications in Industrial and Biological Systems. *Chem. Rev.* **2014**, 114, 8361-87.

(39)   Li, W.; Furlan, A.; Hendriks, K. H.; Wienk, M. M.; Janssen, R. A. J., Efficient Tandem and Triple-Junction Polymer Solar Cells. *J. Am. Chem. Soc.* **2013**, 135, 5529-5532.

(40)   Pavlishchuk, V. V.; Addison, A. W., Conversion Constants for Redox Potentials Measured versus Different Reference Electrodes in Acetonitrile Solutions at 25°C. *Inorg. Chim. Acta* **2000**, 298, 97-102.

(41)   Bard, A. J.; Faulkner, L. R., Electrochemical Methods: Fundamentals and Applications. 2nd ed.; *Wiley: New York*, **2001**.

(42)   Cowie, J.; Arrighi, V., Polymers: Chemistry and Physics of Modern Materials. 3rd ed.; *CRC Press: Boca Raton*, **2007**.

(43)   Suseela, Y. V.; Sasikumar, M.; Govindaraju, T., An Effective and Regioselective Bromination of 1,4,5,8-naphthalenetetracarboxylic Dianhydride using Tribromoisocyanuric Acid. *Tetrahedron Lett.* **2013**, 54, 6314-6318.

(44)   Tyler, A.; Dalmia, A., Direct Sample Analysis/Time-of-Flight Mass Spectrometry. *American Laboratory* **2014**, 46, 38-40.

Chapter 4 – NDI Based Non-fullerene Acceptors for Fine Tuning of the Morphology in Active Layer Blends

4.1 Overview

In this chapter, the four naphthalene diimide (NDI) based small molecules DEHNDI, DONDI, AsNDI and DOBNDI were successfully synthesised in facile, short step procedures. These compounds were explored for use as non-fullerene acceptors (NFA) in binary-quinternary active layer blends in polymer solar cells (PSC). The morphology was tuned via synthetic modification of the pendant side-groups, showing variations in steric hindrance toward intermolecular packing, for the individual acceptor compounds. This synthetic tuning of the crystal forming ability was observed with optical measurements and with differential scanning calorimetry (DSC). Furthermore, the effect on morphology of variations in the active layer blend ratios were explored. The acceptor compounds were paired with the donor polymer TQ1 to study the photovoltaic performance in the inverted device structure for an indium tin oxide (ITO)/zinc oxide (ZnO)/Active layer blend/molybdenum oxide (MoO_x)/silver (Ag) device architecture. Additionally, the active layer was spin coated from the non-chlorinated greener solvent anisole to investigate more environmentally friendly/scalable solution processing conditions. Active layer morphologies experienced phase separation on the micrometre scale under optical microscope and in AFM images for a majority of the active layer blends tested. Thermal annealing or the incorporation of the solvent additive 1-chloronaphthalene (CN) were confirmed to influence both morphology and performance, with the latter consistently improving the PCE. TQ1:DONDI blends achieved a highest PCE of 0.22% despite showing large phase separation, thus, outperforming blends appearing to show favourable morphology, e.g. TQ1:DOBNDI that reached a PCE of 0.09%. If further improvements can be implemented for these active layer blends, the low efficiencies could possibly be overlooked in favour of facile synthesis, environmentally friendly processing and aesthetics, in niche areas such as semitransparent organic photovoltaics (OPV).

4.2 Introduction

The area of polymer solar cells (PSCs) has experienced rapid development during recent years due to the introduction of high-performance non-fullerene acceptor (NFA) materials. These novel materials have contributed to new record PCEs as well as a range of high performing acceptor compounds, with many derived from the highly successful ITIC. However, building blocks such as perylene diimide (PDI) have also experienced high efficiencies. PDI belongs to the rylene diimides out of which both the lower homologue (Figure 4.1), naphthalene diimide (NDI), and higher homologue, terrylene diimide (TDI) have been used in PSC applications.
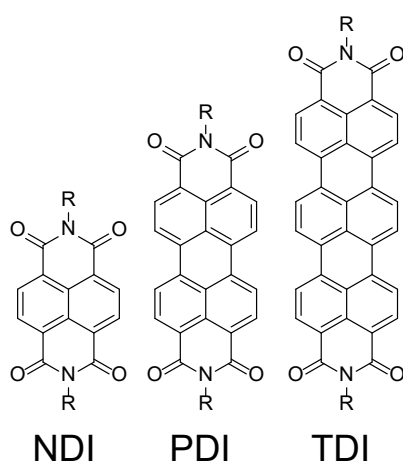
Figure 4.1: From left to right, chemical structures of naphthalene diimide (NDI), perylene diimide (PDI), and terrrylene diimide (TDI).

For NFAs, perylene diimide is almost solely utilised as a building block due to its balanced properties. The crystallinity, absorption, and charge carrier mobility increase with the extended conjugation of the higher homologues.[1] Consequently, NDI with its relatively lower extinction coefficient and mobility as well as superior solubility is a favoured building block for polymeric acceptors, e.g. N2200. Contrarily, the strong crystallinity of TDI could cause phase separation on the micrometre scale due to the strong formation of crystals. This is detrimental to the vital active layer morphology, and thus results in a decrease of PCEs.[2-3] PDI is the most well investigated out of the three for NFA applications, with several acceptor materials reaching PCEs of over 8%.[4-7] However, these high performance PDI structures are mainly processed from chlorinated solvents, or from the non-chlorinated, less harmful solvent trimethylbenzene (TMB). The PCEs so far achieved for small molecule NDI based NFA is relatively modest with the efficiencies currently reaching over 3% for acceptor NDI-Xy-NDI, Figure 4.2.[8] The superior solubility in non-chlorinated, greener solvents of NDI based compounds provide this material with an important advantage making it a viable core building block candidate for upscaling. The NFA BiNDI (Figure 4.2), although processed from chloroform, is soluble in THF and toluene.[9] Though, as previously mentioned this solubility is achieved at the cost of both a lower extinction coefficient and a decrease in mobility.

The application of NDI based NFAs in ternary blends could negate the lower light absorption associated with these lower homologue materials. As discussed in section *2.7.4 Ternary blends* in Chapter 2, ternary blends are known for contributing to enhanced light absorption, efficient charge extraction, high open circuit voltages, and the suppression of charge recombination. Further, analogous improvements are to be expected in both the quaternary[10] and quinternary systems. Additionally, these systems can provide improved thermal stabilities due to the formation of a glassy state, an alloy, and a kinetic trapping effect, locking in the morphology.[10-11] In comparison to the binary systems, the additional active layer components also provide an opportunity for more intricate fine tuning of the morphology via optimisation of the blend ratios. The relatively low mobility of NDI based NFAs indicates that these materials could be suitable as a complementary component in ternary-quinternary blends or in niche applications. These applications could include for example, semi-transparent PSCs for art installations, windows, and greenhouses.[12-13]

BiNDI   Star NDI-S   NDI-Xy-NDI
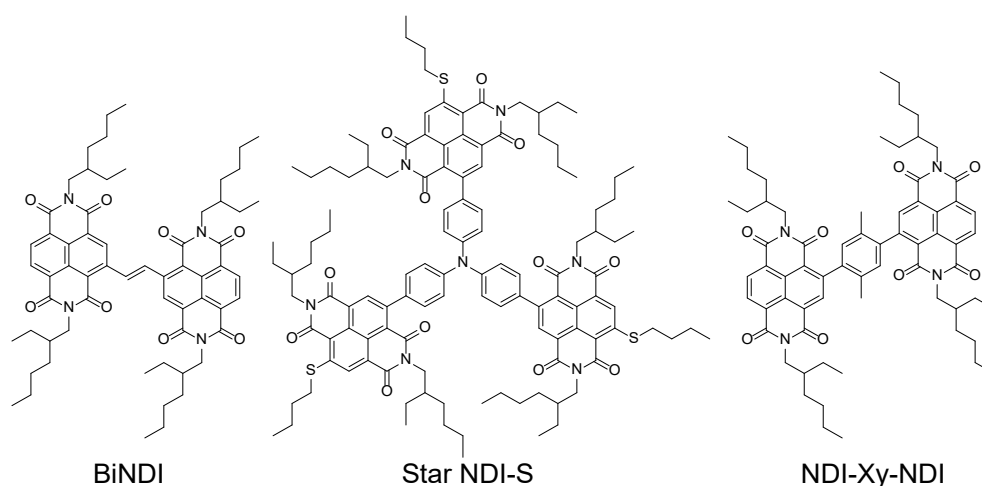
Figure 4.2: From left to right chemical structures of BiNDI, Star NDI-S, and NDI-Xy-NDI.

In this chapter, the synthesis and application of four NDI based small molecule NFA compounds are presented. The compounds 2,7-*bis*(2-ethylhexyl)benzo[lmn][3,8]phenanthroline-1,3,6,8(2*H*,7*H*)-tetrone (DEHNDI), *N,N*'-Bis(octyl)-1,4,5,8-naphthalenetetracarboxylic diimide (DONDI), 2,7-*bis*(2-octyloxyphenyl)benzo[lmn][3,8]phenanthroline-1,3,6,8(2*H*,7*H*)-tetrone (DOBNDI), and 2-(2-dimethoxyphenyl)-7-octyl-benzo[lmn][3,8]phenanthroline-1,3,6,8(2*H*,7*H*)-tetrone (AsNDI) are all synthesised in short and facile steps from relatively inexpensive starting materials. These compounds were designed based on a select number of pre-determined criteria in order to limit structural combinations to a manageable sample size. Firstly, the number of potential compounds were limited to a single NDI core for comparative purposes between side-groups. The side-groups are expected to affect solubility, π-π stacking, and blend-morphology. Additionally, being a prerequisite for large scale manufacturing, the commercial availability/synthesis complexity was also considered. The four NFAs were also developed to each possess a different type of side-group, providing an extensive coverage of side-group types within a small sample set. These four categories are based on commonly utilised side-

groups within the field of OPVs; i) straight alkyl chain (DONDI), ii) branched alkyl chain (DEHNDI), iii) aromatic (DOBNDI), and iv) asymmetric configuration (AsNDI) (Scheme 4.1). Lastly, the introduced side-groups should provide varying level of steric hindrance, influencing the degree of π-π stacking of the NFAs. As a result, the four compounds are expected to possess a varying degree of crystallinity, affecting the morphologies of the active layer.

For the straight and branched alkyl side-groups, 1-octylamine (DONDI) and 2-ethyl-1-hexylamine (DEHNDI) were chosen due to their commercial availability. The identical atomic composition of these two compounds contribute to a straightforward structural comparison, with the latter (branched chain isomer) group expected to provide a larger degree of steric hindrance. However, the character of these side-groups suggests a relatively low steric hindrance in both cases. An alternative to steric interference by aliphatic side-groups is to utilise aromatic components. The aromatic side-group 2-octyloxyaniline (DOBNDI), was made with a straight chain in the ortho position, to limit π-π stacking. This is achieved due to the narrow angle formed between the straight chain of the side-group and the flat NDI core. For the fourth side-group configuration, asymmetry was purposefully introduced. For consistency the side-group choices were narrowed to those that were utilised in the other NFAs. 1-octylamine and 2-octyloxyaniline, providing the smallest and largest steric hindrance respectively, were chosen in an attempt to balance the crystallinity. In addition, the lack of symmetry is expected lower the crystallinity. These four compounds are used in binary-quinternary active layer blends.

The impact on morphology due to fine-tuning of the blend component ratios as well as the effect of thermal and solvent annealing on the device performance are studied. The photovoltaic performance of the binary-quinternary blends is studied in inverted device configuration for indium tin oxide (ITO)/zinc oxide (ZnO)/TQ1:A_1:A_2:A_3:A_4/molybdenum oxide (MoO$_x$)/Ag systems. Devices are fabricated with the active layer spin coated from the non-chlorinated solvent anisole, which is considered a green alternative.[14]

4.3 Experimental

4.3.1 Synthesis
All solvents, reagents and catalysts were purchased from commercial sources and used as received.

4.3.1.1 DEHNDI
NTCDA (4g, 14.9 mmol) was slurried in 80 mL acetic acid in a 250 mL two-necked round-bottom flask (RBF) and stirred under nitrogen atmosphere for 15 minutes. 2-Ethylhexyl amine (11.57 g, 89.5 mmol, 6 eq.) was added to the reaction flask via septum and the temperature increased to reflux for 24 hours. Once cooled to room temperature the reaction mixture was poured on crushed ice and extracted with chloroform (2 x 75 mL). The resulting chloroform solution was first washed with brine (3 x 50 mL) and then washed with a 1M sodium hydrogen carbonate solution prior to drying with magnesium sulfate.

The crude product was recrystallised in ethyl acetate, yielding pure product as an off-white flaky solid. Yield: 4.8 g (65.6 %). TLC: Chloroform-Hexane (1:1), R_f = 0.31.

^{1}H NMR (CDCl$_3$, 600 MHz) δ: 8.75 (s, 4H, H$_{11}$), 4.13 (m, 4H, H$_6$), 1.93 (sep, J = 6.4 Hz, 2H, H$_5$), 1.39 (m, 8H, H$_4$,H$_7$), 1.30 (m, 8H, H$_2$,H$_3$), 0.93 (t, J = 7.4 Hz, 6H, H$_8$), 0.88 (t, J = 6.7 Hz, 6H, H$_1$); ^{13}C NMR (CDCl$_3$, 600 MHz) δ: 163.38 (C$_9$) 131.16 (C$_{11}$), 126.89 (C$_{10}$), 126.74 (C$_{12}$), 44.75 (C$_6$), 38.09 (C$_5$), 30.84 (C$_4$), 28.77 (C$_3$), 24.18 (C$_7$), 23.18 (C$_2$), 14.21 (C$_1$), 10.75 (C$_8$). IR: v_{max} = 2958, 2920sh, 2928, 2871, 2856, 1699, 1652, 1580. MS calcd. for C$_{30}$H$_{38}$N$_2$O$_4$ [[M+H]$^+$]: m/z = 491.29096; MALDI-TOF 489.16 exp, DSA-TOF 491.2905 exp. STA: T_m = 204.2 °C.

4.3.1.2 DONDI
NTCDA (1.5 g, 5.6 mmol) was slurried in DMF (30 mL) to achieve stable mixing. The temperature was then increased to 90 ºC. 1-octylamine (3.62 g, 28 mmol, 5 eq) was added dropwise to the hot solution and the mixture was left to react overnight. Once cooled down to ambient temperature the precipitated crude product was filtered off, leaving a dark-pink solid, which was then further purified by recrystallization in DMF resulting in pink crystals. Yield: 1.41 g (62%). TLC: CHCl$_3$-Hexane (1:1), R_f = 0.26.

^{1}H NMR (CDCl$_3$, 600 MHz) δ: 8.74 (s, 4H, H$_{11}$), 4.18 (t, J = 7.7 Hz, 4H, H$_8$), 1.73 (q, J = 7.6 Hz, 4H, H$_7$), 1.42 (m, 4H, H$_6$), 1.36 (m, 4H, H$_5$), 1.27 (m, 12H, H$_{2-4}$) 0.87 (t, J = 6.9 Hz, 6H, H$_1$); ^{13}C NMR (CDCl$_3$, 600 MHz) δ: 162.97 (C$_9$), 131.05 (C$_{11}$), 126.83 (C$_{10}$), 126.78 (C$_{12}$), 41.14 (C$_8$), 31.93 (C$_3$), 29.42 (C$_5$), 29.32 (C$_4$), 28.23 (C$_7$), 27.23 (C$_6$), 22.77 (C$_2$), 14.22 (C$_1$). IR: v_{max} = 2953, 2922, 2894sh, 2868, 2846, 1702, 1652, 1580. MS calcd. for C$_{30}$H$_{38}$N$_2$O$_4$ [[M+H]$^+$]: m/z = 491.29096; MALDI-TOF 489.16 exp, DSA-TOF 491.2905 exp. STA: T_m = 181.3 °C.

4.3.1.3 2-(octyloxy)aniline
2-aminophenol (10 g, 91.6 mmol) was dissolved in DMF (100 mL) in a RBF that was placed in an ice bath. Sodium hydride in mineral oil (3.66 g, 91.6 mmol, 1 eq) was added in portions over the course of 15 minutes under stirring. 1-bromooctane (26.35 g, 136.5 mmol, 1.5 eq) was added dropwise and the reaction was then slowly allowed to reach ambient temperature at which it was kept at for an additional 24 hours. The reaction mixture was poured into water (300 mL) and extracted with ethyl acetate (3 x 100 mL). The solution was washed with water and brine prior to removing the solvent on a rotary evaporator. The resulting crude product was purified by column chromatography and, the remaining starting material was flushed out with hexane upon which point the polarity was increased to ethyl acetate-hexane (1:19). Pure product was achieved as a rust coloured oil. Yield: 13.2 g (65%). TLC: Ethyl acetate-Hexane (1:9), R_f = 0.3.

4.3.1.4 AsNDI
NTCDA (2 g, 7.5 mmol) was slurried in DMF (40 mL) and bubbled with nitrogen for 15 minutes. 1-octylamine (0.87 g, 6.7 mmol, 0.9 eq) was added dropwise and the temperature increased to 90 ºC for

12 h. 2-(octyloxy)aniline (3.47 g, 15.7 mmol, 2.1 eq) was added and the temperature increased to 125 °C for an additional 24 h.

Once cooled down to ambient temperature the reaction mixture was poured into water (160 mL) and extracted with chloroform (3 x 50 mL). The solvent was removed on a rotary evaporator leaving a dark crude. The crude product was recrystallised in IPA twice achieving pure product as a yellow-green solid. Yield: 0.84 g (23%). TLC: Ethyl acetate-Hexane (3:17), R_f = 0.24.

^{1}H NMR (CDCl$_3$, 600 MHz) δ: 8.79 (s, 4H), 7.48 (t, J = 7.8, 1H), 7.29 (d, J = 7.9 Hz, 1H), 7.13 (m, 2H), 4.23 (t, J = 7.7 Hz, 2H), 3.98 (t, J = 6.3 Hz, 2H), 1.78 (q, J = 7.5 Hz, 2H), 1.55 (m, 2H), 1.47 (m, 2H), 1.40 (m, 2H), 1.29 (m, 6H), 1.16 (m, 10H), 0.89 (t, J = 6.8 Hz, 3H), 0.77 (t, J = 7.3 Hz, 3H) ; ^{13}C NMR (CDCl$_3$, 600 MHz) δ: 163.00, 162.73, 131.27, 131.12, 130.80, 129.80, 127.36, 127.04, 127.03, 126.98, 123.82, 121.07, 113.32, 68.73, 41.16, 31.95, 31.73, 31.68, 29.43, 29.34, 29.26, 29.18, 29.04, 28.25, 27.24, 25.97, 22.79, 22.77, 22.71, 14.26, 14.22, 14.14. FTIR 2956, 2918, 2871, 2847, 1717, 1704, 1673sh, 1660, 1623sh, 1597, 1580. MS calcd. for C$_{36}$H$_{42}$N$_2$O$_5$ [[M+H]$^+$]: m/z = 583.31717; MALDI-TOF 580.26 exp, DSA-TOF 583.3172 exp. STA: T_m = 122.3 °C.

4.3.1.5 DOBNDI
NTCDA (2 g, 7.5 mmol) and 2-(octyloxy)aniline (4.95 g, 22.4 mmol, 3 eq) were dissolved in DMF (50 mL) in a RBF. The formed slurry was bubbled with nitrogen for 15 minutes before the temperature was increased to 125 ºC. The mixture was reacted overnight under nitrogen atmosphere. Once cooled to ambient temperature the reaction mixture was poured into water (200 mL) and extracted with chloroform (3 x 50 mL) resulting in a dark-green colour of the solution. The chloroform was evaporated on a rotary evaporator and the crude product was purified by column chromatography with the eluent hexane-dichloromethane (1:3). Note that the product consists of two rotamers and will hence appear as two spots on TLC. The crude product was further purified by recrystallization in IPA and the pure product was achieved as a mixture of syn- and anti- geometries with a fluffy yellow appearance. Yield: 2.4 g (48%). TLC: Ethyl acetate-Hexane (3:17), R_f = 0.23 & 0.12.

^{1}H NMR (CDCl$_3$, 600 MHz) δ: 8.84 (s, 4H, NDI core), 8.83 (s, 4H, NDI core) 7.53 (t, J = 7.9 Hz, 2H), 7.35 (t, J = 8.0 Hz, 2H), 7.18 (m, 4H), 4.06 (q, J = 6.5 Hz, 4H), 1.65 (m, 4H), 1.26 (m, 20H), 0.84 (t, J = 7.3 Hz, 6H); ^{13}C NMR (CDCl$_3$, 600 MHz) δ: 162.74, 162.70, 154.51, 154.47, 131.31, 130.81, 129.83, 129.78, 127.56, 127.55, 127.24, 127.21, 123.83, 123.72, 121.09, 121.04, 113.35, 113.26, 68.75, 68.73, 31.71, 31.69, 29.28, 29.24, 29.21, 29.17, 29.06, 29.00, 25.99, 25.90, 22.74, 22.70, 14.18, 14.16. IR: ν_{max} = 2950sh, 2920, 2868, 2851, 1715, 1672, 1652sh, 1600, 1580 cm^{-1}. MS calcd. for C$_{42}$H$_{46}$N$_2$O$_6$ [[M+H]$^+$]: m/z = 675.34338; MALDI-TOF 674.31 exp, DSA-TOF 675.3437 exp. STA: T_m = 122.7 °C, 164.8 °C.

C4H9
C2H5
O N O

6 eq. 2-ethylhexyl amine

Acetic acid
reflux
24 h

DEHNDI
(65.6%)

O N O
C2H5
C4H9

NTCDA

O O O

O O O

5 eq. 1-octylamine

DMF
90 ºC
24 h

C8H17
O N O

DONDI
(62%)

O N O
C8H17

O–C8H17
O N O

3 eq. 2-(octyloxy)aniline

DMF
125 ºC
24 h

DOBNDI
(23%)

O N O
O–C8H17

O–C8H17
O N O

1. 0.9 eq. 1-octylamine
2. 2.1 eq. 2-(octyloxy)aniline

DMF
1. 90 ºC, 12 h
2. 125 ºC, 24 h

AsNDI
(48%)

O N O
C8H17
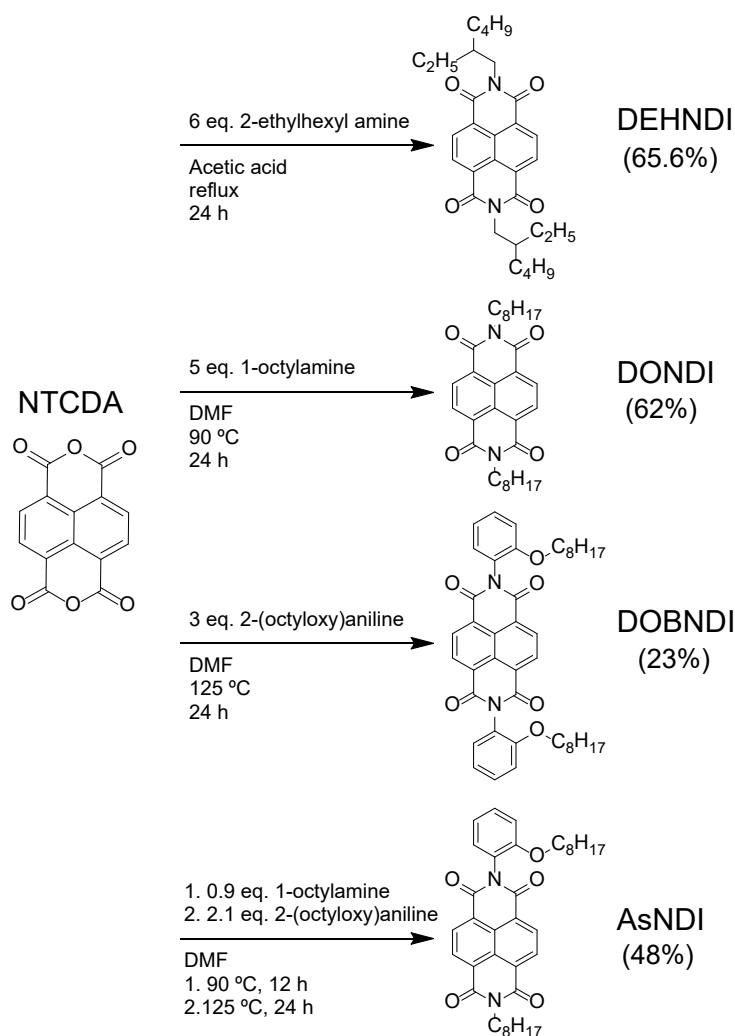
Scheme 4.1: Synthesis routes for the four small molecules investigated for use as acceptors in PSCs.

4.3.2 Material characterisation

4.3.2.1 Thermal analysis

Thermogravimetric analysis (TGA) was performed on a PerkinElmer Thermogravimetric Analyzer 8000. Samples were dried in a vacuum oven at 25ºC for 24 hours prior to the measurement. Measurements were conducted from 25- 400 ºC at a scan rate of 10 ºC minute^{-1}.

Differential scanning calorimetry (DSC) was conducted on pure NFA samples for the determination of crystallisation temperatures. Measurements were conducted under nitrogen on a Discovery DSC (TA Instruments) at a scan rate of 10 °C min^{-1} cycling between 0-200 °C. Note: The relatively low temperature of 200 °C was set to avoid the occurrence of sublimation.

4.3.2.2 Ultraviolet-visible spectroscopy

Optical absorption spectra for the small molecule NFAs were recorded for both solution and thin film on a Perkin Elmer Lambda 950 spectrophotometer at a scan rate of 10 nm s^{-1}.

Additional optical absorption spectra were recorded for the small molecule NFAs in anisole at ambient temperature and at 80 °C on an Agilent Cary 60 UV-Vis Spectrophotometer. The measurements were conducted between 250 to 600 nm at a scan rate of 5 nm s^{-1}.

4.3.2.3 Electrochemistry

SWV and CV measurements were carried out for the determination of reduction/oxidation potentials, from which HOMO/LUMO energy levels were estimated. The SWV and CV traces were recorded on an AUTOLAB PGSTAT potentiostat (Metrohm AG) using a three-electrode setup with platinum wires, both for working electrode and counter electrode and a Ag/Ag$^+$ reference electrode. The peak maxima and the peak onset positions were determined from the recorded square wave voltammograms and cyclic voltammograms, respectively (Appendix, Figure A.1). These were then referred to ferrocene/ferrocenium (Fc/Fc$^+$) by analysing the Fc/Fc$^+$ couple after each measurement. 0.1 M solutions of tetrabutylammonium hexafluorophosphate (Bu$_4$NPF$_6$) in either dichloromethane (DCM) or acetonitrile were used as supporting electrolyte for solution and film measurements, respectively. The latter was specifically applied to DEHNDI due to issues resolving the oxidation peak in solution for this particular compound.

The electrolyte was purged with nitrogen gas for a minimum of 10 minutes prior to the compound of interest being dissolved, then again prior to each measurement. During the measurements, the electrolyte solution surface was kept under nitrogen atmosphere to ensure inert conditions. Energy levels of the materials were calculated by setting the peak potential of Fc/Fc$^+$ vs the normal-hydrogen electrode (NHE) to 0.630 V and the NHE vs the vacuum level to 4.5 V.[15-17]

$$E_{HOMO} = -(E_{ox} + 5.13)$$ (4.1a)

$$E_{LUMO} = -(E_{red} + 5.13)$$ (4.1b)

4.3.2.4 Contact angle

The static contact angles of MilliQ water against the surfaces was measured using a PAT-1 tensiometer (Sinterface Technologies, Germany). Contact angles are reported as an average value of four measurements on different areas of the films. Cleaning of ITO-coated glass substrates (10 Ω/sq, Xin Yan Technology LTD) follow the procedure described in section *4.3.4 Device fabrication*, Chapter 4.

4.3.3 Film properties

4.3.3.1 Profilometer

Thickness measurements were carried out on a mechanical stylus profilometer, DektakXT (Bruker). Films were spun (according to the active layer procedure) with deposition directly on top of ITO coated glass. A scratch was made in the films and the height difference was measured to provide the film thickness. Values are provided as an average over a minimum of three measurements.

4.3.3.2 Photoluminescence spectroscopy (PL)

Photoluminescence (PL) spectra were recorded on a Cary Eclipse Fluorescence Spectrophotometer (Agilent Technologies). The thin film sample was positioned at a 30° angle to the incoming light with a low scan rate. Films were spun on ITO coated glass at 2000 rpm for 60 seconds from 30 mg mL^{-1} TQ1:Acceptor blend solutions with Anisole as solvent. The donor-acceptor ratios measured were 19:1 and 2:1.

4.3.3.3 Atomic force microscopy (AFM)

A multimode atomic force microscopy (AFM) (Bruker) working in tapping mode, with Si cantilevers used to examine the topography of the active layer thin films. These films were spun on a 1 cm^2 ITO-coated glass substrate at 2000 rpm from 30 mg mL^{-1} anisole solutions.

4.3.3.4 Optical microscope

Larger features in the active layer thin films were investigated with an optical microscope (AFM-Raman-TERS) (Nanonics) at 100x magnification. Samples were spun from anisole solutions directly on top of ITO-coated glass substrates following the deposition procedure described under Device fabrication, below.

4.3.4 Device fabrication

4.3.4.1 Cleaning of patterned ITO-coated glass substrates

Patterned ITO-coated glass substrates (10 Ω sq-1, Xin Yan Technology LTD) were cleaned in 5% Pyroneg (Johnson Diversey) solution for 20 minutes at 90 ºC, then rinsed in MilliQ water followed by 10 minutes of sonication for each of the following solvents; MilliQ water, acetone, and 2-propanol. The substrates were then dried under a stream of nitrogen prior to 20 minutes of UV/ozone treatment, after which deposition (spin coating) of the next layer was immediately conducted on the UV/ozone cleaned substrates.

4.3.4.2 Deposition and annealing of ZnO layer

The ZnO solution was prepared according to previously published procedures.[18] Zinc acetate dihydrate (500 mg) (Sigma-Aldrich, 99.9%) and ethanolamine (Sigma-Aldrich, 99.5%, 140 mg) were dissolved under vigorous stirring overnight in 2-methoxyethanol (Sigma-Aldrich, 99.8%, 5 mL). The resulting solution was filtered with a PTFE syringe filter (0.45 μm) prior to being spun on cleaned ITO-coated glass substrates at 3000 rpm for 60 seconds, to give a thin film of ~ 25-30 nm. The formed film was annealed in a 280 ºC preheated furnace in air for 10 minutes.

4.3.4.3 Deposition of the active layer blends

The active layer solutions were prepared by dissolving TQ1 polymer and NFAs under vigorous stirring in anisole (Sigma-Aldrich, ReagentPlus, 99%) at 80 °C over the course of 1 hour. The active layer was spin coated from hot solution at varying speeds (1000-3000 rpm) for 60 seconds. Any thermal annealing was conducted at 120 °C for a period of 10 minutes. All active layer processing and thermal annealing was conducted under inert atmosphere inside a glovebox.

4.3.4.4 Deposition of MoOx and Ag

MoO$_x$ hole-transport layer (12 nm) was thermally evaporated on the BHJ layer using a Covap system (Angstrom Engineering). This was followed by the evaporation of a Ag electrode (80 nm) using a shadow mask, defining the active area to 0.1 cm^2.

4.3.4.5 Measuring of device performance

Devices were measured using an Oriel solar simulator fitted with a 150 W xenon lamp (Newport), filtered to give an output of 100 mW cm^{-2} at AM 1.5 (air mass) standard and calibrated using a silicon reference cell with NIST traceable certification.

4.4 Results and discussion

The synthesis routes for the four different NFAs DONDI, DEHNDI, DOBNDI, and AsNDI are all short and facile (Scheme 4.1). DEHNDI and DONDI are both synthesised in a single step from commercially available materials. The yields are moderate at ~60-65% with reactions taking place in acetic acid and dimethylformamide (DMF) at elevated temperatures for DEHNDI and DONID, respectively. The side-group 2-(octyloxy)aniline, utilised in DOBNDI and AsNDI, was synthesised from 2-aminophenol in a single step procedure with DMF as solvent. NMR revealed that reaction preferentially took place on the hydroxyl group (hydroxyl:primary amine, 4:1), achieving the product in moderate yield. Synthesis of DOBNDI then took place in a second step in DMF providing the pure product in 48% yield. Interestingly, the product was achieved as a mixture of the syn- and anti-rotamers in close to a 1:1 ratio. These rotamers can be seen both on thin layer chromatography (TLC) as two separate spots and in NMR (Appendix – Figure A.18) with peaks present for each rotamer. The properties of the rotamers were not explored further and any change in ratio between the two species are assumed to have negligible impact on the final application. Lastly, AsNDI was synthesised in a one-pot reaction with additions of 1-octylamine taking place at t = 0 h, followed by the addition of 2-(octyloxy)aniline at t = 12 h for total reaction time of 24 h. In this case, the yield was low at 23%. NMR results confirmed that the compounds DEHNDI, DONDI, and DOBNDI were achieved in high purity. For AsNDI a barely noticeable doublet peak was detected in the aromatic region at 8.83 ppm, possibly corresponding to a minor contamination of DOBNDI.

As discussed in Chapter 1, viable upscaling procedures need to be based on solution processing using non-chlorinated and non-toxic solvents. A number of commonly used solvents for the deposition of the active layer in polymer solar cells were screened, with special attention being given to non-chlorinated, greener solvents. Anisole was the solvent investigated with the lowest toxicity and chronic ratings, scoring a 0 in both categories in the Chemwatch system (rating chemicals from 0-4), as shown in Figure 4.3. However, the dissolution time and colour indicate that the solubility of the NFAs appears to be lower in anisole than in chloroform, Figure 4.4.
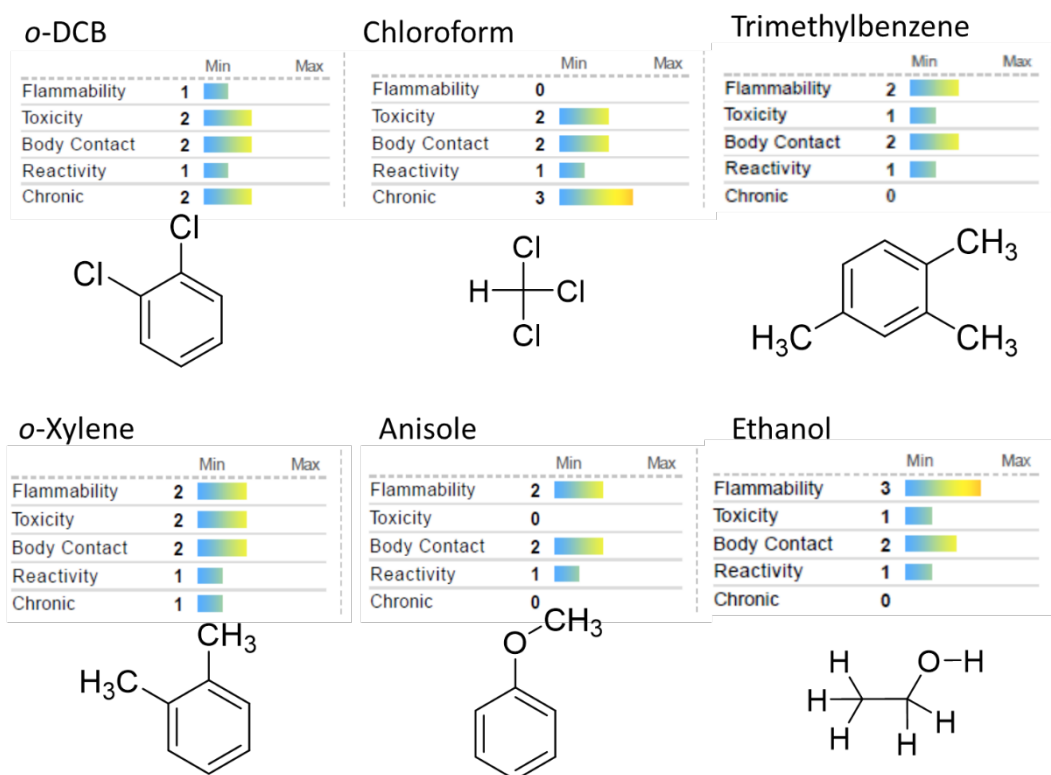
Figure 4.3: Extract of laboratory solvents commonly used for the active layer deposition in polymer solar cells with ethanol shown as a reference in regard to toxicity.

A lower solubility could contribute to pre-aggregation in the solution, and thus influence the morphology. As a result, this could greatly influence the performance. Solution UV/vis spectra were recorded for all four NFAs in anisole to determine the possible presence of pre-aggregates. From Figure 4.7a it is clearly seen that the peaks are much less defined for the anisole solutions than for the $CHCl_3$, they also possess a tail that drops off at about 450 nm. These features are both indicative of pre-aggregation in the solution. A second experiment was conducted to exclude any effects that could arise from π-π interactions between the aromatic anisole and the NFA molecules. The NFA DONDI was measured in pure $CHCl_3$, $CHCl_3$ with 4% anisole, and in pure anisole. The UV/vis spectrum for DONDI in $CHCl_3$ with 4% anisole is almost identical to that of pure $CHCl_3$, indicating that any interactions between DONDI and anisole does not affect the peaks at ~350-400 nm, Figure 4.7b. This pre-aggregation in anisole solution was further studied at elevated temperatures (80 °C), see Figure 4.7a, but no difference could be observed compared to ambient temperature. However, the low toxicity of anisole remains highly attractive and the influence of these aggregates on the final morphology remains unknown without further study. Therefore, anisole was chosen as the main active layer solvent for this study. Elevated temperatures did not have any effect on the pre-aggregates in solution, but appears to assist in achieving higher film quality during spin coating. Hence, all active layers were spun from solutions at 80 °C.
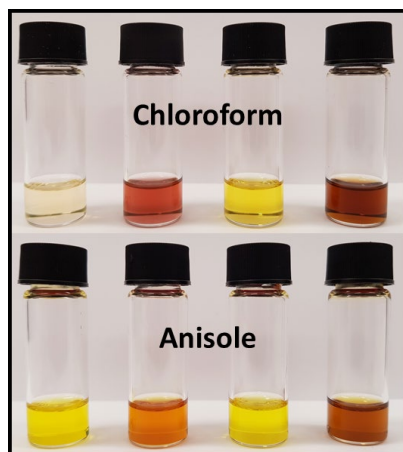
Figure 4.4: From left to right solutions of DEHNDI, DONDI, DOBNDI, and AsNDI.

4.4.1 Material characterisation

The thermal stability was investigated using TGA for the four NFA molecules. They all displayed a good thermal stability with 5% weight loss occurring at 296 °C, 313 °C, 362 °C, and 329 °C for DEHDNI, DONDI, DOBNDI, and AsNDI, respectively (Figure 4.5). It should be noted that sublimation occurred and that large crystals could be observed on the wire holding the sample pan post measurements.
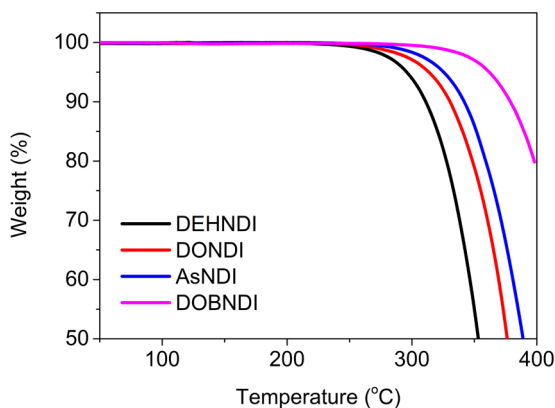
Figure 4.5: TGA spectra of DEHNDI, DONDI, AsNDI, and DOBNDI showing the thermal stability.

The contact angles were measured for the four NFAs showing a relatively small spread with DOBNDI possessing the lowest contact angle of 69.4° and DONDI the highest contact angle of 96.1° (**Figure 4.6**). TQ1 is close to the middle of the range with a contact angle of 80.3° and should therefore possess a reasonable miscibility with the NFAs due to low interfacial tensions. However, these small deviations between the acceptor compounds are unlikely to have a major impact on morphology, or device performance.

Figure 4.6: Contact angles for the four NDI based NFAs as well as for the donor polymer TQ1.

The two major peaks of the NFAs in the UV/Vis spectra, which are attributed to $\pi-\pi*$ transitions, overlap quite well with the secondary peak of the donor polymer TQ1 between 310-440 nm (Figure 4.7d). However, these NDI based NFAs possess relatively low molar extinction coefficients, showing values of 36.0k, 38.0k, 41.5k, and 10.0k M^{-1} cm^{-1} for DEHNDI, DONDI, AsNDI, and DOBNDI respectively at 360 nm (Figure 4.3). This can be compared to the higher homologue PDI, that typically exhibits molar extinction coefficients of $\sim 10^5$ M^{-1} cm^{-1}.[1] Conjugated polymers are known to possess high extinction coefficient, thus TQ1 accounts for a larger contribution to light absorption and charge generation than the NFAs. The photon flux is also lower in the low wavelength (high energy) region, further contributing to this effect. It is clear that TQ1 will be the main light absorber for the ITO/ZnO/TQ1:A_1:A_2:A_3:A_4/MoO$_x$/Ag device configuration. This implies that the entire active layer will take on the pleasant blue colour of TQ1.[19] With the exception of the highly reflective Ag electrode this could be a promising architecture for semi-transparent PSCs for use in applications where the relatively low PCE of NDI based NFAs are offset by their aesthetics.
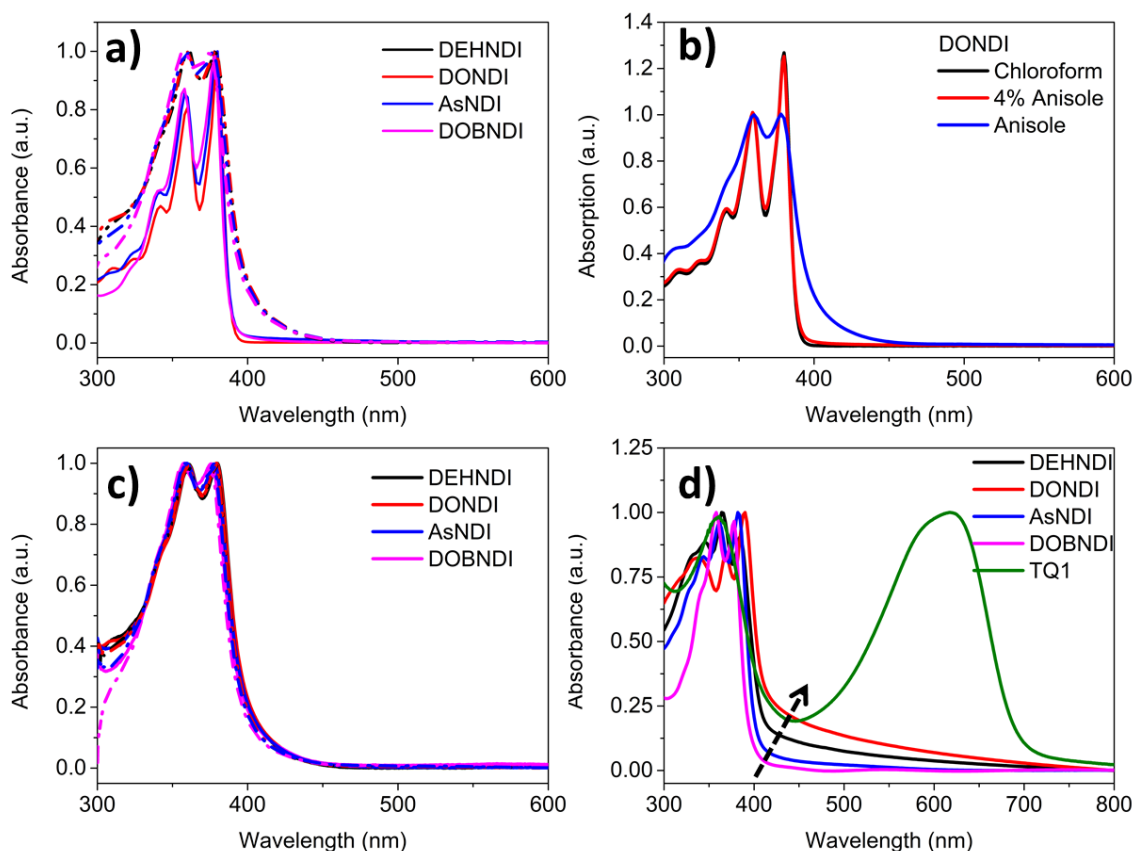
Figure 4.7: a) Comparison of CHCl$_3$ solution (solid) and Anisole solution (dotted) UV-vis spectra for DEHNDI, DONDI, AsNDI, and DOBNDI. b) Solution spectra of DONDI in pure CHCl$_3$, CHCl$_3$ with 4% Anisole and pure Anisole. c) Comparison of solution spectra in anisole at ambient temperature, i.e. 20 °C (solid) and at 80 °C (dotted). d) Thin Film UV/vis spectra of the four NFAs and donor polymer TQ1.

The electrochemistry techniques SWV and CV were employed for the determination of HOMO/LUMO levels for the small molecule NFAs as well as the donor polymer TQ1. From Figure 4.8a, the SWV oxidation/reduction maxima were estimated at 1.55/-1.09 V, 1.61/-1.16 V, and 1.54/-1.04 vs Fc/Fc$^+$ for DONDI, AsNDI, and DOBNDI, respectively. SWV was also performed on DEHNDI but the measurements proved challenging and the oxidation potential was not successfully elucidated due to issues resolving the peak. DEHNDI was measured in both DCM solution, as the other NFAs, as well as a thin film coated on the electrode with anhydrous acetonitrile with both measurements yielding the same results. Thus, the oxidation and reduction potentials for DEHNDI were instead estimated with CV at 1.53 V and -0.98 V vs Fc/Fc$^+$, respectively. These potentials were then recalculated according to equation 4.1a and 4.1b to give -6.66/-4.15 eV, -6.68/-4.04 eV, -6.74/-3.97 eV, and -6.67/-4.09 eV (HOMO/LUMO) for DEHNDI, DONDI, AsNDI, and DOBNDI respectively, see Table 4.1.
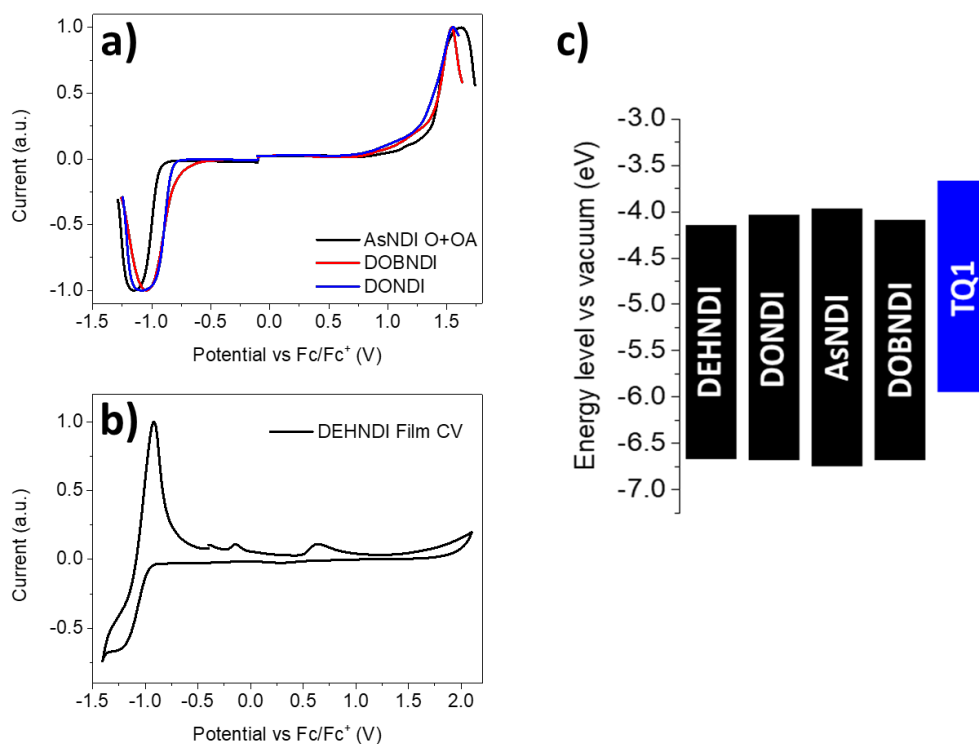
Figure 4.8: a) SWV spectra of the NDI based small molecules DONDI, DOBNDI, and AsNDI in solution, b) CV spectra of DEHNDI film in acetonitrile electrolyte solution taken from the second scan, and c) schematic representation of the energy levels for the four NDI based NFAs and the donor polymer TQ1.

The optical band gap (E_g^{opt}) was calculated according to:

$$E_g^{opt} = \frac{hc}{\lambda_{onset}} \tag{4.2}$$

where h is the Planck constant, c is the speed of light in a vacuum, and λ_{onset} is the absorption onset. λ_{onset} was estimated, according to Figure A.1, from the thin film UV/vis curve of the pure materials spun on microscope glass slides (2.5 x 2.5 cm). The thin film UV/vis spectra of the NFAs are very similar in appearance due to these structures sharing the same aromatic core. Two major overlapping peaks attributed to π−π* transitions at ~350-400 nm are observed with additional, less prominent features appearing below 350 nm. A clear trend is observed for the NFAs with regards to the peak positions (λ_{max}) in the thin film spectra (Table 4.1). Using the solution spectra as a base point a bathochromic shift is present for the NFAs in the order of DOBNDI (0 nm) < AsNDI (3 nm) < DEHNDI (5 nm) < DONDI (10 nm). This type of bathochromic shift can be indicative of aggregates/crystals and correlates well to the expected order of crystallinity due to effects of steric hindrance from pendant side-groups. DOBNDI, containing the bulkiest side-groups as well as being rotamer with two separate configurations, would possibly possess the weakest crystallinity. This is followed by AsNDI with one bulky and one straight alkyl chain pendant group. DEHNDI with its branched alkyl side-groups would then possess the second strongest crystallinity behind DONDI, which possess purely straight alkyl

chains as pendant side-groups. A similar trend is also observed for the broad feature observed from 410 nm. This feature is also indicative of aggregate/crystal induced light absorption or light scattering. Thus, it is probable that the synthetic modification of the NFAs were successful in creating a series of NDI based NFAs with varying degree of crystallinity.

DSC measurements were conducted to study the thermal transitions of the NFAs. For DEHNDI no thermal transitions were detected in the selected temperature range (0-200 °C). The other NFAs experienced various transitions with melting temperatures ranging from 120 °C (AsNDI) to 185 °C (DONDI). The data for DONDI possesses a sharp exothermic peak at ~180 °C, probably corresponding to crystallisation. AsNDI also experiences an exothermic peak, but at lower temperature. Interestingly, DOBNDI appears to undergo an exothermic process during the heating stage, followed rapidly by an endothermic process, which is indicative of crystallisation and melting.
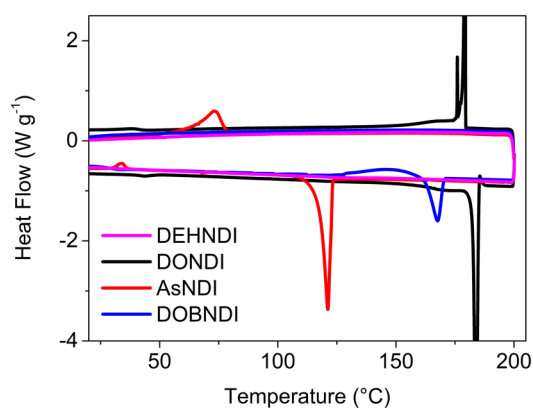
Figure 4.9: Second DSC scan of the small molecule NFAs.

The exciton dissociation efficiency was investigated with PL spectroscopy for each of the NFAs and a blend system, consisting of equal parts of all four NFAs, with TQ1. Thin films of pure TQ1 as well as TQ1 with both 5% and 33% acceptor added was measured. In both cases, complete quenching was observed for each of the NFAs combinations (Figure 4.10) indicating that efficient exciton dissociation is taking place for these donor-acceptor blends.

Table 4.1: Energy level data for the four small molecule NFAs investigated as well as the donor polymer TQ1. Data for the fullerenes $PC_{61}BM$ and $PC_{71}BM$ values are extracted from literature.[20-21] Energy levels for DEHNDI are based on measurements conducted on thin films in acetonitrile electrolyte solution with DONDI, DOBNDI, and AsNDI energy levels are based on measurements conducted in dichloromethane electrolyte solution.

| | Electrochemistry | | | Optical | | | |
| | | | | Solution | Film | | |
Compound	HOMO (eV)	LUMO (eV)	E_g (eV)	λ_{max} (nm)	λ_{max} (nm)	λ_{onset} (nm)	E_g^{opt} (eV)
DEHNDI	-6.66	-4.15	2.51	379	384	412	3.01
DONDI	-6.68	-4.04	2.64	380	390	416	2.98
AsNDI	-6.74	-3.97	2.77	379	382	402	3.08
DOBNDI	-6.67	-4.09	2.58	378	378	395	3.14
TQ1	-5.94	-3.67	2.27	613	618	695	1.78
*$PC_{61}BM$	-6.5	-4.2	2.3	-	-	-	-
*$PC_{71}BM$	-6.44	-4.14	2.3	-	-	-	-
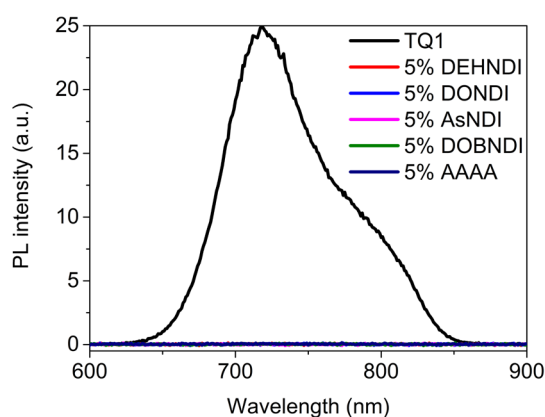
Figure 4.10: Thin film photoluminescence spectra of pure TQ1 donor polymer, TQ1 mixed with 5% DEHNDI, DONDI, AsNDI, DOBNDI and equal parts of DEHNDI, DONDI, AsNDI, DOBNDI. The single acceptors as well as the blend all show strong quenching with no measurable emission.

4.4.2 Film properties

Morphology is one of the most important and indicative parameters of well functioning PSCs. For completely new active layer blend systems, like these investigated here, it is important to utilise a quick method to be able to analyse a large number of systems. For this purpose, an optical microscope with 100x magnification equipped with a high-resolution camera was used to detect features on the μm scale. The three different donor-acceptor ratios of 1:2, 1:1, and 2:1 were investigated in a first optimisation

step. The active layer blends with a 2:1 ratio experienced the best results, based on optical investigation. The films with the four NDI based NFAs differed widely with DEHNDI and DONDI containing films revealing large features of ~1 μm (Figure 4.11). These features grew to a couple of micrometres for DEHNDI and to as big as 10 μm for DONDI upon addition of 2% v/v of the solvent additive 1-chloronaphthalene (CN). These large features seen in Figure 4.11d for TQ1:DONDI films show a highly regular pattern, indicating crystal formations. The AAAA blend (equal parts the four Acceptors) as well as AsNDI and DOBNDI did not reveal any visible features at this magnification when no solvent additive was added. At the addition of 2% v/v to the AAAA, blend features on the micrometre scale appeared (Figure 4.11f). This was also the case for AsNDI and DOBNDI thin films (omitted here), though less prominent.
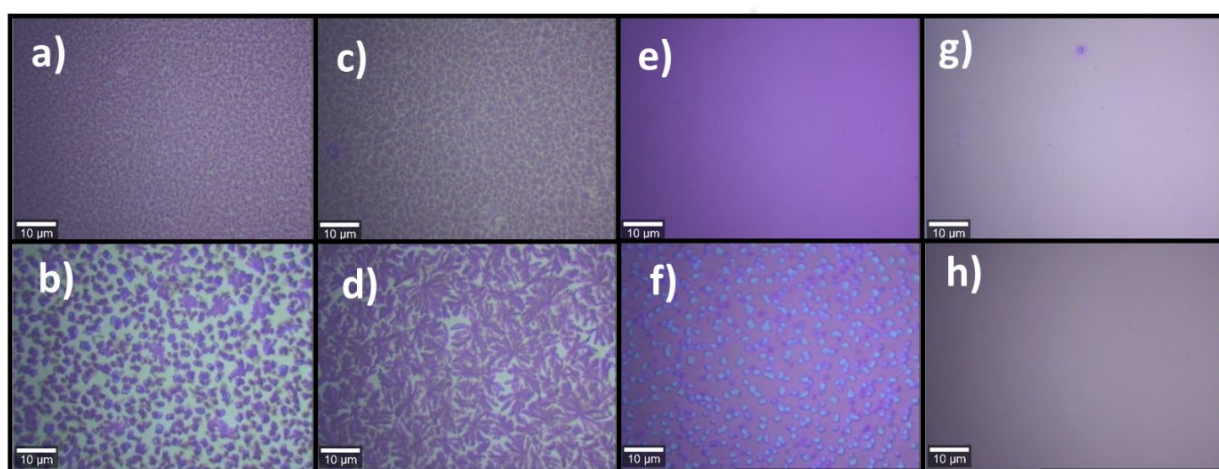
Figure 4.11: Representative microscope images taken at 100x magnification for thin films with a 2:1 ratio TQ1:acceptor for a) DEHDNI with b) 2% v/v CN, c) DONDI with d) 2%v/v CN, e) AAAA with f) 2% v/v CN, g) AsNDI and h) DOBNDI.

The active layer blend thin film morphology was studied further with AFM to elucidate variations in topographical features on the nanometre scale. Measurements were conducted on selected thin films that did not show distinct features in the optical microscope images. Topographical images were recorded for the four samples (TQ1:acceptor, 2:1) with AAAA, DOBNDI, AsNDI, and DONDI:AsNDI (1:1) as acceptor/blend, Figure 4.12. Phase images were also recorded to determine the domain sizes of the chemically distinct phases. The active layer thin film with TQ1:DOBNDI displayed the most favourable topographical features with small height variations across a 3 x 3 μm image (Figure 4.12b and f). The phase image for this samples, also shows what appears to be a finely intermixed blend. However, the other samples all experienced larger topographical features and phase separation with domain sizes in the order of hundreds of nanometres. These large features are especially prominent for TQ1:AsNDI, seen in Figure 4.12c where micrometre long needle like structures are clearly visible. This is likely the result of AsNDI crystal formation. DONDI:AsNDI (1:1) also displays features which likely can be attributed to NFA crystals. Interestingly, the five component blend with TQ1:AAAA show a

fairly uniform topography in combination with the largest domain size out of all the samples. It is unclear if any crystals are present, but a number of larger features can be discerned in the topographical image.

Additionally, profilometer measurements were carried out to determine the thickness of BHJ layer. For a TQ1:acceptor ratio of 2:1 without thermal annealing or addition of solvent additives, the thicknesses were measured at 94 nm, 82 nm, 129 nm, 85 nm, and 96 nm for DEHNDI, DONDI, AsNDI, DOBNDI, and AAAA respectively.
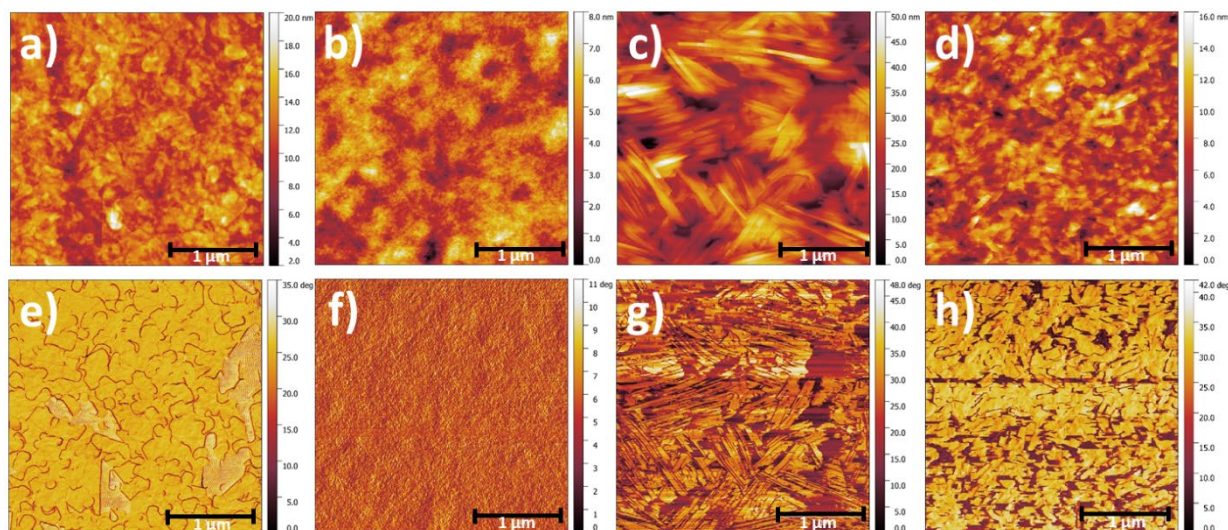
Figure 4.12: Select 3 x 3 µm AFM images of representative active layer blends for TQ1:Acceptor in a 2:1 ratio for NFAs a) AAAA, b), DOBNDI, c) AsNDI, and d) DONDI:AsNDI (1:1) with e)-h) showing the respective phase images.

4.4.3 Photovoltaic performance

The photovoltaic performance of active layer blends were evaluated in the inverted device configuration of ITO/ZnO/active layer blend/MoO$_x$/Ag. The optical microscope images taken for 1:2, 1:1, and 2:1 TQ1:acceptor ratios displayed the 2:1 ratio as the most promising morphologies. Devices were manufactured for all the three ratios with the two acceptors, DEHNDI and DONDI, Table 4.2. The devices incorporating varying ratios of DEHNDI yielded extremely low efficiencies with PCEs under 0.1%. However, a clear trend was observed for the V_{oc}, which increased from 0.185 V through 0.590 V to 0.763 V with increasing proportion of TQ1 from 1:2 to 1:1 and 2:1 in the blend. This same trend was also observed for DONDI, although, less prominently. Comparatively, PCEs were significantly higher for DONDI than DEHNDI, with the best device achieving a PCE of 0.22%. With relatively equal V_{oc} between the two systems, it was the J_{sc} and FF that contributed to this boost in PCE. The J_{sc} remained at a modest ~0.5 mA cm^{-2} for all the ratios tested with the FF fluctuating, but stabilising at 50% for the 2:1 ratio. With an unfavourable morphology, as is seen in Figure 4.11d, this FF appears quite high. However, the value is heavily inflated by the modest J_{sc}, thus, influencing the shape of the J-V curve in favour of higher FF. Although low, the trends are clear in that a donor:acceptor ratio of 2:1 yields the

highest PCEs. More importantly, this ratio consistently produces a high V_{oc} of over 700 mV, indicative of functioning solar cells. Therefore, 2:1 will be the main donor:acceptor ratio used throughout this work.

Additional PSC devices were manufactured based on the optimised 2:1 ratio. These devices include the five acceptor combinations DEHNDI, DONDI, AsNDI, DOBNDI, and AAAA with TQ1 as donor (Table 4.3). The effect of thermal annealing (TA) as well as the addition of a solvent additive on these active layer blends was investigated. The results from the DSC study showed varying melting temperatures of >120 °C for the NFAs, with DEHNDI not appearing in the selected temperature range, and only DONDI and AsNDI possibly experiencing thermal transitions corresponding to crystallisation. Thus, the glass transition temperature (T_g) of TQ1, above which the polymer chains can undergo relaxation processes for a morphological change, was used as a basis for the thermal annealing temperature. TQ1 possesses a T_g of 95 °C, so to improve the likelihood of the entire sample entering the so-called rubbery state the thermal annealing was conducted at 120 °C.[22] As a base point for the solvent additive similar already published systems with TQ1 were considered. The TQ1:PC$_{71}$BM using 2% v/v 1-chloronaphthalene (CN) in *o*-DCB was deemed a reasonable fit.[23-24]

Table 4.2: Photovoltaic performance of devices incorporating varying ratios of DEHNDI and DONDI in the active layer blend.[a]

TQ1:DEH:DO:As:DOB	J_{sc} [mA cm^{-2}]	V_{oc} [V]	FF [%]	PCE [%]	Max
1:2:0:0:0	0.224 ± 0.011	0.185 ± 0.074	27 ± 1	0.01 ± 0.00	0.02
1:1:0:0:0	0.236 ± 0.026	0.590 ± 0.010	43 ± 9	0.07 ± 0.02	0.09
2:1:0:0:0	0.259 ± 0.005	0.763 ± 0.035	37 ± 2	0.08 ± 0.01	0.08
1:0:2:0:0	0.492 ± 0.035	0.429 ± 0.098	32 ± 2	0.07 ± 0.02	0.11
1:0:1:0:0	0.491 ± 0.051	0.495 ± 0.142	50 ± 14	0.09 ± 0.05	0.18
2:0:1:0:0	0.495 ± 0.053	0.714 ± 0.030	47 ± 4	0.17 ± 0.04	0.22

[a]Mean values ± standard deviation from six devices.

Out of the untreated active layer blends TQ1:DONDI experienced the highest PCE of 0.22%. This decreased to 0.12% upon TA with a big drop in J_{sc} from approximately 0.5 to 0.3 mA cm^{-2} and a noticeable loss in V_{oc}. With the exception of TQ1:DOBNDI, TA did in all cases lead to a lower V_{oc} indicating that a less optimal phase separation regime was achieved. This could be the result of major crystal growth and large-scale phase separation for the latter. For DOBNDI, which is the least crystalline of the NFAs, a too homogenous blend could possibly have been achieved with TQ1. In this case, it is likely that the TA contributed to the promotion of two separate phases, increasing the V_{oc}. The

incorporation of 2% v/v CN as a solvent additive proved more successful than the thermal treatment. The best device performance for all of the five active layer blends were achieved for the devices incorporating CN with the J-V curves shown in Figure 4.13. These devices did in all cases possess a higher J_{sc} than their untreated and TA counterparts, while the V_{oc} remained more or less constant with the exception of DOBNDI that experienced a large increase (likely due to the reasons discussed above).

The PCE of 0.25% for TQ1:DONDI was the highest measured for any of the active layer blends. The highest PCEs for remaining active layer blends were 0.12%, 0.06%, 0.09%, and 0.07% for DEHNDI, AsNDI, DOBNDI and AAAA acceptor combinations, respectively. Interestingly, the active layer blend that displays the largest features, TQ1:DONDI (2:1), under an optical microscope has almost double the J_{sc} and PCE of the second highest active layer blend. This difference could possibly arise due to the formation of charge carrier pathways in the micrometre sized crystals present in the TQ1:DONDI active layer blend. Additionally, TQ1:DEHNDI (2:1) based devices reached the second highest PCE, thus revealing a clear indication that higher crystal forming ability contributes to an increased PCE for these materials. As stated earlier, NDI based NFAs tend to have a lower mobility compared to their higher homologues. In combination with a lack of charge carrier pathways, this could prove detrimental to the PCE. As a result the less crystalline materials displays even lower J_{sc} than DONDI.

Yao *et al*. concluded that the formation of fibrillary crystals greatly contributed to a high PCE of 2.41% for the NDI based NFA BiNDI.[9] It is likely that these fibrillary crystals form "highways" for the charge carriers, leading to the high J_{sc} of 5.47 mA cm^{-2}. As a result of the systems presented here likely lacking these pathways, the currents remain at low levels.

However, these systems have proven to require tedious optimisation of processing conditions to reach high PCEs. This was shown by Ren *et al*., who achieved over a tenfold increase in PCE from 0.14% to 1.5% for their P3HT: NDI-3TH (NDI based NFA) system upon addition of 0.2% v/v 1,8-diiodooctane (DIO).[25] Optimal addition of DIO for similarly published structures has been concluded to be ~0-0.5%, far below the 2-3% v/v often used for polymer:polymer or polymer:fullerene solar cells.[9, 25-26] This demonstrates how intricate the optimisation of NDI based NFA systems can be. It also, despite the difference character between these systems, provides insight on what could be prioritised in future work on these structures. From Figure 4.11 it is clear that the addition of 2% v/vCN has major effects on the final morphology of the active layer blend. Tuning this addition would therefore be advisable.

Table 4.3: Device data for TQ1:Acceptor in a 2:1 ratio for DEHNDI, DONDI, AsNDI, DOBNDI, and AAAA. These device configurations are presented as untreated, thermally annealed at 120 °C for 5 minutes, and with incorporation of 2% v/v CN as solvent additive.[a]

TQ1:DEH:DO:As:DOB	J_{sc} [mA cm^{-2}]	V_{oc} [V]	FF [%]	PCE [%]	Max
2:1:0:0:0	0.259 ± 0.005	0.763 ± 0.035	37 ± 2	0.08 ± 0.01	0.08
Annealed	0.265 ± 0.015	0.647 ± 0.017	55 ± 2	0.1 ± 0.01	0.11
2% v/v CN	0.324 ± 0.026	0.733 ± 0.015	44 ± 2	0.11 ± 0.01	0.12
2:0:1:0:0	0.495 ± 0.053	0.714 ± 0.03	47 ± 4	0.17 ± 0.04	0.22
Annealed	0.307 ± 0.012	0.635 ± 0.007	56 ± 3	0.11 ± 0.01	0.12
2% v/v CN	0.645 ± 0.036	0.753 ± 0.021	50 ± 2	0.24 ± 0.01	0.25
2:0:0:1:0	0.130 ± 0.014	0.799 ± 0.056	34 ± 1	0.03 ± 0.01	0.04
Annealed	0.109 ± 0.045	0.756 ± 0.097	31 ± 1	0.02 ± 0.01	0.03
2% v/v CN	0.173 ± 0.012	0.776 ± 0.096	31 ± 3	0.04 ± 0.01	0.06
2:0:0:0:1	0.247 ± 0.008	0.556 ± 0.095	47 ± 9	0.07 ± 0.02	0.08
Annealed	0.227 ± 0.01	0.887 ± 0.005	31 ± 1	0.06 ± 0.01	0.07
2% v/v CN	0.266 ± 0.017	0.899 ± 0.005	30 ± 1	0.07 ± 0.01	0.09
2:0.25:0.25:0.25:0.25	0.162 ± 0.006	0.837 ± 0.006	41 ± 3	0.05 ± 0.01	0.06
Annealed	0.096 ± 0.01	0.663 ± 0.159	29 ± 2	0.02 ± 0.01	0.03
2% v/v CN	0.171 ± 0.008	0.788 ± 0.122	37 ± 4	0.05 ± 0.01	0.07

[a]Mean values ± standard deviation from six devices.
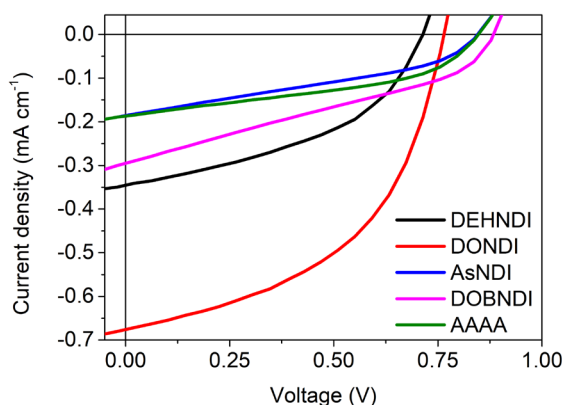
Figure 4.13: J-V characteristics under illumination for the best devices (all with CN) incorporating the NFA blends.

4.5 Conclusion

In summary, four NDI based NFAs were synthesised via facile synthetic routes with a maximum of three steps, starting from commercially available materials. These materials were successfully designed to incorporate a variety of pendant side-groups, as a result forming a series of films with varying degree of crystal forming ability in the decreasing order of DONDI > DEHNDI > AsNDI > DOBNDI. They were paired with the donor polymer TQ1, processed from the relatively green solvent anisole and employed in inverted devices with a configuration of ITO/ZnO/active layer blend/MoOx/Ag in a range of acceptor blends. The variation of donor:acceptor ratio as well as the incorporation of more than one acceptor in the active layer blend lead to an increased control over active layer morphology.

AFM measurements revealed a favourable topography for TQ1:DOBNDI (2:1), but the PCE for this active layer blend was only 0.6% (0.9% with 2% v/v CN), possibly due to a too homogenous sample. A highest PCE of 0.25% was instead reached for the active layer blend TQ1:DONDI (2:1) with addition of 2% v/v CN despite revealing non-ideal micrometre features under optical microscope. TQ1:DEHNDI, TQ1:AsNDI, and TQ1:AAAA performed similarly to DOBNDI with PCEs of 0.12%, 0.6%, and 0.7% with 2% v/v CN, respectively.

These materials are not high performing, but the synthesis routes are short and facile. If the optimisation of the active layer blends can be solved and show a decent thermal stability, it is possible that they could fit niche applications. Semitransparent solar cells were already mentioned in the introduction as a possible field where the demands on performance are less stringent. Another use could be as the third component in polymer:fullerene or polymer:polymer blends, e.g. to facilitate crystallisation or phase separation.

4.6 Contributions

Caroline Pan: Performed AFM and Profilometer measurements and assisted in data interpretation.

Dr. Chris Gibson: Assisted in the acquisition of optical microscope images.

Prof. Mats R. Andersson: Assisted in material development as well as data interpretation for PSC devices and AFM images.

4.7 References

(1)   Zhang, G.; Zhao, J.; Chow, P. C. Y.; Jiang, K.; Zhang, J.; Zhu, Z.; Zhang, J.; Huang, F.; Yan, H., Nonfullerene Acceptor Molecules for Bulk Heterojunction Organic Solar Cells. *Chem. Rev.* **2018**, 118, 3447-3507.

(2)   Bergqvist, J.; Lindqvist, C.; Bäcke, O.; Ma, Z.; Tang, Z.; Tress, W.; Gustafsson, S.; Wang, E.; Olsson, E.; Andersson, M. R.; Inganäs, O.; Müller, C., Sub-glass Transition Annealing Enhances Polymer Solar Cell Performance. *J. Mater. Chem. A* **2014**, 2, 6146-6152.

(3)   Lindqvist, C.; Bergqvist, J.; Bäcke, O.; Gustafsson, S.; Wang, E.; Olsson, E.; Inganäs, O.; Andersson, M. R.; Müller, C., Fullerene Mixtures Enhance the Thermal Stability of a Non-crystalline Polymer Solar Cell Blend. *Appl. Phys. Lett.* **2014**, 104, 153301.

(4)   Zhong, Y.; Trinh, M. T.; Chen, R.; Purdum, G. E.; Khlyabich, P. P.; Sezen, M.; Oh, S.; Zhu, H.; Fowler, B.; Zhang, B.; Wang, W.; Nam, C.-Y.; Sfeir, M. Y.; Black, C. T.; Steigerwald, M. L.; Loo, Y.-L.; Ng, F.; Zhu, X. Y.; Nuckolls, C., Molecular Helices as Electron Acceptors in High-performance Bulk Heterojunction Solar Cells. *Nat. Commun.* **2015**, 6, 8242.

(5)   Zhang, J.; Li, Y.; Huang, J.; Hu, H.; Zhang, G.; Ma, T.; Chow, P. C. Y.; Ade, H.; Pan, D.; Yan, H., Ring-Fusion of Perylene Diimide Acceptor Enabling Efficient Nonfullerene Organic Solar Cells with a Small Voltage Loss. *J. Am. Chem. Soc.* **2017**, 139, 16092-16095.

(6)   Hendsbee, A. D.; Sun, J.-P.; Law, W. K.; Yan, H.; Hill, I. G.; Spasyuk, D. M.; Welch, G. C., Synthesis, Self-Assembly, and Solar Cell Performance of N-Annulated Perylene Diimide Non-Fullerene Acceptors. *Chem. Mater.* **2016**, 28, 7098-7109.

(7)   Meng, D.; Fu, H.; Xiao, C.; Meng, X.; Winands, T.; Ma, W.; Wei, W.; Fan, B.; Huo, L.; Doltsinis, N. L.; Li, Y.; Sun, Y.; Wang, Z., Three-Bladed Rylene Propellers with Three-Dimensional Network Assembly for Organic Electronics. *J. Am. Chem. Soc.* **2016**, 138, 10184-10190.

(8)   Oh, J. T.; Ha, Y. H.; Kwon, S.-K.; Song, S.; Kim, J. Y.; Kim, Y.-H.; Choi, H., Twisted Linker Effect on Naphthalene Diimide-Based Dimer Electron Acceptors for Non-fullerene Organic Solar Cells. *Macromol. Rapid Commun.* **2018**, 39, 1800108.

(9)   Liu, Y.; Zhang, L.; Lee, H.; Wang, H.-W.; Santala, A.; Liu, F.; Diao, Y.; Briseno, A. L.; Russell, T. P., NDI-Based Small Molecule as Promising Nonfullerene Acceptor for Solution-Processed Organic Photovoltaics. *Adv. Energy Mater.* **2015**, 5, 1500195.

(10)   Nam, M.; Cha, M.; Lee, H. H.; Hur, K.; Lee, K.-T.; Yoo, J.; Han, I. K.; Kwon, S. J.; Ko, D.-H., Long-term Efficient Organic Photovoltaics based on Quaternary Bulk Heterojunctions. *Nat. Commun.* **2017**, 8, 14068.

(11)   de Zerio, A. D.; Müller, C., Glass Forming Acceptor Alloys for Highly Efficient and Thermally Stable Ternary Organic Solar Cells. *Adv. Energy Mater.* **2018**.

(12)   Emmott, C. J. M.; Röhr, J. A.; Campoy-Quiles, M.; Kirchartz, T.; Urbina, A.; Ekins-Daukes, N. J.; Nelson, J., Organic Photovoltaic Greenhouses: A Unique Application for Semi-transparent PV? *Energy Environ. Sci.* **2015**, 8, 1317-1328.

(13)   Xue, Q.; Xia, R.; Brabec, C. J.; Yip, H.-L., Recent advances in semi-transparent polymer and perovskite solar cells for power generating window applications. *Energy Environ. Sci.* **2018**, 11, 1688-1709.

(14)   Zhang, S.; Ye, L.; Zhang, H.; Hou, J., Green-solvent-processable Organic Solar Cells. *Mater. Today* **2016**, 19, 533-543.

(15)   Li, W.; Furlan, A.; Hendriks, K. H.; Wienk, M. M.; Janssen, R. A. J., Efficient Tandem and Triple-Junction Polymer Solar Cells. *J. Am. Chem. Soc.* **2013**, 135, 5529-5532.

(16)   Pavlishchuk, V. V.; Addison, A. W., Conversion Constants for Redox Potentials Measured versus Different Reference Electrodes in Acetonitrile Solutions at 25°C. *Inorg. Chim. Acta* **2000**, 298, 97-102.

(17)   Bard, A. J.; Faulkner, L. R., Electrochemical Methods: Fundamentals and Applications. 2nd ed.; *Wiley*, **2001**.

(18)   Sun, Y.; Seo, J. H.; Takacs, C. J.; Seifter, J.; Heeger, A. J., Inverted Polymer Solar Cells Integrated with a Low-Temperature-Annealed Sol-Gel-Derived ZnO Film as an Electron Transport Layer. *Adv. Mater.* **2011**, 23, 1679-1683.

(19)   Wang, E.; Hou, L.; Wang, Z.; Hellström, S.; Zhang, F.; Inganäs, O.; Andersson, M. R., An Easily Synthesized Blue Polymer for High-Performance Polymer Solar Cells. *Adv. Mater.* **2010**, 22, 5240-5244.

(20)   Murto, P.; Genene, Z.; Benavides, C. M.; Xu, X.; Sharma, A.; Pan, X.; Schmidt, O.; Brabec, C. J.; Andersson, M. R.; Tedde, S. F.; Mammo, W.; Wang, E., High Performance All-Polymer Photodetector Comprising a Donor–Acceptor–Acceptor Structured Indacenodithiophene–Bithieno[3,4-c]Pyrroletetrone Copolymer. *ACS Macro Lett.* **2018**, 7, 395-400.

(21)   Li, Z.; Xu, X.; Zhang, W.; Meng, X.; Ma, W.; Yartsev, A.; Inganäs, O.; Andersson, M. R.; Janssen, R. A. J.; Wang, E., High Performance All-Polymer Solar Cells by Synergistic Effects of Fine-Tuned Crystallinity and Solvent Annealing. *J. Am. Chem. Soc.* **2016**, 138, 10935-10944.

(22)   Sharma, A.; Pan, X.; Campbell, J. A.; Andersson, M. R.; Lewis, D. A., Unravelling the Thermomechanical Properties of Bulk Heterojunction Blends in Polymer Solar Cells. *Macromolecules* **2017**, 50, 3347-3354.

(23)   Bjuggren, J. M.; Sharma, A.; Gedefaw, D.; Elmas, S.; Pan, C.; Kirk, B.; Zhao, X.; Andersson, G.; Andersson, M. R., Facile Synthesis of an Efficient and Robust Cathode Interface Material for Polymer Solar Cells. *ACS Appl. Energy Mater.* **2018**, 1, 7130-7139.

(24)   Sharma, A.; Kroon, R.; Lewis, D. A.; Andersson, G. G.; Andersson, M. R., Poly(4-vinylpyridine): A New Interface Layer for Organic Solar Cells. *ACS Appl. Mater. Interfaces* **2017**, 9, 10929-10936.

(25)   Ren, G.; Ahmed, E.; Jenekhe, S. A., Non-Fullerene Acceptor-Based Bulk Heterojunction Polymer Solar Cells: Engineering the Nanomorphology via Processing Additives. *Adv. Energy Mater.* **2011**, 1, 946-953.

(26)   Rundel, K.; Maniam, S.; Deshmukh, K.; Gann, E.; Prasad, S. K. K.; Hodgkiss, J. M.; Langford, S. J.; McNeill, C. R., Naphthalene Diimide-based Small Molecule Acceptors for Organic Solar Cells. *J. Mater. Chem. A* **2017**, 5, 12266-12277.

Chapter 5 – N2200 based copolymers for fine tuning of photovoltaic properties via backbone substitution and alkyl side-group length

5.1 Overview

In this chapter, three novel naphthalene diimide (NDI)-2,2'-bithiophene based statistical copolymer acceptors were successfully synthesised, as complement to three previously published structures, to study the effect of 2-octyldodecyl vs 2-hexyldecyl alkyl side-groups as well as the partial substitution of the 2,2'-bithiophene moiety in N2200 derivatives on the power conversion efficiency (PCE) in all-polymer solar cells. This partial substitution was limited to 10% of the total 2,2'-bithiophene content for either thiophene or 3,3'-ditetradecyl-2,2'-bithiophene. Optical and thermal properties of the six polymers were investigated and the solubilities tested for common, less harmful processing solvents. P(NDI2OD-14T2) showed excellent solubilities in both THF and *o*-xylene with the higher molecular weight polymer PNDI-T10), N2200, and N2300 proving insoluble in these solvents. Photovoltaic performance is studied in the inverted device structure of indium tin oxide (ITO)/zinc oxide (ZnO)/poly(ethylenimine) ethoxylated (PEIE)/Active layer/molybdenum oxide (MoO_x)/silver (Ag) with the high-performance donor polymer PTB7-Th. The bulk heterojunction (BHJ) layer is deposited via spin coating as well as blade coating to explore differences in performance between laboratory scale processing and a bridging technique toward scalable manufacturing. 2-octyldodecyl based polymers were found to outperform their 2-hexyldecyl counterparts with PNDI-T10 achieving a highest PCE of 5.04% and 4.74% for spin coated and blade coated devices respectively. Though, the observed discrepancy in molecular weight for the 2-hexyldecyl based polymers could affect/skew these results. Interestingly, 10% substitution with thiophene (PNDI-T10/P(NDI2HD-T10)) produced higher PCEs while 3,3'-ditetradecyl-2,2'-bithiophene (P(NDI2OD-14T2)/P(NDI2HD-14T2)) achieved on-par results with NDI-2,2'-bithiophene based co-polymer, N2200. Thus, further fine tuning of these N2200 derivatives could be expected to push PCEs even higher. The 2-hexyldecyl counterparts showed inconclusive results, this due to difficulties in assessment stemming from widely varying molecular weights and solubility issues of N2300.

5.2 Introduction

PSCs with small molecule NFAs have achieved incredible efficiencies, with the latest record almost reaching a PCE of 15%,[1] as the current record for all-polymer solar cells sit at 10.3%[2]. While this is quite a large disparity, all-polymer solar cells have a number of attractive properties that have contributed to the large interest in the area. These include a wide and tuneable light absorption range, a robust active layer morphology, good compatibility with large scale production, and high long term stability.[3] The latter two arise from the inherent limited diffusion of polymers compared to small molecules as well as the non-brittle, flexible films that polymer bulk heterojunctions (BHJ) tend to form. The most widely used acceptor polymer is the naphthalene diimide (NDI)-bithiophene based N2200, with 2-octyldodecyl side-groups,[4] for which PCEs of over 10% have been achieved in all-polymer solar cells.[5] Though, the largest contribution is undoubtedly all the high performing derivatives based on the N2200 structure.[6-7]

Chemical modification of N2200 has been largely focused on the development of new compounds as well as the fine tuning of crystallisation. Several strategies for this fine tuning have been developed that each target a different part of the polymer structure. One such strategy, mentioned in the Methodology section, targets the branching point of the pendant side-group on the NDI moiety, effectively influencing the domain spacing for a closer packing.[8] In a strategy developed by Li *et al.*, irregularity was introduced into the polymer backbone via the partial substitution of 2,2'-bithiophene for thiophene.[9] This induced bending of the backbone and reduced the aromatic overlap, consequently reducing the π-π stacking. This resulted in the polymer PNDI-T10, achieving a highest PCE of 9% in all-polymer ternary blends.[10] This polymer also possesses the device record for printed indium tin oxide (ITO) free devices with a highest efficiency of 8.61% when paired with PTB7-Th.[11] In the polymer PNDI2OD-2FT (Figure 5.1) Jung *et al.* fluorinated the 3,3'-positions of the BT, leading to an increased crystallinity and a widened band gap for a highest PCE of 6.71% in all-polymer solar cells.[12]

The co-planarity of 2,2'-bithiophene has also been targeted in the polymer TffBT-TETOR (Figure 5.1) via introduction of functional groups in the bithiophene 3,3'-positions, increasing crystallinity and π-π stacking. Guo *et al.* introduced alkoxy functional groups on the BT, effectively avoiding a head-to-head configuration (e.g. twisted backbone) as well as increasing the co-planarity.[13] This favours a planar configuration due to intramolecular attraction between the sulphur in the thiophene and the alkoxy side-group. However, this has the disadvantage of elevating the HOMO energy level, consequently lowering device performance. To overcome this Chen *et al.* utilised the combination of an alkoxy and an ester functional group in the polymer TffBT-TETOR, thus, maintaining the HOMO level while still inducing co-planarity.[14] A similar strategy was also explored for the N2200 derivative P7 by Huang *et al.*, where a vinylene linker functionalised with alkoxy groups was inserted between the thiophene moieties, resulting in a PCE of 1.7% in all-polymer solar cells with the donor PTB7.[15]
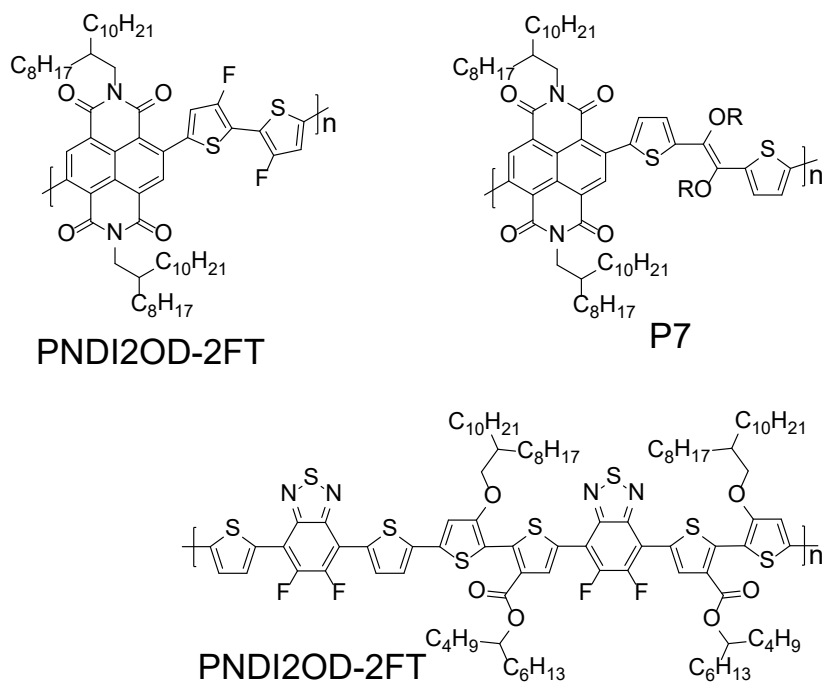
Figure 5.1: Chemical structures of the three polymers PNDI2OD-2FT, P7, and TffBT-TETOR.

As with the broader research field, focus has been on translating the high PCEs of these structures toward greener, scalable fabrication. Zhao *et al.* reached a high PCE of 9% for blade coated devices, concluding that the drying conditions of blade coated devices should emulate the drying conditions of high performance spin coated devices for successful translation between the two processing techniques.[16] Further, less harmful low boiling point solvents are now considered an important tool to optimise optoelectronic functions,[17] with high performance devices, PCEs of ~10%, now published.[5, 18]

In this chapter, six acceptor polymers are synthesised and explored in inverted PSC devices. Out of these polymers, the three novel N2200 derivatives P(NDI2HD-T10), P(NDI2OD-14T2), P(NDI2HD-14T2) are presented in addition to the previously published PNDI-T10[9], poly[[*N,N′*-bis(2-hexyldecyl)-naphthalene-1,4,5,8-bis(dicarboximide)-2,6-diyl]-alt-5,5′-(2,2′-bithiophene)] (N2300)[19] and poly[[*N,N′*-bis(2-octyldodecyl)-naphthalene-1,4,5,8-bis(dicarboximide)-2,6-diyl]-alt-5,5′-(2,2′-bithiophene)] (N2200)[4]. All polymers are synthesised in a three-step facile synthesis route from modified literature procedures, using commercially available starting materials, e.g. 1,4,5,8-naphthalenetetracarboxylic dianhydride (NTCDA). The rationale for these polymer structures was to incorporate structural differences that likely affect co-planarity, crystallinity, solubility, and aggregate formation in solution. Furthermore, the branched alkyl side-groups of the NDI monomers are not photoactive, they are however essential for solution processing as well as formation and stability of favourable morphologies. With the high performing NDI based polymers containing 2-octyldodecyl pendant side-groups it is of interest to investigate if higher or similar PCEs can be achieved with shorter pendant side-groups when utilising modified co-monomers. For this purpose, NDI monomers bearing either 2-octyldodecyl or 2-hexyldecyl side-groups were paired with the three co-monomers thiophene,

2,2'-bithiophene, and 3,3'-ditetradecyl-2,2'-bithiophene in various configurations. The commercially available and widely studied 2,2'-bithiophene containing polymers N2200 and N2300 were included in this study to provide well established reference points.

Incorporation of thiophene in the backbone, yields a three component mixture or random co-polymer, reducing the planarity due to an increase in the torsion angles, as was shown for PNDI-T10 with a reduced crystallinity relative to N2200.[10] This is not the case for 2,2'-bithiophene, for which the two conformers cisoid (sulfurs in close proximity) and transoid (sulfurs opposite each other) are accessible. In an attempt to imitate the crystallinity reduction displayed for thiophene, while retaining the two conformers of 2,2'-bithiophen as well as increasing the solubility, a third co-monomer is introduced. This co-monomer introduced straight alkyl chains in the 3,3'-positions of 2,2'-bithiophene, thus affecting the torsion angles via steric hindrance in addition to providing a solubilising element. Commercially available 3,3'-ditetradecyl-2,2'-bithiophene was utilised for this purpose.

The partial incorporation of 3,3'-ditetradecyl-2,2'-bithiophene (P(NDI2OD-14T2) & P(NDI2HD-14T2)) was explored regarding solubilising effects as well as aggregate formation for these structurally modified N2200 analogues. Lastly, the effect of structural differences on the PCE was explored for the two different alkyl side-group lengths, 2-octyldodecyl (PNDI-T10, P(NDI2OD-14T2), and N2200) versus 2-hexyldecyl (P(NDI2HD-T10), P(NDI2HD-14T2), and N2300).

PSCs in the inverted device architecture for a ITO/zinc oxide (ZnO)/ poly(ethylenimine) ethoxylated (PEIE)/Active layer/molybdenum oxide (MoO$_x$)/silver (Ag) configuration were manufactured to investigate the impacts that structural modifications have on their performance. The active layer deposition was conducted with spin coating (SC) as well as blade coating (BC) to explore differences in performance for laboratory scale versus a bridging technique toward scalable processing. The acceptor polymers are paired with the high efficiency polymer donor poly[4,8-bis(5-(2-ethylhexyl)thiophen-2-yl)benzo[1,2-b;4,5-b']dithiophene-2,6-diyl-alt-(4-(2-ethylhexyl)-3-fluorothieno[3,4-b]thiophene-)-2-carboxylate-2-6-diyl)] (PTB7-Th) to form the BHJ. These donor-acceptor combinations are processed from the chlorinated solvent chlorobenzene (CB), without the presence of solvent additives or the utilisation of thermal treatments.

5.3 Experimental

5.3.1 Synthesis
3,3'-ditetradecyl-2,2'-bithiophene-5,5'-diylbis(trimethylstannane) was purchased from Solarmer Energy Inc. and 5,5'-bis(trimethylstannyl)-2,2'-bithiophene (99%) from SunaTech Inc. with all other solvents, reagents and catalysts acquired from SigmaAldrich and used as received (with the exception of toluene that was dried on molecular sieves and distilled prior to use in polymerisations). The donor

polymer PTB7-Th was purchased from 1-Material Inc. and the acceptor polymer N2200*, used for PSC devices was purchased from Raynergy Tek Inc., with both polymers used as received.

5.3.1.1 diBrNTCDA

NTCDA (5 g, 0.0186 mol) was added to a 1-neck round-bottom flask (RBF) and slurried in 50 mL of 98% sulphuric acid for 15 minutes. Dibromantin (7.99 g, 0.0280 mol) was added in portions over the course of an hour. The RBF was tightly stoppered upon first addition and was then kept sealed in-between additions and during the reaction. Once all dibromantin had been added the temperature was increased to 50 $^\circ$C and the reaction run overnight. The reaction mixture was poured on crushed ice and then filtered off. The remaining yellow solid was washed with copious amounts of water and methanol. The crude product was achieved as a canary-yellow powder. Yield: 6.67 g (84%).

Recrystallisation:

The crude compound was dissolved in minimum amounts of anhydrous N,N-dimethylformamide (DMF) at elevated temperatures upon which the mixture was allowed to cool to ambient temperatures. IPA was slowly added to the mixture until the first sign of precipitate appeared as a finely dispersed light-yellow powder. The flask was then very gentle swirled and placed in the fridge overnight to allow the compound to fall out of solution. The solid was filtered off, washed with ice cold IPA and dried. Pure product was achieved as a faded yellow powder. Yield: ~3.6 g (~45%).

^{1}H NMR (d-DMSO, 600 MHz) δ: 8.77 (s, 2H)

5.3.1.2 DHDNDI

diBrNTCDA (1 g, 0.0023 mol) was slurried in 20 mL acetic acid (AcOH) in a 50 mL two-necked RBF and stirred under nitrogen atmosphere for 15 minutes. 2-hexyldecyl amine (1.7 g, 0.0070 mol) was added to the reaction flask through a septum and the temperature was increased to 130 °C for four hours. Once cooled to room temperature the reaction mixture was poured on crushed ice and then extracted with chloroform (2 x 75 mL). The resulting chloroform solution was washed first with brine (3 x 50 mL) and then washed with a 1M sodium hydrogen carbonate solution prior to drying with magnesium sulfate. The crude product was dry loaded on to a column and run with hexane:chloroform in a 3:1 ratio as eluent. This was followed by a recrystallisation in IPA-hexane, yielding pure product as a faded red powder. Yield: 1.01 g (49%).

^{1}H NMR (CDCl$_3$, 600 MHz) δ: 9 (s, 2H), 4.18-4.13 (d, J = 7.4 Hz, 4H), 2.03-1.95 (m, J = 6.1 Hz, 2H), 1.38-1.18 (m, 48H), 0.89-0.84 (m, 12H); ^{13}C NMR (CDCl$_3$, 600 MHz) δ: 161.22, 161.06, 139.19, 128.39, 127.78, 125.32, 124.12, 45.47, 36.50, 31.90, 31.83, 31.61, 31.57, 30.04, 29.72, 29.56, 29.31, 26.35, 26.33, 22.68, 22.66, 14.13, 14.10. MS calcd. for C$_{46}$H$_{68}$N$_2$O$_4$Br$_2$ [[M+H]$^+$]: m/z = 871.36238; MALDI-TOF 869.32 exp, DSA-TOF 871.3594 exp.

5.3.1.3 DODNDI

diBrNTCDA (1 g, 0.0023 mol) was slurried in 20 mL AcOH in a 50 mL two-necked RBF and stirred under nitrogen atmosphere for 15 minutes. 2-hexyldecyl amine (1.7 g, 0.0070 mol) was added to the reaction flask through a septum and the temperature was increased to 130 °C for four hours. Once cooled to room temperature the reaction mixture was poured on crushed ice and then extracted with chloroform (2 x 75 mL). The resulting chloroform solution was first washed with brine (3 x 50 mL) and then washed with a 1M sodium hydrogen carbonate solution prior to drying with magnesium sulfate. The crude product was dry loaded on to a column and run with hexane:chloroform in a 3:1 to a 6:4 ratio as eluent. This was followed by a recrystallisation in IPA-hexane, yielding pure product as a faded red powder. Yield: 1.38 g (60%).

^{1}H NMR (CDCl$_3$, 600 MHz) δ: 9 (s, 2H), 4.22-4.08 (d, J = 7.4 Hz, 4H), 2.05-1.95 (m, 2H), 1.40-1.18 (m, 64H), 0.9-0.84 (m, 12H); ^{13}C NMR (CDCl$_3$, 600 MHz) δ: 161.20, 161.04, 139.18, 128.39, 127.77, 125.31, 124.11, 45.47, 36.48, 31.94, 31.90, 31.58, 30.04, 29.66, 29.64, 29.61, 29.56, 29.36, 29.31, 26.36, 22.71, 22.69, 14.13. MS calcd. for $C_{54}H_{84}N_2O_4Br_2$ [[M+H]$^+$]: m/z = 983.48758; MALDI-TOF 981.45 exp, DSA-TOF 983.4854 exp.

5.3.1.4 PNDI-T10

Synthesis of PNDI-T10 was conducted according to modified literature procedures with minor changes to starting concentrations, reaction temperatures and reaction times.[9] Synthesis of high molecular weight PNDI-T10 is presented below with medium and low molecular weights synthesised following the same procedure, but with diluted starting concentrations.

2,6-dibromo-1,4,5,8-tetracarboxylic-N,N'-bis(2-octyldodecyl)diimide (DODNDI) (1 g, 1.015 mmol), 5,5'-bis(trimethylstannyl)-2,2'-bithiophene (449 mg, 0.914 mmol), 2,5-bis(trimethylstannyl)thiophene (42 mg, 0.102 mmol), tris(dibenzylideneacetone)dipalladium(0) (Pd$_2$(dba)$_3$) (18.4 mg) and tri(*o*-tolyl)phosphine (24.4 mg) were added to a RBF, then flushed with nitrogen five times prior to addition of 7.6 mL of dry toluene by syringe through a septum. The RBF was lowered into a 115 °C preheated oil bath and the reaction mixture was heated under vigorous stirring for 48 hours. The polymer was end-capped with 2-bromothiophene (0.66 mL) followed by 2-(tributylstannyl)thiophene (2.66 mL) for an hour respectively. The reaction mixture was allowed to cool to ambient temperature and was then poured on 300 mL of acetone. The precipitated material, blue strings, was filtered and collected using a polymer filtration setup with a PTFE membrane. Soxhlet extraction was performed for 24 hours for acetone and diethyl ether prior to an 8 hour collection with chloroform. The chloroform fraction was purified by column, then precipitated on acetone and collected using a polymer filtration setup with a PTFE membrane yielding a dark blue solid. Yield: 0.96 g (96%).

^{1}H NMR (CDCl$_3$, 600 MHz) δ: 8.95, 8.83, 8.53, 7.34, 4.12, 2.00, 1.26, 0.85. SEC$_{High}$: $\overline{M}_n$ = 62 kg mol$^-$^{1}, Đ$_M$ = 2.7, SEC$_{Medium}$: $\overline{M}_n$ = 40 kg mol^{-1}, Đ$_M$ = 3.1, SEC$_{Low}$: $\overline{M}_n$ = 21 kg mol^{-1}, Đ$_M$ = 2.7.

5.3.1.5 P(NDI2HD-T10)

The polymer was prepared by the same procedure as described above for P(NDI2OD-14T2), starting with 2,6-dibromo-1,4,5,8-tetracarboxylic-N,N'-bis(2-hexyldecyl)diimide (DHDNDI) (1 g, 1.1456 mmol), 5,5'-bis(trimethylstannyl)-2,2'-bithiophene (508 mg, 1.031 mmol), and 2,5-bis(trimethylstannyl)thiophene (47 mg, 0.115 mmol). Product was achieved as a dark blue solid. Yield: 0.94 g (94%).

^{1}H NMR (CDCl$_3$, 600 MHz) δ: 8.95, 8.83, 8.52, 7.34, 4.12, 2.00, 1.27, 0.86. SEC: $\overline{M}_n$ = 30 kg mol^{-1}, Đ$_M$ = 3.3.

5.3.1.6 P(NDI2OD-14T2)

2,6-dibromo-1,4,5,8-tetracarboxylic-N,N'-bis(2-octyldodecyl)diimide (DODNDI) (500 mg, 0.508 mmol), 5,5'-bis(trimethylstannyl)-2,2'-bithiophene (225 mg, 0.457 mmol), 3,3'-ditetradecyl-2,2'-bithiophene-5,5'-diylbis(trimethylstannane) (45 mg, 0.051 mmol), Pd$_2$(dba)$_3$ (9.2 mg) and tri(*o*-tolyl)phosphine (12.2 mg) were added to a RBF, then flushed with nitrogen five times prior to addition of 2.5 mL of dry toluene by syringe through a septum. The RBF was lowered into a 115 °C preheated oil bath and the reaction mixture was heated under vigorous stirring for 30 hours. 3.5 mL of additional toluene was added during the initial reaction phase to avoid gelling. The polymer was end-capped with 2-bromothiophene (0.33 mL) followed by 2-(tributylstannyl)thiophene (1.33 mL) for an hour respectively. The reaction mixture was allowed to cool to ambient temperature and was then poured on 150 mL of acetone. The precipitated material was filtered and collected using a polymer filtration setup with a PTFE membrane. Soxhlet extraction was performed for 24 hours for acetone, hexane, and diethyl ether prior to an 8 hour collection with chloroform. The chloroform fraction was purified by column, then precipitated on acetone and collected using a polymer filtration setup with a PTFE membrane yielding a dark blue material. Yield: 0.47 g (90%).

^{1}H NMR (CDCl$_3$, 600 MHz) δ: 8.83, 8.53, 7.34, 4.12, 2.00, 1.26, 0.86. SEC: $\overline{M}_n$ = 30 kg mol^{-1}, Đ$_M$ = 2.5.

5.3.1.7 P(NDI2HD-14T2)

The polymer was prepared by the same procedure as described above for P(NDI2OD-14T2), starting with DHDNDI (500 mg, 0.508 mmol), 5,5'-bis(trimethylstannyl)-2,2'-bithiophene (254 g, 0.516 mmol), and 3,3'-ditetradecyl-2,2'-bithiophene (51 g, 0.057 mmol). Achieved as a dark blue material. Yield: 0.48 g (92%).

^{1}H NMR (CDCl$_3$, 600 MHz) δ: 8.82, 8.53, 7.34, 4.12, 1.99, 1.26, 0.85. SEC: $\overline{M}_n$ = 13 kg mol^{-1}, Đ$_M$ = 2.3.

5.3.1.8 N2200 & N2300

N2200 and N2300 with 2-octyldodecyl and 2-hexyldecyl pendant side-groups, respectively, were synthesised according to modified literature procedures.[19]

N2200 was synthesised via Stille coupling. DODNDI (400 mg, 0.406 mmol) and 5,5'-bis(trimethylstannyl)-2,2'-bithiophene (200 mg, 0.406 mmol) were dissolved in anhydrous toluene. The solution was degassed with nitrogen for 30 min and then lowered into a preheated oil bath at 115 °C. $Pd_2(dba)_3$ (7.4 mg, 0.02 eq.)) and tri(*o*-tolyl)phosphine (12.4 mg, 0.1 eq.) were separately dissolved in toluene, then added with a syringe to the hot monomer solution. The resulting mixture was stirred at reflux for 24 h. After cooling to room temperature, the solution was precipitated into acetone. The precipitated material was filtered and collected using a polymer filtration setup with a PTFE membrane. Soxhlet extraction was performed for 24 hours for acetone, hexane, and diethyl ether prior to an 8 hour collection with chloroform. The chloroform fraction was purified by column, then precipitated on acetone and collected using a polymer filtration setup with a PTFE membrane. Product was collected as a dark blue material. Yield: 0.38 g (95%).

^{1}H NMR ($CDCl_3$, 600 MHz) δ: 8.83, 8.52, 8.09, 7.34, 4.12, 1.99, 1.26, 0.86. SEC: $\overline{M}_n$ = 30 kg mol^{-1}, Đ$_M$ = 2.9.

N2300 was prepared by the same procedure as described above for N2200, starting with DHDNDI (400 mg, 0.458 mmol), 5,5'-bis(trimethylstannyl)-2,2'-bithiophene (225 mg, 0.458 mmol), $Pd_2(dba)_3$ (8.4 mg, 0.02 eq.)) and tri(*o*-tolyl)phosphine (14.0 mg, 0.1 eq.). In addition to the work-up described above, a $CHCl_3$ insoluble fraction was collected in chlorobenzene (CB). This fraction followed the same procedure as for the $CHCl_3$ fraction with purification by a short column to remove catalyst followed by precipitation in acetone. The product was collected using a polymer filtration setup with a PTFE membrane in the form of a dark blue material. Yield: 0.36 g ($CHCl_3$ (~30%) + CB (~60%) = ~90%).

^{1}H NMR ($CDCl_3$, 600 MHz) δ: 8.83, 8.53, 8.08, 7.34, 4.12, 1.99, 1.26, 0.87. SEC$_{Chloroform}$: $\overline{M}_n$ = 37 kg mol^{-1}, Đ$_M$ = 3.3, SEC$_{Chlorobenzene}$: $\overline{M}_n$ = 72 kg mol^{-1}, Đ$_M$ = 2.2.

5.3.2 Material characterisation

5.3.2.1 Gel-permeation chromatography
High temperature gel-permeation chromatography (GPC) was performed on a PL-GPC 220 Integrated High Temperature GPC/SEC System (Agilent) with refractive index and viscometer detectors with 3×PLgel 10 μm MIXED-B LS, 300×7.5 mm columns of type PL1110-6100LS (molecular weight range of 500 to 10 000 000) in series. The eluent, 1,2,4-trichlorobenzene (TCB), was heated to 150 °C. Molecular weights were determined with polystyrene standards and calculated according to the relative calibration.

5.3.2.2 Contact angle

Static contact angle of deionized water against polymer film surfaces was measured using a PAT-1 tensiometer (Sinterface Technologies, Germany). Reported contact angles are average values over four measurements on different areas of the films. Cleaning of ITO-coated glass substrates (10 Ω/sq, Xin Yan Technology LTD) follow the procedure described under section *4.3.4 Device fabrication*, Chapter 4. All polymer samples were deposited from chloroform solutions with concentrations of 10 mg mL^{-1} and spun at 2000 rpm for 60 seconds. Measurements were conducted on freshly prepared films on dry and sunny days with low relative humidity.

5.3.2.3 Ultraviolet-visible spectroscopy

Optical absorption spectra for the small molecule NFAs were recorded for both solution and thin film (polymers spin coated on 2.5 x 2.5 cm glass slides) on a Perkin Elmer Lambda 950 spectrophotometer at a scan rate of 10 nm s^{-1}.

5.3.2.4 Thermal analysis

Thermogravimetric analysis (TGA) was performed on a PerkinElmer Thermogravimetric Analyzer 8000. Samples were dried in a vacuum oven at 25°C for 24 hours prior to the measurement. Measurements were conducted from 25- 400 °C at a scan rate of 10 °C/minute.

5.3.2.5 Electrochemistry

Square-wave voltammetry (SWV) measurements for PNDI-T10, P(NDI2HD-T10), P(NDI2OD-14T2), P(NDI2HD-14T2), N2200, and N2300 were carried out on the same setup presented under section *4.3.2 Material characterisation*, Chapter 4. Thin polymer films were coated on the platinum electrode from 10 mg mL^{-1} CHCl$_3$ solutions. A 0.10 M solution of tetrabutylammonium hexafluorophosphate (Bu4NPF6) in anhydrous acetonitrile was used as the supporting electrolyte.

5.3.3 Device manufacturing

BHJ layers were processed via spin coating as well as blade coating in an ITO/ZnO/PEIE/Active layer/MoO$_x$/Ag device configuration for PNDI-T10, P(NDI2HD-T10), P(NDI2OD-14T2), P(NDI2HD-14T2), and N2300 acceptor polymers. For the spin coated (SC) devices, the BHJ processing and deposition of consecutive layers, was conducted in a glovebox with measurements of encapsulated devices taking place under ambient conditions. The BHJ processing of the blade coated devices were instead deposited under ambient atmosphere in a fume hood with the devices then transferred into a glovebox for evaporation of the top two layers.

Patterned ITO-coated glass substrates were cleaned in a three-step process. The substrates were sonicated first in acetone for 10 minutes and then in IPA for an additional 10 minutes. They were then dried under a nitrogen stream prior to a 10 minute UV/ozone treatment.

The ZnO layer was deposited via spin coating onto the cleaned ITO-coated glass substrates at 3000 rpm for 30 seconds, followed by thermal annealing at 200 °C on a hotplate for 30 minutes. In a second step,

0.4 wt.% PEIE solution was spin coated on top of the ZnO layer at 5000 rpm for 30 seconds with consecutive annealing at 110 °C on a hot plate for 15 minutes.

The BHJ layer was deposited by spin coating from CB, at varying spin speeds (rpms) for 60 seconds, or blade coated at varying speeds. The acceptor polymers were paired with the donor polymer PTB7-Th in a 1:1 ratio.

The two top layers consisted of a 15 nm MoO_x layer and a 100 nm Ag layer that were evaporated in vacuo at ~ 10^{-6} mbar. A shadow mask was used to define electrodes with an active area of 4.5 mm^2. The devices were encapsulated with an epoxy resin and glass cover slides prior to being taken out of the glove box for testing.

5.4 Results and discussion

5.4.1 Synthesis

The synthesis route for the monomers with 2-octyldodecyl and 2-hexyldecyl side-groups, that is DODNDI and DHDNDI, are presented in Scheme 5.1. In the first synthesis step, NTCDA is brominated with the inexpensive bromination reagent, dibromantin according to a modified literature procedure.[20] Particular attention was given to the work-up procedure to avoid complicated column separations in consecutive steps. Through minimisation of the tribromo product during reaction, pure dibromo product could be effectively separated from monobromo product via the preferential crystallisation in a solvent mixture of anhydrous DMF with IPA. This was followed with an alkylation step in AcOH, achieving pure DODNDI (60%) and DHDNDI (49%) monomers in decent yields. Work-up was conducted via column chromatography with a hexane-$CHCl_3$ eluent and was followed by recrystallisation in a hexane-IPA mixture to achieve pure product. Stille coupling was then performed, achieving the statistical copolymers in excellent yields (>90%). Structures of monomers were all confirmed by ^{1}H NMR spectroscopy (Figure A.19) with polymer spectra shown in Figure A.21, Figure A.22, and Figure A.23.
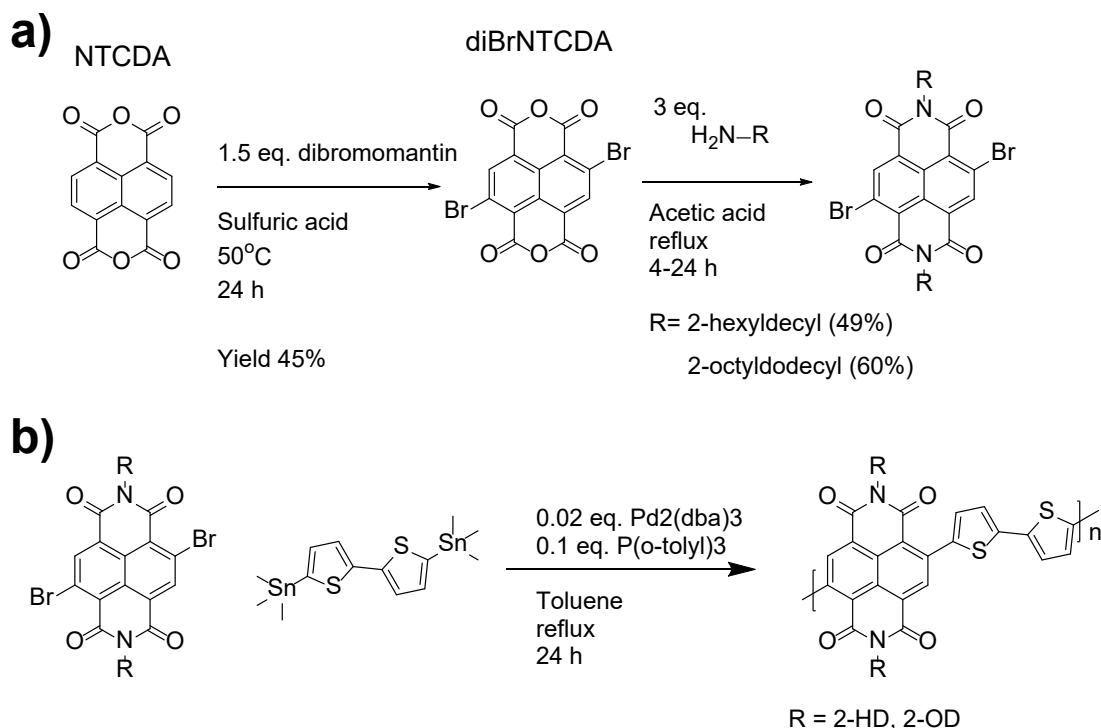
Scheme 5.1: a) Synthesis route for the DHDNDI and DODNDI monomers. b) General procedure for N2200 derivatives with 2-octyldodecyl and 2-hexyldecyl side-groups.

A range of molecular weights were achieved for the different polymers, see Table 5.1 for $\bar{M}_n$ and $\bar{M}_w$ against polystyrene standard with relative calibration. High, medium and low molecular weight versions of the previously published, high performing polymer PNDI-T10 were synthesised for use as benchmark for the other polymers with regards to solubility and performance. The solubility of the acceptor polymers was explored in the greener and less toxic solvent options of tetrahydrofuran (THF), methyltetrahydrofuran (MeTHF), and *ortho*-xylene (*o*-xylene), to identify greener processing solvent alternatives. These solvents were chosen due to previously yielding high performance all-polymer solar cells.[5, 18, 21-23] Interestingly, the low, medium, and high molecular weight batches of PNDI-T10 experienced widely varying solubility in THF. The PNDI-T10$_{Low}$ batch possessed a good solubility at ambient temperature while PNDI-T10$_{Medium}$ batch requiring elevated temperatures under vigorous stirring to dissolve. PNDI-T10$_{High}$ batch however, proved insoluble, barely colouring the solution after 24 hours. Polymers P(NDI2OD-14T2) and P(NDI2HD-14T2), that are of lower $\bar{M}_n$, proved readily soluble at concentrations of 10 mg mL^{-1}. However, P(NDI2HD-T10) and N2300 proved insoluble in THF as well as MeTHF. It was only P(NDI2OD-14T2) that was soluble in MeTHF with the remaining polymers experiencing a lower solubility at elevated temperatures. Additionally, the polymer solubilities were also tested *o*-xylene. PNDI-T10$_{High}$, P(NDI2HD-T10), and N2300 appeared insoluble in *o*-xylene with the rest of the polymers possessing varying degrees of solubility but dissolving completely at elevated temperatures of ~80 °C. P(NDI2OD-14T2) did again prove to be the most soluble at concentrations of over 10 mg mL^{-1} dissolving at ambient temperatures. Of note, N2300

possesses a noticeably lower solubility in CHCl₃ than N2200. This became evident during work-up where a CHCl₃ soluble lower molecular weight fraction (~37 kg mol⁻¹) was separated from the CB soluble high molecular weight fraction (~72 kg mol⁻¹). The high molecular weight CB fraction is thus referred to unless otherwise specified.
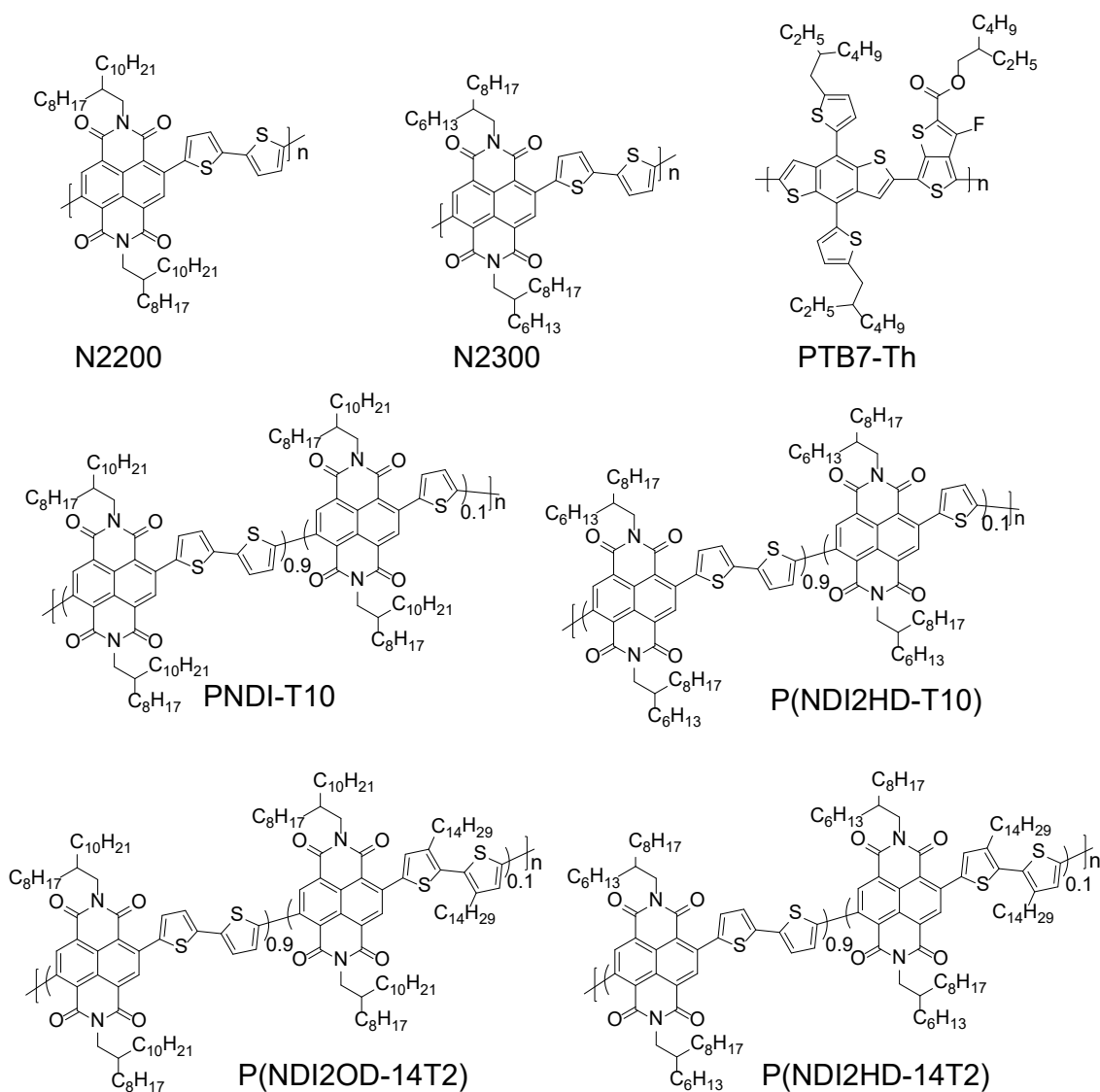
Figure 5.2: Chemical structures of the donor polymer PTB7-Th as well as the acceptor polymers N2200/N2300, PNDI-T10/P(NDI2HD-T10), and P(NDI2OD-14T2)/P(NDI2HD-14T2) with 2-octyldodecyl/2-hexyldecyl side-groups.

Table 5.1: Molecular weights of the acceptor polymers, determined by HT-GPC against polystyrene standard for both relative and universal calibration. *Molecular weights provided by manufacturer Raynergy Tek Inc.

Polymer		Relative calibration		
		$\bar{M}_n$	$\bar{M}_w$	Đ$_M$
PNDI-T10	High	62000	170000	2.7
	Medium	40000	123000	3.1
	Low	21000	57000	2.7
P(NDI2HD-T10)		30000	98000	3.3
P(NDI2OD-14T2)		30000	74000	2.5
P(NDI2HD-14T2)		13000	29000	2.3
N2200		30000	86000	2.9
N2200*		77000	231000	3.0
N2300	CB	72000	159000	2.2
	CHCl$_3$	37000	121000	3.3

5.4.2 Material properties

The contact angles were investigated for the acceptor polymers PNDI-T10, P(NDI2HD-T10), P(NDI2OD-14T2), P(NDI2HD-14T2), N2200, and N2300, Figure 5.3. As expected, due to the similarities in chemical structure, a narrow spread was observed with the acceptor polymers all experiencing contact angles of ~92-97°. This is close to the reported value of PTB7-Th at 96.6° and also a close match to the reported value of N2200 at 99.8°.[24] This close match between the donor and the acceptor polymers indicates that a good miscibility is achieved for these systems due to low interfacial tensions, in turn also affecting the morphologies.[25] While a good miscibility is desired, a too high miscibility can lead to impure domains and low device performance. In contrast, a low miscibility will also affect the performance negatively.[26]
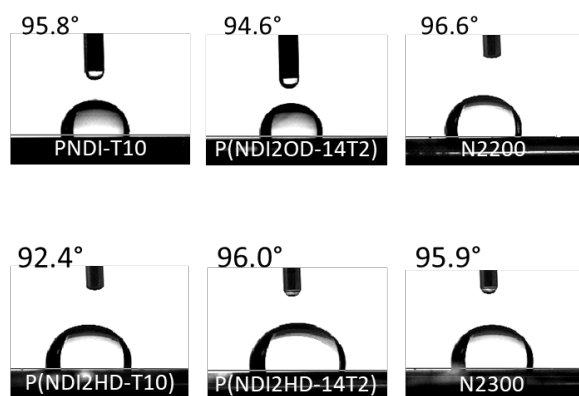
Figure 5.3: Contact angles for PNDI-T10, P(NDI2HD-T10), P(NDI2OD-14T2), P(NDI2HD-14T2), N2200, and N2300.

Thermal stability of the active layer components is important with PSCs operating under temperatures up to 85 °C.[27] The acceptor polymers were studied with TGA (Figure 5.4), showing excellent thermal stabilities with 5% weight loss occurring for P(NDI2HD-T10), P(NDI2OD-14T2), and P(NDI2HD-14T2) at >300 °C. The other polymers did not experience 5% weight loss in the temperature range (30-400 °C). Interestingly, the copolymers N2200 and N2300 appear to possess the highest thermal stability, outperforming the three component statistical copolymers.
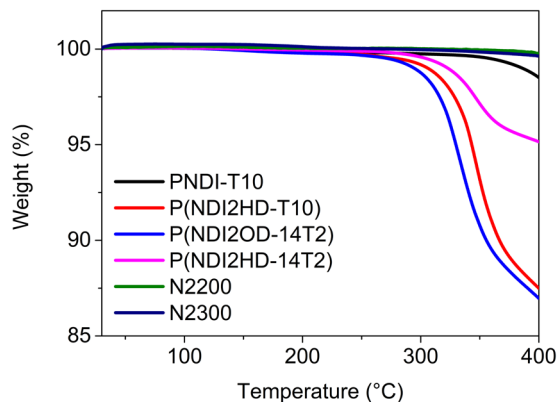
Figure 5.4: Thermogravimetric analysis data for the six NDI based acceptor polymers.

Energy levels of the six NDI based acceptor polymers were estimated from electrochemistry measurements conducted with the SWV technique. From Figure 5.5a-b the SWV oxidation/reduction maxima were estimated. These potentials were then recalculated according to equation 4.1a (Chapter 4), yielding close lying HOMO/LUMO levels of -6.33/-4.01, -6.29/-4.06, -6.34/-4.00, -6.32/-3.97, -6.33/-4.13, and -6.30/-4.13 for PNDI-T10, P(NDI2HD-T10), P(NDI2OD-14T2), P(NDI2HD-14T2), N2200, and N2300 respectively. Despite the differences in the backbones of the polymers, that are expected to influence the energy levels, no clear trends or shifts were observed. This indicates that the energy level differences are too small to be accurately measured with SWV.
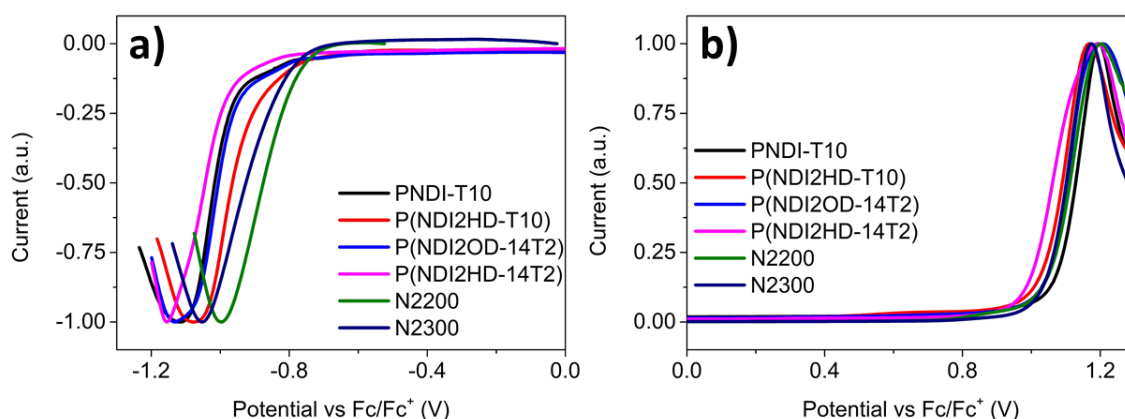
Figure 5.5: SWV spectra of PNDI-T10, P(NDI2HD-T10), P(NDI2OD-14T2), P(NDI2HD-14T2), N2200, and N2300 showing a) reduction and b) oxidation.

In addition to the SWV data, UV/vis spectroscopy was conducted and the optical band gap (E_g^{opt}) was calculated from the absorption onset in thin films according to equation 4.2 (Chapter 4), Table 5.2. From the UV/vis spectra in Figure 5.6a-b a clear trend is observed for peaks in the 500-800 nm regime. The polymers incorporating thiophene (PNDI-T10$_{High}$ & P(NDI2HD-T10)) in the backbone experiences a hypsochromic shift in solution with regards to the polymers incorporating 2,2'-bithiophene (N2200 & N2300). This hypsochromic shift grows even larger for the polymers incorporating 3,3'-ditetradecyl-2,2'-bithiophene (P(NDI2OD-14T2) & P(NDI2HD-14T2)). These polymers were designed to twist in solution with the incorporation of 10% 3,3'-ditetradecyl-2,2'-bithiophene in the backbone providing steric hindrance to intra-/intermolecular interactions of the polymer backbone (Figure 5.2). This disturbs/hinders the pre-formation of aggregates in solution. Less twisting is experienced in the solid state reducing the steric hindrance to intra-/intermolecular interaction, allowing a good π-π stacking. However, P(NDI2OD-14T2) and P(NDI2HD-14T2) also displays a shoulder in the UV/vis solution spectra at ~680-760 nm, indicating the presence of aggregates. The shoulder appears more prominent in P(NDI2OD-14T2), possibly due to the higher molecular weight compared to P(NDI2HD-14T2). This shoulder overlaps with the 2,2'-bithiophene containing polymers N2200 and N2300 with peak maxima, estimated according to Figure A.1, located at 695 nm and 700 nm respectively. With structural similarities between these polymer pairs it is possible that the shoulder arose from sequences in the polymer backbone of P(NDI2OD-14T2) and P(NDI2HD-14T2) lacking the presence of 3,3'-ditetradecyl-2,2'-bithiophene, thus, appearing in the same region as the pure 2,2'-bithiophene polymers.
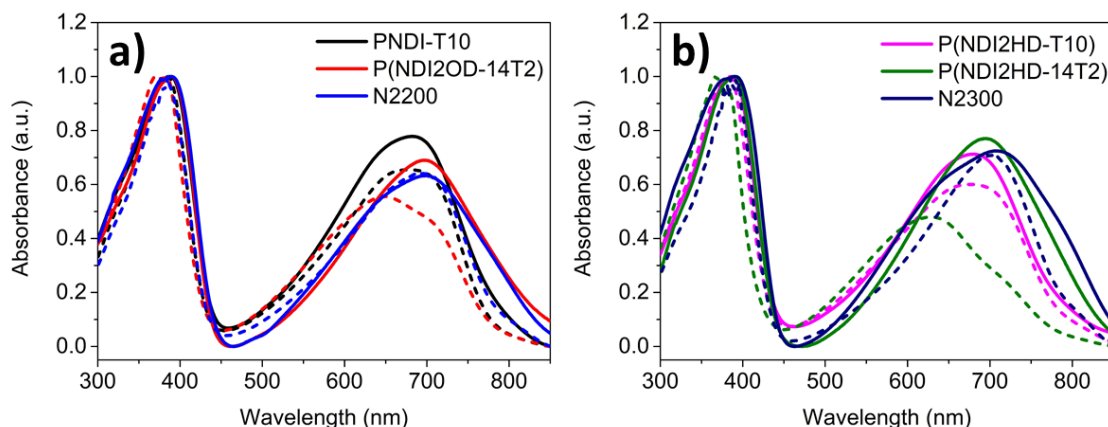
Figure 5.6: UV/vis spectra with solution (dotted) and film (solid) for the NDI based acceptor polymers with a) 2-octyldodecyl side-groups and b) 2-hexyldecyl side-groups.

The thin film UV/vis spectra revealed a large bathochromic shift for P(NDI2OD-14T2) and P(NDI2HD-14T2) compared to solution. Therefore, it is likely that the polymer backbone takes on a planar configuration in the solid sample, allowing for strong π-π stacking that contributes to the large bathochromic shifts of 50 nm and 70 nm respectively for the two polymers. In contrast, the other four polymers display minimal or no shift when comparing spectra for the thin film to solution (Table 5.2). This provides a clear indication that these polymers inherently possess a stronger driving force to form aggregates in solution. It should be noted that the molecular weights vary greatly between these compounds. This molecular weight disparity could possibly cause the greater difference experienced between P(NDI2HD-14T2) and N2300, compared to the complete overlap observed for P(NDI2OD-14T2) with N2200, displaying a close to identical peak maxima.

Table 5.2: Energy level data for the six NDI based acceptor polymers investigated.

| Compound | Electrochemistry | | | Optical | | | |
| | | | | Solution | Film | | |
	HOMO (eV)	LUMO (eV)	E_g (eV)	λ_{max} (nm)	λ_{max} (nm)	λ_{onset} (nm)	E_g^{opt} (eV)
PNDI-T10	-6.33	-4.01	2.32	677	682	796	1.56
P(NDI2HD-T10)	-6.29	-4.06	2.23	680	679	783	1.58
P(NDI2OD-14T2)	-6.34	-4.00	2.34	650	698	838	1.48
P(NDI2HD-14T2)	-6.32	-3.97	2.35	628	694	846	1.47
N2200	-6.33	-4.13	2.20	695	699	839	1.48
N2300	-6.30	-4.08	2.22	704	708	855	1.45

5.4.3 Photovoltaic performance

The performance of acceptor polymers was evaluated in all-polymer solar cells for a device configuration of ITO/ZnO/PEIE/Active layer/MoO$_x$/Ag, with PTB7-Th as the polymer donor. These active layer combinations were processed from CB, with no solvent additives present, via spin coating (SC) as well as blade coating (BC). BC is considered a bridging technique between laboratory and large-scale processing,[11, 28] and was applied to study the performance when moving toward scalable fabrication. Given the experimental setup, it proved unfeasible to produce comparable BC devices for N2300, this due to the low solubility experienced by the polymer in CB. Therefore, BC N2300 devices were omitted from this study.

Data from the best devices for each acceptor polymer is presented in Figure 5.7a-d, Table 5.3. From the available data three clear trends are observed; i) the SC devices experience higher efficiencies than the BC devices, in 4/5 cases, ii) the acceptor polymers with 2-octyldodecyl side-groups outperform their 2-hexyldecyl counterparts and iii) BC devices with low $\bar{M}_n$ acceptor polymers produce higher PCEs than their SC counterparts, and contrarily, the SC devices with high $\bar{M}_n$ producing higher PCE than their BC counter parts. Note that the first two trends could be influenced by the $\bar{M}_n$, and as has already been confirmed by HT-GPC, the molecular weights of these polymers differ widely and therefore care must be taken with assumptions based on this data.

At a closer look, the difference in PCE between SC and BC devices for P(NDI2HD-T10) and P(NDI2OD-14T2) is caused by a decrease in J$_{sc}$ for the BC devices, from 9.99 to 8.96 mA cm^{-2} and 11.46 to 10.39 mA cm^{-2} respectively. These drops in current are both ~10% and almost solely responsible for the decrease in PCE of ~13% for both these systems. Conversely, PNDI-T10$_{High}$ experiences a close to identical current with a minor decrease in FF for a slightly lower PCE of 4.74% for BC devices, compared to 5.04% for SC devices. This is the highest PCE achieved for any of the tested systems for both the SC and BC devices, see Figure 5.8 for I-V curves. These are quite promising results for BC, with SC devices showing slightly lower efficiencies compared to the 5.6% previously published (excluding solvent annealing),[9] with FF being the main contributor.
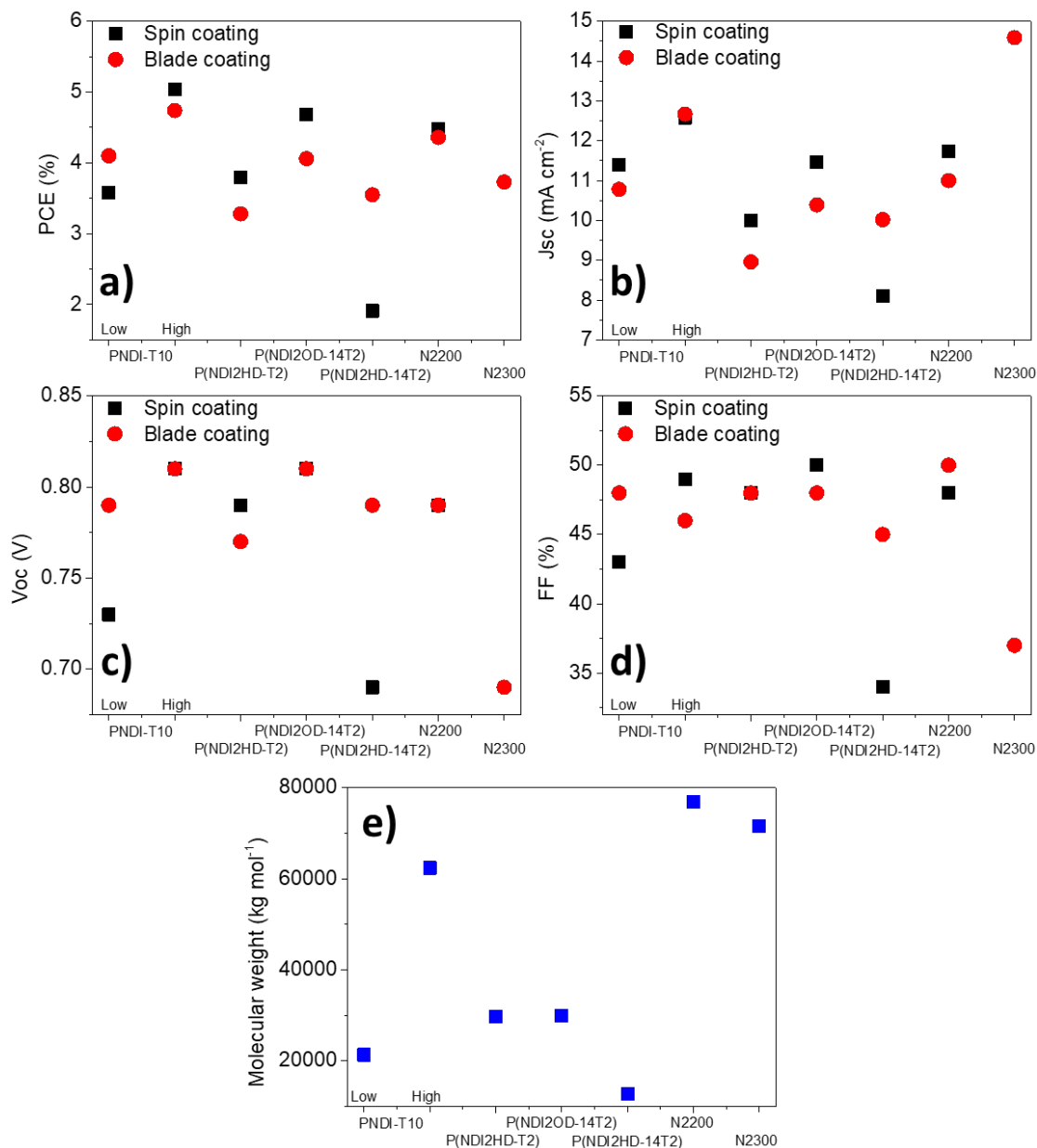
Figure 5.7: Comparison of photovoltaic performance of the best devices for PNDI-T10$_{Low}$, PNDI-T10$_{High}$, P(NDI2HD-T10), P(NDI2OD-14T2), and P(NDI2HD-14T2) with PTB7-Th processed via spin coating or blade coating with a) showing PCE, b) J$_{sc}$, c) V$_{oc}$, and d) FF, and e) showing the molecular weights.

In all cases, the PCE decreases when going from polymers with 2-octyldodecyl side-groups to their counterparts with 2-hexyldecyl side-groups (Table 5.3), and the molecular weight of the polymers appear to correlate relatively well with this decrease (Table 5.1, Figure 5.7e). PNDI-T10$_{High}$ to P(NDI2HD-T10) sees a decrease in molecular weight from 62.4 to 29.7 kg mol^{-1} with corresponding drops in PCE from 5.04% to 3.79% and 4.74% to 3.28% for SC and BC devices respectively. Similarly, P(NDI2OD-14T2) to P(NDI2HD-14T2) experiences a decrease in molecular weight from 30 to 12.8 kg mol^{-1} with corresponding drops in PCE from 4.68% to 1.91% and 4.06% to 3.55% for SC and BC

devices respectively. This trend is clearly visualised in Figure 5.7 with consistent drops for J_{sc}, V_{oc}, and FF for reduced alkyl side-group length from 2-octyldodecyl to 2-hexyldecyl, with the only exception seen in the case of an increase in FF from PNDI-T10$_{High}$ to P(NDI2HD-T10), that possibly could stem from an almost 30% decrease in J_{sc} for said system.

However, despite N2300 having only a marginally lower $\overline{M}_n$ than that of N2200*, the efficiency is still observed to lag that of its 2-octyldodecyl counterpart. PCEs of the two systems are 4.48% and 3.73% for N2200* and N2300 respectively, showing decrease of ~20% for shorter alkyl side-groups. This difference between N2200* (2-octyldodecyl) and N2300 (2-hexyldecyl), originating from a lower V_{oc} and FF, corresponds well with the data collected for the other systems. Though, it must be noted that the J_{sc} of 14.59 mA cm^{-2} was the highest measured for any of these devices. Conversely, the results in this study for said system conflicts results of an earlier study of the alkyl side-group length by Lee *et al.*, who concluded that for N2200 derivatives the 2-hexyldecyl side-groups were superior to the longer 2-octyldodecyl and 2-decyltetradecyl side-groups.[29] This difference, stemming from increases in J_{sc}, also seen in this study, was attributed to crystalline face-on orientation and finely phase separated domains. Lower $\overline{M}_n$ and different processing conditions in the study by Lee *et al.* could greatly influence the PCE. It is therefore plausible that the high molecular weight and low solubility experienced in this study could result in a different morphology for the N2300 containing devices. For example, the higher J_{sc} and lower V_{oc} indicates that the N2300 active layers could possess a smaller domain size than the N2200* counterpart. Furthermore, the V_{oc} remains about 0.1 V lower when comparing to the remainder of the systems, with only the very low molecular weight P(NDI2HD-14T2) experiencing a comparable V_{oc}. Though, the lower PCE of N2300 is not unexpected the record PCEs for all-polymer solar cells with this polymer has reached over 6% in cases where no thermal treatment or solvent additive had been utilised.[19, 30] As mentioned earlier in the chapter, N2200 record PCEs sits at above 10%, highlighting a major difference in the literature. For PTB7-Th:N2200 devices the record efficiencies are 9.27% and 5.7% for ternary blends and two component BHJ single layer devices respectively.[19, 31-32] This is slightly higher than achieved in this project, with differences potentially arising processing conditions, device architectures or molecular weights.
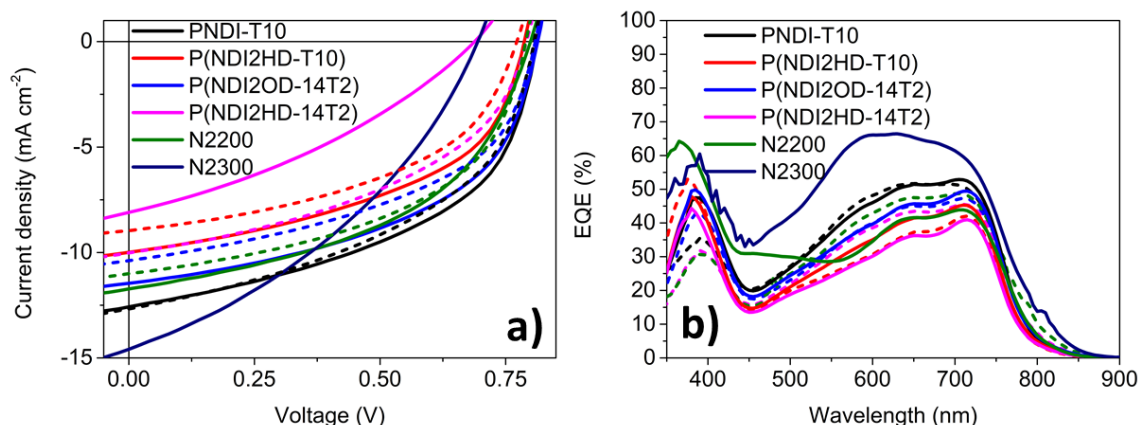
Figure 5.8: a) I-V curves and b) EQE curves for the best performing spin coated (solid) and blade coated (dotted) devices.

Interestingly, the BC devices with P(NDI2HD-14T2) vastly outperform the SC devices with PCEs of 3.55% and 1.91%, respectively. Where the molecular weight of P(NDI2HD-14T2) is the lowest of all polymers at 12.7 kg mol^{-1}. Similarly, PNDI-T10$_{Low}$ with a molecular weight of 21 kg mol^{-1}, experienced PCEs of 4.10% and 3.58% for BC and SC devices respectively. The opposite trend is clearly observed in Figure 5.7 for the polymers of higher molecular weight. This indicates that, for at least these active layer systems, BC is molecular weight insensitive compared to SC, which appears to show a larger dependence on the molecular weight of the acceptor component. It is theorised that a lower side-group to conjugated backbone ratio could be used for BC devices due to this molecular weight insensitivity, possibly contributing to a better performance at low molecular weights.

At 10% substitution of the 2,2'-bithiophene in N2200* with thiophene (PNDI-T10$_{High}$) an increase in PCE could be seen for both SC and BC devices. Similarly, an increase was seen for 3,3'-ditetradecyl-2,2'-bithiophene substitution (P(NDI2OD-14T2)) for SC devices, however, the BC devices possess a ~7% lower PCE than their N2200* counterpart. Taking the molecular weight into account it became clear that the PCEs of PNDI-T10 and P(NDI2OD-14T2) are highly promising, Figure 5.7. On the other hand, the results for N2300 derivatives with 2-hexyldecyl side-groups are inconclusive, with the N2300 BC devices omitted and the P(NDI2HD-14T2) SC devices for which the low $\overline{M}_n$ of ~13 kg mol^{-1} contributes to a lowest PCE out of all the systems at 1.91%. Overall the substitutions have led to polymers with on-par or higher efficiencies than the original N2200*/N2300 2,2'-bithiophene polymers.

Table 5.3: Photovoltaic performance for the acceptor polymers PNDI-T10, P(NDI2HD-T10), P(NDI2OD-14T2), P(NDI2HD-14T2), and N2300 with the donor polymer PTB7-Th.[a]

BHJ	Processing conditions	J_{sc} [mA cm^{-2}]	V_{oc} [V]	FF [%]	PCE [%]
PTB7-Th:PNDI-T10) (low)	SC (4000 rpm)	11.40	0.73	43	3.58
	BC (80 mm s^{-1})	10.78	0.79	48	4.10
PTB7-Th:PNDI-T10) (high)	SC (6000 rpm)	12.58	0.81	49	5.04
	BC (40 mm s^{-1})	12.67	0.81	46	4.74
PTB7-Th:P(NDI2HD-T10)	SC (6000 rpm)	9.99	0.79	48	3.79
	BC (20 mm s^{-1})	8.96	0.77	48	3.28
PTB7-Th: P(NDI2OD-14T2)	SC (3000 rpm)	11.46	0.81	50	4.68
	BC (60 mm s^{-1})	10.39	0.81	48	4.06
PTB7-Th: P(NDI2HD-14T2)	SC (3000 rpm)	8.10	0.69	34	1.91
	BC (60 mm s^{-1})	10.02	0.79	45	3.55
PTB7-Th:N2200*	SC (800 rpm)	11.73	0.79	48	4.48
	BC (mm s^{-1})	11	0.79	50	4.36
PTB7-Th:N2300	SC (1000 rpm)	14.59	0.69	37	3.73
	-	-	-	-	-

[a]Mean values from a minimum of four devices.

5.5 Conclusion

In summary, three new NDI-2,2'-bithiophene/thiophene/3,3'-ditetradecyl-2,2'-bithiophene based statistical copolymers (P(NDI2HD-T10), P(NDI2OD-14T2), and P(NDI2HD-14T2)) were synthesised. These were complemented by the previously published PNDI-T10, N2200, and N2300, and successfully applied in inverted all-polymer solar cells, exploring 2-octyldodecyl vs 2-hexyldecyl side-groups and the partial substitution of 2,2'-bithiophene in the backbone.

PNDI-T10, P(NDI2OD-14T2), and N2200* were the highest performing polymers from each category with PCEs of 5.04%/4.74%, 4.68%/4.06%, and 4.48%/4.36% (SC/BC) respectively. Thus, the 2-octyldodecyl compounds performed better than their 2-hexyldecyl counterparts, but with this difference correlating relatively well with the molecular weights of the polymers it remains unclear if these results would be comparable at equal molecular weights. PCEs are lower than previously published results for all-polymer solar cells, not utilising thermal annealing or solvent additives, but provide a good starting point for further exploration of the new systems. However, the difference in polymer batches could possibly explain any variations in efficiencies.

Incorporation of 10% thiophene or 10% BT-14C yielded PCEs on-par or better than for pure NDI-2,2'-bithiophene copolymers for the 2-octyldodecyl systems, while the data available for the 2-hexyldecyl systems proved insufficient to draw any further conclusions. P(NDI2OD-14T2), showing the second highest PCE, is the most soluble polymer in MeTHF, THF, and *o*-Xylene, and therefore a good contender for processing in greener solvents and further testing in scalable fabrication.

Interestingly, blade coating appeared more molecular weight insensitive than spin coating in regard to PCE, outperforming the small-scale technique at lower molecular weights but with opposing results observed at higher molecular weights. This could favour the use of non-chlorinated greener solvents due to an increased solubility in these solvents by lower molecular weight polymers. It is also positive from a synthesis perspective for which the complexity is lowered with the lowered demand of high molecular weight polymers for high performance devices.

Future prospects for this group of acceptor polymers are promising. Especially so for P(NDI2OD-14T2), for which all-polymer solar cell devices processed from greener solvents in fully scalable fabrication methods already are close to being a reality. Though, to fully evaluate the choice of side-groups and elucidate the effect of the molecular weight on the performance, a more extensive study is required. Additionally, the percentage of substitution, or loading, of 3,3'-ditetradecyl-2,2'-bithiophene in the polymer backbone was outside the scope of this study and should be investigated for determination of an optimal loading with regards to PCE as well as solubility.

5.6 Contributions

Dr. Chao Wang: *Performed device fabrication and testing for all-polymer solar cells.*

Dr. Anders Mårtensson: *Performed High temperature GPC measurements and analysis.*

Prof. Mats R. Andersson: *Assisted in material design/development as well as interpretation of solar cell device data.*

5.7 References

(1)   Zheng, Z.; Hu, Q.; Zhang, S.; Zhang, D.; Wang, J.; Xie, S.; Wang, R.; Qin, Y.; Li, W.; Hong, L.; Liang, N.; Liu, F.; Zhang, Y.; Wei, Z.; Tang, Z.; Russell, T. P.; Hou, J.; Zhou, H., A Highly Efficient Non-Fullerene Organic Solar Cell with a Fill Factor over 0.80 Enabled by a Fine-Tuned Hole-Transporting Layer. *Adv. Mater.* **2018**, 1801801.

(2)   Yao, H.; Bai, F.; Hu, H.; Arunagiri, L.; Zhang, J.; Chen, Y.; Yu, H.; Chen, S.; Liu, T.; Lai, J. Y. L.; Zou, Y.; Ade, H.; Yan, H., Efficient All-Polymer Solar Cells based on a New Polymer Acceptor Achieving 10.3% Power Conversion Efficiency. *ACS Energy Lett.* **2019**, 417-422.

(3)   Wang, G.; Melkonyan, F. S.; Facchetti, A.; Marks, T. J., All-Polymer Solar Cells: Recent Progress, Challenges, and Prospects. *Angew. Chem., Int.* **2019**, 131, 2–16.

(4)   Chen, Z.; Zheng, Y.; Yan, H.; Facchetti, A., Naphthalenedicarboximide- vs Perylenedicarboximide-Based Copolymers. Synthesis and Semiconducting Properties in Bottom-Gate N-Channel Organic Transistors. *J. Am. Chem. Soc.* **2009**, 131, 8-9.

(5)   Fan, B.; Ying, L.; Zhu, P.; Pan, F.; Liu, F.; Chen, J.; Huang, F.; Cao, Y., All-Polymer Solar Cells Based on a Conjugated Polymer Containing Siloxane-Functionalized Side Chains with Efficiency over 10%. *Adv. Mater.* **2017**, 29, 1703906.

(6)   Zhou, N.; Facchetti, A., Naphthalenediimide (NDI) Polymers for All-polymer Photovoltaics. *Mater. Today* **2018**, 21, 377-390.

(7)   Genene, Z.; Mammo, W.; Wang, E.; Andersson, M. R., Recent Advances in n-Type Polymers for All-Polymer Solar Cells. *Adv. Mater.* **2019**, 1807275.

(8)   You, H.; Kim, D.; Cho, H.-H.; Lee, C.; Chong, S.; Ahn, N. Y.; Seo, M.; Kim, J.; Kim, F. S.; Kim, B. J., Shift of the Branching Point of the Side-Chain in Naphthalenediimide (NDI)-Based Polymer for Enhanced Electron Mobility and All-Polymer Solar Cell Performance. *Adv. Funct. Mater.* **2018**, 28, 1803613.

(9)   Li, Z.; Xu, X.; Zhang, W.; Meng, X.; Ma, W.; Yartsev, A.; Inganäs, O.; Andersson, M. R.; Janssen, R. A. J.; Wang, E., High Performance All-Polymer Solar Cells by Synergistic Effects of Fine-Tuned Crystallinity and Solvent Annealing. *J. Am. Chem. Soc.* **2016**, 138, 10935-10944.

(10)   Li, Z.; Xu, X.; Zhang, W.; Meng, X.; Genene, Z.; Ma, W.; Mammo, W.; Yartsev, A.; Andersson, M. R.; Janssen, R. A. J.; Wang, E., 9.0% Power Conversion Efficiency from Ternary All-polymer Solar Cells. *Energy Environ. Sci.* **2017**, 10, 2212-2221.

(11)   Lin, Y.; Dong, S.; Li, Z.; Zheng, W.; Yang, J.; Liu, A.; Cai, W.; Liu, F.; Jiang, Y.; Russell, T. P.; Huang, F.; Wang, E.; Hou, L., Energy-effectively Printed All-polymer Solar Cells Exceeding 8.61% Efficiency. *Nano Energy* **2018**, 46, 428-435.

(12)   Jung, J. W.; Jo, J. W.; Chueh, C.-C.; Liu, F.; Jo, W. H.; Russell, T. P.; Jen, A. K.-Y., Fluoro-Substituted n-Type Conjugated Polymers for Additive-Free All-Polymer Bulk Heterojunction Solar Cells with High Power Conversion Efficiency of 6.71%. *Adv. Mater.* **2015**, 27, 3310-3317.

(13)   Guo, X.; Liao, Q.; Manley, E. F.; Wu, Z.; Wang, Y.; Wang, W.; Yang, T.; Shin, Y.-E.; Cheng, X.; Liang, Y.; Chen, L. X.; Baeg, K.-J.; Marks, T. J.; Guo, X., Materials Design via Optimized Intramolecular Noncovalent Interactions for High-Performance Organic Semiconductors. *Chem. Mater.* **2016**, 28, 2449-2460.

(14)   Chen, J.; Liao, Q.; Wang, G.; Yan, Z.; Wang, H.; Wang, Y.; Zhang, X.; Tang, Y.; Facchetti, A.; Marks, T. J.; Guo, X., Enhancing Polymer Photovoltaic Performance via Optimized Intramolecular Ester-Based Noncovalent Sulfur···Oxygen Interactions. *Macromolecules* **2018**, 51, 3874-3885.

(15)   Huang, H.; Zhou, N.; Ortiz, R. P.; Chen, Z.; Loser, S.; Zhang, S.; Guo, X.; Casado, J.; López Navarrete, J. T.; Yu, X.; Facchetti, A.; Marks, T. J., Alkoxy-Functionalized Thienyl-Vinylene Polymers for Field-Effect Transistors and All-Polymer Solar Cells. *Adv. Funct. Mater.* **2014**, 24, 2782-2793.

(16)   Zhao, K.; Hu, H.; Spada, E.; Jagadamma, L. K.; Yan, B.; Abdelsamie, M.; Yang, Y.; Yu, L.; Munir, R.; Li, R.; Ndjawa, G. O. N.; Amassian, A., Highly Efficient Polymer Solar Cells with Printed Photoactive Layer: Rational Process Transfer from Spin-coating. *J. Mater. Chem. A* **2016**, 4, 16036-16046.

(17)   Bazan, G. C., Over 9% Efficiency Achieved for All-polymer Solar Cells Processed by a Green Solvent. *Sci. China: Chem.* **2017**, 60, 1109-1110.

(18)   Fan, B.; Ying, L.; Wang, Z.; He, B.; Jiang, X.-F.; Huang, F.; Cao, Y., Optimisation of Processing Solvent and Molecular Weight for the Production of Green-solvent-processed All-polymer Solar Cells with a Power Conversion Efficiency over 9%. *Energy Environ. Sci.* **2017**, 10, 1243-1251.

(19)   Lee, W.; Lee, C.; Yu, H.; Kim, D.-J.; Wang, C.; Woo, H. Y.; Oh, J. H.; Kim, B. J., Side Chain Optimization of Naphthalenediimide–Bithiophene-Based Polymers to Enhance the Electron Mobility and the Performance in All-Polymer Solar Cells. *Adv. Funct. Mater.* **2016**, 26, 1543-1553.

(20)   Sasikumar, M.; Suseela, Y. V.; Govindaraju, T., Dibromohydantoin: A Convenient Brominating Reagent for 1,4,5,8-Naphthalenetetracarboxylic Dianhydride. *Asian J. Org. Chem.* **2013**, 2, 779-785.

(21)   Fan, B.; Zhu, P.; Xin, J.; Li, N.; Ying, L.; Zhong, W.; Li, Z.; Ma, W.; Huang, F.; Cao, Y., High-Performance Thick-Film All-Polymer Solar Cells Created Via Ternary Blending of a Novel Wide-Bandgap Electron-Donating Copolymer. *Adv. Energy Mater.* **2018**, 8.

(22)   Li, S.; Zhang, H.; Zhao, W.; Ye, L.; Yao, H.; Yang, B.; Zhang, S.; Hou, J., Green-Solvent-Processed All-Polymer Solar Cells Containing a Perylene Diimide-Based Acceptor with an Efficiency over 6.5%. *Adv. Energy Mater.* **2016**, 6, 1501991.

(23)   Zhou, L.; He, X.; Lau, T.-K.; Qiu, B.; Wang, T.; Lu, X.; Luszczynska, B.; Ulanski, J.; Xu, S.; Chen, G.; Yuan, J.; Zhang, Z.-G.; Li, Y.; Zou, Y., Nonhalogenated Solvent-Processed All-Polymer Solar Cells over 7.4% Efficiency from Quinoxaline-Based Polymers. *ACS Appl. Mater. Interfaces* **2018**, 10, 41318-41325.

(24)   Kang, H.; Kim, K.-H.; Choi, J.; Lee, C.; Kim, B. J., High-Performance All-Polymer Solar Cells Based on Face-On Stacked Polymer Blends with Low Interfacial Tension. *ACS Macro Lett.* **2014**, 3, 1009-1014.

(25)   Cho, H.-H.; Cho, C.-H.; Kang, H.; Yu, H.; Oh, J. H.; Kim, B. J., Molecular Structure-device Performance Relationship in Polymer Solar Cells based on Indene-C60 Bis-adduct Derivatives. *Korean J. Chem. Eng.* **2015**, 32, 261-267.

(26)   Ye, L.; Collins, B. A.; Jiao, X.; Zhao, J.; Yan, H.; Ade, H., Miscibility–Function Relations in Organic Solar Cells: Significance of Optimal Miscibility in Relation to Percolation. *Adv. Energy Mater.* **2018**, 8, 1703058.

(27)   E1171-15, A., Standard Test Methods for Photovoltaic Modules in Cyclic Temperature and Humidity Environments. In ASTM International, **2015**.

(28)   Sankaran, S.; Glaser, K.; Gärtner, S.; Rödlmeier, T.; Sudau, K.; Hernandez-Sosa, G.; Colsmann, A., Fabrication of Polymer Solar Cells from Organic Nanoparticle Dispersions by Doctor Blading or Ink-jet Printing. *Org. Electron.* **2016**, 28, 118-122.

(29)   Lee, C.; Kang, H.; Lee, W.; Kim, T.; Kim, K.-H.; Woo, H. Y.; Wang, C.; Kim, B. J., High-Performance All-Polymer Solar Cells Via Side-Chain Engineering of the Polymer Acceptor: The Importance of the Polymer Packing Structure and the Nanoscale Blend Morphology. *Adv. Mater.* **2015**, 27, 2466-2471.

(30)   Jung, J.; Lee, W.; Lee, C.; Ahn, H.; Kim, B. J., Controlling Molecular Orientation of Naphthalenediimide-Based Polymer Acceptors for High Performance All-Polymer Solar Cells. *Adv. Energy Mater.* **2016**, 6, 1600504.

(31)   Mori, D.; Benten, H.; Okada, I.; Ohkita, H.; Ito, S., Highly efficient charge-carrier generation and collection in polymer/polymer blend solar cells with a power conversion efficiency of 5.7%. *Energy Environ. Sci.* **2014**, 7, 2939-2943.

(32)   Li, Z.; Fan, B.; He, B.; Ying, L.; Zhong, W.; Liu, F.; Huang, F.; Cao, Y., Side-chain modification of polyethylene glycol on conjugated polymers for ternary blend all-polymer solar cells with efficiency up to 9.27%. *Sci. China: Chem.* **2018**, 61, 427-436.

Chapter 6 – Facile Synthesis of an Efficient and Robust Cathode Interface Material for Polymer Solar Cells

.

This chapter is a modified version of the published article *Facile Synthesis of an Efficient and Robust Cathode Interface Material for Polymer Solar Cells* (adapted with permission from (*ACS Appl. Energy Mater.* 2018, 1, 12, 7130-7139) Copyright 2019 American Chemical Society) with additional experiments and measurements added. These include; measurements of the work function of samples in the ageing/stability study, photodoping experiments conducted on the PNDIT10N polymer, and AFM measurements of ITO/PNDIT10N, ITO/PNDIT10N/TQ1:PC$_{71}$BM, and ITO/PNDIT10N/TQ1:PC$_{71}$BM with solvent additive.

6.1 Overview

In this chapter, an alcohol soluble novel naphthalene diimide (NDI)-thiophene based cathode interface layer (CIL), PNDIT10N, is reported. PNDIT10N was synthesised in a facile three-step method, processed from environmentally friendly benzyl alcohol (BnOH) and employed in inverted polymer solar cells (PSCs). The three polymer donors TQ1, PTNT and PTB7-Th were paired with the fullerene acceptor $PC_{71}BM$ for bulk heterojunction (BHJ) layers to evaluate the CIL. The modification of the indium tin oxide (ITO) electrode with a ~3 nm thin layer of PNDIT10N yielded a significant reduction of 0.8 eV in the work function, reducing it from 4.6 eV to 3.8 eV, effectively transforming ITO to a functioning cathode. PSCs with $TQ1:PC_{71}BM$ BHJ layer and incorporating PNDIT10N interlayer were found to have a high J_{sc} of 10.5 mA cm^{-2}, V_{oc} of 909 mV and a FF of 68 % resulting in a highest PCE of 6.7 % for TQ1 donor in inverted device structure. Of note, the interface layer showed a good stability in ambient atmosphere for a 10-day indoor ageing period, both in darkness and exposed to direct sunlight. Additionally, flexible PSCs incorporating slot-die coated PNDIT10N, processed from a BnOH-acetone solution, and BHJ layer in air achieved a PCE of 1.6%.
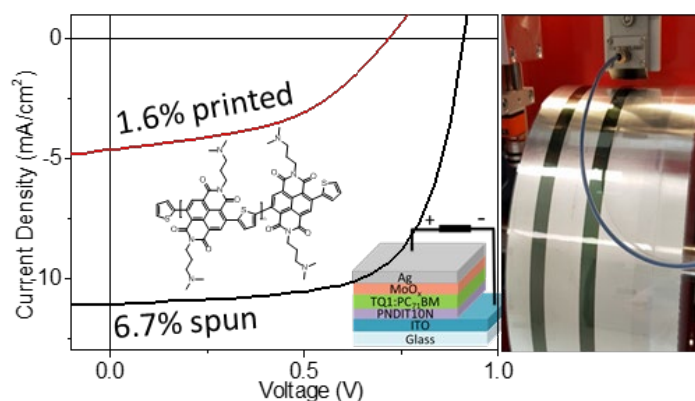
6.2 Introduction

Interface materials play an important role in device engineering as one of the main strategies used to increase efficiencies. The incorporation of an interface layer can significantly improve the collection of electrons or holes at the respective cathode or anode. For organic interface materials with pendant amino side-groups a twofold effect can be realised. The ability to i) modify the work functions of common metal and metal-oxide electrodes, e.g. ITO, metallic silver (Ag), and aluminium (Al), as well as ii) provide increased solubility in green solvents caused by the highly polar/hydrophilic side-groups.[9-10] Poly [(9,9-bis(3'-(N,N-dimethylamino)propyl)-2,7-fluorene)-alt-2,7-(9,9–dioctylfluorene)] (PFN), polyethyleneimine (PEI), and polyethylenimine ethoxylated (PEIE) are three examples of organic interface materials, which were processed from green solvents, that have contributed to increased PCEs.[11-13] This type of amino containing material is not inherently soluble in water and alcohols. However, improvement to the solubility has been achieved through the addition of trace amounts of low boiling point acids, as solvent additives, during processing.[14-19] Additional strategies for increasing the solubility include the conversion of tertiary amine groups to quaternary amine salts or to zwitterionic *N*-oxides, which both possess high solubility in water.[20-21] The *N*-oxide, much like the amino groups, interacts strongly with many common electrodes, modifying the work function. These new types of interface materials combine high efficiencies with green solvent processing. However, the existing library of materials, though promising, is still relatively small requiring further effort within the development of new interface layers for potential commersialisation.[22-27]

In this work, we present the synthesis and application of a novel versatile polymer poly[N,N'-bis(3-dimethylaminopropyl)naphthalene-1,4,5,8-bis(dicarboximide)-2,6-diyl]-alt-2,5-thiophene) (PNDIT10N), Scheme 1, as a cathode interface layer (CIL), which is processed from alcohol. PNDIT10N is synthesised in a facile three-step process utilising relatively low cost, commercially available materials. The polymer possesses a good solubility in benzyl alcohol (BnOH) but is close to insoluble in many of the organic solvents commonly used for bulk heterojunction (BHJ) layer processing. Thus, proves to be an excellent candidate for orthogonal solvent processing. PNDIT10N is processed from BnOH at ambient temperatures as a direct replacement for zinc oxide (ZnO), which is a commonly used inorganic CIL. As a comparison, ZnO is either processed from a zinc acetate solution, requiring high annealing temperatures, or deposited from nanoparticle ink.[28-30] The photovoltaic performance of PNDIT10N CIL is studied in inverted configuration for ITO/PNDIT10N/BHJ layer/molybdenum oxide (MoO_x)/Ag systems. This is due to the better stability offered by inverted device configuration in comparison with conventional devices, providing an advantage for upscaling via roll-to-roll processing under ambient conditions.[31] The efficacy of PNDIT10N as a CIL has been tested and is reported in this work for a range of donor-acceptor systems namely poly[2,3-bis-(3-octyloxyphenyl)quinoxaline-5,8-diyl- alt -thiophene-2,5-diyl] (TQ1): [6,6]-phenyl-C_{71}-butyric acid methyl ester ($PC_{71}BM$), poly[2,5-thiophene-alt-4,9-bis(2-hexyldecyl)-4,9-dihydrodithieno[3,2-c:3′,2′-

h][1,5]naphthyridine-5,10-dione] (PTNT):PC$_{71}$BM, and poly[4,8-bis(5-(2-ethylhexyl)thiophen-2-yl)benzo[1,2-b;4,5-b']dithiophene-2,6-diyl-alt-(4-(2-ethylhexyl)-3-fluorothieno[3,4-b]thiophene-)-2-carboxylate-2-6-diyl)] (PTB7-Th):PC$_{71}$BM. The changes in the device performance as a function of PNDIT10N ageing has also been systematically studied. To further demonstrate the applicability of PNDIT10N in printed PSCs, we also report the application of PNDIT10N in partially printed flexible PSCs incorporating slot-die coated PNDIT10N and TQ1: [6,6]-phenyl-C$_{61}$-butyric acid methyl ester (PC$_{61}$BM), BHJ layer.

6.3 Experimental

6.3.1 Synthesis

All solvents, reagents and catalysts were purchased from commercial sources and used as received, with the exception of toluene, which was dried on molecular sieves and distilled prior to use in synthesis. The synthesis of DANDI[32] and diBrDANDI[33-34] are based on on modified literature procedures.

6.3.1.1 DANDI

1,4,5,8-Naphthalenetetracarboxylic dianhydride (NTCDA) (Sigma-Aldrich) (0.8 g, 3 mmol) and water (10 mL) were added to a microwave vial (35 mL) with pressure regulating lid. 3-dimethylamino-1-propylamine (0.67 g, 6.6 mmol) was added dropwise to the vial upon which the colour started changing from grey-brown to yellow indicating that the start of the reaction. The resulting slurry was stirred vigorously for 10 minutes and then sonicated for an additional 10 minutes prior to reaction in the Discover SP microwave (CEM). The reaction mixture was heated to 50 ºC with the microwave at a power of 100 W, this temperature was then held for 5 seconds prior to reaction end. This resulted in the formation of a solid which was filtered off and washed several times ethanol. The material was dried and collected as a yellow-golden solid. Yield: 1.19 g (92%).

^{1}H NMR (CDCl$_3$, 600 MHz) δ: 8.76 (s, 4H), 4.27 (t, J = 7.5 Hz, 4H), 2.44 (t, J = 7.1 Hz, 4H), 2.23 (s, 12H), 1.92 (dd, J = 7.3, 7.2 Hz, 4H). MS calcd. for C$_{24}$H$_{28}$N$_4$O$_4$ [[M+H]$^{+}$]: m/z = 437.21102; DSA-TOF exp. 437.2185.

6.3.1.2 diBrDANDI

DANDI (3 g, 6.9 mmol) was dissolved in 9 mL 98 % sulphuric acid under stirring in a 100 mL round-bottom flask (RBF). Dibromantin (Sigma-Aldrich, 98%) (1.97 g, 6.9 mmol) was divided in to four portions which were added at 12 hour intervals. The RBF was tightly stoppered upon addition of the first portion and the temperature was raised to 50 ºC. This procedure was repeated for the remaining three portions. The reaction mixture was, after a total reaction time of 48 hours, poured on crushed ice and then neutralised with sodium hydroxide pellets. The colour of the solution went from a strong yellow to grey-brown and material started precipitating. The grey-brown suspension was extracted with chloroform 3 times leaving a strong red solution. The chloroform solution was dried over potassium

sulphate and then concentrated on a rotary evaporator. After purification by column chromatography (19:1 chloroform: triethylamine) a red-orange solid was obtained. Yield: 2.26 g (55%).

^{1}H NMR (CDCl$_3$, 600 MHz) δ: 9 (s, 2H), 4.27 (t, J = 7.5 Hz, 4H), 2.49 (t, J = 7 Hz, 4H), 2.26 (s, 12H), 1.95 (dd, J = 7.3, 7.1 Hz, 4H). MS calcd. for C$_{24}$H$_{26}$N$_4$O$_4$Br$_2$ [[M+H]$^+$]: m/z = 593.03987; MALDI-TOF 591.04 exp, DSA-TOF 593.0376 exp.

6.3.1.3 PNDIT10N

diBrDANDI (1 g, 1.6826 mmol), 2,5-bis(trimethylstannyl)thiophene (Sigma-Aldrich, 97%) (0.6268 g, 1.5297 mmol), tris(dibenzylideneacetone)dipalladium(0) (Sigma-Aldrich, 97%) (0.0308 g, 0.0337 mmol) and tri(o-tolyl)phosphine (Sigma-Aldrich, 97%) (0.0616 g, 0.2025 mmol) were added to a 100 mL dry two-necked RBF upon which it was flushed with nitrogen five times. 50 mL of dry toluene (Chem-Supply) was added by syringe through a septum. The RBF was lowered in to a 120 ºC preheated oil bath and was covered from light, the reaction mixture was heated under vigorous stirring for 24 hours. 2-(tributylstannyl)thiophene (0.6279 g, 1.6826 mmol) was added for endcapping and the reaction was continued for an additional hour. The reaction mixture was allowed to cool to ambient temperature and was then poured on 200 mL of hexane. The precipitated material, a fine dark purple powder, was filtered and collected. Soxhlet extraction was performed for 24 hours for each of the solvents; hexane, acetone, methanol, ethyl acetate and chloroform. The chloroform fraction was poured on hexane and precipitated product was collected using a polymer filtration setup with a PTFE membrane, yielding a dark purple material. Yield: 0.41 g (38%).

^{1}H NMR (CDCl3, 600 MHz) δ: 8.95 (m, 1H), 8.93 (s, 1H), 8.78 (s, 1H), 7.59 (d, J = 5.1 Hz, 1H), 7.46 (m, 2H), 4.22 (m, 8H), 2.42 (m, 8H), 2.23 (s, 24H), 1.91 (m, 12H), 1.42 (s, 1H), 0.85 (m, 6H).

High molecular weight fraction (processing): The remaining polymer (~30% of theoretical yield) was collected and stirred in a methanol-formic acid solution 9:1 (40 mL) under nitrogen atmosphere for 48 hours. The solution was filtered, and the product was then precipitated in a 2-propanol-triethylamine solution 10:1 (165 mL). The resulting suspension was filtered off using a polymer filtration setup with a PTFE membrane and washed with 150 mL of the following solvents; methanol, 2-propanol and acetone, yielding additional dark purple solid. Yield: 0.15 g (14%). This adds up to a total yield for both fractions of 52% (38% + 14%).

Donor & acceptor polymers

TQ1 and PTNT were all synthesised according to previously published procedures.[35-36]

6.3.2 Film characterisation

Neutral impact collision ion scattering spectroscopy (NICISS) measurements were carried out to determine film thicknesses. PNDIT10N solutions (0.50, 1.0, 5.0, and 10 mg mL^{-1} in BnOH) were spun on 1 cm square ITO-coated glass substrates following the same procedure as for device fabrication. The

NICISS measurement was carried out on a machine designed for ion scattering using beam energy of up to 10 keV with a current density around 0.1 μA/mm^2 of the pulsed ion beam. The ion beam energy used here was 3 keV and the ions incident direction was normal to the solid surfaces. The ion beam was chopped into pulses with period of 20 μs with a duty cycle of less than 0.1% for time-of-flight analyses. The back scattered projectiles are almost all in a neutral state and were detected by microchannel plates with a deflection angle of 168° and the anode pulses were then registered as digital signals by a multichannel analyser. The blank ITO surface was bombarded with the non-pulsed ion beam and large beam spot for 20 minutes to remove potential contamination. The total dose was approximately $1 \cdot 10^{16}$ He$^+$ cm^{-2}. The kinetic energy of the helium ion projectiles (He$^+$) employed (~3 keV) yields a detection depth up to 300 Å with a resolution of ~3 Å.

The energy loss during the transport of a projectile through a material can be described with the concept of stopping-power, that is, the energy loss of a projectile caused by the interactions between projectile and medium, resulting in deceleration of the projectile. The relation of thickness d and energy loss ΔE, caused by stopping-power Sp, can be describe by

$$\Delta E = Sp \times d/(1 + 1/\cos(12°)). \qquad (6.1)$$

The stopping-power for low energy ion scattering has been determined on self-assembled alkanethiolate monolayer of known thickness.[37]

6.3.3 Material characterisation

Static contact angle of deionized water against the surfaces was measured using a PAT-1 tensiometer (Sinterface Technologies, Germany). Reported contact angles are average values over four measurements on different areas of the films Cleaning of ITO-coated glass substrates (10 Ω/sq, Xin Yan Technology LTD) follow the procedure described under *4.3.4 Device fabrication* in Chapter 4. Deposition of CIL follow the same procedure as described under Device fabrication with the exception of deposition volume (200 μL) due to larger substrates (3 x 3 cm). DANDI was deposited from chloroform (5 mg mL^{-1}, 200 μL) and spin coated at 3000 rpm for 60 seconds. An *o*-DCB wash was applied to PNDIT10N by spin coating *o*-DCB (200 μL) at 500 rpm for 60 seconds followed by 2000 rpm for 30 seconds.

Simultaneous thermal analysis (STA) was performed on a PerkinElmer Simultaneous Thermal Analyzer 8000. Measurements were conducted on pure PNDIT10N samples from 25- 400 ºC at a scan rate of 10 ºC/minute. Samples were dried in a vacuum oven at 25ºC for 24 hours prior to the measurement. Samples were then further dried in the instrument under a nitrogen stream at 25 ºC for 30 minutes.

Optical absorption spectra of the samples were recorded for both solution and thin film on a Perkin Elmer Lambda 950 spectrophotometer at a scan rate of 5 nm s^{-1}. Additional absorption spectra were

recorded at 5 nm s^{-1} for thin films prior to as well as after illumination. These thin films were stored in darkness for a minimum of 48 hours before the measurement, and then illuminated with a handheld UV lamp (UVGL-58, UVP) with light of a wavelength of 365 nm prior to being remeasured. This procedure was repeated three times for a combined illumination time of 30 min. PNDIT10N solutions with concentrations of 0.50, 1.0, 5.0, and 10 mg/mL were prepared by dissolving the polymer in BnOH at 80 ºC over the course of 1 hour. Glass substrates of 1 inch square and patterned ITO-coated glass substrates were cleaned following the procedure described under device fabrication. Transmittance measurements were carried out for thin films spin coated on patterned ITO-coated device substrates. These films were prepared, using the same procedure as for devices, that is from concentrations of 0.50, 1.0, 5.0, and 10 mg/mL, yielding Films 0.5, 1, 5, and 10, see NICISS section and Figure 6.1a for thicknesses. Solution spectra were measured for dilute BnOH solutions.

Square-wave voltammetry (SWV) measurements were carried out for determination of reduction/oxidation potentials, and in turn highest occupied molecular orbital (HOMO)/ lowest unoccupied molecular orbital (LUMO) energy levels. An AUTOLAB PGSTAT (Metrohm AG) using a three-electrode setup with platinum wires, both for working electrode and counter electrode and a Ag/Ag$^+$ reference electrode were used. A 0.10 M solution of tetrabutylammonium hexafluorophosphate (Bu$_4$NPF$_6$) in anhydrous acetonitrile was used as supporting electrolyte. The recorded square wave voltammograms were referred to ferrocene/ferrocenium (Fc/Fc$^+$) by analysing the Fc/Fc$^+$ couple after each measurement. The working electrode was coated with polymer film by dipping it into the respective solutions. PNDIT10N sample was processed from BnOH:chloroform (CHCl$_3$) solution in 1:19 solvent volume ratio, while all other polymers were coated from CHCl$_3$ solutions. The electrolyte was purged with nitrogen gas for a minimum of 10 minutes prior to each measurement. During the measurements, the electrolyte solution surface was kept under nitrogen atmosphere to ensure inert conditions. Energy levels of the materials were calculated by setting the peak potential of Fc/Fc$^+$ vs the normal-hydrogen electrode (NHE) to 0.630 V and the NHE vs the vacuum level to 4.5 V.[38-40] That is $E_{HOMO} = -(E_{ox,maxima} + 5.13)$ and $E_{LUMO} = -(E_{red,maxima} + 5.13)$.

6.3.4 Electron spectroscopy

Ultraviolet photoelectron spectroscopy (UPS) measurements were performed in an ultra-high vacuum chamber built by SPECS (Germany), using a low intensity UV light (He I line) with an excitation energy of 21.21 eV. The spectra of photo-emitted electrons were recorded at a pass energy of 10 eV with a hemispherical analyser, at which the energy resolution of the analyser is 400 meV, as evaluated from the Fermi edge of polycrystalline silver. All measurements were performed with the base pressure of 10^{-10} mbar in the UHV chamber. The work function of the sample is determined as the difference between the excitation energy and the length of the spectrum.[41]

6.3.5 Device fabrication

CIL and BHJ layers were processed via spin coating as well as slot die coating. In both cases a MoO_x hole-transport layer (12 nm) was thermally evaporated on the BHJ layer using a Covap system (Angstrom Engineering). This was followed by the evaporation of a Ag electrode (80 nm) using a shadow mask, defining the active area to 0.1 cm^2. Devices were measured using an Oriel solar simulator fitted with a 150 W xenon lamp (Newport), filtered to give an output of 100 mW cm^{-2} at AM 1.5 (air mass) standard and calibrated using a silicon reference cell with NIST traceable certification.

Spin coated devices were fabricated in an ITO/CIL/BHJ layer/MoOx/Ag device configuration for the three BHJ layers of TQ1:PC_{71}BM, PTNT:PC_{71}BM, and PTB7-Th:PC_{71}BM. Cleaning of the patterned ITO-coated glass substrates (10 Ω sq^{-1}, Xin Yan Technology LTD) is described under *4.3.4 Device fabrication* in Chapter 4.

The PNDIT10N solutions were prepared by dissolving the polymer under vigorous stirring in benzyl alcohol (Sigma-Aldrich, ReagentPlus, >99%) at 80 °C over the course of 1 hour PNDIT10N was spincoated at 3000 rpm for 60 seconds upon which they were allowed to dry prior to active layer deposition.

The stability of PNDIT10N CIL was investigated in inert and ambient atmosphere for films stored in darkness versus films stored on benchtop with several hours of direct sunlight per day. These devices were fabricated in the same manner as described above with the exception of a 10-day storage period between CIL and BHJ layer deposition.

The ZnO solution was prepared according to previously published procedures[28]. Zinc acetate dihydrate (500 mg) (Sigma-Aldrich, 99.9%) and ethanolamine (Sigma-Aldrich, 99.5%, 140 mg) were dissolved under vigorous stirring overnight in 2-methoxyethanol (Sigma-Aldrich, 99.8%, 5 mL). The resulting solution was filtered with a PTFE syringe filter (0.45 µm) prior to being spun on cleaned ITO-coated glass substrates at 3000 rpm for 60 seconds, to give a thin film of ~ 25-30 nm. The formed film was annealed in a 280 ºC preheated furnace in air for 10 minutes.

6.3.5.1 BHJ Processing conditions

All BHJ solutions were prepared in a glovebox with inert (N_2) atmosphere.

TQ1:PC_{71}BM: TQ1 and PC_{71}BM were dissolved in a 1:2.5 weight ratio at 80 ºC under stirring for a minimum of 3 hours in 1,2-dichlorobenzene with addition of 2% v/v 1-chloronaphthalene (CN), offering a final concentration of 25 mg mL^{-1}. Films were then spun from the warm (80 ºC) solution at 500 rpm for 60 seconds followed by 2000 rpm for 30 seconds.

PTNT:PC_{71}BM: PTNT and PC_{71}BM were dissolved in a 1:2 ratio at 80 ºC under stirring for a minimum of 3 hours in 1,2-dichlorobenzene with addition of 2% v/v CN, offering a final concentration of 20 mg mL^{-1}. Films were then spun from the warm (80 ºC) solution at 1000 rpm for 60 seconds.

PTB7-Th:PC$_{71}$BM: PTB7-Th and PC$_{71}$BM were dissolved in a 1:1.5 ratio at 70 °C under stirring overnight in chlorobenzene with addition of 3% v/v 1,8-diiodooctane (DIO), offering a final concentration of 25 mg mL^{-1}. Films were then spun at 2000 rpm for 60 seconds.

6.3.5.2 Slot-die coating

Printed devices were fabricated in a PET/ITO/PNDIT10N/TQ1:PC$_{61}$BM/MoOx/Ag device configuration. The flexible ITO Electrode Roll (FOM Technologies) was attached to the FOM Polymer Solar Cell Mini Roll Coater (FOM Technologies) and wiped with 2-propanol soaked TeriWipes at a rotation speed of 2 m/minute. The tubing and slot-die coating head were washed with CHCl$_3$ prior to assembly and the slot-die coating head was disassembled for cleaning in between deposition of each layer. PNDIT10N ink was prepared by dissolving the polymer in BnOH (10 mg mL^{-1}) at 80 °C over the course of 1 hour. The resulting solution was cooled to 50 °C and acetone was added dropwise under vigorous stirring until a final concentration of 1 mg mL^{-1} was achieved. This ink was printed at an injection rate of 0.1 mL minute^{-1}, controlled with a syringe pump, for a drum speed of 2 m minute^{-1} and drum temperature of 45 °C. The active layer ink was prepared from TQ1:PC$_{61}$BM (30 mg mL^{-1}) in a 1:2 weight ratio in CHCl$_3$:o-DCB (20:80) with 2% v/v 1-chloronaphthalene (CN). The BHJ layer was printed at 0.1 mL minute^{-1} for a drum speed of 1 m minute^{-1} and a drum temperature of 70 °C. The wet and dry thickness PNDIT10N were calculated according to:

$$d_{wet} = \frac{f}{S\,w} \qquad\qquad (2)$$

and

$$d_{dry} = \frac{f}{S\,w}\,\frac{c}{\rho} \qquad\qquad (3)$$

where d is the thickness in cm, f is the flow rate in cm^3 min^{-1}, S is the drum rotation speed in cm min^{-1}, w is the meniscus guide width in cm, c is the solid content in the ink in g cm^{-3} and, ρ is the density of the dried coating in g cm^3.[42] The densities of all polymers were estimated at 1 g cm^{-3}. This resulted in a respective wet and dry thickness of 4 μm and 4 nm for PNDIT10N. Similarly the wet and dry thickness was calculated for the active layer to 8 μm and 195 nm respectively, for a PC$_{61}$BM density of 1.3 g cm^{-3}[43]. After deposition of the active layer the devices were transferred in to a glovebox for deposition of MoO$_x$ followed by Ag, as described earlier.

6.4 Results & discussion

6.4.1 Synthesis

The synthesis route for novel n-type polymer PNDIT10N is presented in Scheme 6.1. Monomer 4,9-Dibromo-2,7-bis[3-(dimethylamino)propyl]benzo[lmn][3,8]phenanthroline-1,3,6,8(2H,7H)-tetrone (diBrDANDI) was synthesised in a two-step process starting from the commercially available compound 1,4,5,8-Naphthalenetetracarboxylic dianhydride (NTCDA). Intermediate 2,7-bis[3-

(dimethylamino)propyl]-benzo[lmn][3,8]phenanthroline-1,3,6,8(2H,7H)-tetrone (DANDI) was synthesised according to modified literature procedures in a microwave reactor using water as the solvent.[44-45] This resulted in a facile reaction requiring minimum work-up, and filtering of crude product followed by an ethanol wash gave pure DANDI in excellent yield (94%), using only green solvents. DANDI was further converted in a second, and final step to diBrDANDI via bromination in concentrated sulphuric acid, using the brominating reagent dibromantin.[33-34] Structures of monomers and intermediates were all confirmed by ^{1}H NMR spectroscopy, see Figure A.24 and Figure A.25. Stille coupling copolymerisation of diBrDANDI and 2,5-bis(tributylstannyl)thiophene was finally performed with 10% excess of diBrDANDI, achieving CHCl$_3$ extracted PNDIT10N in 38% yield from Soxhlet extraction. However, this only takes into account the "lower" molecular weight portion of the polymer, thus, the yield can increase with further processing. The portion remaining after Soxhlet extraction with CHCl$_3$, equating ~30% of total solid, was processed in an ethanol-formic acid mixture and then precipitated in a solution of 2-propanol and triethylamine. This step added a further 14%, bringing the total yield of PNDIT10N to 52%, resulting in an overall yield of 24%. When using 1:1 of diBrDANDI:thiophene a lower yield of 25% CHCl$_3$ processable material was achieved. All devices presented herein are based on material from the CHCl$_3$ processed Soxhlet fraction for polymerisation with 10% excess of diBrDANDI (1.1:1 diBrDANDI:thiophene).
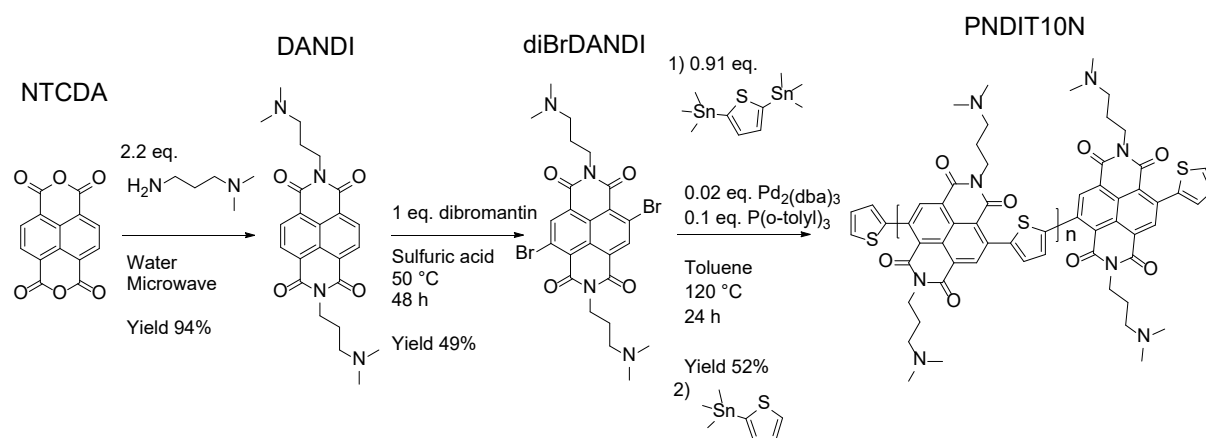
Scheme 6.1: Synthesis route of the n-type cathode interface material PNDIT10N.

PNDIT10N is insoluble in many of the organic solvents commonly used for active layer deposition in polymer solar cell fabrication, e.g. 1,2-dichlorobenzene (*o*-DCB), as well as more industrially relevant solvents such as methyl tetrahydrofuran, anisole and 1,2-xylene. Further, the solubility of PNDIT10N also makes it a suitable choice for inverted devices utilising alcohol/water based nanoparticle dispersions for the active layer processing[46-47]. However, the material experiences limited solubility in CHCl$_3$, is fairly soluble in short chain alcohol-acid combinations and is readily dissolved in BnOH, thus, making it a perfect candidate for orthogonal solvent processing in inverted devices. The toxicity of BnOH is lower than for the commonly used chlorinated solvents; CHCl$_3$, chlorobenzene (CB) and *o*-

DCB, it is readily used in the pharmaceutics and cosmetic industries.[48] This low toxicity is also promising for the future upscaling of the deposition method.

Molecular weight determination of PNDIT10N by size exclusion chromatography proved difficult. High temperature gel permeation chromatography was initially performed, however the molecular weight was not elucidated due to the strong interactions between the polymer pendant amine groups and stationary phase as well as limited solubility in mobile phase (1,3,5-trichlorobenzene (TCB)). Matrix assisted laser desorption ionisation (MALDI) was successfully performed on the monomer diBrDANDI with the matrix trans-2-[3-(4-tert-nutylphenyl)-2-methyl-2-propenylidene]malononitrile (DCTB), shown in Figure A.31. However, PNDIT10N did not show any response for a number of different sample preparation methods with the DCTB matrix. This indicates that no low molecular weight segments, e.g. dimers, are present in the final PNDIT10N product.

6.4.2 Film thickness

The film thickness of the polymer interlayer on ITO-coated glass substrates was investigated with NICISS. The film thickness has been determined from the energy loss of the He projectiles in the PNDIT10N films. The energy loss of the projectiles has been determined from the shift of the onset of contribution to the NICISS spectrum of He projectiles backscattered from the In and Sn forming the substrate. In Figure 6.1c the NICISS time of flight (TOF) spectra of PNDIT spin coated onto ITO are shown. The onset of the spectrum of heated and sputtered ITO is at the lowest TOF at around 3.8 μs. The TOF of 3.8 μs represents the surface of ITO. The onset is shifting to longer TOF with increasing concentration of PNDIT showing that the polymer layer increases in thickness. The energy loss of the projectiles in the PNDIT10N films converted to the polymer film thickness is shown in Figure 6.1a. The films spin coated from 0.50, 1.0, 5.0, and 10 mg mL^{-1} PNDIT10N solutions with BnOH (hereafter referred to as Films 0.5, 1, 5 and 10 respectively) yielded thicknesses of about 2.5-10 nm. Interestingly the two lower concentrations resulted in film thicknesses overlapping within the experimental error at approximately 2.5-3 nm.
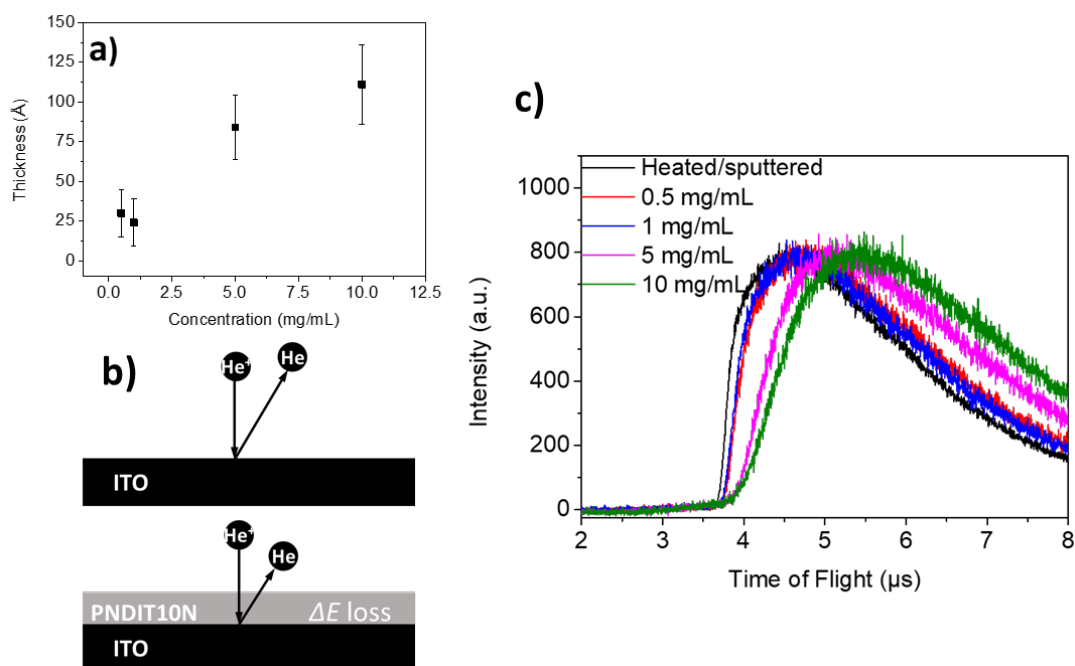
Figure 6.1: a) PNDIT10N film thickness as function of the PNDIT10N solution concentration with b) top, no significant energy loss other than classical energy transfer between projectile (He) and target (In); bottom extra energy loss caused by the projectiles traversing the PNDIT10N layer. c) Time of flight NICISs spectra of heated/sputtered ITO-coated glass substrate and PNDIT10N layers of various thickness spin coated onto ITO.

6.4.3 Material properties

The active layer is processed on top of the CIL via orthogonal processing. It is therefore important that the interface layer film possess a good stability to avoid dissolution and/or partial washing off the film. The contact angle was measured for a PNDIT10N film spun on top of ITO-coated glass prior to and after washing with *o*-DCB, revealing that the contact angle remained unchanged after washing (Table 6.1). This indicates that the film coverage remains intact, thus, showing a good stability towards orthogonal processing with *o*-DCB.

Table 6.1: Contact angles presented as an average over four measurements.

Sample	Contact angle (deg.)
ITO	25
ITO/ZnO	40
ITO/PNDIT10N	46
ITO/PNDIT10N (*o*-DCB)	46

The thermal stability of PSCs is important due to devices being able to reach high working temperatures at industry standard operating temperatures of up to 85 ºC.[49] The thermal stability of PNDIT10N was measured by simultaneous thermal analysis (STA), with results showing a 5% percentage weight loss at 270 ºC (Figure 6.2). This is well over what is required of PSC materials/components under normal operation.
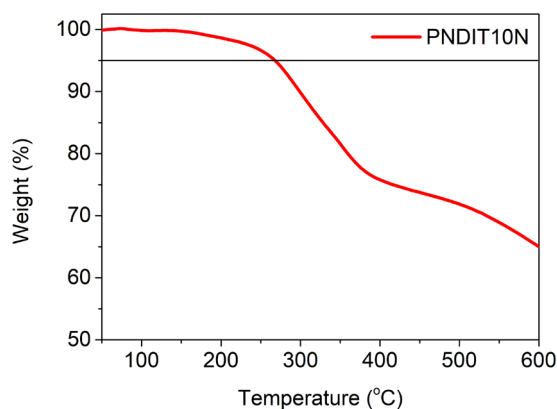
Figure 6.2: STA spectra of polymer PNDIT10N.

PNDIT10N interface material, being suitable for orthogonal solvent processing, was evaluated using the inverted device configuration. Thus, light absorbed by this material will be prevented from reaching the active layer, lowering the light harvesting from the photoactive layer. The UV/vis spectrum of the polymer PNDIT10N in dilute BnOH solution is compared with thin film (solid state) in Figure 6.3a. The polymer exhibits two major peaks at around 350 nm and 500-600 nm in film, which are attributed to π-π^* transitions and intramolecular charge transfer effects between NDI units and thiophene units, respectively. The optical band gap ($E_{g,opt}$) was calculated from thin PNDIT10N film according to:

$$E_{g,opt} = \frac{hc}{\lambda_{onset}}$$ (4)

where h is the Planck constant, c is the speed of light in vacuum, and λ_{onset} is the absorption onset in the low-energy region. λ_{onset} was estimated at 695 nm resulting in an $E_{g,opt}$ of 1.78 eV. The thin film spectra experience a bathochromic shift compared to the solution, which is commonly seen due to intermolecular aggregation of conjugated polymer in the solid state. This strong shift of 45 nm for maxima between solution and films resulted in a close alignment with the absorption of the BHJ layers. However, it should be noted that the interface layer might contribute to the charge carrier generation via synergistic effects.[50] That is, the charge transfer between donor and PNDIT10N at the BHJ layer-PDNIT10N interface.

Further optical measurements were carried out to elucidate to what extent the transmittance decreases with increasing thickness of CIL. Figure 6.3b shows the transmittance for stacks of glass/ITO/CIL over

the absorbance range of 300-800 nm with air as reference. This includes the PNDIT10N Films 0.5, 1, 5 and 10 spanning a thickness range of ~2.5-10 nm, and a ZnO film with a thickness of 25-30 nm[51]. The greatest drop in transmittance for all PNDIT10N films was observed at 600 nm, directly aligning it with the strong absorption peak of TQ1:$PC_{71}BM$ with local maxima close to 600 nm[36]. This transmittance reduction affects all PSC active layers investigated, though the alignment is less pronounced for PTNT:$PC_{71}BM$ and PTB7-Th:$PC_{71}BM$ [35, 52-53]. However, for a wavelength of 600 nm the transmittance decrease is quite low at 2.2, 3.0, 4.7, and 7.6% for Films 0.5, 1, 5, and 10 respectively. This is the largest decrease seen when compared to bare ITO in the 500-675 nm wavelength regime. It is worth noting that the close alignment with the active layer absorption arises from a bathochromic absorption shift of the polymer when coated on ITO. The peak positions of the glass/ITO/ZnO stack appears at higher wavelengths compared to the glass/ITO/PNDIT10N stack, additionally an increase in the transmittance in the lower wavelength region, Figure 6.3b, is observed. This increase might originate from either a difference in wave-guiding caused by a thickness difference between the two stacks[54] or a decrease in reflectance[55]. However, the active layer absorption is low in this area and the two stacks perform comparably at longer wavelengths, where the active layers in question possess strong absorption peaks. From these results, it is clear that the thickness of the PNDIT10N layer should be minimised for optimal OPV performance from a purely optical perspective.
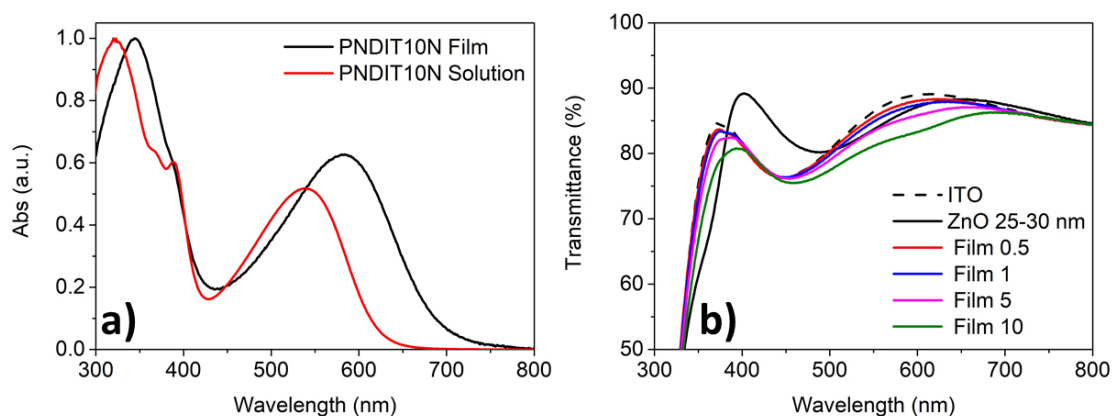
Figure 6.3: a) UV/vis spectra of PNDIT10N as film and in BnOH, b) Transmittance comparison between ITO-coated with PNDIT10N of varied thicknesses and ITO-coated with a 25-30 nm thick layer of ZnO.

The presence of an intramolecular photodoping mechanism for PNDIT10N was investigated with UV/vis. Figure 6.4 reveals an emerging peak with increasing absorbance in the IR range upon illumination of the PNDIT10N sample with UV light (365 nm). This peak in the IR region was also observed by Naab et al. for the NDI-bithiophene based polymer N2200 upon the addition of external dopants.[56] This provides a clear indication that photodoping is present in PNDIT10N.
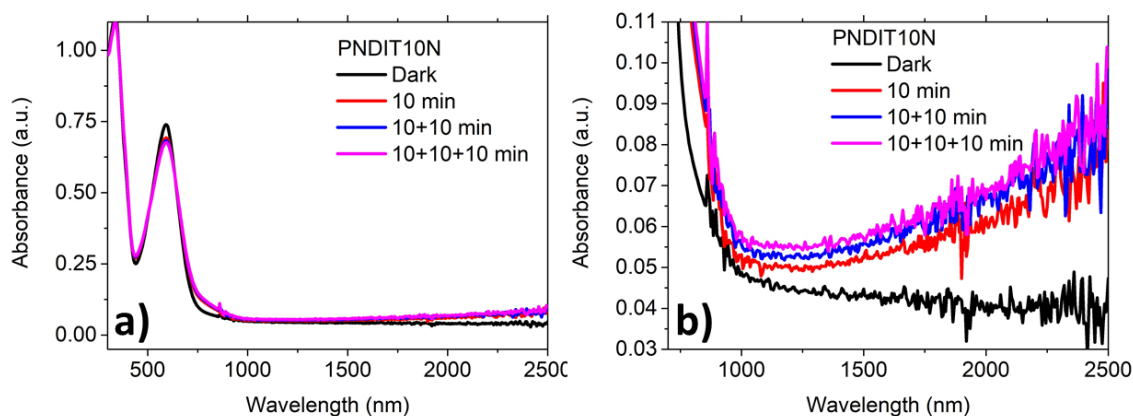
Figure 6.4: a) UV/vis spectra showing photo-doping of PNDIT10N and its response after illumination with light (wavelength of 365 nm) with a handheld UV-lamp for 10 minute increments. b) Infrared part of the UV/vis spectra, clearly showing the increased absorbance in this region.

Square-wave voltammetry (SWV) was employed for estimation of HOMO and LUMO energy levels of PNDIT10N, TQ1, PTNT, and PTB7-Th. It is worth noting that the pendant amine side-group as well as the low solubility of PNDIT10N, had two clear effects on the measurements; i) poor film coating quality on the electrode and ii) partial dissolution of the polymer during reduction. In certain cases, flakes of polymer could be seen detaching from the electrode during immersion in the electrolyte solution, indicating poor coating quality. It was therefore highly likely that further detachment/delamination could have occurred during the measurement. However, high scan rates of 100 mV/s were employed, leading to minimal dissolution. PNDIT10N oxidation and reduction maxima in SWV were estimated at 1.24 V and -0.75 V vs Fc/Fc$^+$ respectively. Thus, giving a HOMO/LUMO of -6.37 eV/-4.14 eV for PNDIT10N. In this same manner, the energy levels for the other polymers, depicted in Figure 6.5b, were estimated at -5.94/-3.67, -6.35/-3.40, and -5.60/-3.47 HOMO/LUMO for TQ1, PTNT, and PTB7-Th respectively. This indicates a low energy barrier for extraction of electrons from the active layer. Additionally a suitable energy level alignment was achieved for PNDIT10N, providing the ability to function as a hole-blocking layer, in regards to the donor materials measured.[57] This energy level alignment arises from the strong acceptor character of the semiconducting naphthalene diimide (NDI)-thiophene based backbone, contributing to a low band gap, endowing the polymer with the ability to function as a hole-blocking layer. For SWV spectra of the polymers refer to Figure 6.5a.
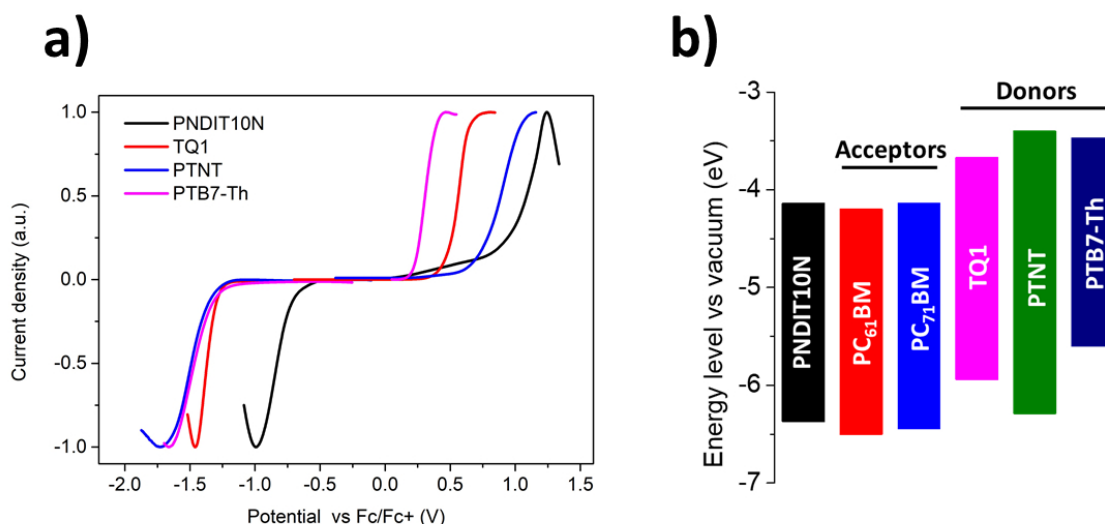
Figure 6.5: a) SWV spectra of the polymers used in this study. b) Illustration of bandgaps estimated from square wave voltammetry. $PC_{61}BM$ and $PC_{71}BM$ values are extracted from literature.[53, 58]

6.4.4 Work function modification

Amine functionalised materials are known to modify the work function of ITO and this modification was investigated for PNDIT10N coated ITO. A ~3 nm thin PNDIT10N layer (Film 0.5) was found to significantly reduce the ITO work function by over 0.8 eV, from 4.6 eV to 3.8 eV for ITO and ITO-PNDIT10N respectively. Figure 6.6a show the shift in the secondary electron cut-off of the ultraviolet photoelectron spectroscopy (UPS) spectra and schematically depicts the corresponding vacuum level shift at the ITO-PNDIT10N interface, as a result of surface modification. The observed reduction in the work function agrees well with literature values for amino containing interface materials with tertiary amine or pyridine pendant groups.[12, 17, 29, 51, 59-60] This notable work function reduction is related to the free electron pair on the nitrogen in the PNDIT10N side-group forming an interfacial dipole.[9] This interfacial dipole further facilitates the electron collection and transport from the BHJ layer to the ITO cathode.[61] Additional measurements were carried out as part of the stability study of PNDIT10N thin films. These films were measured after a 10 day ageing period, revealing that the work function increases upon storage, see Figure 6.6**a**. A largest increase of 0.4 eV was observed for the thin film stored in ambient conditions inside with several hours of direct sunlight per day. This increase possibly arose from degradation of the PNDIT10N thin film and/or the adsorption of contaminants on the surface.
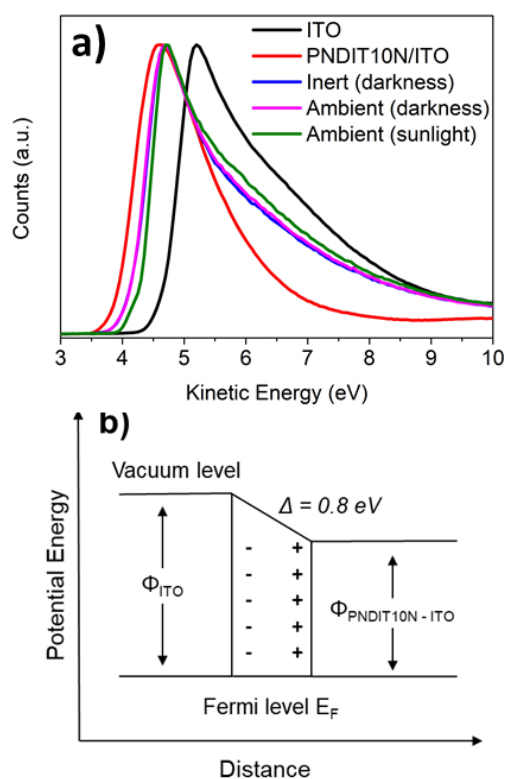
Figure 6.6: a) UPS spectra of bare ITO and PNDIT10N (~3 nm) coated ITO under four different ageing conditions; non-aged, 10 days under dark in N_2 atmosphere, 10 days under dark in ambient atmosphere, and 10 days in sunlight under ambient atmosphere. b) Schematic diagram showing the origin of work function change due to the presence of PNDIT10N on the ITO surface.

6.4.5 Photovoltaic performance

The material performance of PNDIT10N CIL was evaluated through the fabrication of solar cells in the inverted device configuration of (ITO/CIL/BHJ layer/MoOx/Ag). The thickness dependence of PNDIT10N as CIL was investigated for a TQ1:PC$_{61}$BM BHJ layer (Figure A.11). The PCE decreased significantly, as the film thickness increased between Film 0.5 and 10, revealing that the thinner films perform better. Although less prominent, this trend has previously been observed for polymeric interface materials with pendant amino side-groups.[16] Unlike previous studies it must be noted that no light soaking or photo doping effect was observed for PNDIT10N during device testing. However, UV/vis measurements indicate that a photo doping mechanism may be present in the material. It is theorised that the effect is diminished during device testing due to the material already being light soaked from exposure to ambient light during fabrication. The decrease in PCE was mainly driven by the current loss, with a large drop between the thicknesses of Film 0.5 to 10, as only small variations in an open-circuit voltage (V_{oc}) and FF were observed in the same thickness regime. Interestingly a decoupling between transmittance decrease and current decrease was observed for TQ1:PC$_{71}$BM BHJ layer devices with CN as additive for PNDIT10N thicknesses of Films 0.5 and 5 (Table 1, Table S2).

This thickness regime experiences a quite low transmittance decrease at ~3% as the current experiences a 9% drop with the increased film thickness. Thus, the transmittance and PCE, or current, are decoupled for PDNIT10N CIL. This effect is even more pronounced for devices with PTNT:PC$_{71}$BM BHJ layer (Table A.2) which experiences a current loss of 17% between PNDIT10N Films 0.5 and 5. Interestingly V$_{oc}$ and FF remains more or less constant while the R$_s$ is slightly lower for the thicker interface layer. Further, the optimisation of the thickness, when incorporating a TQ1:PC$_{71}$BM BHJ layer with the use of CN as an additive, revealed that Film 0.5 and 1 consistently performed equivalent with regards to PCE. Thus, Film 0.5 and 1 were considered equally in regard to device processing, resulting in an optimal performance at a thickness of ~3 nm for PNDIT10N CIL.

TQ1:PC$_{71}$BM BHJ layer in inverted PSCs incorporating a ~3 nm PNDIT10N CIL were found to have a short-circuit current density (J$_{sc}$) of 10.5 mA cm^{-2}, V$_{oc}$ of 909 mV, and a fill factor (FF) of 68%, resulting in a maximum PCE of 6.7 %. This is, to the best of our knowledge, the highest PCE measured for a TQ1:PC$_{71}$BM active layer in inverted device configuration.[36, 62] The high V$_{oc}$ is comparable to previously reported values and further confirms that PNDIT10N successfully modifies the ITO work function.[38] Thus, facilitating charge transport across the ITO-active layer interface in an energetically favourable manner. Moreover, the high J$_{sc}$ of 10.5 is in agreement with reported values[51] and suggests a favourable D/A morphology, which is also reflected by the high FF measured for these devices.

Up scaling via roll-to-roll processing is commonly done in an ambient atmosphere and materials stable under these conditions are hence pursued. Thus, the stability of bare PNDIT10N films was explored under different storage conditions for a 10-day ageing period. As seen in Figure 6.7a, PNDIT10N experiences good stability in darkness both in inert and ambient atmosphere. To evaluate the degradation OPV devices were prepared from the aged PNDIT10N films. These devices retain high V$_{oc}$ for films stored in darkness, however, the respective J$_{sc}$, 9.6 mA cm^{-2} and 8.6 mA cm^{-2}, is reduced for both inert and ambient with the latter decreasing by ~20% (Table 6.2). The decrease in FF is close to identical for these conditions but drops further for light exposed films. Moreover, the V$_{oc}$ of light exposed films underwent a significant reduction and was measured to be below 0.8 V. Devices fabricated without a CIL, i.e. with the BHJ layer deposited directly on ITO-coated glass, experienced low V$_{oc}$ values of about 0.3 V, with J$_{sc}$ and FF faring better at 6.5 mA cm^{-2} and 38% respectively. This could indicate that the material loses part of the ability to function as a CIL through modification of the ITO work function. An increase in work function of the aged films was confirmed with UPS additional measurements. These showed a clear trend for the increase in work function from 3.8 eV (non-aged) through 4.0 eV (glovebox and ambient in darkness) to 4.2 eV (ambient in sunlight). The drop in efficiency is hence likely to originate from degradation of the PNDIT10N layer and/or adsorption of contaminants on the surface. The devices fabricated with aged PNDIT10N films experienced reductions in PCE (Table 6.2), however, with a 10-day ageing period in darkness efficiencies of 4.8% and 4.3% was achieved for inert and ambient storage conditions, respectively. Thus, PNDIT10N retained a good

stability in inert and ambient atmosphere in darkness. Though, the PCE decreases to 3.3% for PNDIT10N films stored in air indoors and exposed to several hours of direct sunlight per day. However, keeping in mind that the film is only ~3 nm it is remarkable that the devices work at all.

Table 6.2: Stability study for a ITO/PNDIT10N ~3 nm/TQ1:PC71BM (1:2.5)/MoOx/Ag configuration was carried out by storing PNDIT10N films spin coated on ITO-coated glass substrates for 10 days in different environments.[a]

	J_{sc} [mA cm^{-2}]	V_{oc} [V]	FF [%]	PCE [%]	Max [%]	WF [eV]
Glovebox (darkness)	9.6 ± 0.3	0.889 ± 0.021	54 ± 2	4.6 ± 0.2	4.8	4.0
Ambient (darkness)	8.6 ± 0.4	0.865 ± 0.028	53 ± 2	4.0 ± 0.2	4.3	4.0
Ambient (sunlight)	8.2 ± 0.1	0.791 ± 0.020	50 ± 2	3.2 ± 0.1	3.3	4.2
Without CIL	6.5 ± 0.2	0.303 ± 0.028	38 ± 3	0.8 ± 0.1	0.9	4.6

[a] Mean value ± standard deviation from six devices.

The versatility of PNDIT10N as a CIL was further investigated for PTNT:PC$_{71}$BM and PTB7-Th:PC$_{71}$BM BHJ layer systems. PCEs of 5.7% and 7 % were achieved for PTNT:PC$_{71}$BM and PTB7-Th:PC$_{71}$BM BHJ layers respectively (Figure 6.7b, Table 6.3). This was on par with the PCEs of 5.1% and 7.5% achieved for corresponding ZnO device configuration, showing the excellent versatility of PNDIT10 as a CIL, for a range of different active layer systems. It is also, to the best of our knowledge, the highest PCE reported for devices incorporating the donor polymer PTNT.[35] From Table S2 it is clear that these systems experienced elevated J_{sc}, although less prominent for PTB7-Th:PC$_{71}$BM BHJ layer when paired with PNDIT10N. The increase in J_{sc} could possibly be related to the strength of the electric dipole layer[49], arising from the interaction of the pendant amino groups with the BHJ layer[51]. Thus, leading to a more efficient charge extraction.

Table 6.3: Photovoltaic performance for devices incorporating a PNDIT10N layer of ~3 nm or ZnO (25-30nm) as CIL, with slot die coated/printed devices incorporating PNDIT10N of 4 nm [a]

CIL	BHJ	J_{sc} [mA cm^{-2}]	V_{oc} [V]	FF [%]	R_s [Ω cm^{-2}]	PCE [%]	Max [%]
PNDIT10N Film A (~3 nm)	TQ1:PC$_{71}$BM	10.5 ± 0.3	0.909 ± 0.001	68 ± 1	1.2	6.5 ± 0.2	6.7
	PTNT:PC$_{71}$BM	9.2 ± 0.4	0.891 ± 0.003	64 ± 8	2.7	5.3 ± 0.3	5.7
	PTB7-Th:PC$_{71}$BM	16.4 ± 0.5	0.728 ± 0.015	55 ± 1	2.2	6.6 ± 0.2	7.0
PNDIT10N Printed (4 nm) [b]	TQ1:PC$_{61}$BM	4.0 ± 0.4	0.712 ± 0.008	42 ± 3	-	1.2 ± 0.2	1.6

[a] Mean value $\pm$ standard deviation from six devices. [b] Calculated dry thickness of PNDIT10N layer.

The applicability of PNDIT10N as a CIL in scalable fabrication methods, e.g. roll-to-roll processing, was investigated. Flexible devices (PET/ITO/PNDIT10N/TQ1:PC$_{61}$BM/MoOx/Ag), built on poly(ethylene terephthalate) (PET) foil, incorporating slot-die coated PNDIT10N (4 nm) processed from a BnOH:acetone blend (1:9) and BHJ layer (195 nm) in ambient atmosphere were fabricated. For these printed devices, a maximum PCE of 1.6% was achieved (Figure 6.7c). Further, a V_{oc} of 712 mV was obtained, while J_{sc} and FF experienced modest values of 4 mA cm^{-2} and 42% respectively. Importantly, the V_{oc} is in agreement with literature values[63] and thus proves that the printed PNDIT10N interlayer successfully modifies the ITO surface in an energetically favourable manner. The relatively lower PCE and significantly reduced J_{sc} and FF of printed devices compared to the spin coated counterparts are to be attributed to a number of different factors. These include: i) the difference in the sheet resistance, roughness and optical properties of ITO coated PET foil and ITO-coated glass, ii) the use of PC$_{61}$BM instead of PC$_{71}$BM as in spin coated devices, iii) fabrication taking place in ambient atmosphere, iv) resultant thickness differences of the interface layer as well as BHJ layer, and v) potentially different BHJ morphology as the active layer was slot-die coated on a preheated substrate (from o-DCB, CHCl$_3$ and CN) whereas spin-coating was performed at room temperature (from o-DCB and CN).
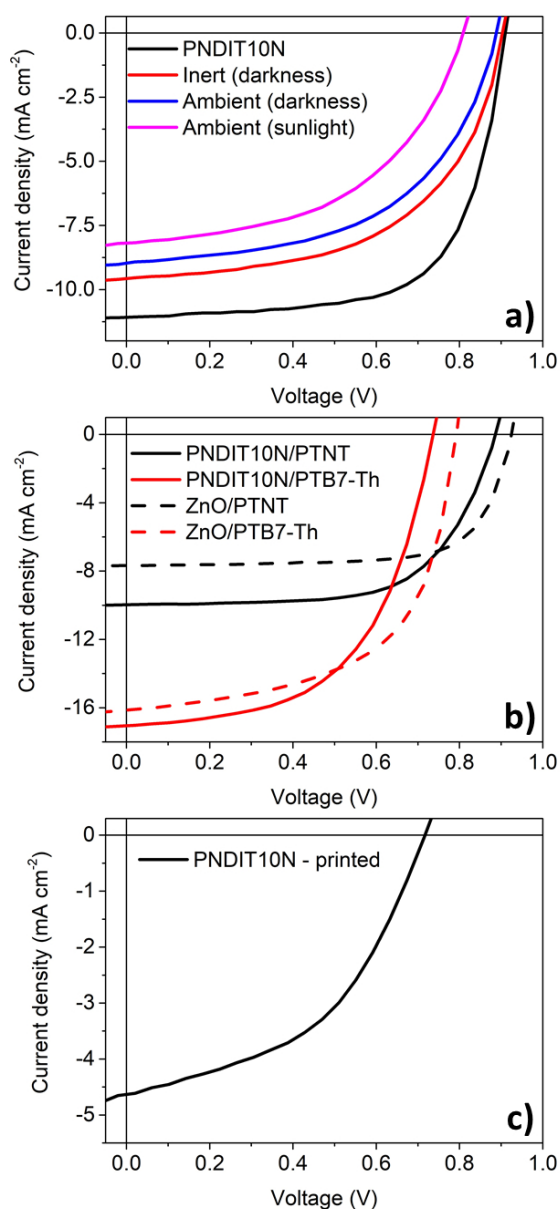
Figure 6.7: J-V characteristics under illumination for a) TQ1:PC71BM BHJ layer including a 10 day stability study of PNDIT10N CIL, b) representative best device for PTNT:PC71BM and PTB7-Th:PC71BM BHJ layer, and c) representative slot-die coated device.

It must be emphasized that the preliminary printed device parameters reported here are primarily to demonstrate the applicability of BnOH-acetone processed PNDIT10N interlayer for large-scale fabrication via printing. It is hence likely that, future optimisation of the thickness could lead to higher currents and better overall performance of the slot die coated devices. Thus, the importance does not lie in the efficiency achieved but in that, PNDIT10N, without any optimisation, can provide functioning devices when printed in air on a flexible substrate. This is highly promising, again showing the versatility of the material.

6.5 Conclusion

In summary, the n-type conjugated polymer PNDIT10N was successfully synthesised in a facile three-step procedure from commercially available materials. PNDIT10N was orthogonally solution processed from alcohol and applied as a CIL in inverted device configuration. The work function of ITO was revealed to be modified with a ~3 nm thin layer of polymer, agreeing with the improved performance of devices incorporating a PNDIT10N interlayer. In regard to the donor materials employed in this study, PNDIT10N, inherently being a strong acceptor, has the ability to function as a hole-blocking layer due to its low-lying HOMO level.

Of significance, the PCE of 6.7% achieved for TQ1:$PC_{71}BM$ BHJ layer is the highest value obtained for this active layer in the inverted device architecture. Similarly, the PCE of 5.7% is the highest on record for devices incorporating the donor polymer PTNT in the active layer. Devices with PTB7-Th:$PC_{71}BM$ active layer experienced a highest PCE of 7% for PNDIT10N interlayer. Thus, PNDIT10N has delivered high performance devices for three separate BHJ layers, revealing record PCEs for two out of the three donors with PTB7-Th:$PC_{71}BM$ performing close to its ZnO counterpart.

The stability of the PNDIT10N polymer proved excellent under darkness in inert and ambient conditions; after a 10-day ageing period the respective PCE was 4.8% and 4.3% for devices built on the aged PNDIT10N films. This decreased to 3.3% for films aged in ambient and exposed to direct sunlight. Lastly, PNDIT10N interlayers processed from a BnOH:acetone blend were successfully slot-die coated and employed in partially printed PSCs. This resulted in a PCE of 1.6% for non-optimised devices, thus, indicating a good applicability for roll-to-roll processing. This is of great significance for any future upscaling attempts of the CIL fabrication process.

The PNDIT10N polymer constitutes a highly versatile and robust CIL, working well with a range of polymer-fullerene BHJ layers. The short as well as facile synthesis route and demonstrated slot die coated devices paints the picture of a highly promising material, which extends the already existing range of organic CILs for polymer solar cell applications.

6.6 Author contributions

Dr. Anirudh Sharma: *Performed most of the device fabrication and the UPS measurements, including data interpretation, for ITO and PNDIT10N/ITO.*

Dr.Desta Gedefaw: *Assisted with electrochemistry measurements and data interpretation.*

Dr.Sait Elmas: *Assisted with electrochemistry measurements and data interpretation.*

Caroline Pan: *Assisted with device fabrication and data interpretation.*

Bradley Kirk: *Performed the NICISS measurements and data interpretation.*

Xianyuan Zhao: *Performed the NICISS measurements and data interpretation.*

Prof. Gunther Andersson: *Assisted with NICISS and UPS data interpretation.*

Prof. Mats R. Andersson: *Assisted with analysis and interpretation of device data.*

Work not included in the publication:

Amira Ramadan Alghamdi: *Performed UPS measurements on aged PNDIT10N films.*

Dr. Anirudh Sharma: *Performed AFM measurements of active layers.*

6.7 References

(9)   van Reenen, S.; Kouijzer, S.; Janssen, R. A. J.; Wienk, M. M.; Kemerink, M., Origin of Work Function Modification by Ionic and Amine-Based Interface Layers. *Adv. Mater. Interfaces* **2014**, 1, 1400189.

(10)   Zhou, Y.; Fuentes-Hernandez, C.; Shim, J.; Meyer, J.; Giordano, A. J.; Li, H.; Winget, P.; Papadopoulos, T.; Cheun, H.; Kim, J.; Fenoll, M.; Dindar, A.; Haske, W.; Najafabadi, E.; Khan, T. M.; Sojoudi, H.; Barlow, S.; Graham, S.; Brédas, J.-L.; Marder, S. R.; Kahn, A.; Kippelen, B., A Universal Method to Produce Low–Work Function Electrodes for Organic Electronics. *Science* **2012**, 336, 327-332.

(11)   Huang, F.; Wu, H.; Wang, D.; Yang, W.; Cao, Y., Novel Electroluminescent Conjugated Polyelectrolytes Based on Polyfluorene. *Chem. Mater.* **2004**, 16, 708-716.

(12)   Zhang, Y.; Chen, L.; Hu, X.; Zhang, L.; Chen, Y., Low Work-function Poly(3,4-ethylenedioxylenethiophene): Poly(styrene sulfonate) as Electron-transport Layer for High-efficient and Stable Polymer Solar Cells. *Sci. Rep.* **2015**, 5, 12839.

(13)   Woo, S.; Hyun Kim, W.; Kim, H.; Yi, Y.; Lyu, H.-K.; Kim, Y., 8.9% Single-Stack Inverted Polymer Solar Cells with Electron-Rich Polymer Nanolayer-Modified Inorganic Electron-Collecting Buffer Layers. *Adv. Energy Mater.* **2014**, 4, 1301692.

(14)   Jia, T.; Sun, C.; Xu, R.; Chen, Z.; Yin, Q.; Jin, Y.; Yip, H.-L.; Huang, F.; Cao, Y., Naphthalene Diimide Based n-Type Conjugated Polymers as Efficient Cathode Interfacial Materials for Polymer and Perovskite Solar Cells. *ACS Appl. Mater. Interfaces* **2017**, 9, 36070-36081.

(15)   Wang, J.; Lin, K.; Zhang, K.; Jiang, X.-F.; Mahmood, K.; Ying, L.; Huang, F.; Cao, Y., Crosslinkable Amino-Functionalized Conjugated Polymer as Cathode Interlayer for Efficient Inverted Polymer Solar Cells. *Adv. Energy Mater.* **2016**, 6, 1502563.

(16)   Wu, Z.; Sun, C.; Dong, S.; Jiang, X.-F.; Wu, S.; Wu, H.; Yip, H.-L.; Huang, F.; Cao, Y., n-Type Water/Alcohol-Soluble Naphthalene Diimide-Based Conjugated Polymers for High-Performance Polymer Solar Cells. *J. Am. Chem. Soc.* **2016**, 138, 2004-2013.

(17)   He, Z.; Zhong, C.; Su, S.; Xu, M.; Wu, H.; Cao, Y., Enhanced Power-conversion Efficiency in Polymer Solar Cells using an Inverted Device Structure. *Nat. Photonics* **2012**, 6, 591.

(18)   Zhang, K.; Zhong, C.; Liu, S.; Mu, C.; Li, Z.; Yan, H.; Huang, F.; Cao, Y., Highly Efficient Inverted Polymer Solar Cells Based on a Cross-linkable Water-/Alcohol-Soluble Conjugated Polymer Interlayer. *ACS Appl. Mater. Interfaces* **2014**, 6, 10429-10435.

(19)   Kang, R.; Oh, S.-H.; Kim, D.-Y., Influence of the Ionic Functionalities of Polyfluorene Derivatives as a Cathode Interfacial Layer on Inverted Polymer Solar Cells. *ACS Appl. Mater. Interfaces* **2014**, 6, 6227-6236.

(20)   Zhang, Z.-G.; Qi, B.; Jin, Z.; Chi, D.; Qi, Z.; Li, Y.; Wang, J., Perylene Diimides: a Thickness-insensitive Cathode Interlayer for High Performance Polymer Solar Cells. *Energy Environ. Sci.* **2014**, 7, 1966-1973.

(21)   Zhao, K.; Ye, L.; Zhao, W.; Zhang, S.; Yao, H.; Xu, B.; Sun, M.; Hou, J., Enhanced Efficiency of Polymer Photovoltaic Cells via the Incorporation of a Water-soluble Naphthalene Diimide Derivative as a Cathode Interlayer. *J. Mater. Chem. C* **2015**, 3, 9565-9571.

(22)   Xiao, B.; Wu, H.; Cao, Y., Solution-processed Cathode Interfacial Layer Materials for High-efficiency Polymer Solar Cells. *Mater. Today* **2015**, 18, 385-394.

(23)   Bini, K.; Xu, X.; Andersson, M. R.; Wang, E., Alcohol-Soluble Conjugated Polymers as Cathode Interlayers for All-Polymer Solar Cells. *ACS Appl. Energy Mater* **2018**, 1, 2176-2182.

(24)   Hu, Z.; Xu, R.; Dong, S.; Lin, K.; Liu, J.; Huang, F.; Cao, Y., Quaternisation-polymerized N-type Polyelectrolytes: Synthesis, Characterisation and Application in High-performance Polymer Solar Cells. *Mater. Horiz.* **2017**, 4, 88-97.

(25)   Hu, Z.; Chen, Z.; Zhang, K.; Zheng, N.; Xie, R.; Liu, X.; Yang, X.; Huang, F.; Cao, Y., Self-Doped N-Type Water/Alcohol Soluble-Conjugated Polymers with Tailored Backbones and Polar Groups for Highly Efficient Polymer Solar Cells. *Sol. RRL* **2017**, 1, 1700055.

(26)   Hu, Z.; Zheng, N.; Dong, S.; Liu, X.; Chen, Z.; Ying, L.; Duan, C.; Huang, F.; Cao, Y., Phosphonium Conjugated Polyelectrolytes as Interface Materials for Efficient Polymer Solar Cells. *Org. Electron.* **2018**, 57, 151-157.

(27)   Jiao, W.; Ma, D.; Lv, M.; Chen, W.; Wang, H.; Zhu, J.; Lei, M.; Chen, X., Self N-doped [6,6]-phenyl-C61-butyric acid 2-((2-(trimethylammonium)ethyl)-(dimethyl)ammonium) Ethyl Ester Diiodides as a Cathode Interlayer for Inverted Polymer Solar Cells. *J. Mater. Chem. A* **2014**, 2, 14720-14728.

(28)   Sun, Y.; Seo, J. H.; Takacs, C. J.; Seifter, J.; Heeger, A. J., Inverted Polymer Solar Cells Integrated with a Low-Temperature-Annealed Sol-Gel-Derived ZnO Film as an Electron Transport Layer. *Adv. Mat.* **2011**, 23, 1679-1683.

(29)   Sharma, A.; George, Z.; Bennett, T.; Lewis, D. A.; Metha, G. F.; Andersson, G. G.; Andersson, M. R., Stability of Polymer Interlayer Modified ITO Electrodes for Organic Solar Cells. *Aust. J. Chem.* **2016**, 69, 735-740.

(30)   Li, M.; Gao, K.; Wan, X.; Zhang, Q.; Kan, B.; Xia, R.; Liu, F.; Yang, X.; Feng, H.; Ni, W.; Wang, Y.; Peng, J.; Zhang, H.; Liang, Z.; Yip, H.-L.; Peng, X.; Cao, Y.; Chen, Y., Solution-processed Organic Tandem Solar Cells with Power Conversion Efficiencies >12%. *Nat. Photonics* **2016**, 11, 85-90.

(31)   Jørgensen, M.; Norrman, K.; Gevorgyan, S. A.; Tromholt, T.; Andreasen, B.; Krebs, F. C., Stability of Polymer Solar Cells. *Adv. Mat.* **2012**, 24, 580-612.

(32)   Zhong, C. J.; Kwan, W. S. V.; Miller, L. L., Self-assembly of Delocalized. Pi.-stacks in Solution. Assessment of Structural Effects. *Chem. Mater.* **1992**, 4, 1423-1428.

(33)   Doria, F.; Nadai, M.; Sattin, G.; Pasotti, L.; Richter, S. N.; Freccero, M., Water Soluble Extended Naphthalene Diimides as pH Fluorescent Sensors and G-quadruplex Ligands. O*rg. Biomol. Chem.* **2012**, 10, 3830-3840.

(34)   Sasikumar, M.; Suseela, Y. V.; Govindaraju, T., Dibromohydantoin: A Convenient Brominating Reagent for 1,4,5,8-Naphthalenetetracarboxylic Dianhydride. *Asian J. Org. Chem.* **2013**, 2, 779-785.

(35)   Kroon, R.; Diaz de Zerio Mendaza, A.; Himmelberger, S.; Bergqvist, J.; Bäcke, O.; Faria, G. C.; Gao, F.; Obaid, A.; Zhuang, W.; Gedefaw, D.; Olsson, E.; Inganäs, O.; Salleo, A.; Müller, C.; Andersson, M. R., A New Tetracyclic Lactam Building Block for Thick, Broad-Bandgap Photovoltaics. *J. Am. Chem. Soc.* **2014**, 136, 11578-11581.

(36)   Wang, E.; Hou, L.; Wang, Z.; Hellström, S.; Zhang, F.; Inganäs, O.; Andersson, M. R., An Easily Synthesized Blue Polymer for High-Performance Polymer Solar Cells. *Adv. Mat.* **2010**, 22, 5240-5244.

(37)   Andersson, G.; Morgner, H., Determining the stopping power of low energy helium in alkanethiolates with Neutral Impact Collision Ion Scattering Spectroscopy (NICISS). *Nucl. Instrum. Methods Phys. Res., Sect. B* **1999**, 155, 357-368.

(38)   Li, W.; Furlan, A.; Hendriks, K. H.; Wienk, M. M.; Janssen, R. A. J., Efficient Tandem and Triple-Junction Polymer Solar Cells. *J. Am. Chem. Soc.* **2013**, 135, 5529-5532.

(39)   Pavlishchuk, V. V.; Addison, A. W., Conversion Constants for Redox Potentials Measured versus Different Reference Electrodes in Acetonitrile Solutions at 25°C. *Inorg. Chim. Acta* **2000**, 298, 97-102.

(40)   Bard, A. J.; Faulkner, L. R., Electrochemical Methods: Fundamentals and Applications. 2nd ed.; Wiley: New York, **2001**.

(41)   Hisao, I.; Kiyoshi, S.; Eisuke, I.; Kazuhiko, S., Energy Level Alignment and Interfacial Electronic Structures at Organic/Metal and Organic/Organic Interfaces. *Adv. Mat.* **1999**, 11, 605-625.

(42)   Krebs, F. C., Fabrication and Processing of Polymer Solar Cells: A Review of Printing and Coating Techniques. *Sol. Energy Mater. Sol. Cells* **2009**, 93, 394-412.

(43)   Kiel, J. W.; Kirby, B. J.; Majkrzak, C. F.; Maranville, B. B.; Mackay, M. E., Nanoparticle Concentration Profile in Polymer-based Solar Cells. *Soft Matter* **2010**, 6, 641-646.

(44)   Matsunaga, Y.; Goto, K.; Kubono, K.; Sako, K.; Shinmyozu, T., Photoinduced Color Change and Photomechanical Effect of Naphthalene Diimides Bearing Alkylamine Moieties in the Solid State. *Chem. - Eur. J.* **2014**, 20, 7309-7316.

(45)   Baumgartner, B.; Svirkova, A.; Bintinger, J.; Hametner, C.; Marchetti-Deschmann, M.; Unterlass, M. M., Green and Highly Efficient Synthesis of Perylene and Naphthalene Bisimides in Nothing but Water. *Chem. Commun.* **2017**, 53, 1229-1232.

(46)   Xie, C.; Tang, X.; Berlinghof, M.; Langner, S.; Chen, S.; Späth, A.; Li, N.; Fink, R. H.; Unruh, T.; Brabec, C. J., Robot-Based High-Throughput Engineering of Alcoholic Polymer: Fullerene Nanoparticle Inks for an Eco-Friendly Processing of Organic Solar Cells. *ACS Appl. Mater. Interfaces* **2018**, 10, 23225-23234.

(47)   Pan, X.; Sharma, A.; Gedefaw, D.; Kroon, R.; Diaz de Zerio, A.; Holmes, N. P.; Kilcoyne, A. L. D.; Barr, M. G.; Fahy, A.; Marks, M.; Zhou, X.; Belcher, W.; Dastoor, P. C.; Andersson, M. R., Environmentally friendly preparation of nanoparticles for organic photovoltaics. *Org. Electron.* **2018**, 59, 432-440.

(48)   Final Report on the Safety Assessment of Benzyl Alcohol, Benzoic Acid, and Sodium Benzoate. *Int. J. Toxicol.* **2001**, 20, 23-50.

(49)   E1171-15, A., Standard Test Methods for Photovoltaic Modules in Cyclic Temperature and Humidity Environments. In ASTM International, **2015**.

(50)   Shi, H.; Xia, R.; Sun, C.; Xiao, J.; Wu, Z.; Huang, F.; Yip, H.-L.; Cao, Y., Synergic Interface and Optical Engineering for High-Performance Semitransparent Polymer Solar Cells. *Adv. Energy Mater.* **2017**, 7, 1701121.

(51)   Sharma, A.; Kroon, R.; Lewis, D. A.; Andersson, G. G.; Andersson, M. R., Poly(4-vinylpyridine): A New Interface Layer for Organic Solar Cells. *ACS Appl. Mater. Interfaces* **2017**, 9, 10929-10936.

(52)   He, Y.; Li, Y., Fullerene Derivative Acceptors for High Performance Polymer Solar Cells. *Phys. Chem. Chem. Phys.* **2011**, 13, 1970-1983.

(53)   Li, Z.; Xu, X.; Zhang, W.; Meng, X.; Ma, W.; Yartsev, A.; Inganäs, O.; Andersson, M. R.; Janssen, R. A. J.; Wang, E., High Performance All-Polymer Solar Cells by Synergistic Effects of Fine-Tuned Crystallinity and Solvent Annealing. *J. Am. Chem. Soc.* **2016**, 138, 10935-10944.

(54)   Pettersson, L. A. A.; Roman, L. S.; Inganäs, O., Modeling Photocurrent Action Spectra of Photovoltaic Devices Based on Organic Thin Films. *J. Appl. Phys.* **1999**, 86, 487-496.

(55)   Chavhan, S. D.; Hansson, R.; Ericsson, L. K. E.; Beyer, P.; Hofmann, A.; Brütting, W.; Opitz, A.; Moons, E., Low Temperature Processed NiO_x Hole Transport Layers for Efficient Polymer Solar Cells. *Org. Electron.* **2017**, 44, 59-66.

(56)   Naab, B. D.; Gu, X.; Kurosawa, T.; To, J. W. F.; Salleo, A.; Bao, Z., Role of Polymer Structure on the Conductivity of N-Doped Polymers. *Adv. Electron. Mater.* **2016**, 2, 1600004.

(57)   Liao, S.-H.; Li, Y.-L.; Jen, T.-H.; Cheng, Y.-S.; Chen, S.-A., Multiple Functionalities of Polyfluorene Grafted with Metal Ion-Intercalated Crown Ether as an Electron Transport Layer for Bulk-Heterojunction Polymer Solar Cells: Optical Interference, Hole Blocking, Interfacial Dipole, and Electron Conduction. *J. Am. Chem. Soc.* **2012**, 134, 14271-14274.

(58)   Murto, P.; Genene, Z.; Benavides, C. M.; Xu, X.; Sharma, A.; Pan, X.; Schmidt, O.; Brabec, C. J.; Andersson, M. R.; Tedde, S. F.; Mammo, W.; Wang, E., High Performance All-Polymer Photodetector Comprising a Donor–Acceptor–Acceptor Structured Indacenodithiophene–Bithieno[3,4-c]Pyrroletetrone Copolymer. *ACS Macro Lett.* **2018**, 7, 395-400.

(59)   George, Z.; Xia, Y.; Sharma, A.; Lindqvist, C.; Andersson, G.; Inganas, O.; Moons, E.; Muller, C.; Andersson, M. R., Two-in-one: Cathode Modification and Improved Solar Cell Blend Stability Through Addition of Modified Fullerenes. *J. Mater. Chem. A* **2016**, 4, 2663-2669.

(60)   Courtright, B. A.; Jenekhe, S. A., Polyethylenimine Interfacial Layers in Inverted Organic Photovoltaic Devices: Effects of Ethoxylation and Molecular Weight on Efficiency and Temporal Stability. *ACS Appl. Mater. Interfaces* **2015**, 7, 26167-26175.

(61)   Lee, J.-H.; Jeong, S. Y.; Kim, G.; Park, B.; Kim, J.; Kee, S.; Kim, B.; Lee, K., Reinforcing the Built-In Field for Efficient Charge Collection in Polymer Solar Cells. *Adv. Funct. Mater.* **2018**, 28, 1705079.

(62)   Kim, Y.; Yeom, H. R.; Kim, J. Y.; Yang, C., High-efficiency Polymer Solar Cells with a Cost-effective Quinoxaline Polymer Through Nanoscale Morphology Control Induced by Practical Processing Additives. *Energy Environ. Sci.* **2013**, 6, 1909-1916.

(63)   Andersson, L. M., Fully Slot–Die-Coated All-Organic Solar Cells. *Energy Technol.* **2015**, 3, 437-442.

Chapter 7 – The effect of linker and side-group modification on the electron transport in n-type NDI based polymer cathode interface materials for polymer solar cells

7.1 Overview

In this chapter, six n-type naphthalene diimide (NDI) based cathode interface layer (CIL) polymers P(NDI3N-T), P(NDI3N-P), P(NDI3N-F8), P(NDI3N-T-Br), P(NDI3N-P-Br), and P(NDI3N-F8-Br) are reported. These polymers were successfully synthesised to incorporate thiophene, benzene, or fluorene as linker units, in between the n-type NDI structures, bearing either tertiary amine or quaternary amine pendant side-groups. The effect of chemical structural modification on doping efficiency and electron transport ability was investigated. Modification of the electrode, indium tin oxide (ITO), with CIL layers resulted in significant work function reductions of ~0.8-0.9 eV compared to pure ITO. Furthermore, doping was observed for all CILs except P(NDI3N-P) with tertiary amines found to photodope, as quaternary amines instead contribute to inherent doping. Importantly, the highly polar quaternary amine pendant side-groups were found to have adverse effects on the film forming abilities of the CILs when deposited on a hydrophobic all-polymer BHJ layer, with only P(NDI3N-F8-Br) achieving full coverage. Therefore, limiting applicability in conventional devices. The CILs were employed in preliminary inverted polymer solar cells (PSC) with a TQ1:PC$_{71}$BM BHJ layer to study the photovoltaic performance. The benzene, quaternary amine containing CIL, P(NDI3N-P-Br), was found to achieve a highest PCE of 3.4%, caused by simultaneous improvement in J$_{sc}$ and FF, compared to ZnO based reference devices at a PCE of 2.7%. To expand on and complement these results further experiments are needed. This involves a comparison of photovoltaic performance for conventional and inverted PSCs as well as devices with CIL and BHJ layer fabricated from more environmentally friendly, greener solvents. Lastly, an in-depth study of doping and the correlation to conductivity should be conducted.

7.2 Introduction

The rapid progress within the area of polymer solar cells (PSC) has seen materials such as $PC_{71}BM$, ITIC, N2200, PTB7-Th, and PM6 push the boundaries of power conversion efficiencies (PCE) ever onward. Similarly, cathode interface materials has experienced strong progress, starting with the introduction of poly[(9,9-bis(3'-(N,N-dimethylamino)propyl)-2,7-fluorene)-alt-2,7-(9,9-dioctylfluorene)] (PFN) by Huang *et al.* in 2004[1]. This was later followed by the utilisation of commercially available PEI and PEIE as cathode interface layers (CIL),[2] and the emerging of charged species such as conjugated poly(electrolytes) and the *N*-oxide structures of PDINO and NDIO.[3-4] These materials all possesses good solubilities in greener, more environmentally friendly solvents, e.g. short chain alcohols, which is required for environmentally friendly large scale roll-to-roll processing.

Interface engineering have proved integral for reaching high PCEs, with interface materials playing an important role in the device architectures of any PSC. Liu *et al.* described an ideal cathode interface material as a layer that reduce the electrode work function, possess orthogonal solvent processability toward the active layer, exhibit good film forming properties, inhibits exciton quenching, has a suitable electron affinity, is selective toward electrons, and possess a good long term stability.[5] However, the most widely used building block for cathode interface materials is fluorene with a large range of PFN derivatives now published.[6-9] These fluorene based, p-type, interface materials tend to have relatively high-lying HOMO levels compared to many of the donor materials used in the active layer, and thus they are unable to function as hole blocking layers, meaning charge selectivity is not fully achieved.[10-11] Moreover, Tan *et al.* concluded that the location of the polar groups on the polymer chain as well as the number of groups affects the doping strength.[12] When the polar groups were situated on the p-type fluorene unit a lower self-doping was observed compared to if the polar groups instead were situated on the n-type diketopyrrolopyrrole (DPP) unit (Figure 7.1), where access to doping of the backbone was found to be elevated. These observations would support the use of strong n-type acceptor materials as building blocks for cathode interface material conjugated poly(electrolytes). Though, molecular orientation is also found to influence the doping strength with Chen *et al.* concluding that an edge on orientation results in a stronger dipole moment, and higher PCE than a face on orientation due to the increased charge density at the interface.[7]

Two naphthalene diimide (NDI)-fluorene based polymers with hole-blocking capability PNDIT-F3N and PNDIT-F3N-Br were introduced by Wu *et al*. (Figure 7.1).[13] The doping mechanisms were studied and it was observed that PNDIT-F3N, with tertiary amine side-groups, showed a response in conductivity upon illumination, which was attributed to the donation of an electron from the side-group to the polymer backbone, e.g. photodoping. PNDIT-F3N-Br did not experience a photo response but showed a consistently high conductivity that was attributed to inherent doping caused by the bromine counterion. Additionally, it was observed that both these polymers functioned as hole-blocking layers

due to their low-lying HOMO levels, originating from the strong n-type building block of NDI. Further work was conducted by Liu *et al*. on a similar system, for which they varied the loading of NDI in the polymers via substitution with fluorene units, bearing straight alkyl chains.[14] They concluded that conjugated poly(electrolytes) with a greater loading of n-type NDI units resulted in a larger electron mobility and a highest PCE.
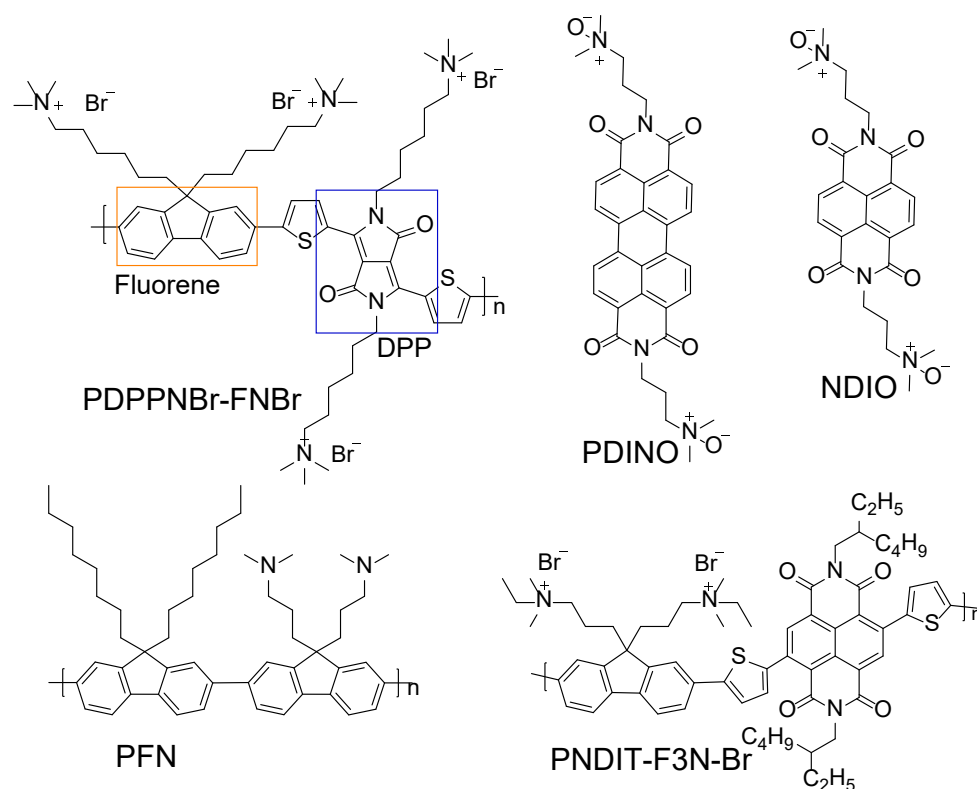
Figure 7.1: Chemical structures of the interface materials PDPPNBr-FNBr, NDIO, PDINO, PFN, and PNDIT-F3N-Br.

In this chapter, preliminary results are reported for six NDI based CIL polymers of varying structures. The six polymers poly[*N,N′*-bis(3-dimethylaminopropyl)naphthalene-1,4,5,8-bis(dicarboximide)-2,6-diyl]-alt-2,5-thiophene) (P(NDI3N-T)), poly[*N,N′*-bis(3-dimethylaminopropyl)naphthalene-1,4,5,8-bis(dicarboximide)-2,6-diyl]-alt-1,4-benzene) (P(NDI3N-P)), poly[*N,N′*-bis(3-dimethylaminopropyl)naphthalene-1,4,5,8-bis(dicarboximide)-2,6-diyl]-alt-2,7-(9,9'-dihexylfluorene)) (P(NDI3N-F8)), poly[(*N,N′*-bis(3-(*N,N*-dimethyl)-*N*-ethylammonium)propyl)naphthalene-1,4,5,8-bis(dicarboximide)-2,6-diyl)-alt-2,5-thiophene)]dibromide (P(NDI3N-T-Br)), poly[(*N,N′*-bis(3-(*N,N*-dimethyl)-*N*-ethylammonium)propyl)naphthalene-1,4,5,8-bis(dicarboximide)-2,6-diyl)-alt-1,4-benzene)]dibromide (P(NDI3N-P-Br)), and poly[(*N,N′*-bis(3-(*N,N*-dimethyl)-*N*-ethylammonium)propyl)naphthalene-1,4,5,8-bis(dicarboximide)-2,6-diyl)-alt-2,7-(9,9'-dihexylfluorene))]dibromide (P(NDI3N-F8-Br)) were successfully synthesised in a Suzuki cross coupling reaction. This reaction protocol involves the use of less toxic reagents and is a more environmentally friendly alternative to the Stille coupling

reaction, used in Chapter 6 for the synthesis of PNDIT10N. Note that P(NDI3N-T) has an identical chemical structure to PNDIT10N, however, a distinction is made between the two polymers due to the different reaction conditions used to form this material. These new polymers are modified via the incorporation of new linker units to yield a more favourable light absorption profile, i.e. a smaller overlap with the active layer components. As a result, this leads to a lower parasitic absorption in the interface layer, hence contributing to a higher J_{sc} and increased efficiencies. Two new linkers/co-monomers of varying donor strength are introduced in an attempt to achieve an hypsochromic shift. Additionally, the polarities are considered as these will have a large impact on the film formation in orthogonal processing, for inverted as well as conventional device architectures. Bridging units 9,9'-dihexylfluorene and benzene are chosen as new linkers due to their donor strengths, expected to increase in the order of benzene < fluorene < thiophene,[15-16] as well as their non-polar character. Though a downshift of the energy levels is expected compared to thiophene due to the lower donor strengths (discussed under *Band gap*, Chapter 2), there are other factors such as co-planarity and torsion angles that will affect the energy levels. In regard to polarity, a balanced surface energy is desired to promote film formation during deposition of; i) interface material on electrode, ii) active layer on of interface layer, and iii) interface material on active layer. Additionally, the effects on photoconductivity are investigated for these arrangements/polymers for the incorporation of either tertiary amine or quaternary amine, with bromine counterion, pendant side-groups on the NDI moiety. As a result, these compounds were divided in the non-charged P(NDI3N-T), P(NDI3N-P), AND P(NDI3N-F8) and the conjugated poly(electrolytes) P(NDI3N-T-Br), P(NDI3N-P-Br), AND P(NDI3N-F8-Br) with each group containing the respective linkers thiophene, benzene, and 9,9-dihexylfluorene.

The impact of these structural changes, and their effect on performance, was investigated. Moreover, initial tests in polymer solar cells (PSC) were performed for a device architecture of indium tin oxide (ITO)/CIL/TQ1:PC$_{71}$BM/molybdenum oxide (MoO$_x$)/silver (Ag). Deposition of the CILs were conducted from benzyl alcohol (BnOH) for P(NDI3N-T), P(NDI3N-P), AND P(NDI3N-F8), with option to use methanol-formic acid solvent combinations, and from methanol for P(NDI3N-T-Br), P(NDI3N-P-Br), AND P(NDI3N-F8-Br). All organic layers in the devices were processed via spin coating, with plans to conduct scalable slot-die coating processing on a Mini Roll Coater when thicknesses and orthogonal solvent processing conditions have been optimised.

For further information regarding cathode interface materials, refer to Chapter 6.

7.3 Experimental

7.3.1 Synthesis
All solvents, reagents and catalysts were purchased from commercial sources and used as received. The synthesis procedures for the NDI based monomers and polymers are presented below. The quaternary amine containing polymers were synthesised according to a modified literature procedure.[13] The

synthesis details for DANDI and diBrDANDI are found under *6.3.1 Synthesis* in Chapter 6. monoBrDANDI, used for endcapping, is based on a modified literature procedure.[17] Synthesis of P(NDI3N-T-Br), P(NDI3N-P-Br), AND P(NDI3N-F8-Br) are also based on a modified literature with increased equivalents of reactants.[13]

7.3.1.1 monoBrDANDI

DANDI (3 g, 6.9 mmol) was dissolved in 9 mL 98 % sulphuric acid under stirring in a 100 mL round-bottom flask (RBF). Dibromantin (Sigma-Aldrich, 98%) (1.97 g, 6.9 mmol) was divided in to four portions which were added at 15 minute intervals. The RBF was tightly sealed upon addition of the first portion and then re-sealed after each addition. The reaction mixture was, after a total reaction time of 12 hours, poured on crushed ice and then neutralised with sodium hydroxide pellets. The colour of the solution went from a strong yellow to grey-brown and material started precipitating. The grey-brown suspension was extracted with chloroform 3 times leaving a strong red solution. The chloroform solution was dried over potassium sulphate and then concentrated on a rotary evaporator. After purification by column chromatography (19:1 chloroform: triethylamine) a red-orange solid was obtained. Yield: 1.95 g (55%).

^{1}H NMR (CDCl$_3$, 600 MHz) δ: 8.94 (s, 1H), 8.82 (d, t = 7.6 Hz, 1H), 8.77 (d, t = 7.6 Hz, 1H), 4.29 (m, 4H), 2.48 (m, 4H), 2.25 (d, t = 7.7 Hz, 12H), 1.97 (m, 4H).

7.3.1.2 P(NDI3N-T) / PNDIT10N

diBrDANDI (0.6 g, 1.0096 mmol), 2,5-Thiophenediylbisboronic acid (0.1561 g, 0.9086 mmol, eq. 0.9), tris(dibenzylideneacetone)dipalladium(0) (0.0185 g, 0.0202 mmol) and tri(*o*-tolyl)phosphine (0.0246 g, 0.0808 mmol) were added to a RBF. The flask was consequently flushed with nitrogen five times. Toluene (40 mL), water (2.02 mL) and Aliquat 336 (6 drops) were added to the flask by syringe through a septum. The reaction vessel was lowered in to a 90 °C preheated oil bath and reacted for 48 hours under vigorous stirring. The polymer was endcapped, first with monoBrDANDI and then with phenylboronic acid pinacol ester (40 mg).

The reaction mixture was allowed to cool to room temperature and was the poured on 150 mL of hexane. The resulting precipitate, a fine dark-orange powder, was filtered and collected. Soxhlet extraction was performed for 24 hours for each of the solvents; hexane, acetone, ethyl acetate, and chloroform. The chloroform fraction was poured on hexane and precipitated product was collected using a polymer filtration setup with a PTFE membrane yielding a black product. Yield: 182 mg (53%).

^{1}H NMR (CDCl3, 600 MHz) δ: 8.96 (m, 1H), 7.45 (m, 1H), 4.22 (m, 4H), 2.43 (m, 4H), 2.23 (m, 12H), 1.92 (m, 4H), 1.25 (s, 2H), 0.86 (m, 2H). IR: v_{max} = 2966sh, 2935, 2858, 2813, 2762, 2719sh, 1702, 1655, 1568, 1526, 1512sh

7.3.1.3 P(NDI3N-P)

diBrDANDI (0.5 g, 0.8413 mmol), 1,4-benzenediboronic acid bis(pinacol)ester (0.2777 g, 0.8413 mmol), tris(dibenzylideneacetone)dipalladium(0) (0.0154 g, 0.0168 mmol) and tri(*o*-tolyl)phosphine (0.0205 g, 0.0673 mmol) were added to a RBF. The flask was consequently flushed with nitrogen five times. Toluene (34 mL), Water (1.68 mL) and Aliquat 336 (5 drops) were added to the flask by syringe through a septum. The the reaction vessel was lowered in to a 90 °C preheated oil bath and reacted for 48 hours under vigorous stirring. The polymer was endcapped, first with phenylboronic acid pinacol ester (40 mg) and then with bromobenzene (0.25 mL).

The reaction mixture was allowed to cool to room temperature and was the poured on 150 mL of hexane. The resulting precipitate, a fine dark-orange powder, was filtered and collected. Soxhlet extraction was performed for 24 hours for each of the solvents; hexane, acetone, ethyl acetate, and chloroform. The chloroform fraction was poured on hexane and precipitated product was collected using a polymer filtration setup with a PTFE membrane yielding a black product. Yield: 200 mg (48%).

^{1}H NMR (CDCl3, 600 MHz) δ: 8.89 (m, 2H), 7.65 (m, 4H), 4.25 (m, 4H), 2.47 (m, 4H), 2.29 (m, 12H), 1.96 (m, 4H). IR: v_{max} = 2937, 2857, 2815, 2770, 1702, 1659, 1608, 1576, 1512

7.3.1.4 P(NDI3N-F8)

diBrDANDI (0.5 g, 0.8413 mmol), 9,9-dihexylfluorene-2,7-diboronic acid (0.2777 g, 0.8413 mmol), tris(dibenzylideneacetone)dipalladium(0) (0.0154 g, 0.0168 mmol) and tri(*o*-tolyl)phosphine (0.0205 g, 0.0673 mmol) were added to a RBF. The flask was consequently flushed with nitrogen five times. Toluene (27 mL), Water (1.35 mL) and Aliquat 336 (5 drops) were added to the flask by syringe through a septum. The reaction vessel was lowered in to a 90 °C preheated oil bath and reacted for 48 hours under vigorous stirring. The polymer was endcapped, first with phenylboronic acid pinacol ester (40 mg) and then with bromobenzene (0.25 mL).

The reaction mixture was allowed to cool to room temperature and was the poured on 150 mL of hexane. The resulting precipitate, a fine dark red powder, was filtered and collected. Soxhlet extraction was performed for 24 hours for each of the solvents; hexane, acetone, ethyl acetate, and chloroform. The chloroform fraction was poured on hexane and precipitated product was collected using a polymer filtration setup with a PTFE membrane yielding a black-red product. Yield: 241 mg (38%).

^{1}H NMR (CDCl3, 600 MHz) δ: 8.83 (s, 2H), 7.95 (m, 2H), 7.50 (m, 2H), 7.45 (s, 2H), 4.19 (m, 4H), 2.39 (m, 4H), 2.23 (s, 12H), 1.89 (m, 4H), 1.17 (m, 16H), 0.81 (m, 6H). IR: v_{max} = 2952sh, 2923, 2896sh, 2866sh, 2853, 2813, 2783sh, 2762, 2718, 1704, 1662, 1609, 1578

7.3.1.5 P(NDI3N-T-Br)

P(NDI3N-T) (100 mg) was added to a dry RBF and flushed with nitrogen three times. Anhydrous THF (40 mL) and DMF (20 mL) were added and the resulting solution was stirred vigorously to suspend the polymer in the solvent combination. The RBF was covered with aluminium foil to shield the reaction

from ambient light. Bromoethane, in ~80 times excess, was added and the reaction was stirred vigorously for 96 h under nitrogen atmosphere in the dark. The reaction flask was uncovered prior to removing the THF and DMF on a rotary evaporator. Interestingly, the product was initially suspended in the solvent but appeared to slowly dissolve as the THF and bromoethane were removed. The polymer was then precipitated in THF and the resulting suspension was centrifuged at 4000 rpm for 20 minutes. The supernatant was discarded and the solid was washed with THF five times. The product was dried in the centrifuge tube and collected as a dark blue/black solid. Yield: 126 mg (90%).

IR: v_{max} = 3018, 2959, 2922sh, 2880sh, 2857sh, 2717, 2687, 1702, 1655, 1612, 1572, 1524

7.3.1.6 P(NDI3N-P-Br)
P(NDI3N-P-Br) was prepared by the same procedure as described above for P(NDI3N-T-Br). The reaction was run with P(NDI3N-P) (100 mg) as starting material. Product was achieved as a dark blue/black solid. Yield: 125 mg (89%).

IR: v_{max} = 3020, 2952, 2863sh, 2822, 2698, 1699, 1653, 1606, 1574, 1514

7.3.1.7 P(NDI3N-F8-Br)
P(NDI3N-F8-Br) was prepared by the same procedure as described above for P(NDI3N-T-Br). The reaction was run with P(NDI3N-F8) (100 mg) as starting material. Product was achieved as a dark red solid. Yield: 116 mg (94%).

IR: v_{max} = 3020, 2953sh, 2923, 2899sh, 2864sh, 2848, 1700, 1658, 1616sh, 1576

7.3.2 Material characterisation

7.3.2.1 Thermogravimetric analysis (TGA)
Thermogravimetric analysis (TGA) was performed on a PerkinElmer Thermogravimetric Analyzer 8000. Samples were dried in a vacuum oven at 25ºC for 24 hours prior to the measurement and then for an additional 30 minutes under a dry nitrogen stream in the instrument. Measurements were conducted from 25- 400 ºC at a scan rate of 10 ºC/minute.

7.3.2.2 Electrochemistry
Square-wave voltammetry (SWV) measurements for P(NDI3N-T), P(NDI3N-P), and P(NDI3N-F8) were carried out according to the procedure for polymer PNDIT10N presented under *6.3.3 Material characterisation* in Chapter 6, that is as thin films on the platinum electrode with a 0.10 M solution of tetrabutylammonium hexafluorophosphate (Bu$_4$NPF$_6$) in anhydrous acetonitrile as supporting electrolyte. P(NDI3N-T-Br), P(NDI3N-P-Br), and P(NDI3N-F8-Br) were measured, with the same supporting electrolyte, in solution instead of film.

7.3.2.3 Ultra-violet visible spectroscopy
Optical absorption spectra for the small molecule NFAs were recorded for both solution and thin film on a Perkin Elmer Lambda 950 spectrophotometer at a scan rate of 10 nm s^{-1}.

Solution spectra were measured in BnOH for both the tertiary (P(NDI3N-T), P(NDI3N-P), AND P(NDI3N-F8)) as well as quaternary (P(NDI3N-T-Br), P(NDI3N-P-Br), AND P(NDI3N-F8-Br)) amine containing polymers. Thin film spectra were measured on thin films drop casted from a methanol solution with addition of 5% v/v formic acid for P(NDI3N-T), P(NDI3N-P), AND P(NDI3N-F8) both prior to/after thermal annealing of the films at 130 °C for 5 minutes. Thin film absorbance/transmission spectra for P(NDI3N-T-Br), P(NDI3N-P-Br), AND P(NDI3N-F8-Br) were instead recorded on films spun from 0.5 and 20 mg mL^{-1} methanol solutions at 2000 and 3000 rpm respectively for 60 seconds.

Photodoping absorption spectra were recorded for thin films. These thin films were drop casted from solutions with concentrations of 10 mg mL^{-1} with a solvent combination of BnOH:CHCl$_3$ in a 1:9 ratio for P(NDI3N-T), P(NDI3N-P), AND P(NDI3N-F8) and methanol for P(NDI3N-T-BR), P(NDI3N-P-BR), AND P(NDI3N-F8-BR). The thin films were stored in darkness for a minimum of 48 hours before the measurement, and then illuminated with a handheld UV lamp (UVGL-58, UVP) with light of a wavelength of 365 nm for a 10 minute sequence prior to being remeasured. This procedure was repeated three times for a combined illumination time of 30 minutes. The films were removed from the spectrophotometer for the UV treatment, meaning the original position could not be guaranteed, therefore, all data was normalised based on the major polymer peaks.

7.3.2.4 Contact angle measurements

Static contact angle of deionized water against the surfaces was measured using a PAT-1 tensiometer (Sinterface Technologies, Germany). Reported contact angles are average values over four measurements on different areas of the films.

The cleaning procedure of ITO-coated glass substrates (10 Ω/sq, Xin Yan Technology LTD) is described under *4.3.4 Device fabrication* in Chapter 4.

CILs were deposited from a 0.5 mg mL^{-1} MeOH solution with 100 µL deposition volume and spin coated at 2000 rpm for 60 seconds. Washing solvent deposition volumes were kept to 100 µL, with the exception of chloroform for which 200 µL was used, to imitate deposition of the active layer. The active layers were deposited according to:

TQ1 and PC$_{71}$BM were dissolved in a 1:2.5 weight ratio at 80 °C under stirring for a minimum of 3 hours in 1,2-dichlorobenzene (*o*-DCB) with addition of 2% v/v 1-chloronaphthalene (CN), offering a final concentration of 25 mg mL^{-1}. Films were then spun from the warm (80 °C) solution at 500 rpm for 60 seconds followed by 2000 rpm for 30 seconds.

TQ1 and PNDI-T10 were dissolved in a 1:1 weight ratio in chloroform under stirring at a concentration of 9 mg mL^{-1}. Films were spun at 2000 rpm for 60 seconds for a deposition volume of 200 µL, followed by thermal annealing at 130 °C for 10 minutes.

7.3.3 Electron spectroscopy

Ultraviolet photoelectron spectroscopy (UPS) follows the procedure presented under *6.3.4 Electron spectroscopy* in Chapter 6.

7.3.4 Film characterisation

7.3.4.1 Profilometer

Thickness measurements were carried out on a mechanical stylus profilometer, DektakXT (Bruker). Films were spun from a 20 mg mL^{-1} methanol solution at 2000 rpm for 60 seconds. A scratch was made in the films and the height difference was measured to provide the film thickness. Values are provided as an average over a minimum of three measurements.

7.3.4.2 NICISS

Neutral impact collision ion scattering spectroscopy (NICISS) measurements were carried out to determine film thicknesses, following the same procedure presented under *6.3.2 Film characterisation* in Chapter 6.

7.3.5 Device fabrication

The device fabrication followed the procedure described under *Device fabrication* in Chapter 6.

P(NDI3N-T), P(NDI3N-P), AND P(NDI3N-F8) were dissolved in BnOH under vigorous stirring at ambient temperatures for a concentration of 0.5 mg mL^{-1}. P(NDI3N-T-Br), P(NDI3N-P-Br), and P(NDI3N-F8-Br) were instead dissolved in MeOH under vigorous stirring at ambient temperatures for concentrations 0.5 mg mL^{-1}. The solutions were deposited via spin coated at 3000 rpm for 60 seconds.

For the active layer, TQ1 and PC$_{71}$BM were dissolved in a 1:2.5 weight ratio at 80 ºC under stirring for a minimum of 3 hours in *o*-DCB for a concentration of 25 mg mL^{-1}. Films were then spun from the warm (80 ºC) solution at 500 rpm for 60 seconds followed by 2000 rpm for 30 seconds.

7.4 Results and discussion

7.4.1 Synthesis

The monomer DANDI was synthesised in an environmentally friendly step, described in Chapter 6, with only water as solvent for an excellent yield of 94%. MonoBrDANDI and diBrDANDI, also described in Chapter 6, were brominated in a consecutive step achieving moderate yields. Structures of monomers and intermediates were all confirmed by ^{1}H NMR spectroscopy, see Figure A.26. The synthesis routes for the tertiary amine containing polymers P(NDI3N-T), P(NDI3N-P), AND P(NDI3N-F8) are presented in Scheme 7.1. These polymers were synthesised in a palladium catalysed Suzuki cross coupling reaction in moderate yields of ~40-50% and then further reacted in a second step to achieve the quaternary amine containing polymers P(NDI3N-T-Br), P(NDI3N-P-Br), AND P(NDI3N-F8-Br) in excellent yields. This reaction was conducted under darkness, utilising a large excess of

bromoethane. The reaction started as a dispersion with the starting material insoluble in the reaction mixture with the solubility steadily increasing during the course of the reaction. However, the product was found to adhere to the walls of the flask at the end of the reaction, complicating collection of the material, thereby lowering the yield.

Polymers P(NDI3N-T-Br), P(NDI3N-P-Br), AND P(NDI3N-F8-Br) experienced elevated solubilities in MeOH compared to their insoluble, tertiary amine containing, counterparts. Solutions of P(NDI3N-T-Br) and P(NDI3N-F8-Br) in MeOH formed films without visual defects from spin-coating at concentrations as high as 10 mg mL^{-1}. This was not the case for P(NDI3N-P-Br) for which defects were observed at concentrations above 5 mg mL^{-1}. Differences in solubility between the polymers were attributed to varying polarities and bulkiness of the linker moieties as well as molecular weight variations. P(NDI3N-F8)/P(NDI3N-F8-Br) with a highly non-polar fluorene linker is expected to possess the highest solubility in common laboratory solvents. Interestingly, P(NDI3N-T)/P(NDI3N-T-Br) appeared to easily dissolve in chloroform and is therefore expected to possess a lower molecular weight than PNDIT10N (Chapter 6) which proved near insoluble in common chlorinated processing solvents. Though, no molecular weights could be elucidated for any of the CILs with size exclusion chromatography (SEC) due to strong interactions between the polymer pendant side-groups and the stationary phase, as is discussed for PNDIT10N in section *6.4.1 Synthesis*, Chapter 6. All polymers proved insoluble in less toxic processing solvents such as THF and *o*-xylene. Thus, these solvents would be good candidates for active layer deposition in orthogonal solvent processing for inverted device structures.
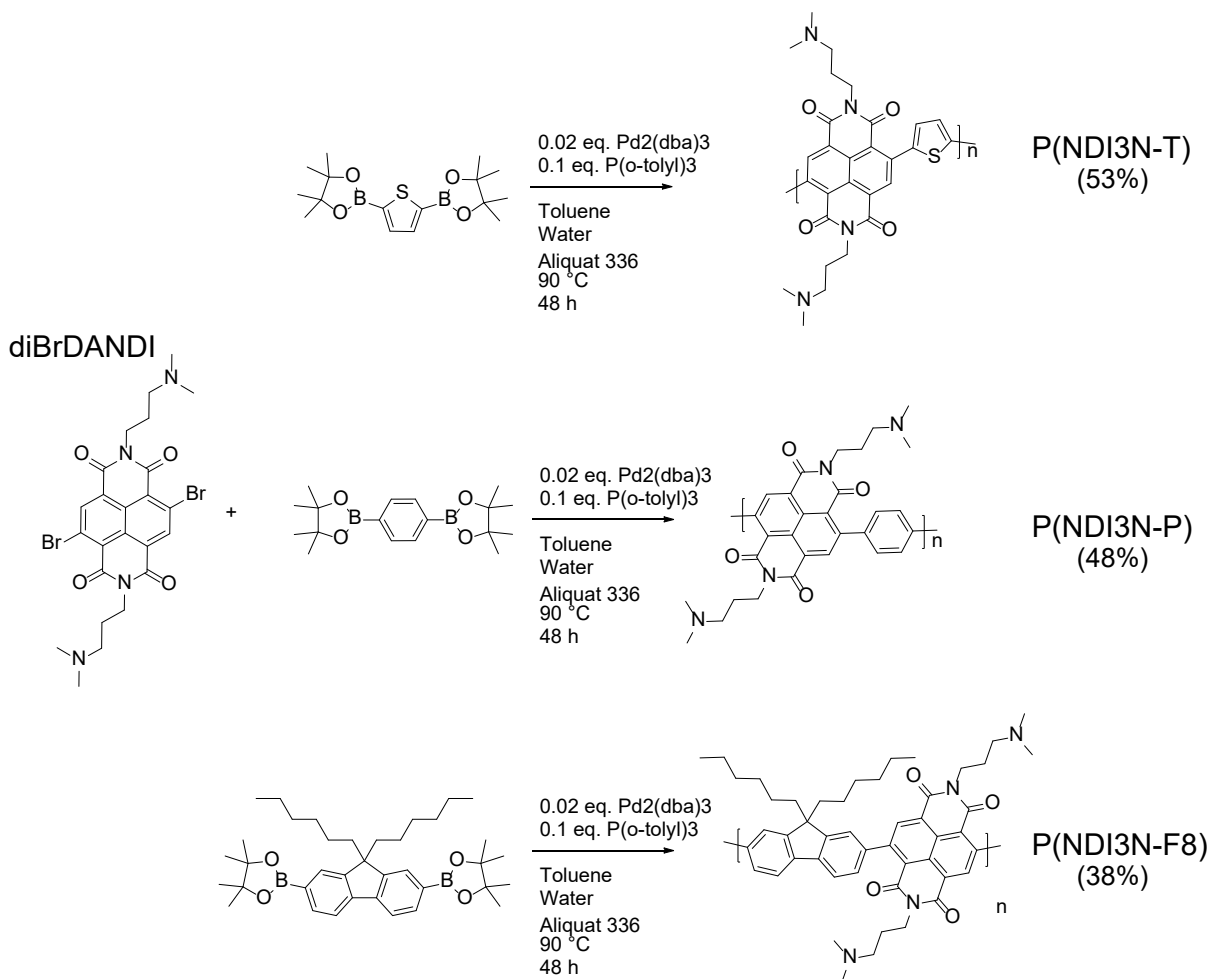
Scheme 7.1: Synthesis routes for the three tertiary amine containing polymers P(NDI3N-T), P(NDI3N-P), and P(NDI3N-F8).

7.4.2 Film thicknesses

The thicknesses of the ultra-thin CIL films coated on top of ITO-coated glass were studied with neutral impact collision ion scattering spectroscopy (NICISS). As in Chapter 6 under *6.4.2 Film thickness* the thicknesses were determined from the delayed onset of indium (In) and tin (Sn) due to the energy loss experienced by the helium projectiles when traversing the CIL. Thicker films were instead investigated by profilometer. Ultra-thin films were achieved for the CILs when spin coated from 0.5 mg mL^{-1} BnOH solution at 3000 rpm for 60 seconds with thicknesses determined to be 2.3 nm, 2.3 nm, 1.6 nm, 1.9 nm, 1.9 nm, and 1.9 nm for P(NDI3N-T), P(NDI3N-P), P(NDI3N-F8), P(NDI3N-T-Br), P(NDI3N-P-Br), and P(NDI3N-F8-Br) respectively. Additional films deposited from MeOH solutions were measured for thicknesses of 5.2 nm/103 nm, 2.5 nm/141 nm, and 3.8 nm/150 nm for P(NDI3N-T-Br), P(NDI3N-P-Br), and P(NDI3N-F8-Br) respectively when spin coated from 0.5 mg mL^{-1}/20 mg mL^{-1} solutions at 3000 rpm/2000 rpm, Table 7.1.

Table 7.1: Tabulated thicknesses for the CILs when deposited on top of ITO-coated glass under various conditions. Ultra-thin films were measured with NICISS with thicker films measured by profilometer.

| CIL | NICISS | | Profilometer |
	BnOH, 0.5 mg mL^{-1} [nm]	MeOH, 0.5 mg mL^{-1} [nm]	MeOH, 20 mg mL^{-1} [nm]
P(NDI3N-T)	2.3	-	-
P(NDI3N-P)	2.3	-	-
P(NDI3N-F8)	1.6	-	-
P(NDI3N-T-Br)	1.9	5.2	103
P(NDI3N-P-Br)	1.9	2.5	141
P(NDI3N-F8-Br)	1.9	3.8	150

7.4.3 Material properties

The thermal stabilities of the six CILs were measured by thermogravimetric analysis (TGA), with results showing a 5% weight loss at 230-290 °C and 200-240 °C for P(NDI3N-T), P(NDI3N-P), and P(NDI3N-F8) and P(NDI3N-T-Br), P(NDI3N-P-Br), AND P(NDI3N-F8-Br) respectively. These differences between tertiary amine containing and quaternary amine containing CILs could arise due to the formation of hydrates for the latter. These hydrates would be stable under the pre-drying conducted at ambient temperature and reduced pressure in a vacuum oven prior to the measurements, as is illustrated with fourier transform infrared spectroscopy (FTIR) in Figure A.6, showing corresponding water peaks for P(NDI3N-T-Br), P(NDI3N-P-Br), AND P(NDI3N-F8-Br) post pre-drying of the samples. The FTIR samples were also pre-dried in a vacuum oven at ambient temperature and reduced pressure, showing large peaks in the 3100-3700 nm region for P(NDI3N-T-Br), P(NDI3N-P-Br), and P(NDI3N-F8-Br) indicating the presence of O-H stretches and water in the samples.
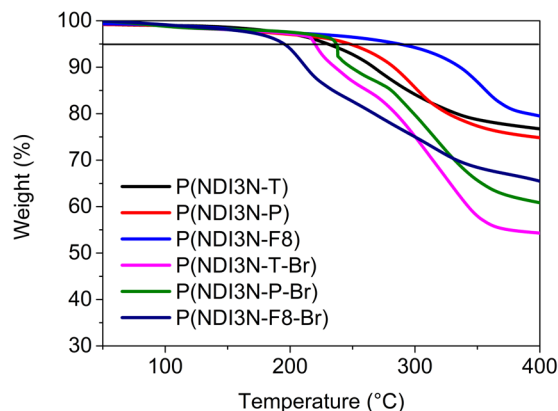
Figure 7.2: TGA spectra of tertiary amine containing polymers P(NDI3N-T), P(NDI3N-P), AND P(NDI3N-F8) and quaternary amine containing polymers P(NDI3N-T-BR), P(NDI3N-P-BR), AND P(NDI3N-F8-BR) showing the thermal stability.

To investigate the film forming abilities of the CILs when employed in conventional device structure the contact angles were measured. In the inverted device structure, the CILs are deposited directly on ITO, forming an interfacial dipole that contributes to the good film forming ability. In the conventional structure the wetting of the CILs, or conjugated polyelectrolytes, might be limited on the hydrophobic surfaces of the active layers due to their strong hydrophilic character that is endowed by the charged side-groups.[18] For the quaternary amine containing polymers P(NDI3N-T-Br) and P(NDI3N-P-Br) contact angles of 82.4° and 76.0° respectively were measured, for the CILs spin coated on top of TQ1:PNDI-T10 with a contact angle of 88.5°, simulating an all polymer solar cell active layer (Table 7.2). These contact angles measured could be an indication of partial coverage of the CIL due to a bad film forming ability on the more hydrophobic active layer. Conversely, the more hydrophobic character of P(NDI3N-F8-BR), originating from the hexyl side-groups on the fluorene unit, appeared to contribute to a uniform coverage with a contact angle of 43.5°, compared to 45.0° when coated on ITO and 44.3° when coated on TQ1:PC$_{71}$BM. To further investigate if these unexpectedly high contact angles were caused by a bad film forming ability P(NDI3N-T-Br) and P(NDI3N-P-Br) were spin coated on top of a polymer:fullerene blend, possessing a somewhat lower contact angle of 81.9° than the 90.7° of TQ1:PNDI-T10. Additionally, amine containing compounds are known to interact with the fullerenes,[19-20] possibly assisting in the film forming process. Under the same processing conditions a decrease in contact angles to 32.5° and 30.7° was observed for P(NDI3N-T-Br) and P(NDI3N-P-Br) respectively. Thus, a more uniform film was probably achieved with this system, indicating that the film formation, or wetting, could prove complex in the conventional device structure. This is an issue for both cathode and anode interface materials when employed in conventional and inverted devices structures respectively.[18] Maximising the charges contributes to a strong interfacial dipole, low work function, efficient charge extraction and high PCEs,[7-8, 14] but could compromise the wettability and film

forming ability on top of the active layer. Moreover, the wettability of the active layer is affected in inverted devices as well when spin coated on top of the hydrophilic CIL.

Table 7.2: Contact angles of the six CILs on ITO, ITO/TQ1:PNDI-T10, and ITO/TQ1:PC$_{71}$BM. W=wetting at a contact angle of <20°.

CIL	ITO	TQ1:PNDI-T10	TQ1:PC$_{71}$BM
No CIL	27.8°	90.7°	81.9°
P(NDI3N-T-BR)	W	82.4°	30.7°
P(NDI3N-P-BR)	W	76.0°	32.5°
P(NDI3N-F8-BR)	45.0°	43.5°	44.3°

Depending on if the CILs are applied in conventional or inverted device structure this layer will hinder light from reaching the active layer, thus, reducing the J_{sc} and PCE of the PSC device. This is more crucial in inverted devices where the light will pass through the CIL before reaching the active layer. For conventional devices the light will instead pass through the active layer first, with negative effects only present if the device contains a reflective back electrode, allowing reflected light to pass the active layer. To elucidate any possible negative effects due to light absorption in the CILs the absorption of the six polymers were measured with UV/vis for solution and thin film, Figure 7.3a-c. In the thin film UV/vis spectrum it was observed that the two polymers with benzene and fluorene linker experienced a hypsochromic shifted onset of 556/533 nm and 635/596 nm, for P(NDI3N-P)/P(NDI3N-P-Br) and P(NDI3N-F8)/P(NDI3N-F8-Br) respectively, compared to the polymers with thiophene linker with onsets at 714/683 nm for P(NDI3N-T)/P(NDI3N-T-Br) (Table 7.3). These major peaks are attributed to π-π^{*} transitions and intramolecular charge transfer effects between the NDI units and the linkers. This peak position is correlated to the donor strength of the linkers, increasing in the order of benzene < fluorene < thiophene. P(NDI3N-P) and P(NDI3N-P-Br), with absorption maxima at 463 nm and 478 nm respectively, show a good compatibility with active layer polymer, which typically possess strong absorption at wavelengths of 600-700 nm resulting in a minimal overlap. P(NDI3N-F8) and P(NDI3N-F8-Br) experience strong absorption in part of this region with P(NDI3N-T) and P(NDI3N-T-Br) showing almost complete overlap. Interestingly, the quaternary amine containing polymers (P(NDI3N-T-BR), P(NDI3N-P-Br), AND P(NDI3N-F8-Br)) experience a hypsochromic shift of about 20-40 nm compared to their tertiary amine counterparts, possibly related to doping of the polymer backbone.
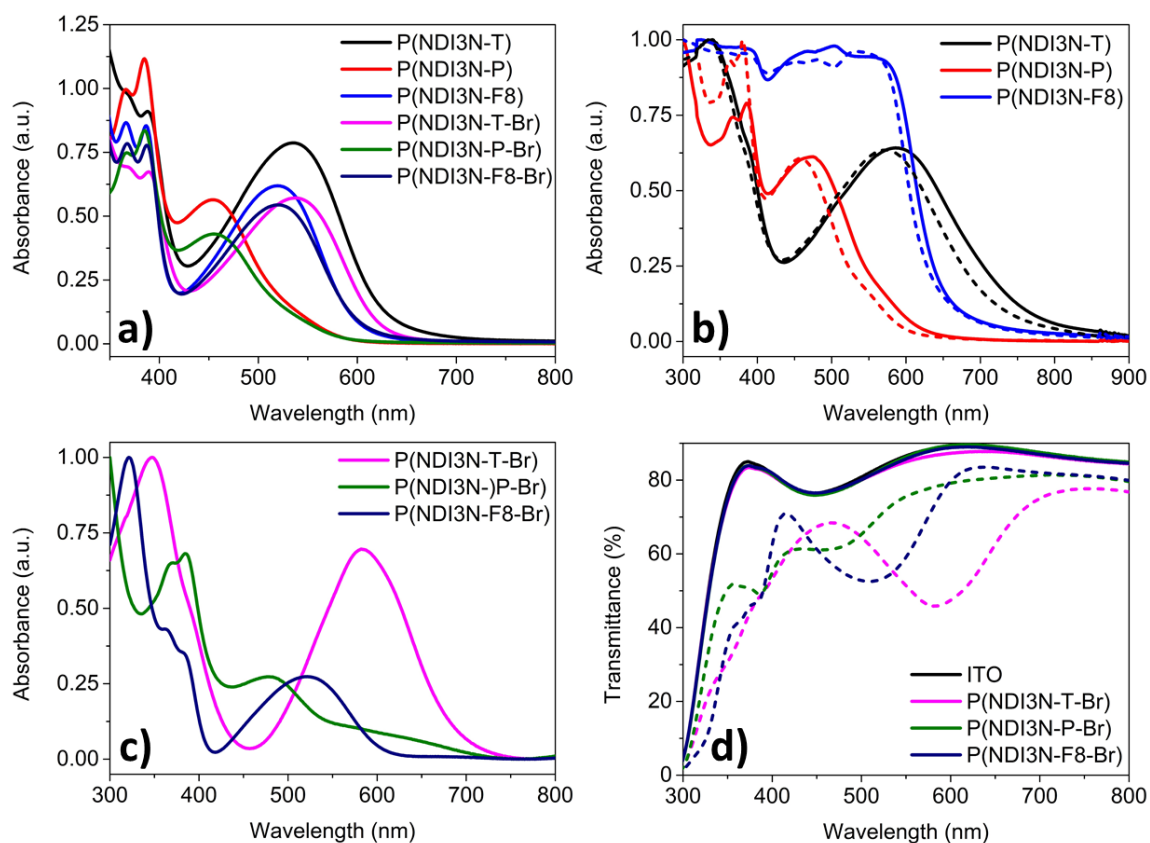
Figure 7.3: UV/vis absorption spectra for a) P(NDI3N-T), P(NDI3N-P), AND P(NDI3N-F8) and P(NDI3N-T-Br), P(NDI3N-P-Br), AND P(NDI3N-F8-Br) in a BnOH solution, b) P(NDI3N-T), P(NDI3N-P), AND P(NDI3N-F8) films spun from methanol with 5% formic acid solutions (solid) and annealed at 130 °C (dotted) with c) showing P(NDI3N-T-Br), P(NDI3N-P-Br), AND P(NDI3N-F8-Br) films spun from methanol. d) Transmittance measurements for P(NDI3N-T-Br), P(NDI3N-P-Br), AND P(NDI3N-F8-Br) for films spun at 2000 rpm from methanol solutions with concentrations of 0.5 (solid) and 20 (dotted) mg mL^{-1}.

Additional measurements were carried out to determine the transmittance of the ITO/conjugated poly(electrolyte) stack for the three conjugated poly(electrolytes) in this region, Figure 7.3d. One thin and one thick film was deposited on ITO-coated glass with spin coating for each of the three conjugated poly(electrolytes). The transmittance at 600 nm is 90% for the ITO-coated glass with P(NDI3N-T-Br), P(NDI3N-P-Br), and P(NDI3N-F8-Br) experiencing transmittance of 87%, 90%, and 89% for thicknesses of 5.2 nm, 2.5 nm and 3.8 nm respectively. For the thicker films the transmittance of P(NDI3N-P-Br) and P(NDI3N-F8-Br) is very similar at 79% and 80% for thicknesses of 141 nm and 150 nm respectively while P(NDI3N-T-Br) experiences a larger drop with a transmittance of 47% despite a thinner film of 103 nm. Therefore, thicker layers of the conjugated poly(electrolytes) will result in lower short-circuit current (J_{sc}) with the biggest drops expected to occur for P(NDI3N-T-Br).

The presence of a photodoping mechanism was investigated for the six CILs, with PNDIT10N already confirmed to photodope in Chapter 6. The same trend, though not as prominent, was observed for

P(NDI3N-T) with the appearance of a broad peak in the IR region, Figure 7.4a. However, P(NDI3N-T-Br) did not show any photo-response other then a slight bathochromic shift of the peak at 1250-2000 nm. This peak is not present in P(NDI3N-T) and could be a result of the inherent doping experienced by the polymer. Similarly, P(NDI3N-P-Br) experiences a peak at 1000-1750 nm that is missing in P(NDI3N-P) and likely originates from the inherent doping, Figure 7.4f. For P(NDI3N-P) a small photo-response was observed after a total of 30 minutes illumination at a wavelength of 365 nm. This delayed response as well as the shape of the curve are not indicative of photo-doping and the emerging peaks are possibly caused by another mechanism. In Figure A.4 and Figure A.5 a gradual decrease in absorbance and split of the major polymer peak at ~450-600 nm is observed in the visible region showing a characteristic photo-doping response.[21] This gradual absorbance decrease contributes to an inflated response in the infrared (IR) region upon normalisation, Figure 7.4g. Though, a small response is still observed in the non-normalised spectra, providing further evidence that the polymer might undergo photodoping.
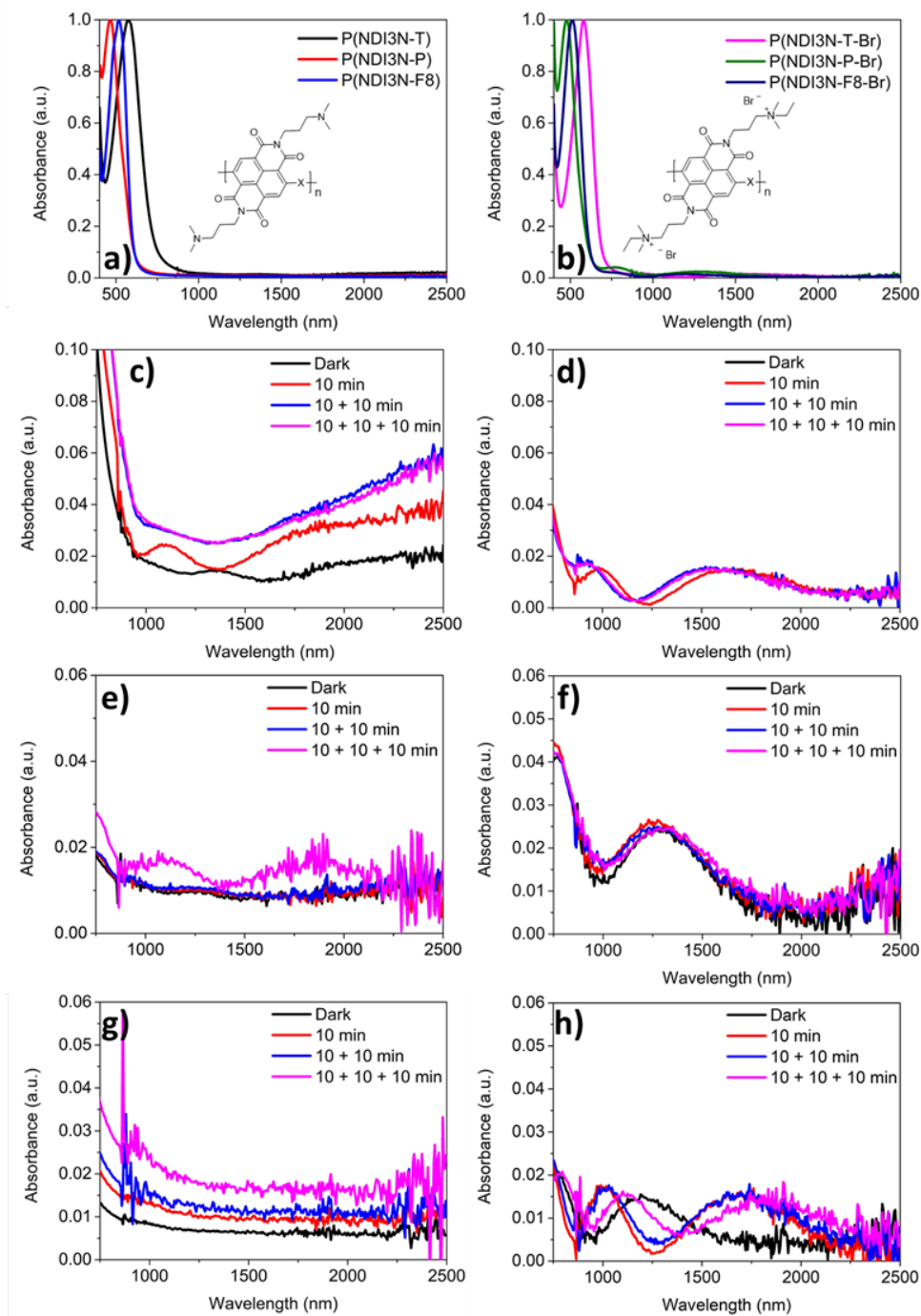
Figure 7.4: Normalised UV/vis spectra showing a) tertiary amine containing polymers and b) quaternary amine containing polymers after 96 h storage in darkness. The photo-doping response is shown in c) for P(NDI3N-T), d) for P(NDI3N-T-Br), e) for P(NDI3N-P), f) for P(NDI3N-P-Br), g) for P(NDI3N-F8), and h) for P(NDI3N-F8-Br) upon illumination with light (wavelength of 365 nm) with a handheld UV-lamp for 10 minute increments.

Square-wave voltammetry (SWV) was measured for estimation of the HOMO and LUMO energy levels of the six CILs. For P(NDI3N-P) and P(NDI3N-P-Br), utilising a benzene linker, no oxidation potentials were observed in the stable potential window of acetonitrile[22]. Despite the application of various scan rates, no peak could be elucidated between 0-2.5 V vs Fc/Fc[+]. Given the results from UV/vis

spectroscopy indicating that these two polymers possess the largest band gap, a higher potential of above 1.2 V would be expected. Oxidation/reduction potentials of 1.24 V/-0.99 V, 1.37 V/-1.10 V, 1.32 V/-1.00 V, and 1.29 V/-1.09 V vs Fc/Fc$^+$ were estimated for P(NDI3N-T), P(NDI3N-F8), P(NDI3N-T-Br), and P(NDI3N-F8-Br), respectively (**Figure 7.5**). Thus, according to equations 4.1a and 4.1b, HOMO/LUMO energy levels of -4.14 eV/-6.37 eV, -4.13 eV/-6.50 eV, -4.03 eV/-6.45 eV, and -4.04 eV/-6.42 eV were calculated for P(NDI3N-T), P(NDI3N-F8), P(NDI3N-T-Br), and P(NDI3N-F8-Br), respectively (Table 7.3). Similarly, the reduction potentials for P(NDI3N-P) and P(NDI3N-P-Br) were estimated (-1.10 V and -1.12 V), and the LUMO levels calculated to -4.03 eV and -4.01 eV, respectively.
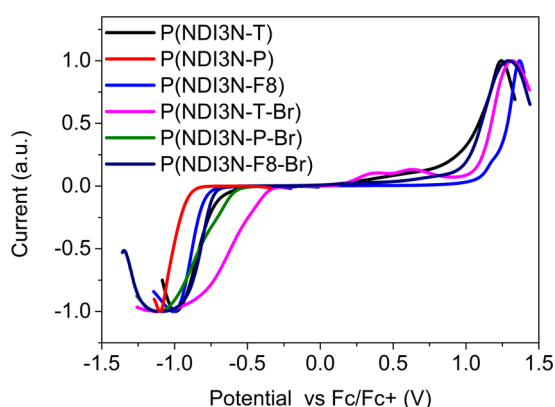
Figure 7.5: SWV spectra of the six polymer CILs investigated in this study.

7.4.4 Work function modification

One function of CILs is to reduce the work function of the electrode to increase the efficiency of the charge carrier extraction via an increase in the internal built in field (E_{in}).[23] This reduction, stemming from the formation of an interfacial dipole,[24] was investigated for the six polymers, when coated on top of ITO-coated glass. These polymers were found to greatly reduce the ITO work functions to 3.8, 3.7, 3.7, 3.9, 3.8, and 3.7 eV for P(NDI3N-T), P(NDI3N-P), P(NDI3N-F8), P(NDI3N-T-Br), P(NDI3N-P-Br), and P(NDI3N-F8-Br) respectively (Table 7.2). These observed reductions in the work function of ~0.8-0.9 eV, compared to ITO at 4.6 eV,[25] are in line or slightly larger than previously reported values of ~0.8 eV for interface materials with tertiary amine or pyridine pendant groups.[26-31] The ultraviolet photoelectron spectroscopy (UPS) spectra in Figure 7.6a-b show the valence band edge and the fermi level band edge, from which the secondary electron cut-offs were estimated.
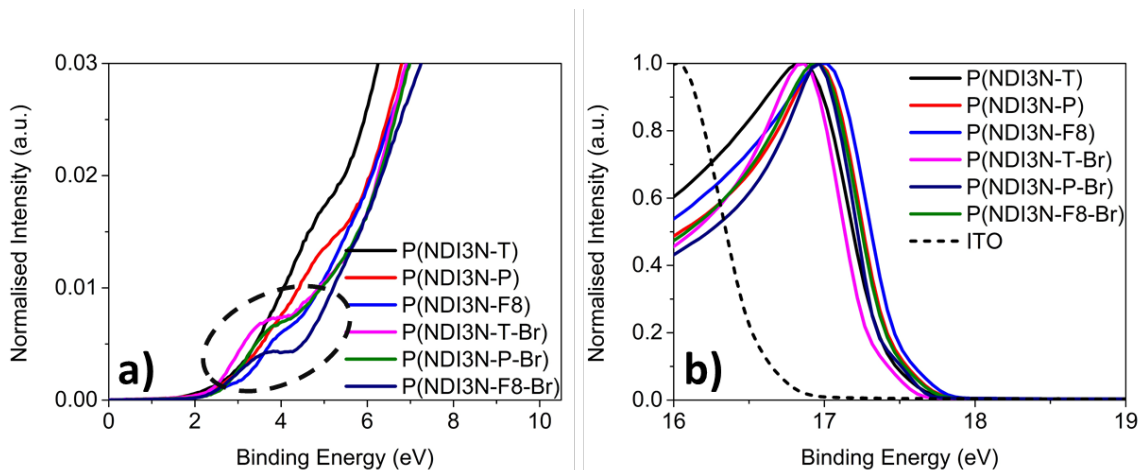
Figure 7.6: UPS spectra of the six conjugated polymer interface materials coated on top of ITO-coated glass with a) showing the valence band edge and b) showing the fermi level edge.

Interestingly, in Figure 7.6a a plateau is observed for the polymers with pendant side-groups containing quaternary amines, though, only minor shoulders in the curves are present for the tertiary amine pendant side-groups. These plateaus are likely originating from the inherent doping of the backbone in P(NDI3N-T-Br), P(NDI3N-P-Br), and P(NDI3N-F8-Br) due to the donation of an electron from the counterion in the pendant side-group to the polymer backbone. This could then indicate that any shoulder in the curves for P(NDI3N-T), P(NDI3N-P), and P(NDI3N-F8) are caused by photodoping, due to the irradiation of UV-light that takes place during the measurement. With these features likely to originate from the pendant side-groups they were omitted for the estimation of the ionisation potential, HOMO level (Table 7.3). This complicated the processing and interpretation of the spectra, contributing to a larger error. However, a reasonable agreement with the electrochemistry of ~0.2 eV is seen for P(NDI3N-T), P(NDI3N-F8), P(NDI3N-T-Br), and P(NDI3N-F8-Br).

Table 7.3: Energy level data for the six cathode interface materials investigated as well as the donor polymer TQ1. Electro chemistry energy levels for P(NDI3N-T), P(NDI3N-P), AND P(NDI3N-F8) are based on measurements conducted on thin film and in solution for P(NDI3N-T-Br), P(NDI3N-P-Br), AND P(NDI3N-F8-Br) with both set of measurements conducted in acetonitrile electrolyte solution. *Data for the fullerenes $PC_{61}BM$ and $PC_{71}BM$ are extracted from literature.[32-33] **Data for TQ1 is taken from Chapter 6.

| | Electrochemistry | | | Optical | | | | UPS | |
| | | | | Solution | Film | | | | |
Polymer	HOMO (eV)	LUMO (eV)	E_g (eV)	λ_{max} (nm)	λ_{max} (nm)	λ_{onset} (nm)	E_g^{opt} (eV)	HOMO (eV)	WF (eV)
P(NDI3N-T)	-6.37	-4.14	2.23	534	574	714	1.74	-6.59	3.8
P(NDI3N-P)	-	-4.03	-	454	463	556	2.23	-6.49	3.7
P(NDI3N-F8)	-6.50	-4.13	2.47	520	541	635	1.95	-6.37	3.7
P(NDI3N-T-Br)	-6.45	-4.03	2.42	538	583	683	1.82	-6.24	3.9
P(NDI3N-P-Br)	-	-4.01	-	455	478	533	2.33	-6.36	3.8
P(NDI3N-F8-Br)	-6.42	-4.04	2.38	519	521	596	2.08	-6.55	3.7
**TQ1	-5.94	-3.67	2.27	613	618	695	1.78	-	-
*$PC_{61}BM$	-6.5	-4.2	2.3	-	-	-	-	-	-
*$PC_{71}BM$	-6.44	-4.14	2.3	-	-	-	-	-	-

7.4.5 Photovoltaic performance

The performance of the six CILs were investigated in the inverted device structure of ITO/CIL/Active layer/MoO_x/Ag for a TQ1:$PC_{71}BM$ active layer. The photovoltaic performance for the CILs, with ZnO for comparison, is shown in Table 7.4 and Figure 7.7. Interestingly, no data was attained for P(NDI3N-T) due to widespread shorting of the PSC devices. With P(NDI3N-T) experiencing an elevated solubility compared to PNDIT10N (Chapter 6) it is possible that the material was partially, or fully, washed away during deposition of the BHJ layer, thereby contributing to the large number of shorts.

The remainder of the CILs experienced varying efficiencies with a highest PCE of 3.4% achieved for P(NDI3N-P-BR). This is also higher than the 2.7% of the best ZnO device that was fabricated for comparison. The better performance of P(NDI3N-P-BR) based devices originates from simultaneous improvements in J_{sc} and fill factor (FF) of 7.14 mA cm^{-2} and 51% respectively. This could be considered large improvements compared to a J_{sc} of 5.74 mA cm^{-2} and FF of 47% for ZnO based reference devices. Though, the PCE was only slightly lower for the tertiary amine counterpart, P(NDI3N-P), with a highest PCE of 3.1%. P(NDI3N-P) experienced comparably high currents but possessed a lower FF of 42%, resulting in the overall lower PCE. The rest of the CILs performed below ZnO with PCEs of 2.3%, 2.6%, and 2.0% for P(NDI3N-T-BR), P(NDI3N-F8), and P(NDI3N-F8-BR) respectively. Of note, the open circuit voltages (V_{oc}) of P(NDI3N-F8) and P(NDI3N-F8-BR), with a fluorene linker unit, were lower than the other devices by about 0.11-0.12 V. Moreover, the large uncertainties in J_{sc} and V_{oc} seen for P(NDI3N-F8-BR) in Figure 7.7 could be an indication of another system experiencing partial coverage of the CIL, resulting in major differences over the individual devices on each substrate. Conversely, the highest performing P(NDI3N-P-BR) devices experienced the smallest uncertainty out of all systems.

Table 7.4: Photovoltaic performance for the six CILs in inverted device structure with a TQ1:PC$_{71}$BM (1:2.5) active layer.

CIL	J_{sc} [mA cm^{-2}]	V_{oc} [V]	FF [%]	PCE [%]	Max
P(NDI3N-T)	-	-	-	-	-
P(NDI3N-P)	6.91± 0.13	0.881±0.022	42±4	2.6±0.3	3.1
P(NDI3N-F8)	6.46±0.49	0.741±0.046	40±4	1.9±0.4	2.6
P(NDI3N-T-BR)	5.43±0.31	0.878±0.019	42±4	2.0±0.2	2.3
P(NDI3N-P-BR)	7.14±0.18	0.862±0.004	52±1	3.2±0.1	3.4
P(NDI3N-F8-BR)	6.54±0.91	0.731±0.148	31±9	1.4±0.4	2.0
ZnO	5.74±0.25	0.877±0.038	47±4	2.4±0.3	2.7
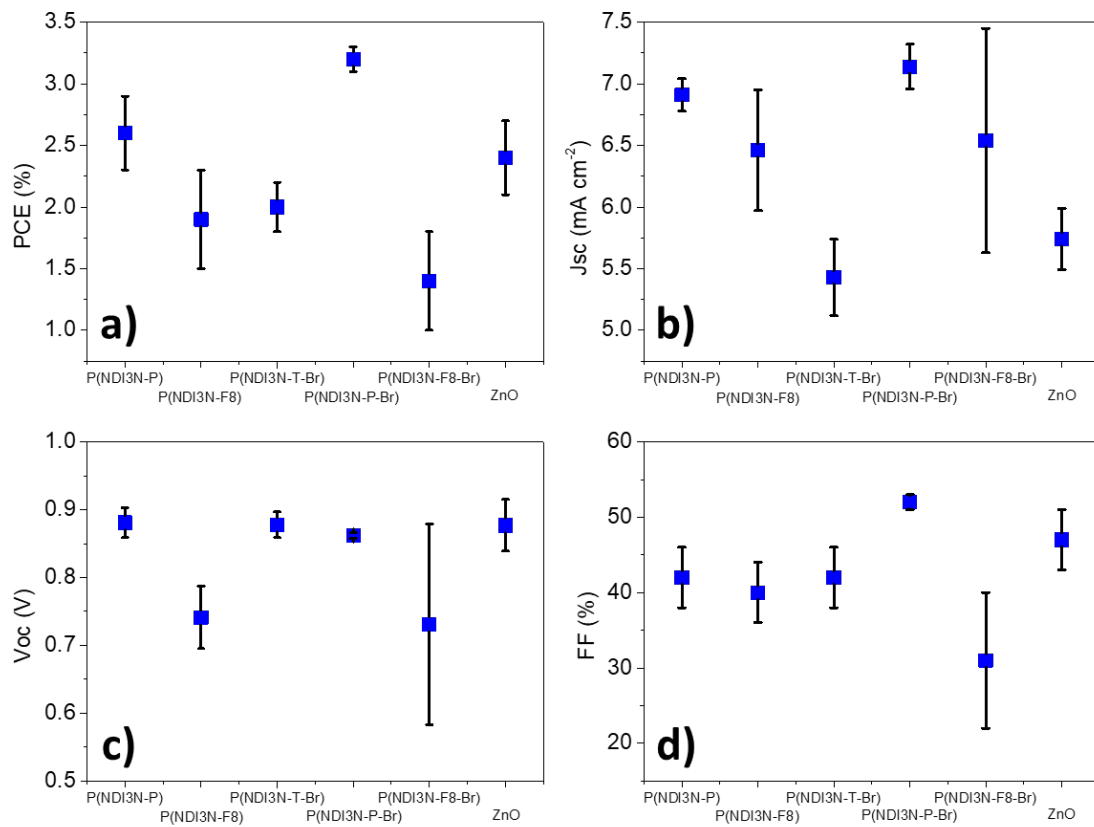
Figure 7.7: Comparison of photovoltaic performance of the best TQ1:PC$_{71}$BM devices incorporating the polymeric CILs with a) showing PCE, b) J$_{sc}$, c) V$_{oc}$, and d) FF.

7.5 Conclusion

In summary, the six n-type CILs were successfully synthesised in a Suzuki coupling reaction. Incorporating a thin layer of these CILs on top of ITO-coated glass were found to reduce the work function of ITO by ~0.8-0.9 eV, showing results in line with literature.

Contact angle measurements concluded that the film forming ability of the quaternary amine containing CILs is limited in conventional devices for all-polymer solar cells. For ultra-thin layers only P(NDI3N-F8-BR) with a non-polar fluorene linker, was successfully spin coated on top of a simulated all-polymer BHJ layer, achieving comparable contact angles to when deposited on ITO-coated glass. However, deposition on top of polymer:fullerene BHJ layer succeeded for all systems.

The doping mechanism of the quaternary amine containing polymers was shown to be inherent to the structure and no photo response was observed in the UV/vis/NIR spectra between 400-2500 nm. For P(NDI3N-T) and P(NDI3N-F8) a photo response, indicative of photodoping, was observed in the visible and IR region respectively upon illumination with UV light. For P(NDI3N-P) with a stronger p-type linker these peaks could not be observed, indicating that no photo doping is present for this polymer at these conditions. Despite the polymers possessing close to identical LUMO levels according to electrochemistry.

Preliminary performance tests for ultra-thin CILs were conducted in inverted solar cells with a device architecture of ITO/CIL/TQ1:PC$_{71}$BM/MoOx/Ag. These devices experienced low efficiencies for P(NDI3N-T-BR) and P(NDI3N-F8-BR) with P(NDI3N-F8) and P(NDI3N-P-BR) instead outperforming ZnO based devices. A highest PCE of 3.4%, attributed to simultaneous improvement in J$_{sc}$ and FF, was achieved for P(NDI3N-P-BR) at a thickness of 2.5 nm. P(NDI3N-T) experienced excessive shorting and it is assumed the layer was washed off by the active layer processing solvent due to a high solubility, caused by low molecular weight.

Further fine tuning of these materials is needed to achieve robust CILs for use in PSC devices. For this purpose, molecular modelling would be beneficial, providing a preliminary comparison between different linkers/co-monomers. Polarity as well as molecular weight tuning is needed to achieve orthogonal processing in both conventional and inverted device structures for these CILs. Moreover, an in-depth study of the doping mechanism could elucidate the effects of irradiation, correlating it to the degree of doping and also conductivity. Additional work is also required to determine the role of the interfacial dipole strength on charge extraction efficiency from the active layer. Lastly, the working mechanism for charge transport of ultra-thin to thicker layers needs further attention to elucidate at what thickness tunnelling is overcome by conduction as the major charge transport phenomena, thus, also clarifying when low lying HOMO levels, or hole blocking, starts to play a role in the PCE.

7.6 Contributions

Amira Ramadan Alghamdi: Performed NICISS and electron spectroscopy measurements including part of the interpretation and analysis.

Dr. Yanting Yin: Assisted in the interpretation of electron spectroscopy data.

Dr. Sait Elmas: Performed FTIR measurements.

Prof. Gunther Andersson: Has assisted in the analysis of NICISS and electron spectroscopy data.

Prof. Mats R. Andersson: Contributed to the design and synthesis strategy of the six CILS as well as the analysis of photovoltaic performance data.

7.7 References

(1)   Huang, F.; Wu, H.; Wang, D.; Yang, W.; Cao, Y., Novel Electroluminescent Conjugated Polyelectrolytes Based on Polyfluorene. *Chem. Mater.* **2004**, 16, 708-716.

(2)   Zhou, Y.; Fuentes-Hernandez, C.; Shim, J.; Meyer, J.; Giordano, A. J.; Li, H.; Winget, P.; Papadopoulos, T.; Cheun, H.; Kim, J.; Fenoll, M.; Dindar, A.; Haske, W.; Najafabadi, E.; Khan, T. M.; Sojoudi, H.; Barlow, S.; Graham, S.; Brédas, J.-L.; Marder, S. R.; Kahn, A.; Kippelen, B., A Universal Method to Produce Low–Work Function Electrodes for Organic Electronics. *Science* **2012**, 336, 327-332.

(3)   Zhang, Z.-G.; Qi, B.; Jin, Z.; Chi, D.; Qi, Z.; Li, Y.; Wang, J., Perylene Diimides: a Thickness-insensitive Cathode Interlayer for High Performance Polymer Solar Cells. *Energy Environ. Sci.* **2014**, 7, 1966-1973.

(4)   Zhao, K.; Ye, L.; Zhao, W.; Zhang, S.; Yao, H.; Xu, B.; Sun, M.; Hou, J., Enhanced Efficiency of Polymer Photovoltaic Cells via the Incorporation of a Water-soluble Naphthalene Diimide Derivative as a Cathode Interlayer. *J. Mater. Chem. C* **2015**, 3, 9565-9571.

(5)   Liu, Y.; Duzhko, V. V.; Page, Z. A.; Emrick, T.; Russell, T. P., Conjugated Polymer Zwitterions: Efficient Interlayer Materials in Organic Electronics. *Acc. Chem. Res.* **2016**, 49, 2478-2488.

(6)   Chen, L.; Xie, C.; Chen, Y., Influences of Charge of Conjugated Polymer Electrolytes Cathode Interlayer for Bulk-heterojunction Polymer Solar Cells. *Org. Electron.* **2013**, 14, 1551-1561.

(7)   Chen, L.; Liu, X.; Wei, Y.; Wu, F.; Chen, Y., Alcohol-soluble Interfacial Fluorenes for Inverted Polymer Solar Cells: Sequence Induced Spatial Conformation Dipole Moment. *Phys. Chem. Chem. Phys.* **2016**, 18, 2219-2229.

(8)   Liu, H.; Hu, L.; Wu, F.; Chen, L.; Chen, Y., Polyfluorene Electrolytes Interfacial Layer for Efficient Polymer Solar Cells: Controllably Interfacial Dipoles by Regulation of Polar Groups. *ACS Appl. Mater. Interfaces* **2016**, 8, 9821-9828.

(9)   Lim, K.-G.; Park, S. M.; Woo, H. Y.; Lee, T.-W., Elucidating the Role of Conjugated Polyelectrolyte Interlayers for High-Efficiency Organic Photovoltaics. *ChemSusChem* **2015**, 8, 3062-3068.

(10)   Liao, S.-H.; Li, Y.-L.; Jen, T.-H.; Cheng, Y.-S.; Chen, S.-A., Multiple Functionalities of Polyfluorene Grafted with Metal Ion-Intercalated Crown Ether as an Electron Transport Layer for Bulk-Heterojunction Polymer Solar Cells: Optical Interference, Hole Blocking, Interfacial Dipole, and Electron Conduction. *J. Am. Chem. Soc.* **2012**, 134, 14271-14274.

(11)   Gu, C.; Hu, W.; Yao, J.; Fu, H., Naphthalenediimide-Benzothiadiazole Copolymer Semiconductors: Rational Molecular Design for Air-Stable Ambipolar Charge Transport. *Chem. Mater.* **2013**, 25, 2178-2183.

(12)   Tan, Y.; Chen, L.; Wu, F.; Huang, B.; Liao, Z.; Yu, Z.; Hu, L.; Zhou, Y.; Chen, Y., Regulation of the Polar Groups in n-Type Conjugated Polyelectrolytes as Electron Transfer Layer for Inverted Polymer Solar Cells. *Macromolecules* **2018**, 51, 8197-8204.

(13)   Wu, Z.; Sun, C.; Dong, S.; Jiang, X.-F.; Wu, S.; Wu, H.; Yip, H.-L.; Huang, F.; Cao, Y., n-Type Water/Alcohol-Soluble Naphthalene Diimide-Based Conjugated Polymers for High-Performance Polymer Solar Cells. *J. Am. Chem. Soc.* **2016**, 138, 2004-2013.

(14)   Liu, X.; Chen, Z.; Xu, R.; Zhang, R.; Hu, Z.; Huang, F.; Cao, Y., Finely Tuned Composition in Conjugated Polyelectrolytes for Interfacial Engineering of Efficient Polymer Solar Cells. *Small Methods* **2018**, 2, 1700407.

(15)   Hung, Y.-C.; Jiang, J.-C.; Chao, C.-Y.; Su, W.-F.; Lin, S.-T., Theoretical Study on the Correlation between Band Gap, Bandwidth, and Oscillator Strength in Fluorene-Based Donor−Acceptor Conjugated Copolymers. *The Journal of Physical Chemistry B* **2009**, 113, 8268-8277.

(16)   Köse, M. E., Evaluation of Acceptor Strength in Thiophene Coupled Donor–Acceptor Chromophores for Optimal Design of Organic Photovoltaic Materials. *The Journal of Physical Chemistry A* **2012**, 116, 12503-12509.

(17)   Sasikumar, M.; Suseela, Y. V.; Govindaraju, T., Dibromohydantoin: A Convenient Brominating Reagent for 1,4,5,8-Naphthalenetetracarboxylic Dianhydride. *Asian J. Org. Chem.* **2013**, 2, 779-785.

(18)   Xu, B.; Hou, J., Solution-Processable Conjugated Polymers as Anode Interfacial Layer Materials for Organic Solar Cells. *Adv. Energy Mater.* **2018**, 8, 1800022.

(19)   Sun, Y.-P.; Ma, B.; Lawson, G. E., Electron Donor-Acceptor Interactions of Fullerenes C60 and C70 with Triethylamine. *Chem. Phys. Lett.* **1995**, 233, 57-62.

(20)   Ghosh, H. N.; Pal, H.; Sapre, A. V.; Mittal, J. P., Charge Recombination Reactions in Photoexcited Fullerene C60-amine Complexes Studied by Picosecond Pump Probe Spectroscopy. *J. Am. Chem. Soc.* **1993**, 115, 11722-11727.

(21)   Naab, B. D.; Gu, X.; Kurosawa, T.; To, J. W. F.; Salleo, A.; Bao, Z., Role of Polymer Structure on the Conductivity of N-Doped Polymers. *Adv. Electron. Mater.* **2016**, 2, 1600004.

(22)   Elgrishi, N.; Rountree, K. J.; McCarthy, B. D.; Rountree, E. S.; Eisenhart, T. T.; Dempsey, J. L., A Practical Beginner's Guide to Cyclic Voltammetry. *J. Chem. Educ.* **2018**, 95, 197-206.

(23)   Lee, J.-H.; Jeong, S. Y.; Kim, G.; Park, B.; Kim, J.; Kee, S.; Kim, B.; Lee, K., Reinforcing the Built-In Field for Efficient Charge Collection in Polymer Solar Cells. *Adv. Funct. Mater.* **2018**, 28.

(24)   van Reenen, S.; Kouijzer, S.; Janssen, R. A. J.; Wienk, M. M.; Kemerink, M., Origin of Work Function Modification by Ionic and Amine-Based Interface Layers. *Adv. Mater. Interfaces* **2014**, 1, 1400189.

(25)   Bjuggren, J. M.; Sharma, A.; Gedefaw, D.; Elmas, S.; Pan, C.; Kirk, B.; Zhao, X.; Andersson, G.; Andersson, M. R., Facile Synthesis of an Efficient and Robust Cathode Interface Material for Polymer Solar Cells. *ACS Appl. Energy Mater.* **2018**, 1, 7130-7139.

(26)   George, Z.; Xia, Y.; Sharma, A.; Lindqvist, C.; Andersson, G.; Inganas, O.; Moons, E.; Muller, C.; Andersson, M. R., Two-in-one: Cathode Modification and Improved Solar Cell Blend Stability through Addition of Modified Fullerenes. *J. Mater. Chem. A* **2016**, 4, 2663-2669.

(27)   Sharma, A.; Kroon, R.; Lewis, D. A.; Andersson, G. G.; Andersson, M. R., Poly(4-vinylpyridine): A New Interface Layer for Organic Solar Cells. *ACS Appl. Mater. Interfaces* **2017**, 9, 10929-10936.

(28)   Zhang, Y.; Chen, L.; Hu, X.; Zhang, L.; Chen, Y., Low Work-function Poly(3,4-ethylenedioxylenethiophene): Poly(styrene sulfonate) as Electron-transport Layer for High-efficient and Stable Polymer Solar Cells. *Sci. Rep.* **2015**, 5, 12839.

(29)   Courtright, B. A.; Jenekhe, S. A., Polyethylenimine Interfacial Layers in Inverted Organic Photovoltaic Devices: Effects of Ethoxylation and Molecular Weight on Efficiency and Temporal Stability. *ACS Appl. Mater. Interfaces* **2015**, 7, 26167-75.

(30)   He, Z.; Zhong, C.; Su, S.; Xu, M.; Wu, H.; Cao, Y., Enhanced Power-conversion Efficiency in Polymer Solar Cells using an Inverted Device Structure. *Nat. Photonics* **2012**, 6, 591.

(31)   Sharma, A.; George, Z.; Bennett, T.; Lewis, D. A.; Metha, G. F.; Andersson, G. G.; Andersson, M. R., Stability of Polymer Interlayer Modified ITO Electrodes for Organic Solar Cells. *Aust. J. Chem.* **2016**, 69, 735-740.

(32)   Murto, P.; Genene, Z.; Benavides, C. M.; Xu, X.; Sharma, A.; Pan, X.; Schmidt, O.; Brabec, C. J.; Andersson, M. R.; Tedde, S. F.; Mammo, W.; Wang, E., High Performance All-Polymer Photodetector Comprising a Donor–Acceptor–Acceptor Structured Indacenodithiophene–Bithieno[3,4-c]Pyrroletetrone Copolymer. *ACS Macro Lett.* **2018**, 7, 395-400.

(33)   Li, Z.; Xu, X.; Zhang, W.; Meng, X.; Ma, W.; Yartsev, A.; Inganäs, O.; Andersson, M. R.; Janssen, R. A. J.; Wang, E., High Performance All-Polymer Solar Cells by Synergistic Effects of Fine-Tuned Crystallinity and Solvent Annealing. *J. Am. Chem. Soc.* **2016**, 138, 10935-10944.

Chapter 8 – Summary

This thesis presents the results of studies on small molecule NFAs, polymer acceptors, and CILs based on NDI core structures with the aim to develop simple and more environmentally friendly materials. For each material class, a range of compounds were synthesised, incorporating minor chemical structural modifications for the fine tuning of solubilities as well as morphological, and/or optoelectronic properties. The influence on electronic properties and overall device performance was also investigated.

The four NDI based small molecule NFAs DEHNDI, DONDI, AsNDI, and DOBNDI were synthesised via facile synthesis routes and studied in binary-quintenary active layer blends in Chapter 4. Variations in crystal forming ability, due to incorporation of pendant side-groups of varying size/steric hindrance, was observed with UV/vis spectroscopy, DSC, and optical microscopy. The photovoltaic performance, studied in inverted device structure with the donor polymer TQ1, was overall very low at <0.5%. Fine tuning of the donor:acceptor ratios and the incorporation of multiple acceptor components in the active layer blend led to elevated morphological control. Moreover, microscope images revealed that the best performing active layer blend with DONDI experienced micrometre scale phase separation with other active layer blends displaying a more suitable topography in AFM experiencing much lower PCEs. This difference was attributed to a lack of charge carrier pathways in the blends observed to possess lower phase separation and smaller crystal features. Thus, the electron transporting ability of the NFAs is likely correlated to their morphology, with increased phase separation and larger crystal domains enhancing the charge transport.

Apart from extending the conjugation via structural chemical modification, considered to be outside of the scope of this thesis, these compounds should be tested in ternary blends as sole NDI NFA. That is, application of the compounds as third component in ternary blends of donor:acceptor$_1$:acceptor$_2$ structure, where acceptor$_1$ ≠ NDI NFA and acceptor$_2$ = NDI NFA. However, fine tuning of the devices will not explain the low J_{sc} and a general strategy must be applied to elucidate the structure-morphology/crystallinity-performance relationship. While this was touched upon in Chapter 4 further experiments needs to be carried out. These include thermal analysis, mobility measurements, conductivity measurements, as well as additional topography and morphology measurements (e.g. AFM and GIWAXS). Until such measurements are carried out, it can only be theorised that large crystal domains are essential for charge carrier transport in these materials.

In Chapter 5, the influence of alkyl side-group length and/or partial substitution of 2,2'-bithiophene on solubility and photovoltaic performance was studied for six NDI-2,2'-bithiophene based acceptor polymers. Variations in the alkyl side-group length from 2-hexyldecyl to 2-octyldodecyl were studied, with the longer 2-octyldoddcyl groups providing higher PCEs in inverted devices with high performing donor polymer PTB7-Th processed via both spin coating and blade coating. The increase in PCE was observed to correlate well with the higher molecular weights also experienced by the 2-octyldodecyl polymers. Incorporation of 10 mol% thiophene or 3,3'-ditetradecyl-2,2'-bithiopheno was found to yield on-par or better PCEs than pure BT based N2200/N2300. 2-octyldodecyl polymers PNDI-T10 and P(NDI2OD-14T2) showed highest PCEs of 5.04%/4.74% and 4.68%/4.06% (SC/BC), respectively. Furthermore, P(NDI2OD-14T2) was also identified to possess the highest solubility in more environmentally friendly processing solvents such as o-xylene and THF, while PNDI-T10 had a higher PCE compared to N2200* at 4.48%/4.36% for SC/BC devices.

Optimisation of loading of the third co-monomer (3,3'-ditetradecyl-2,2'-bithiophene) as well as variations of its chain length should be explored due to the potential to further elevate the PCEs. The PCE could potentially also be improved via the utilisation of annealing (solvent or thermal) or the use of solvent additives. In a wider perspective, additional experiments are needed to confirm the molecular weight insensitivity observed for blade coating, comparatively to spin-coating, and determine its causes. This would require in-depth study of morphologies achieved for both the techniques at similar drying kinetics. Finally, to determine if these polymers are suitable for large scale manufacturing environmentally friendly synthesis and processing must be considered. Switching from Stille coupling polymerisation to direct arylation polymerisation (DAP) as well as improving atom economy would be a first step towards green processing. For the processing, more environmentally friendly solvents should be employed in roll-to-roll processes, producing minimal waste.

The CIL PNDIT10N was synthesised in facile short-step procedure and investigated in inverted polymer:fullerene solar cells when processed with the more environmentally friendly solvent, BnOH, in Chapter 6. Investigation with UPS revealed a significant work function reduction of the ITO electrode when coated with an ultra-thin layer of CIL. PNDIT10N was found to contribute to record efficiencies for two out of the three donor polymers, achieving a highest PCE of 6.7% for TQ1 and 5.7% for PTNT with PTB7-Th, performing comparably to ZnO based devices. The photovoltaic performance was further studied in scalable fabrication for preliminary devices with CIL and active layer slot die coated under ambient conditions, revealing a PCE of 1.6%. The formation of an interfacial dipole contributed to efficient charge extraction combined with the presence of photodoping, studied with UV/vis/NIR spectroscopy, were proposed to contribute to the high J_{sc} observed for devices incorporating PNDIT10N as a CIL. Importantly, a good stability of an ultra-thin PNDIT10N layer was observed for a 10-day ageing period with films exposed to filtered sunlight retaining part of the work function reduction and high V_{oc}.

Preliminary results for a study on the influence of structural modifications of PNDIT10N derivatives on doping efficiencies and electron transport ability are presented in Chapter 7. A set of six NDI based CILs with tertiary amine or quaternary amine pendant side-groups incorporating thiophene, benzene or fluorene linker units, were synthesised in facile procedures with Suzuki cross coupling applied for polymerisation. As for PNDIT10N, significant reductions of the ITO work functions were observed with UPS. The film forming abilities, studied with static contact angle, proved to be lacking in conventional devices due to the strong hydrophilicity endowed by the exclusive use of amine containing side-groups. Doping of the tertiary amine containing CILs was identified with UV/vis/NIR to be photo dependent with quaternary amine containing CILs instead possessing an inherent doping. Further, the latter was also observed to possess good solubilities in short chain alcohols with the tertiary amine CILs requiring the use acid-short chain alcohol combinations or BnOH. The photovoltaic performance was also investigated in inverted PSCs with a highest PCE achieved for P(NDI3N-P-BR) (benzene linker, quaternary amine) of 3.4% for a TQ1:PC$_{71}$BM active layer, outperforming ZnO based devices.

The three separate areas of self-doping, interfacial dipole strength, and orthogonal processing should be pursued further in order provide a better understanding of this type of amine containing conjugated polymer interface materials. Firstly, self-doping, either inherent or due to photodoping is essential for a high conductivity, allowing for the utilisation of thicker interface layers (~20-100 nm). As a result, these materials can be printed in scalable processes, which typically are unable to deposit ultra-thin films. The doping mechanism is recognised, but the differences between tertiary amines and quaternary amines needs to be thoroughly investigated when using the strong NDI acceptor units. Furthermore, the self-doping efficiency determines the transferability to other materials, thus it should be elucidated. Secondly, the interfacial dipole formation also requires further attention. A comparison between tertiary amine and quaternary amine containing polymers as well as analysis of the polymer orientation on the electrode/active layer surface could provide insight on the relevance of amine density and type. Lastly, to fully determine the structural influence on photovoltaic performance, additional devices in both conventional and inverted structure need to be fabricated, utilising a variety of active layer processing solvents. Structural fine tuning of the CILs is also required to determine the balance between optimal amine group loading and a good film forming ability on hydrophobic (active layer) and hydrophilic (e.g. ITO) surfaces. However, structural changes will also influence the energy levels, light absorption and the incorporation of linkers with varying donor character should be considered. With molecular modelling a large number of potential linker units could be scanned relatively quickly, providing estimates for polymer energy levels.

To conclude, in the particular case of the small molecule NFAs, the photovoltaic performance was extremely low. A possible explanation provided in Chapter 4 is the existence of a trade-off between charge carrier pathways in larger NFA crystals and a suitable morphology for charge carrier generation, which would effectively hamper the PCE. Further studies are needed to confirm this theory, however,

if the hypotheses hold, an extended conjugation is proposed as a possible route to enhance charge carrier transport. Overall, the NDI based materials can be considered well suited for PSC applications with short step facile synthesis routes as well as a good potential for translating results achieved in small scale laboratory setups to more scalable fabrication. The utilisation of an NDI core structure in both acceptor polymers and CILs have yielded high performing materials, showcasing the versatility realised with this n-type building block.

One, remember to look up at the stars and not down at your feet. Two, never give up work. Work gives you meaning and purpose and life is empty without it. Three, if you are lucky enough to find love, remember it is there and don't throw it away.

— Stephen Hawking

Appendix
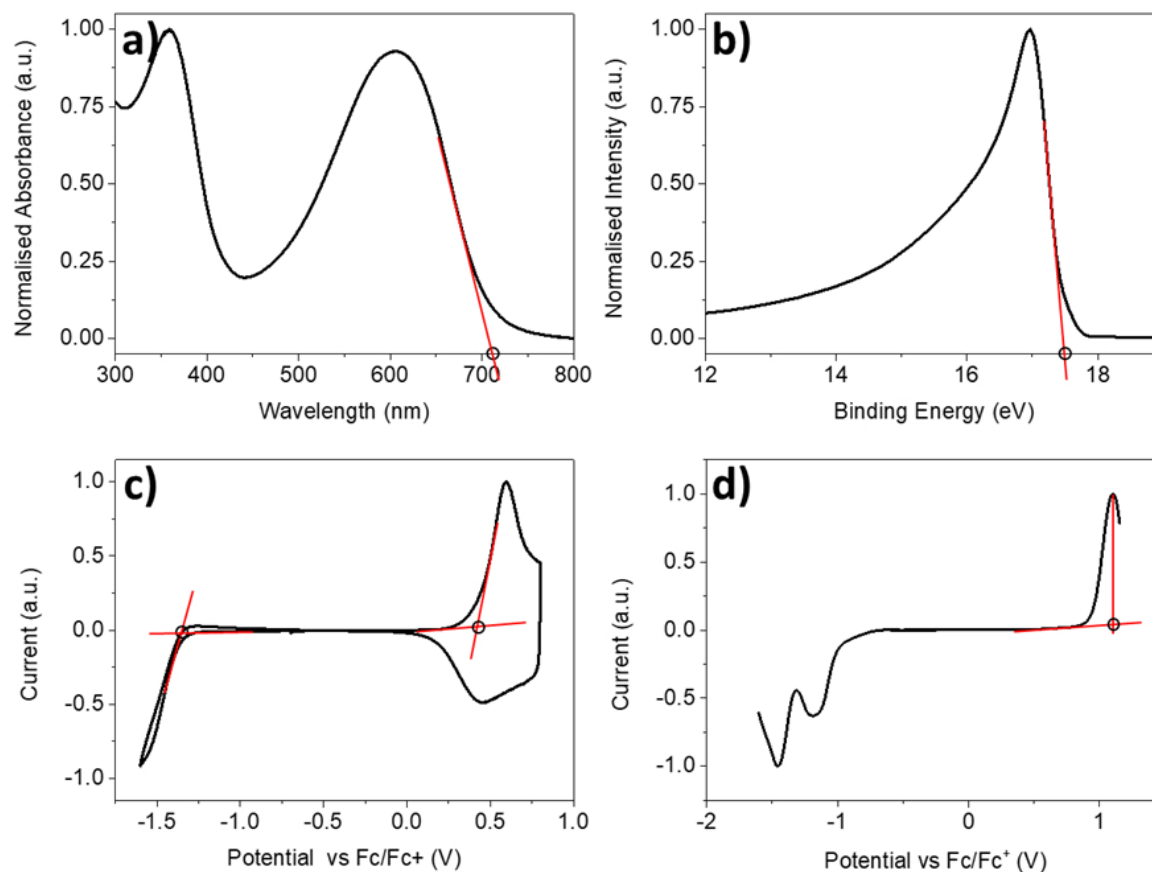
Figure A.1: Illustration of the determination of peak onset in a) UV/vis, b) UPS, and c) CV (electrochemistry) spectra and of peak maxima in d) SWV (electrochemistry) spectra.

A.1 Electrochemistry
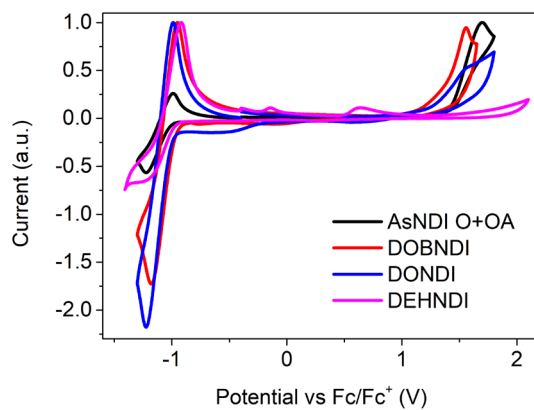
Figure A.2: CV spectra of AsNDI, DOBNDI, and DONDI in dichloromethance electrolyte solution with DEHNDI measured as thin film immersed in acetonitrile electrolyte solution.

Table A.1: Electrochemical properties.

	Polymer	HOMO (eV)	LUMO (eV)	E_g^{ec} (eV)
CIL	PNDIT10N	-6.37	-4.14	2.23
Acceptor	PNDI-T10	-6.34	-4	2.34
	PC$_{61}$BM [a]	-6.5	-4.2	2.3
	PC$_{71}$BM [a]	-6.44	-4.14	2.3
Donor	TQ1	-5.94	-3.67	2.27
	PTNT	-6.29	-3.4	2.89
	PTB7-Th	-5.6	-3.47	2.13

[a] Values taken from literature.[1-2]

A.2 Optical properties

A.2.1 Molar extinction coefficients – SM NFAs

Optical absorption spectra were recorded using 1 x 1 cm quartz cuvettes at a range of concentrations below ~10^{-4} M. The absorbance at 360 nm was determined for the four NFAs and plotted against the concentrations, yielding a linear relation from which the molar extinction coefficients were determined according to the Beer-Lambert-Bouguer law;

$$A = \varepsilon * l * c$$

where A is the absorbance, ε is the molar extinction coefficient, l is the path-length, and c is the concentration. Thus the slope in **Figure A.3** is equal to the molar extinction coefficient, yielding ε of 36.0k, 37.9k, 41.5k, and 10.0k M^{-1} cm^{-1} for DEHNDI, DONDI, AsNDI, and DOBNDI respectively.
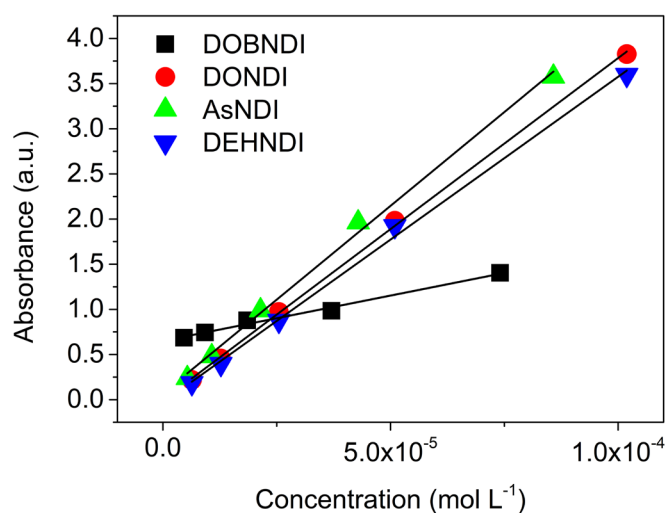
Figure A.3: Absorbance plotted versus concentration for determination of the slope and consequently molar extinction coefficient.

A.2.2 UV/vis – Photodoping CILs
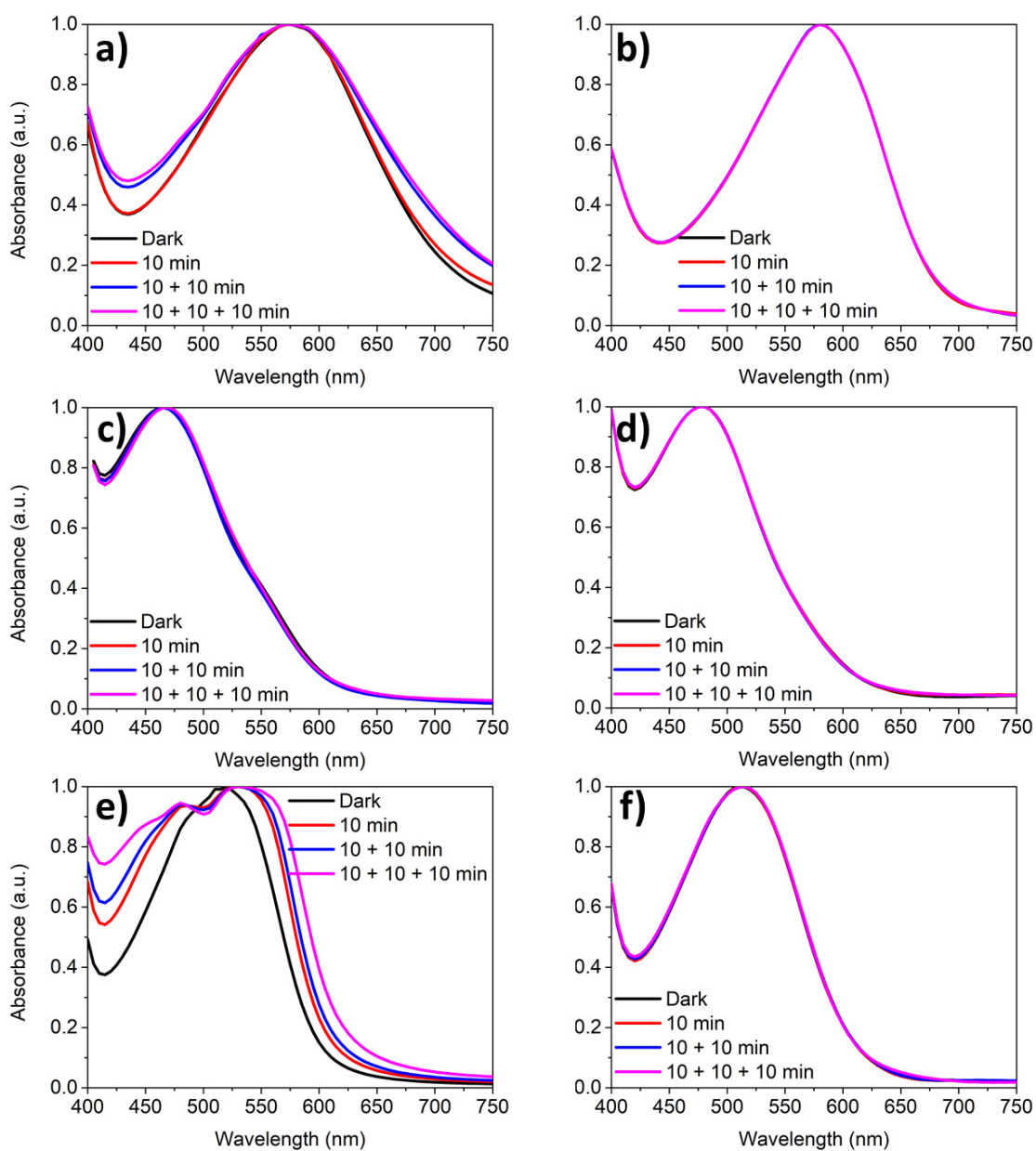
Figure A.4: Normalised UV/vis spectra of tertiary amine and quaternary amine containing polymers after 96 h storage in darkness with a) P(NDI3N-P), b) P(NDI3N-T-BR), c) P(NDI3N-F8), d) P(NDI3N-P-BR), e) P(NDI3N-F8) and f) P(NDI3N-F8-BR) showing the photo-doping response upon illumination with light (wavelength of 365 nm) with a handheld UV-lamp for 10 minute increments.
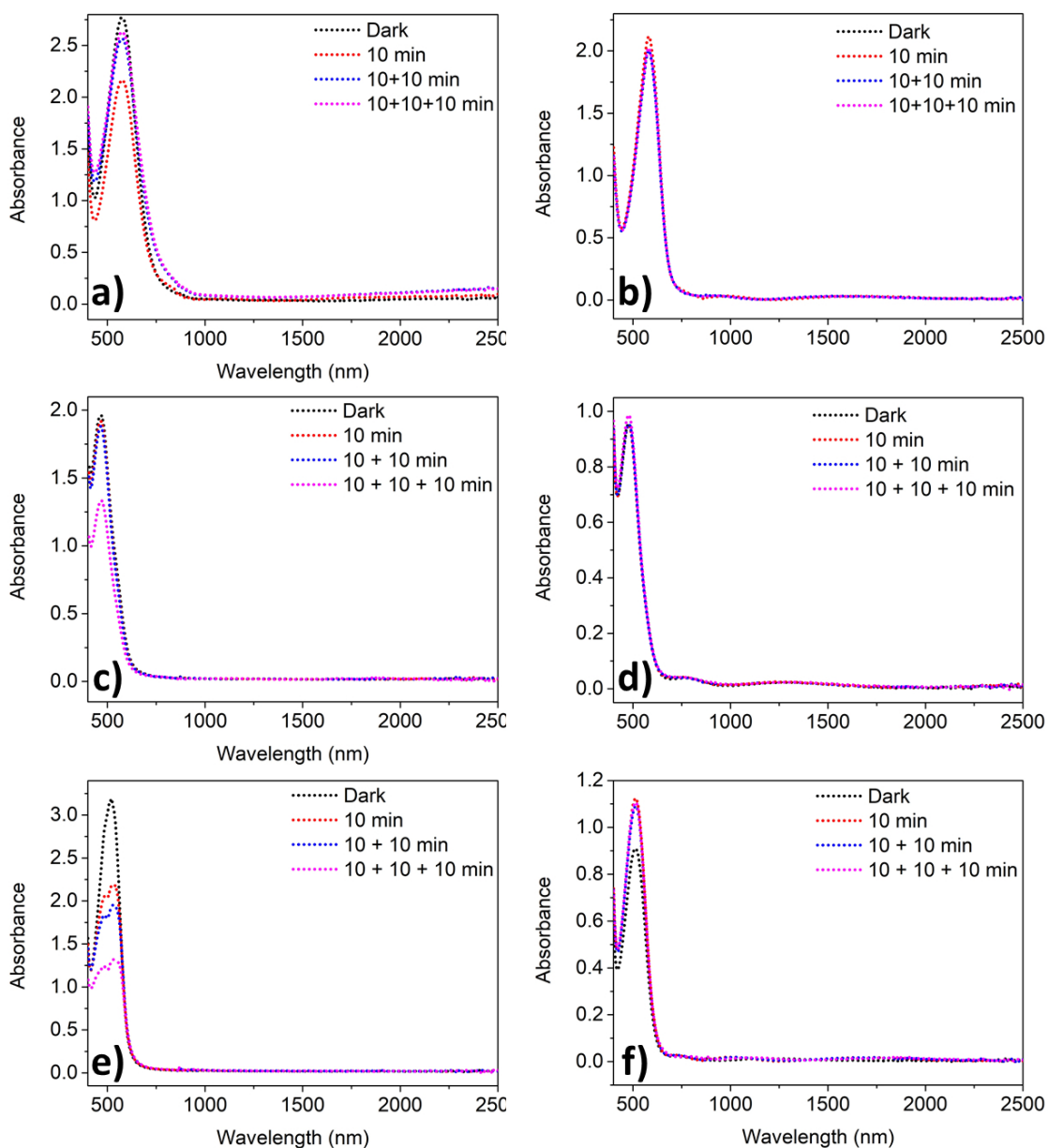
Figure A.5: Non-normalised UV/vis spectra of tertiary amine and quaternary amine containing polymers after 96 h storage in darkness with a) P(NDI3N-P), b) P(NDI3N-T-BR), c) P(NDI3N-F8), d) P(NDI3N-P-BR), e) P(NDI3N-F8) and f) P(NDI3N-F8-BR) showing the photo-doping response upon illumination with light (wavelength of 365 nm) with a handheld UV-lamp for 10 minute increments

A.2.3 Fourier transform infrared spectroscopy (FTIR) - CILs

Thin films of the six polymer interface materials were drop casted on 2.5 x 2.5 cm glass slides. Tertiary amine containing polymers were drop casted from a mixture of $CHCl_3$-BnOH in a 9:1 solvent ratio at 50 °C. Quaternary amine containing polymers were instead drop casted from a MeOH solution at ambient temperatures. The casted films were dried in a vacuum oven at 25ºC for 24 hours prior to the measurements. Measurements were then carried out on a Nexus Nicolet 870 FTIR spectrometer supplied by Thermo Fisher Scientific.
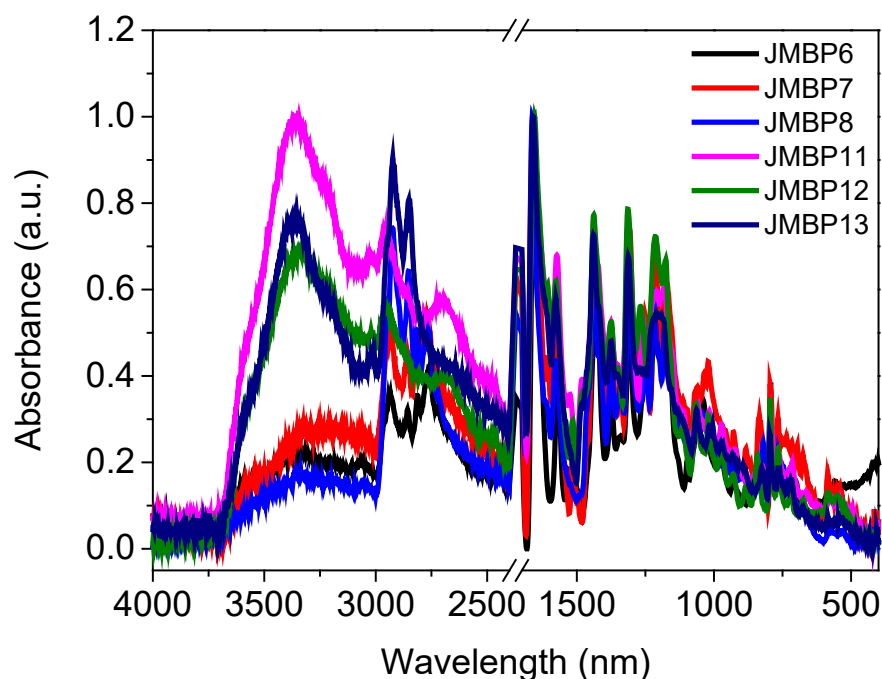
Figure A.6: FTIR spectra of the three tertiary amine containing polymers P(NDI3N-T), P(NDI3N-P), and P(NDI3N-F8) as well as the three quaternary amine containing polymers P(NDI3N-T-BR)-13 with bromine counter-ions.
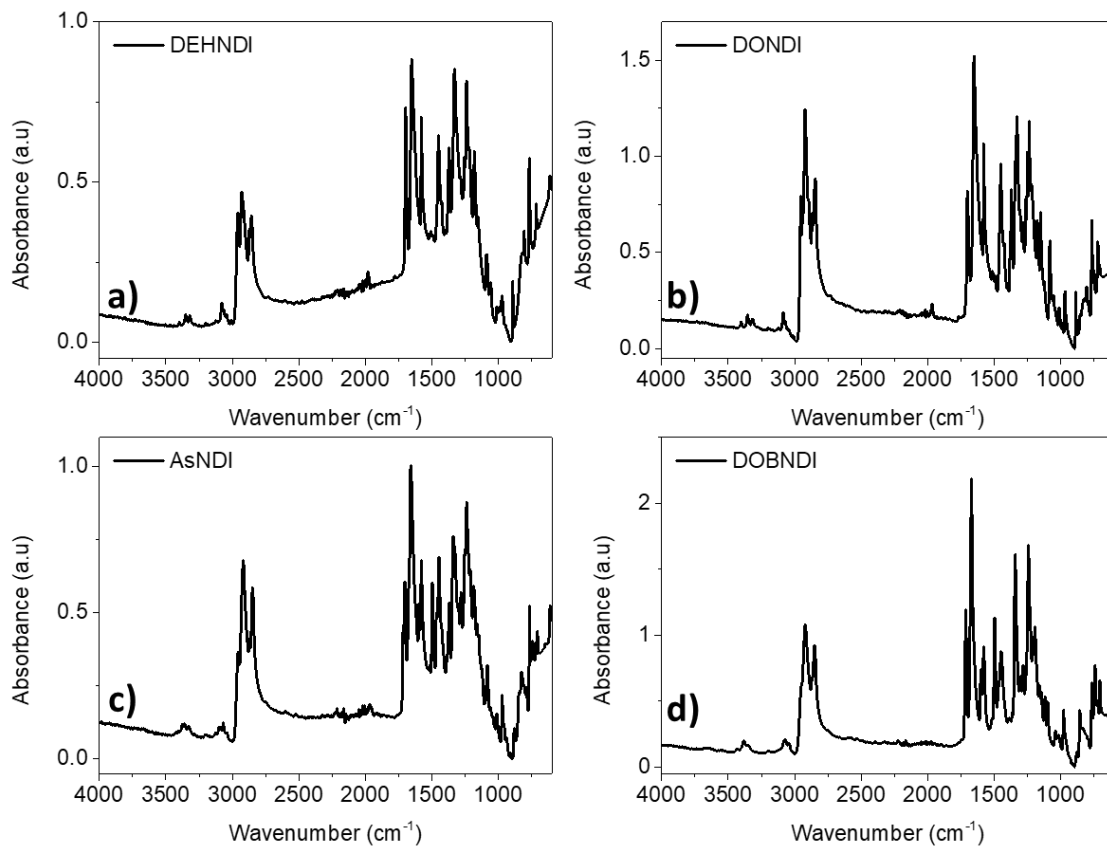
Figure A.7: FTIR spectra of the SM NFAs a) DEHNDI, b) DONDI, c) AsNDI, and d) DOBNDI.

A.2 Optical microscope & AFM
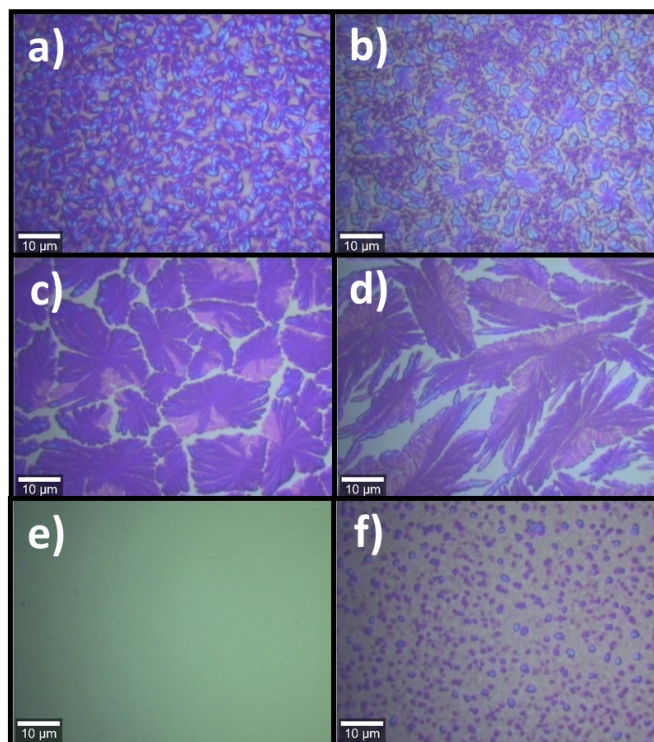
Figure A.8: Representative microscope images taken at 100x magnification for thin films with a 1:1 ratio TQ1:acceptor for a) DEHDNI with b) 2% CN, c) DONDI with d) 2% CN, and a 1:1 ratio TQ1-HD:acceptor for e) AAAA with f) 2% CN.
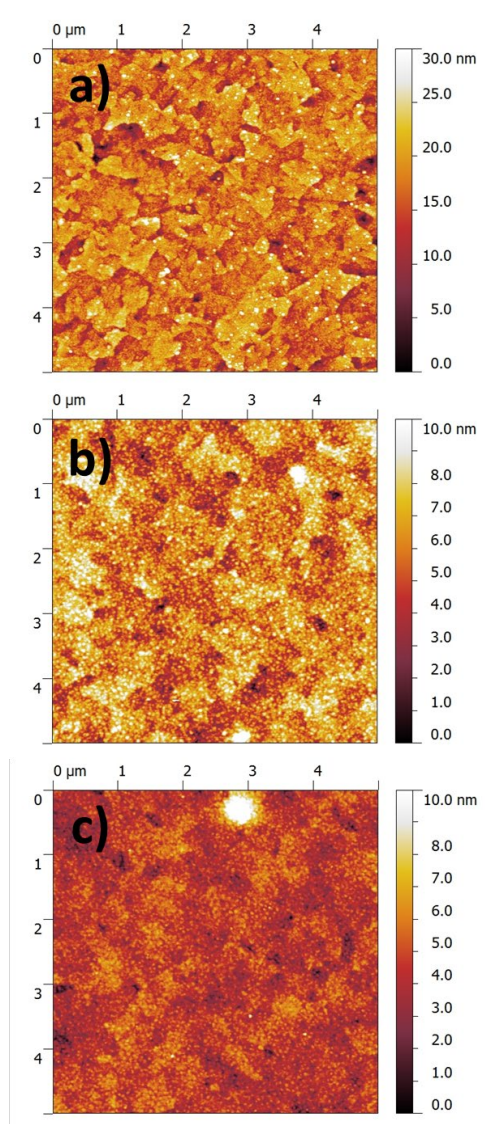
Figure A.9: 5 x 5 µm AFM images of a) PNDIT10N (~3nm) coated on ITO coated glass with b) active layer on top, and c) active layer on top incorporating 2% of the solvent additive 1-chloronaphthalene (CN).

A.3 Thermal analysis
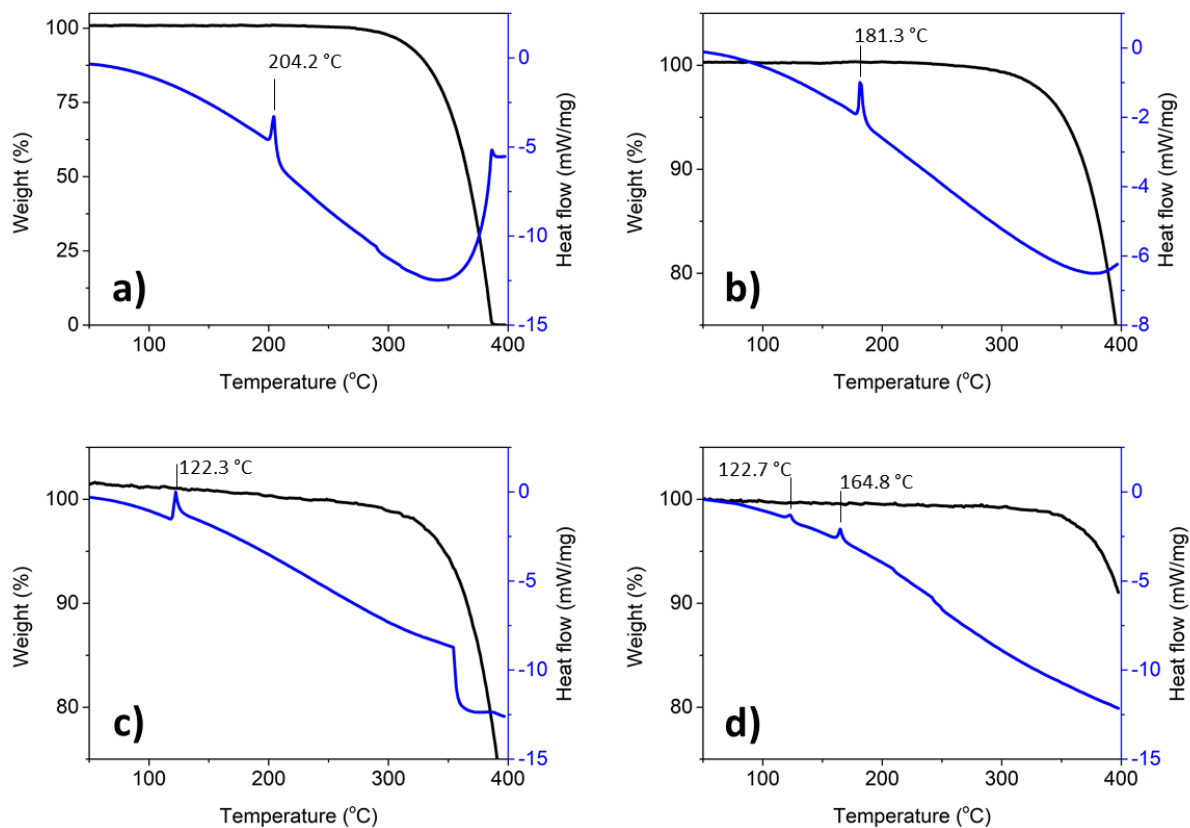
Figure A.10: STA spectra of a) DEHNDI, b) DONDI, c) AsNDI, and d) DOBNDI with the endothermic melting point peaks highlighted.

A.4 Photovoltaic Performance

Table A.2: Photovoltaic performance for devices incorporating PNDIT10N of ~3 nm and ~8.5 nm or ZnO (25-30nm) as CIL [a]

CIL	BHJ	J_{sc} [mA cm^{-2}]	V_{oc} [V]	FF [%]	R_s [Ω cm^{-2}]	PCE [%]	Max [%]
PNDIT10N Film 5 (~8.5 nm)	TQ1:PC$_{71}$BM	9.6 ± 0.3	0.907 ± 0.005	68 ± 1	1.10	5.9 ± 0.2	6.3
	PTNT:PC71BM	7.7 ± 0.2	0.869 ± 0.004	64 ± 8	2.22	4.3 ± 0.1	4.4
ZnO	PTNT:PC$_{71}$BM [b]	7.24 ± 0.24	0.93 ± 0.01	72 ± 1	1.73	4.8 ± 0.2	5.1
	PTB7-Th:PC$_{71}$BM	15.8 ± 0.3	0.789 ± 0.002	58 ± 1	1.04	7.3 ± 0.2	7.5

[a] Mean values ± standard deviation from six devices. [b]Values taken from literature.[3]
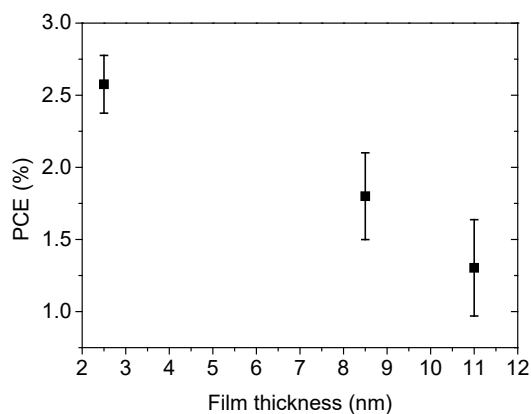
Figure A.11: Thickness dependence for PNDIT10N interface layer in TQ1:PC$_{61}$BM active layer devices. These were manufactured in the same manner as TQ1:PC$_{71}$BM devices with the exception that no solvent additive was used.

A.5 Nuclear Magnetic Resonance (NMR)

[1]H spectra were recorded on a Bruker 600 MHz NMR spectrophotometer with trimethylsilane (TMS) as internal standard. Measurements were conducted in deuterated chloroform (CDCl$_3$) with chemical shifts denoted as δ values (ppm) in regard to TMS.
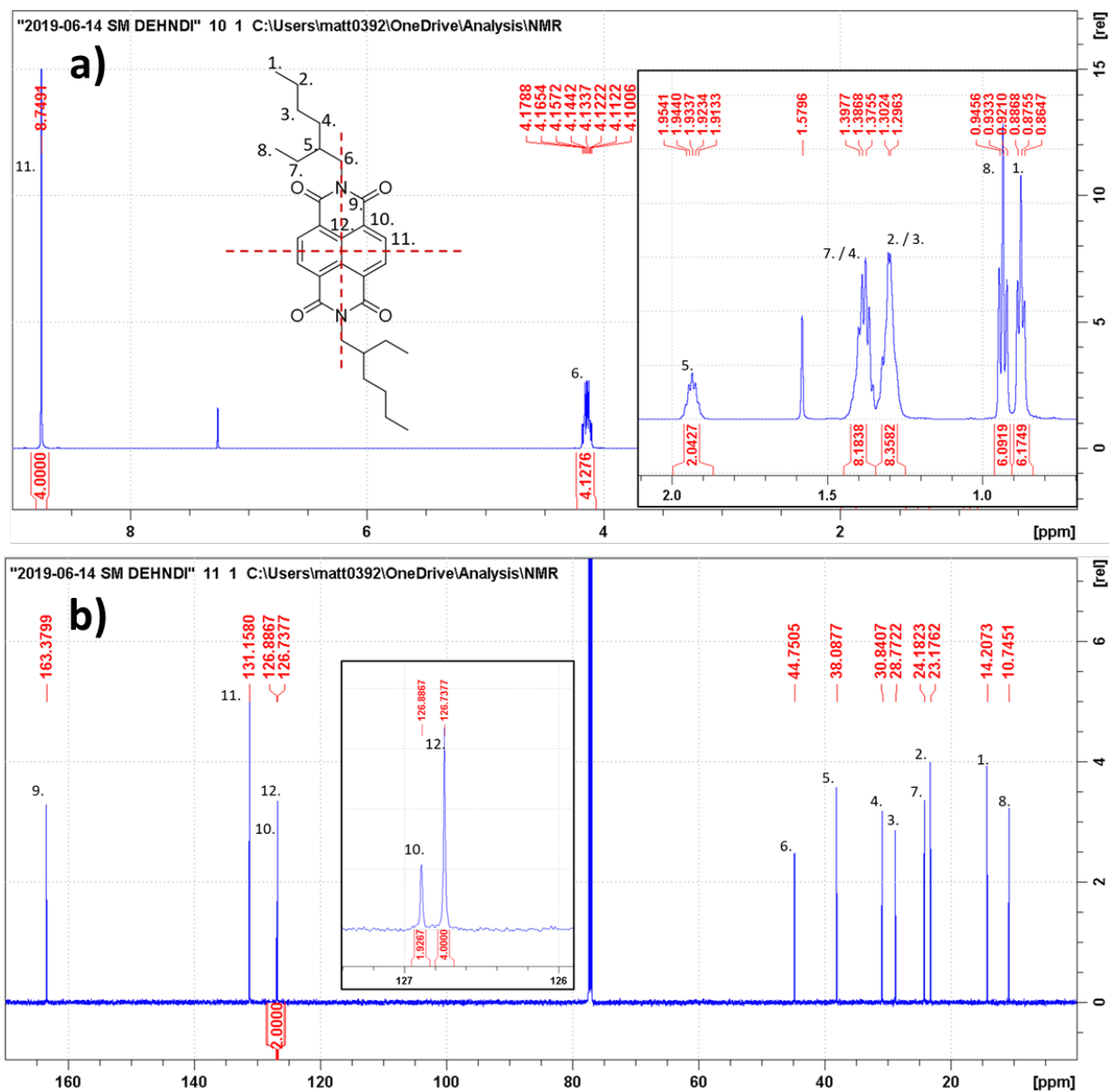
Figure A.12: a) ^{1}H NMR and b) ^{13}C NMR spectra of DEHNDI recorded in CDCl$_3$.
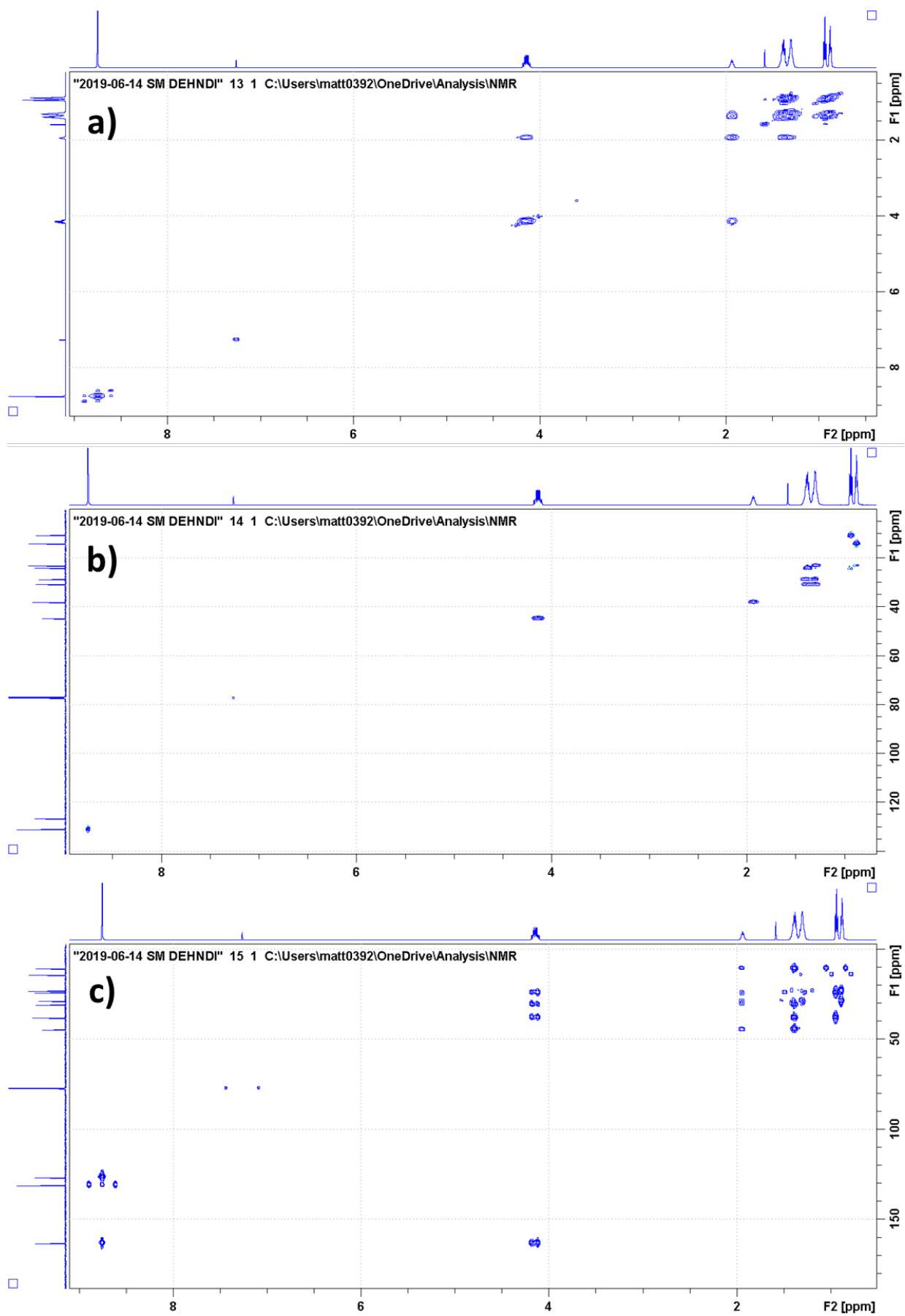
Figure A.13: NMR spectra of DEHNDI recorded in CDCl$_3$, with a) COSY, b) HSQC, and c) HMBC.
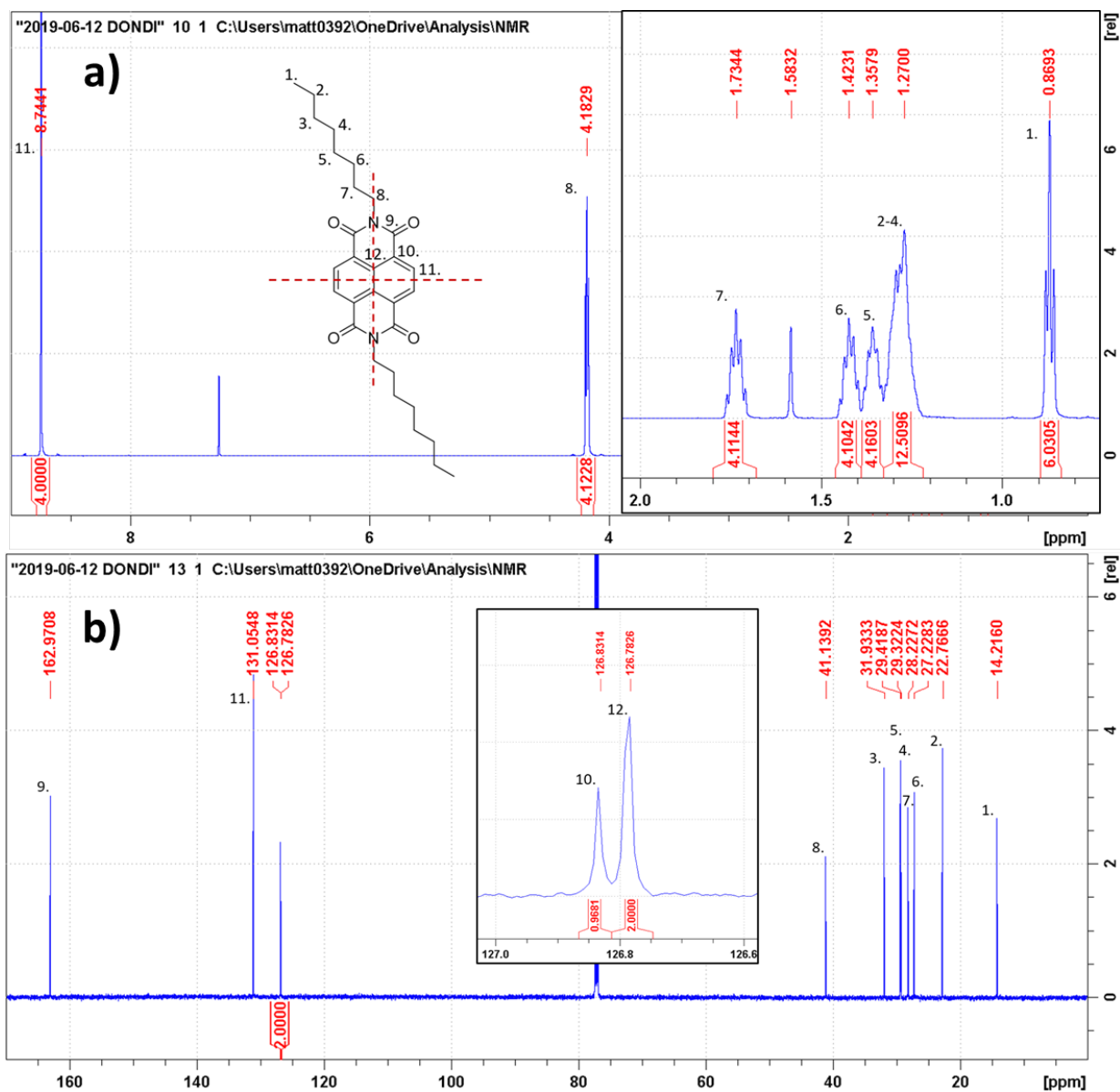
Figure A.14: a) ^{1}H NMR and b) ^{13}C NMR spectra of DONDI recorded in CDCl$_3$.
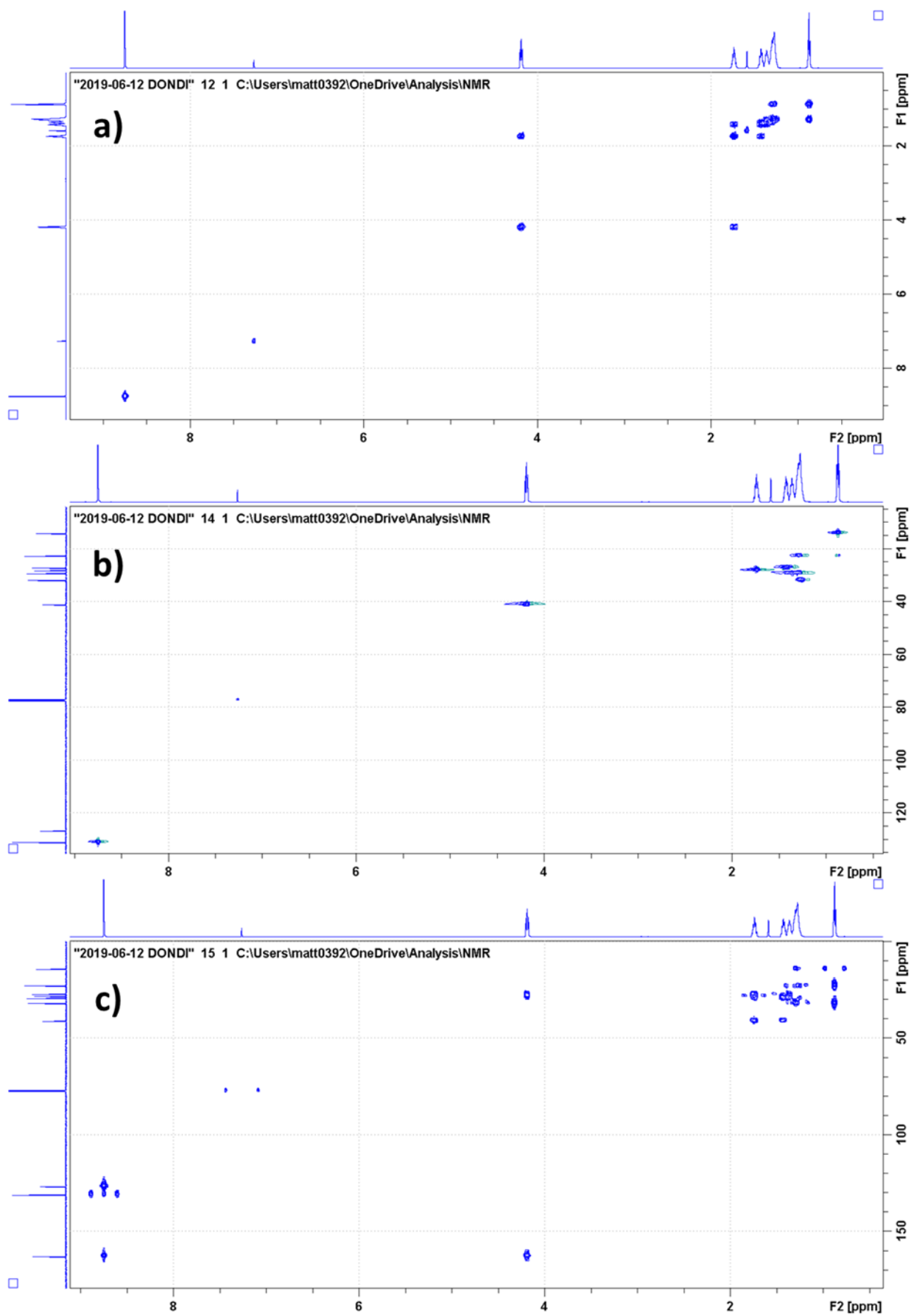
Figure A.15: NMR spectra of DONDI recorded in CDCl$_3$, with a) COSY, b) HSQC, and c) HMBC.
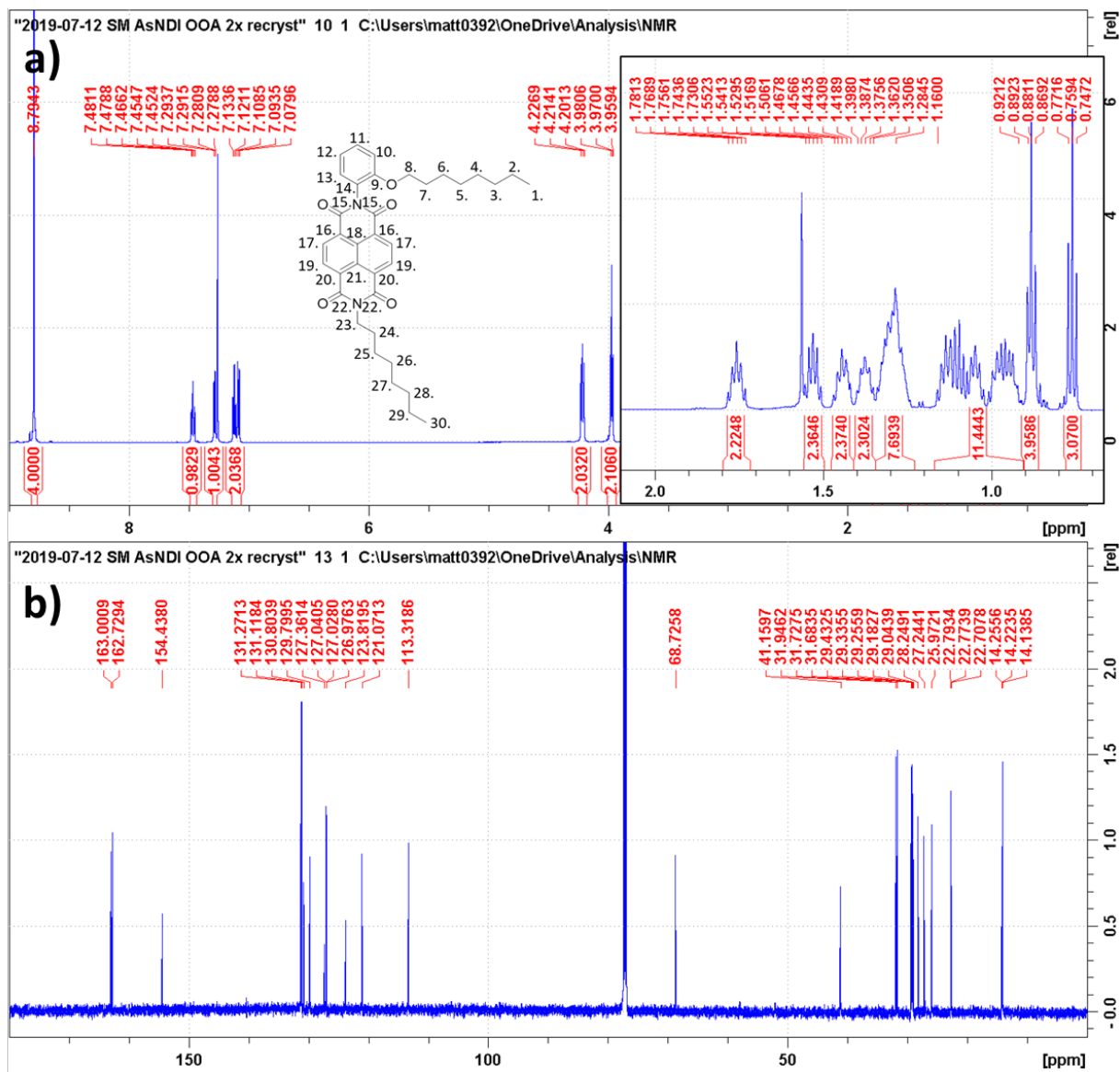
Figure A.16: a) ^{1}H NMR and b) ^{13}C NMR spectra of AsNDI recorded in CDCl$_3$.
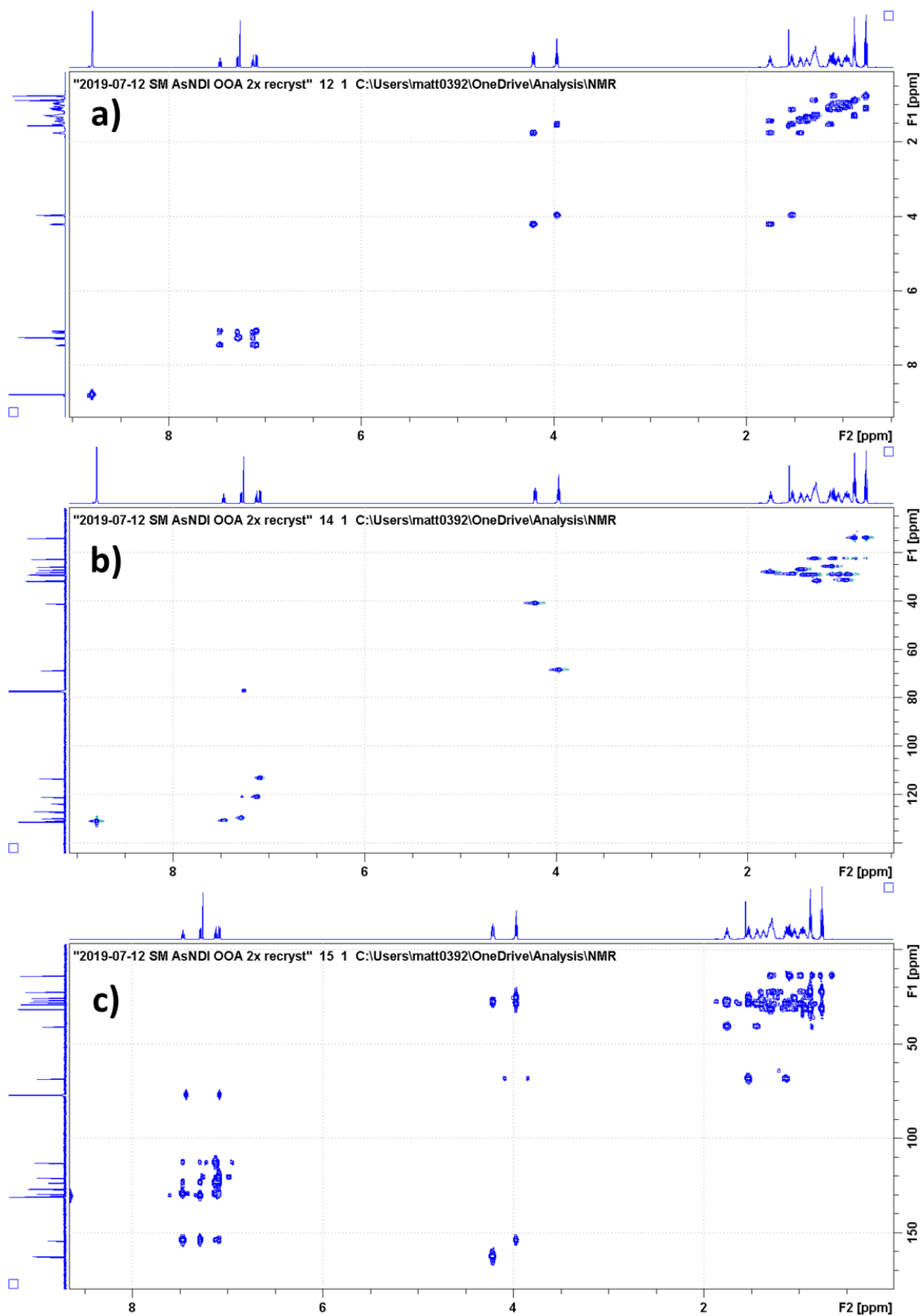
Figure A.17: NMR spectra of AsNDI recorded in CDCl₃, with a) COSY, b) HSQC, and c) HMBC.
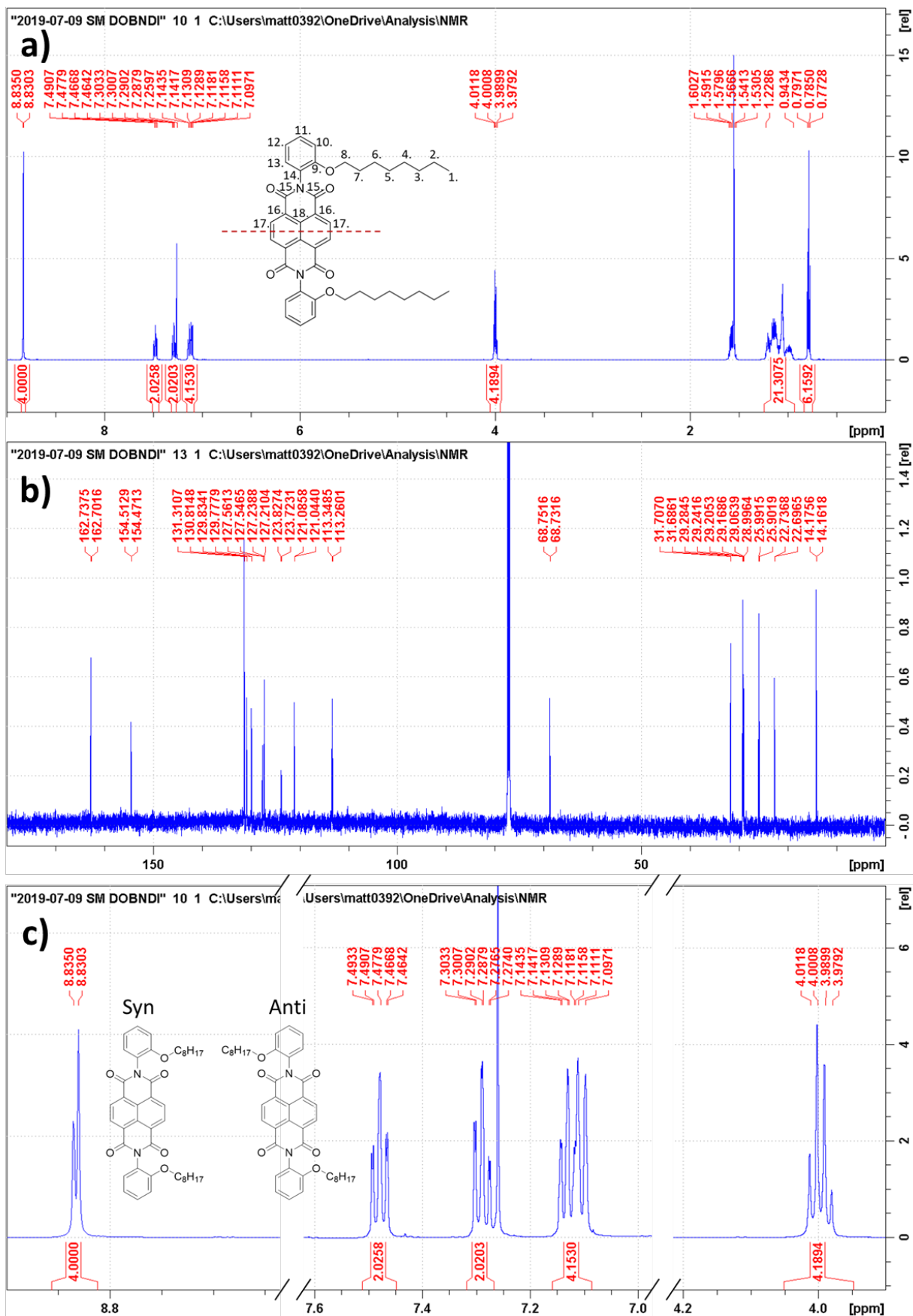
Figure A.18: a) ^{1}H NMR and b) ^{13}C NMR spectra of DOBNDI recorded in CDCl$_3$, with c) showing peaks indicating the presence of syn and anti rotamers.
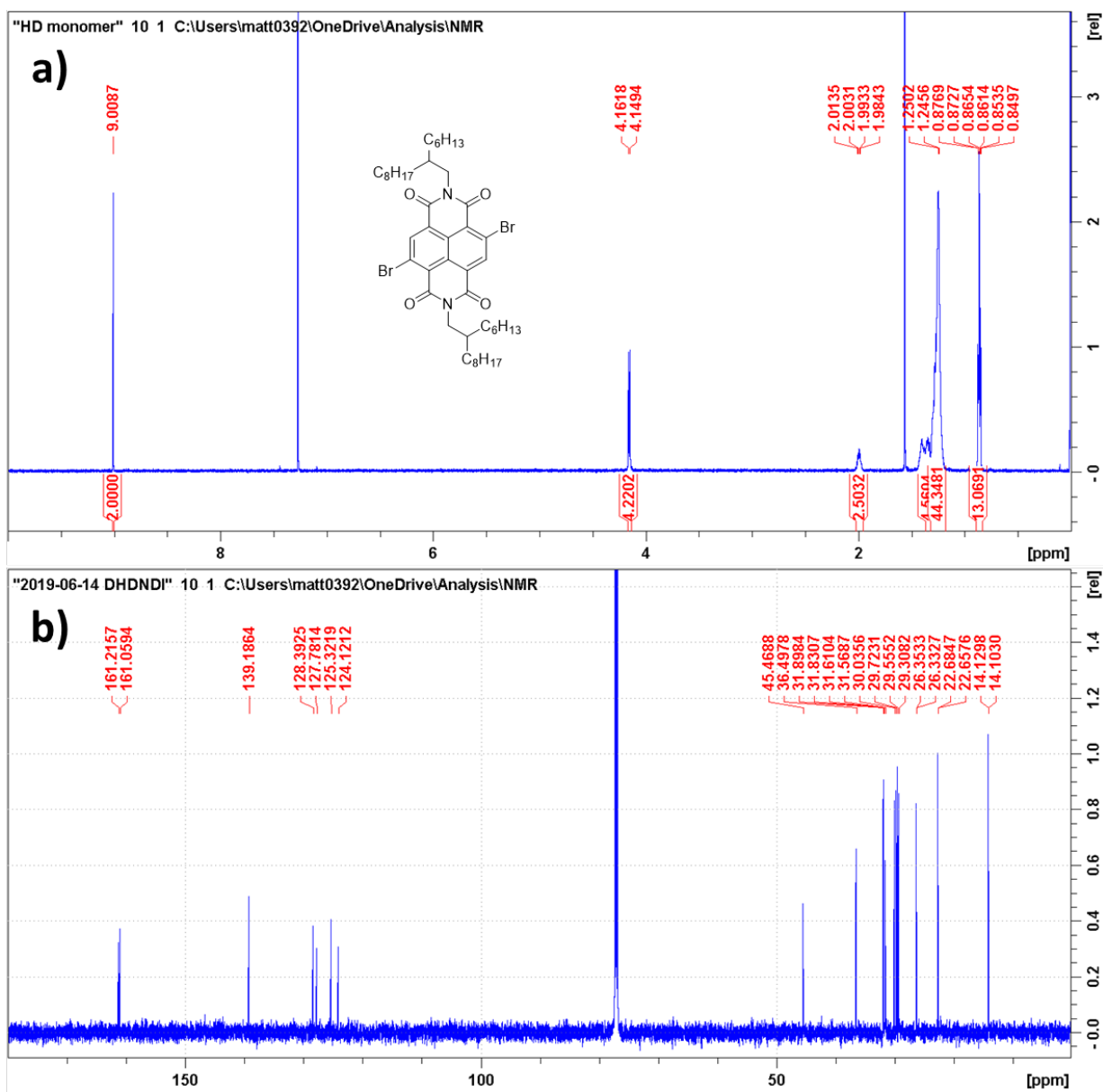
Figure A.19: a) ^{1}H NMR and b) ^{13}C NMR spectra of the monomer DHDNDI.
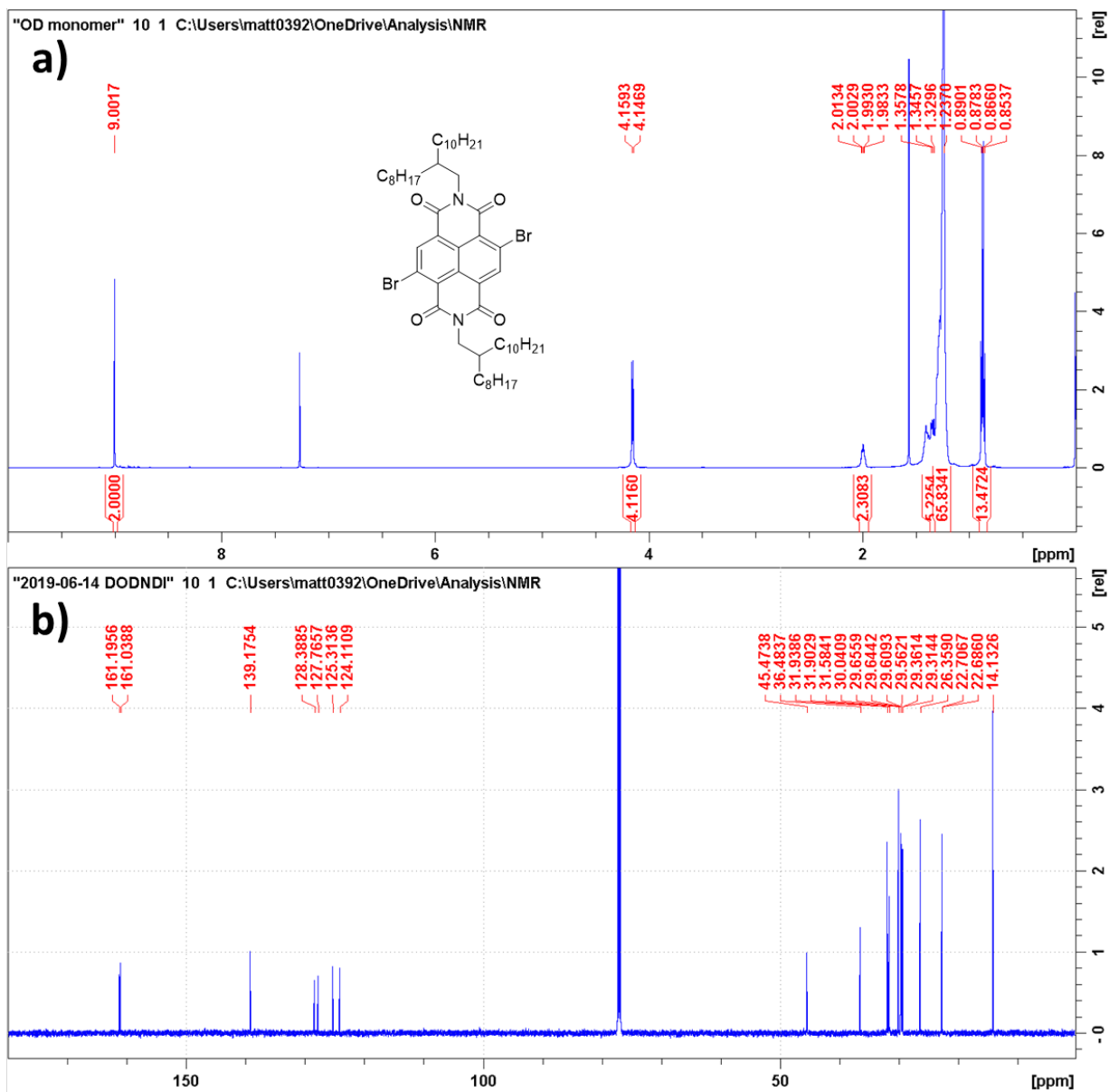
Figure A.20: a) ^{1}H NMR and b) ^{13}C NMR spectra of the monomer DODNDI.
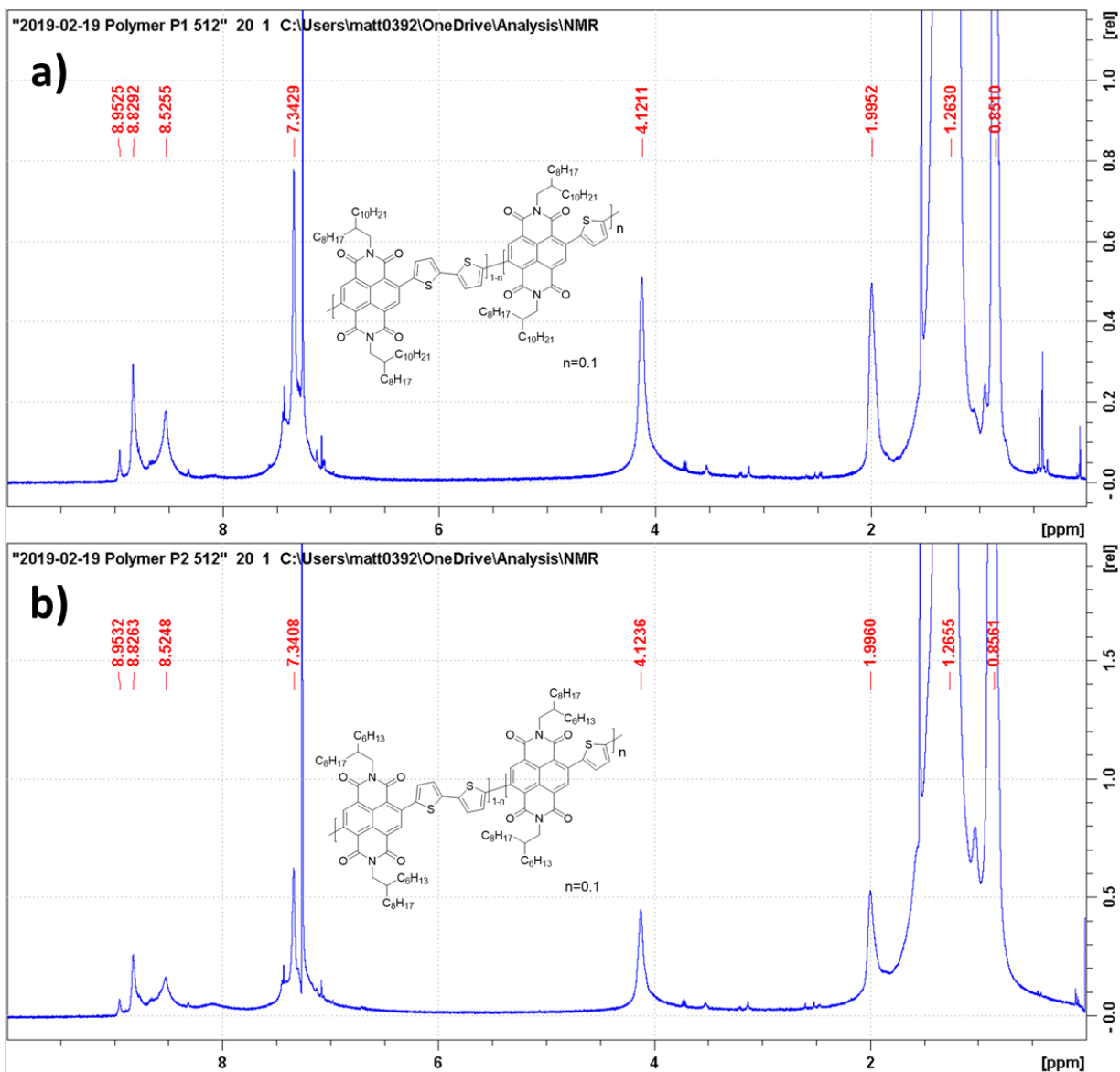
Figure A.21: NMR spectra of the n-type polymers a) P(NDI2OD-T10) and b) P(NDI2HD-T10).
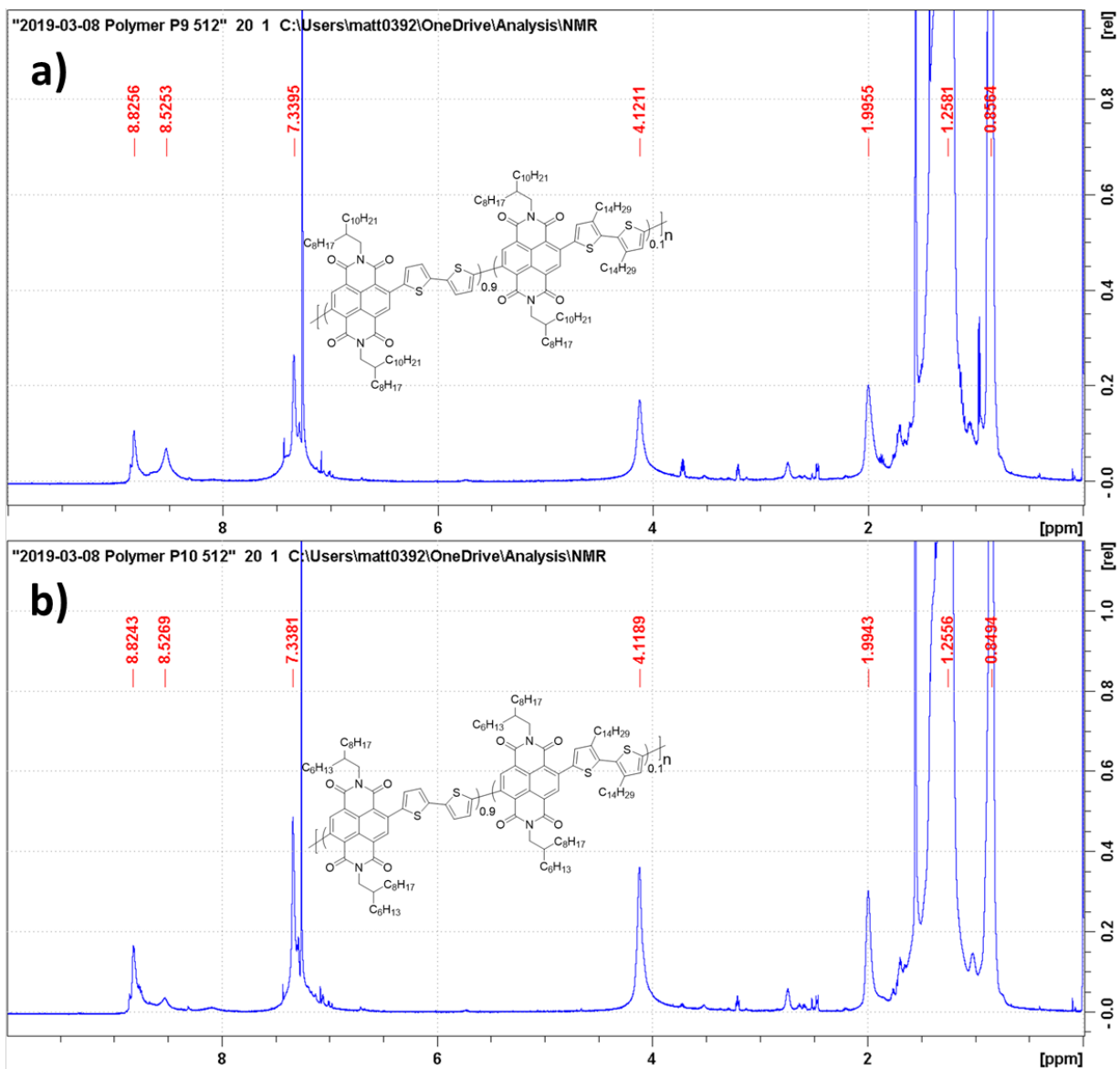
Figure A.22: NMR spectra of the n-type polymers a) P(NDI2OD-14T2) and b) P(NDI2HD-14T2).
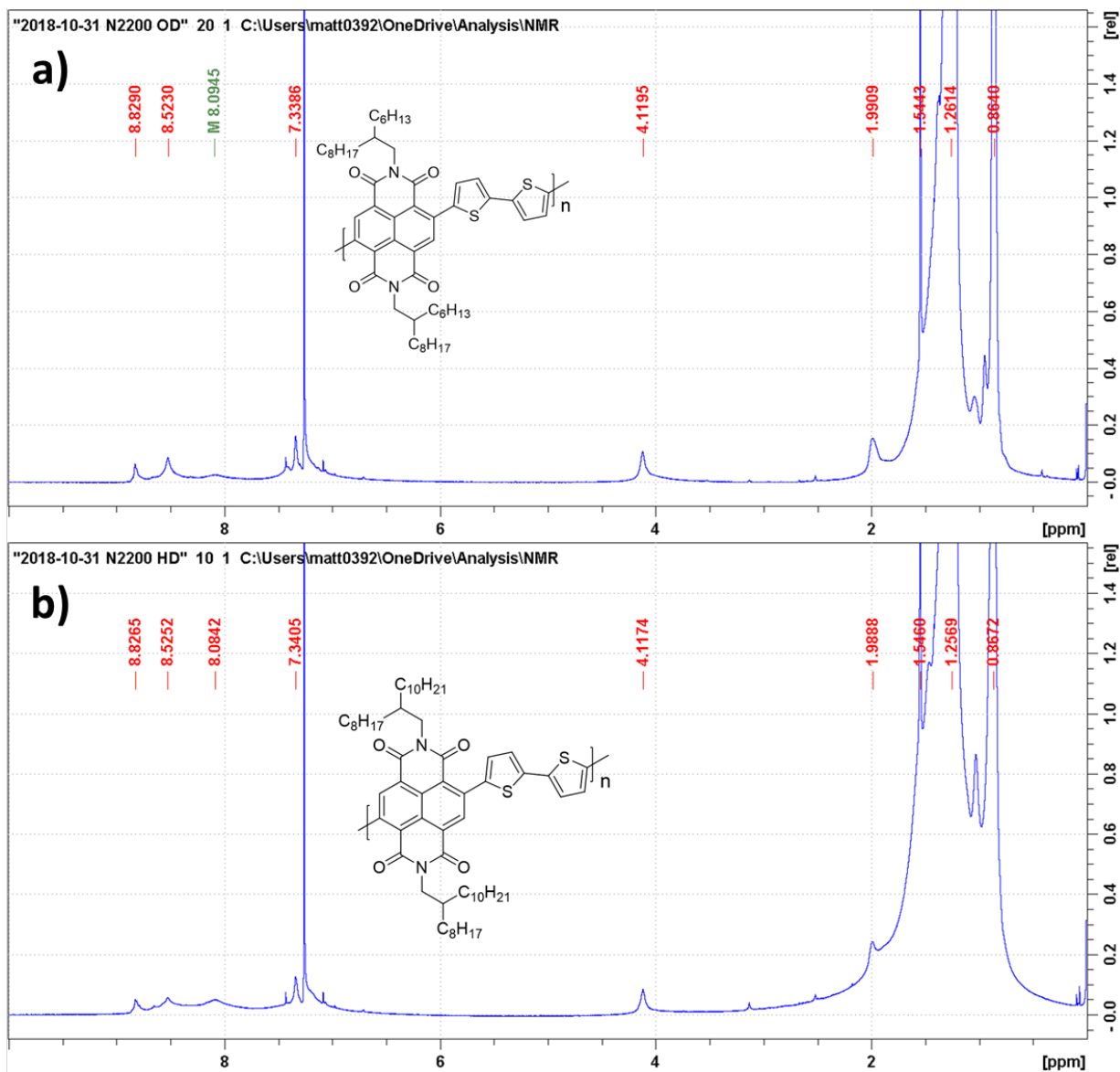
Figure A.23: NMR spectra of the n-type polymers a) N2200 and b) N2300.
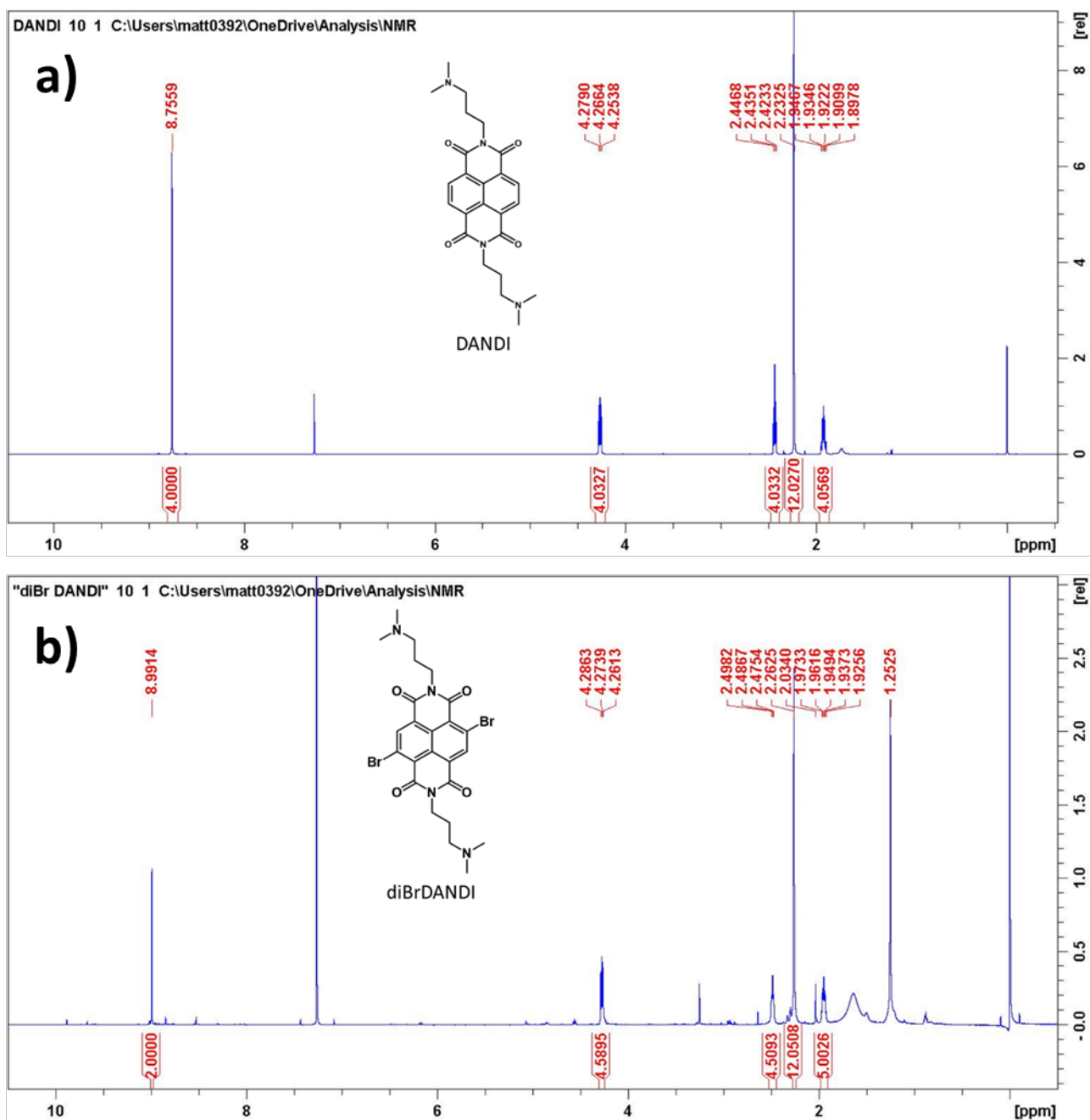
Figure A.24: NMR spectra of a) DANDI and b) diBrDANDI.
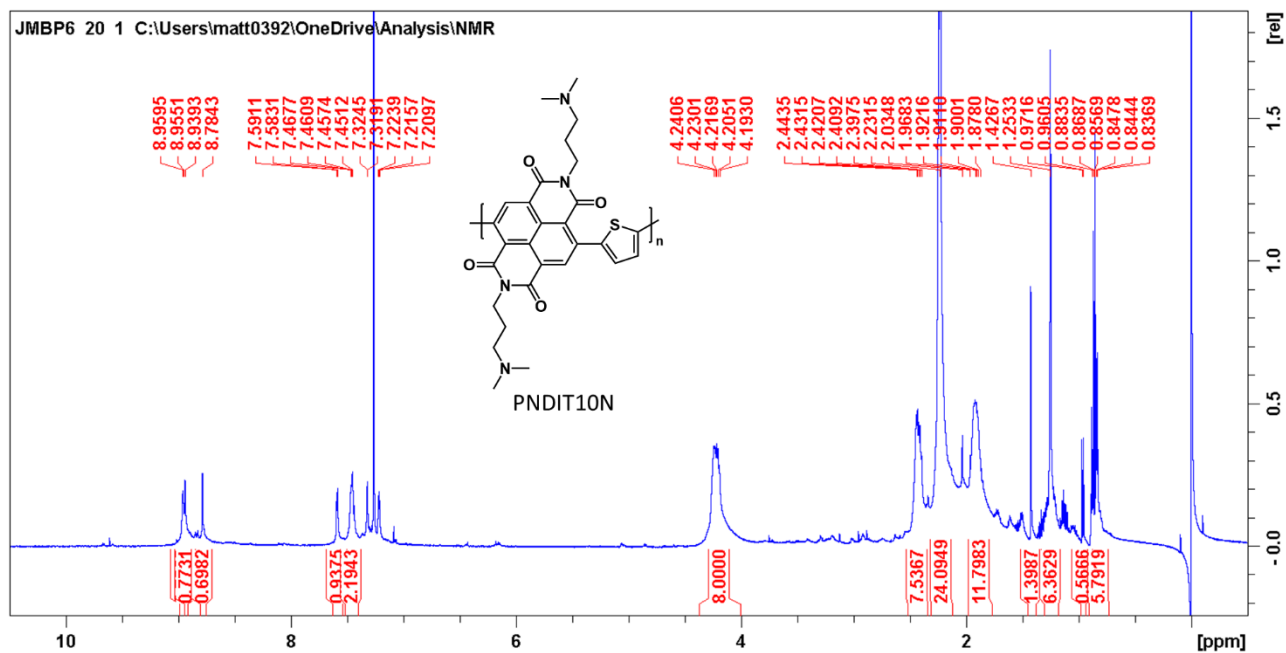
Figure A.25: NMR spectra of PDNIT10N
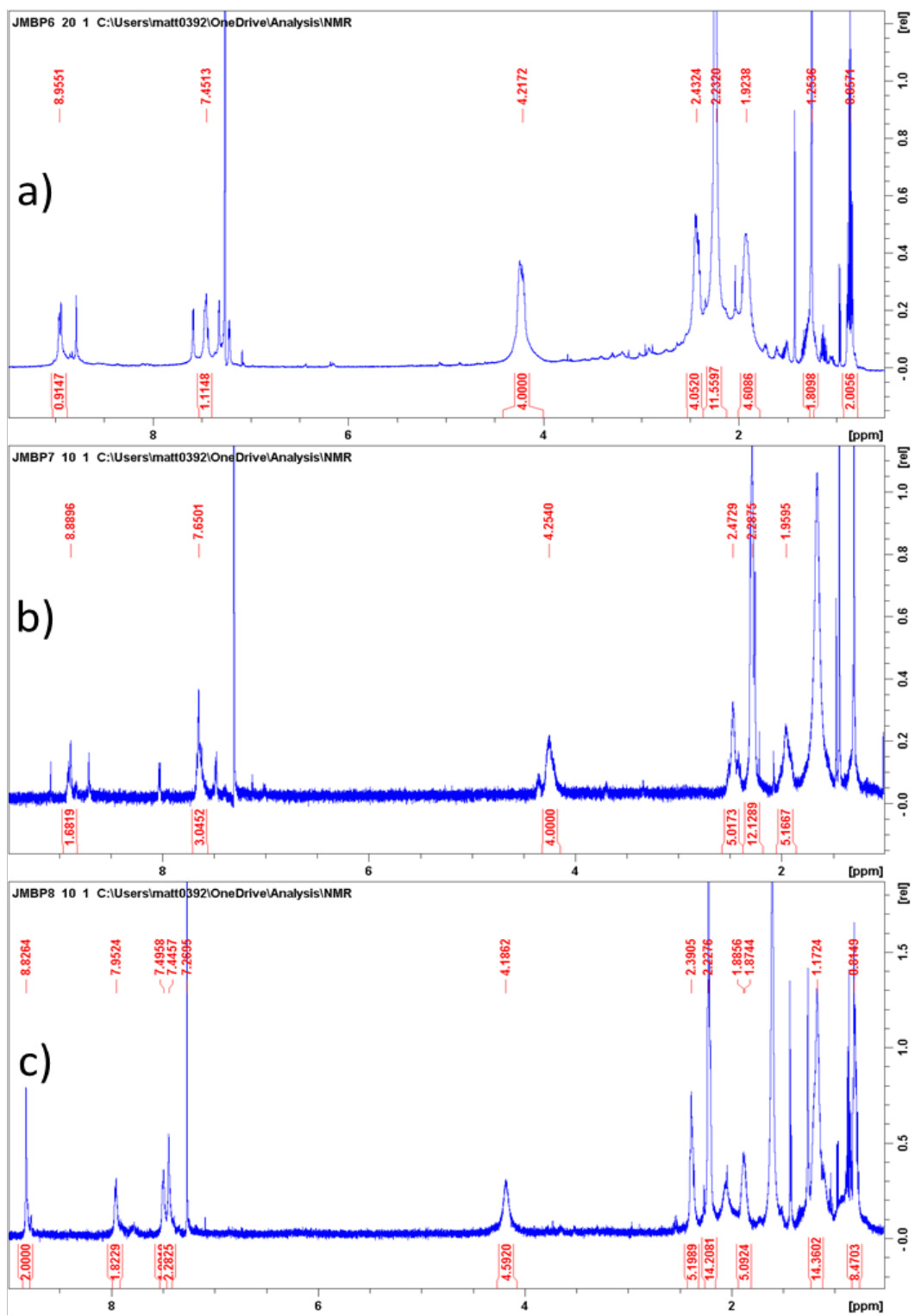
Figure A.26: NMR spectra of polymers a) P(NDI3N-T), b) P(NDI3N-P) and c) P(NDI3N-F8).

A.6 Mass-spectrometry

A.6.1 MALDI-TOF

Matrix assisted laser desorption ionisation – time of flight (MALDI-TOF) mass spectra was obtained on a Bruker Autoflex III MALDI MS/MS (Bruker, USA) equipped with a 355nm UV laser. Samples were prepared from a 20 mg/mL trans-2-[3-(4-tert-Butylphenyl)-2-methyl-2-propenylidene]malononitrile (DCTB) solution and a 10 mg/mL diBrDANDI solution, both in chloroform, mixed in a 20:3 ratio. 1 µL of the resulting solution was used for deposition of the sample.
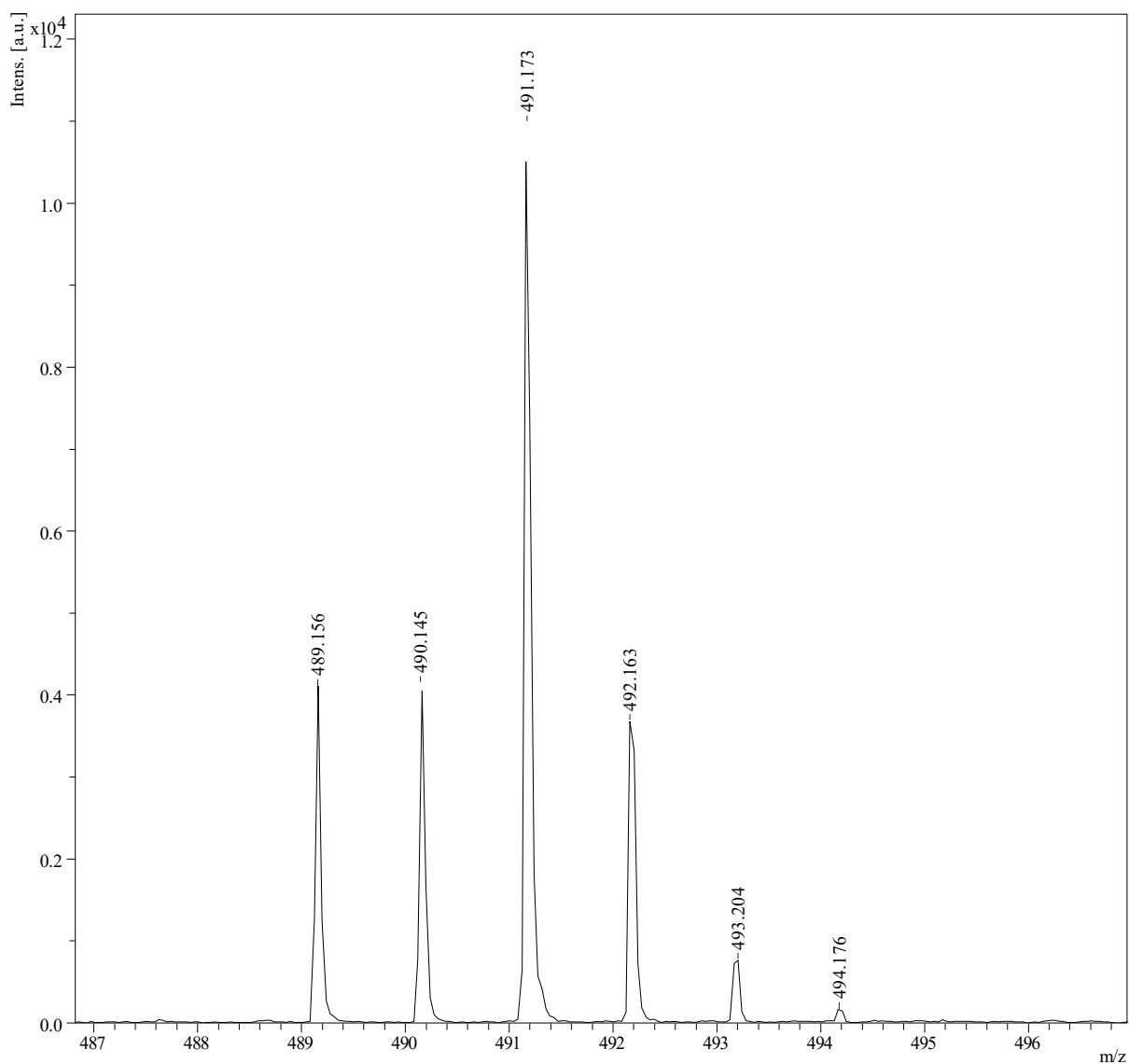
Figure A.27: MALDI spectra of DEHNDI prepared from a chloroform solution with DCTB matrix
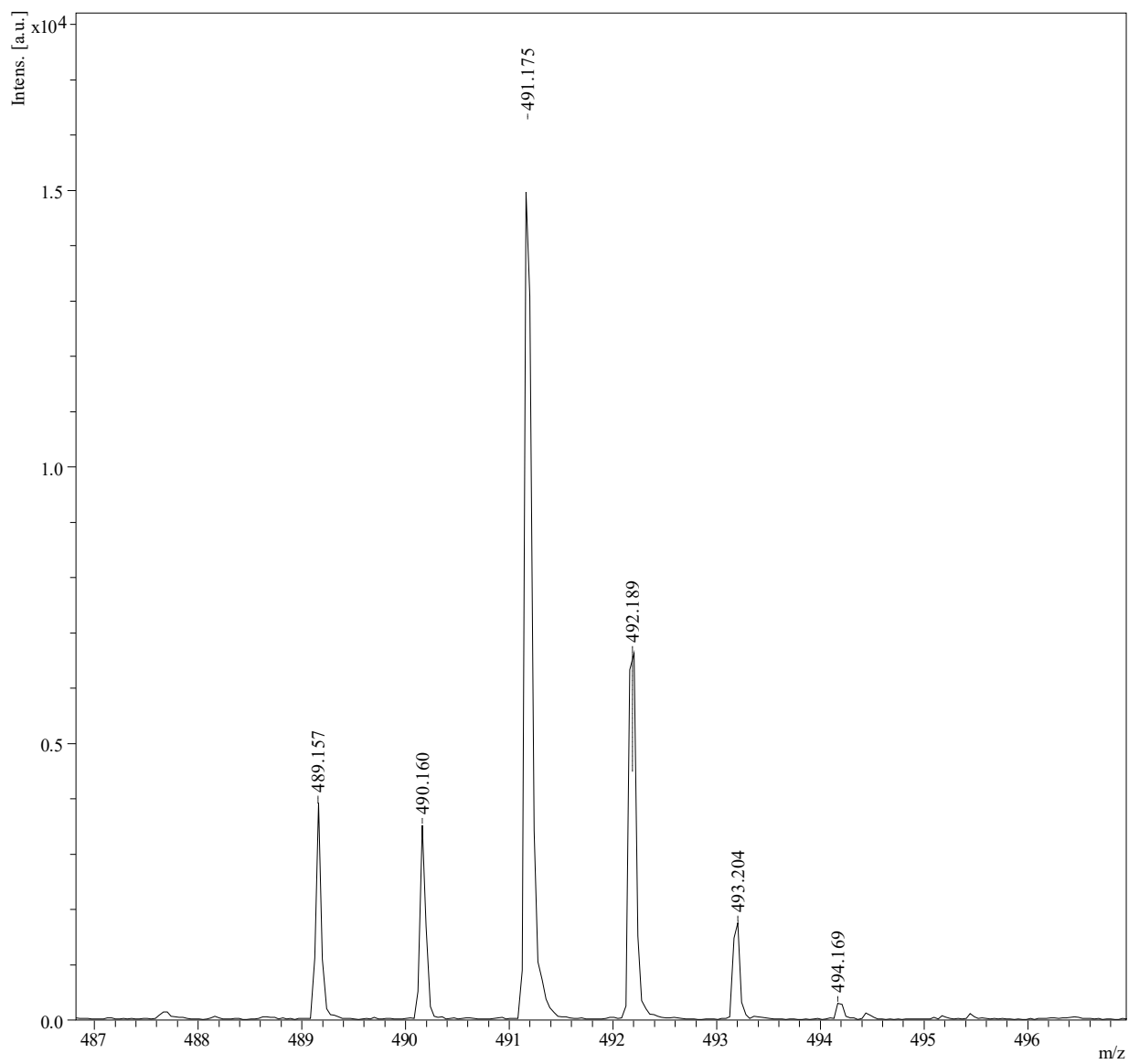
Figure A.28: MALDI spectra of DONDI prepared from a chloroform solution with DCTB matrix
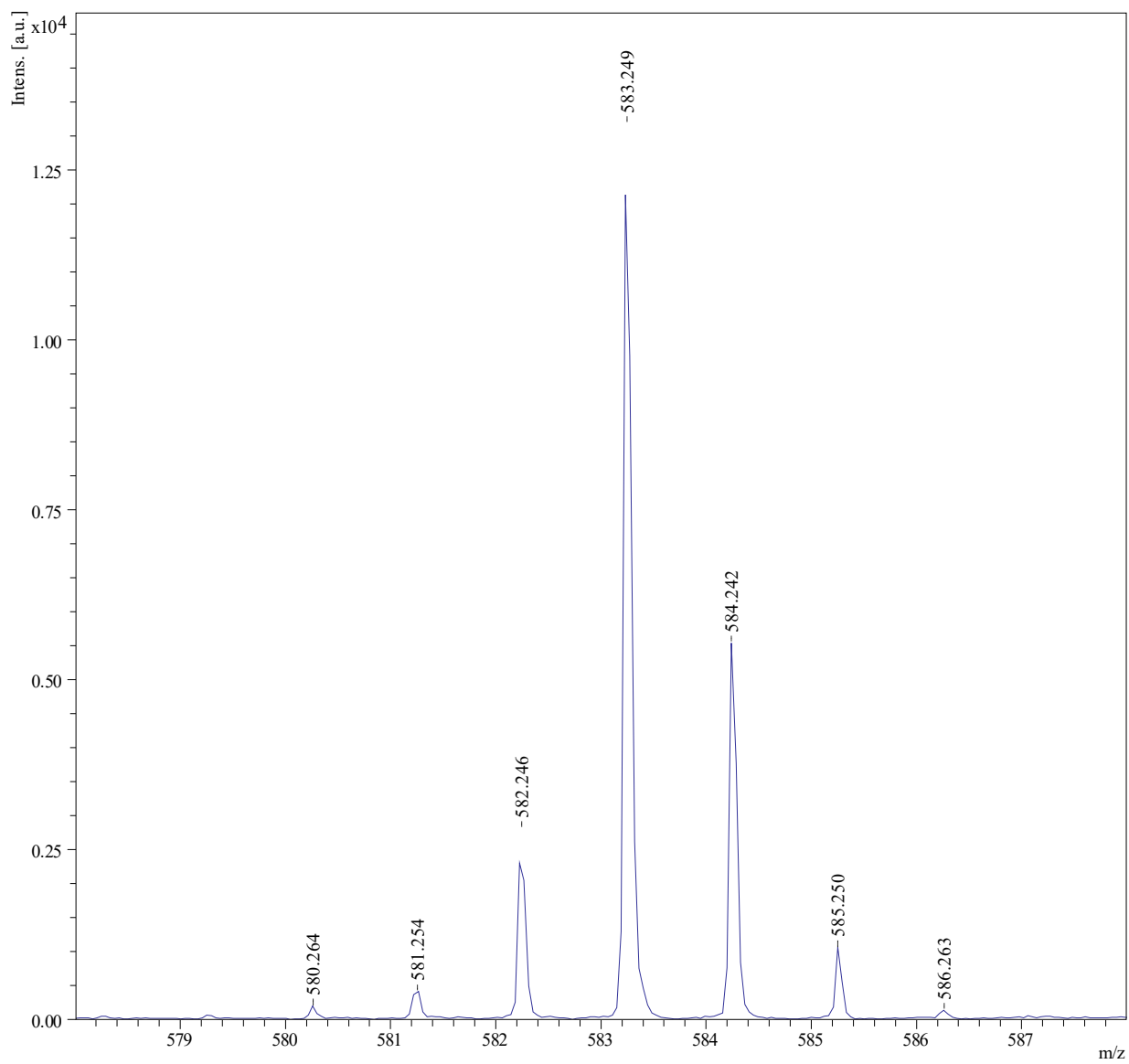
Figure A.29: MALDI spectra of AsNDI prepared from a chloroform solution with DCTB matrix
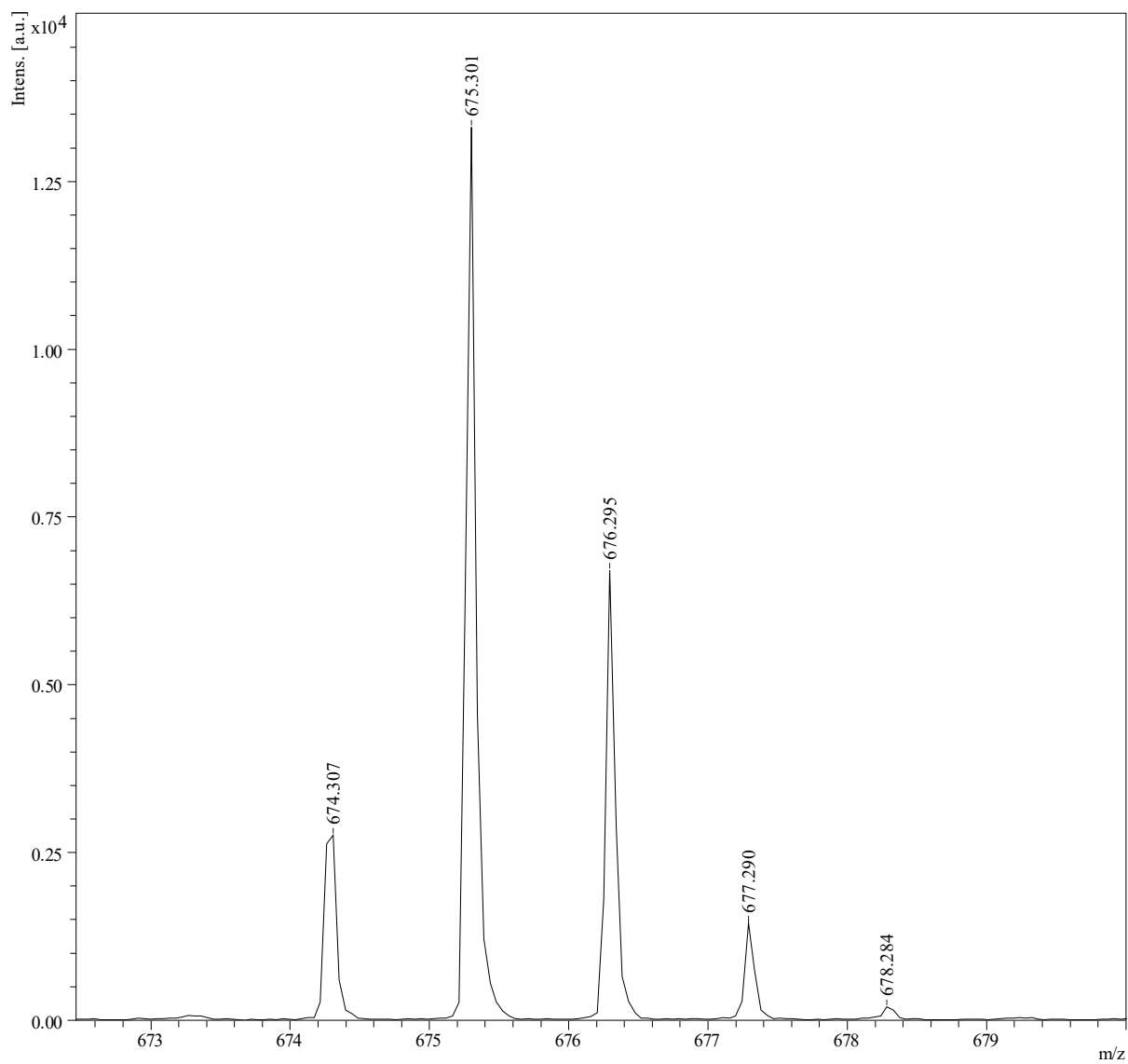
Figure A.30: MALDI spectra of DOBNDI prepared from a chloroform solution with DCTB matrix
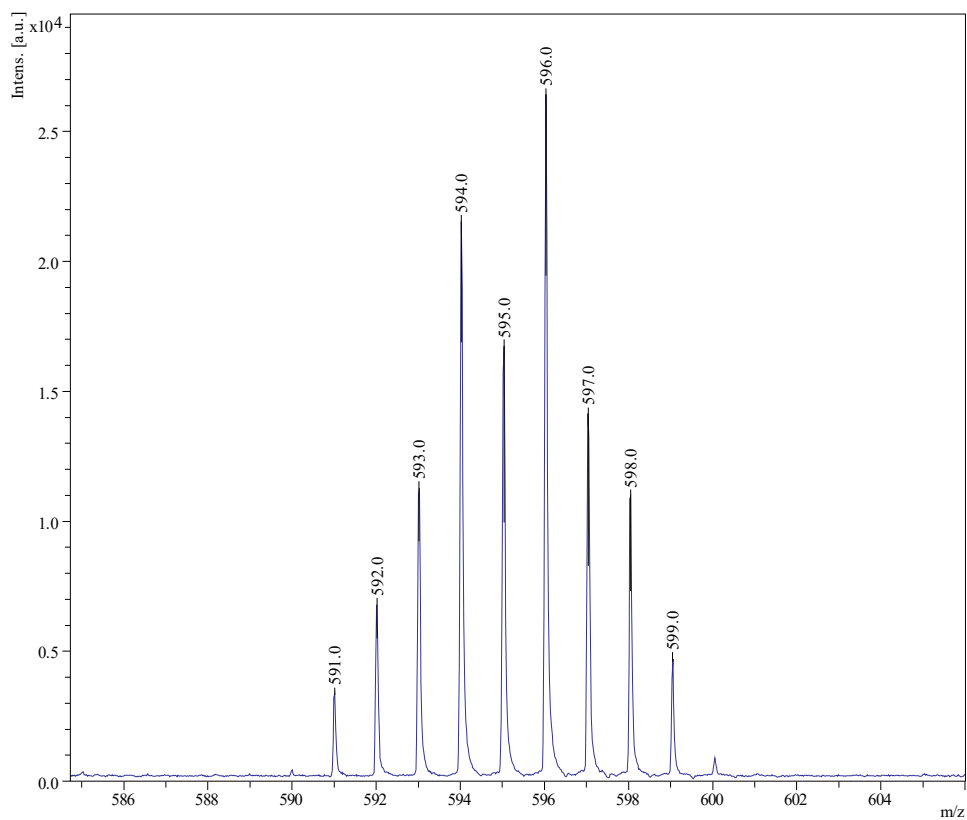
Figure A.31: MALDI spectra of the monomer diBrDANDI with DCTB matrix
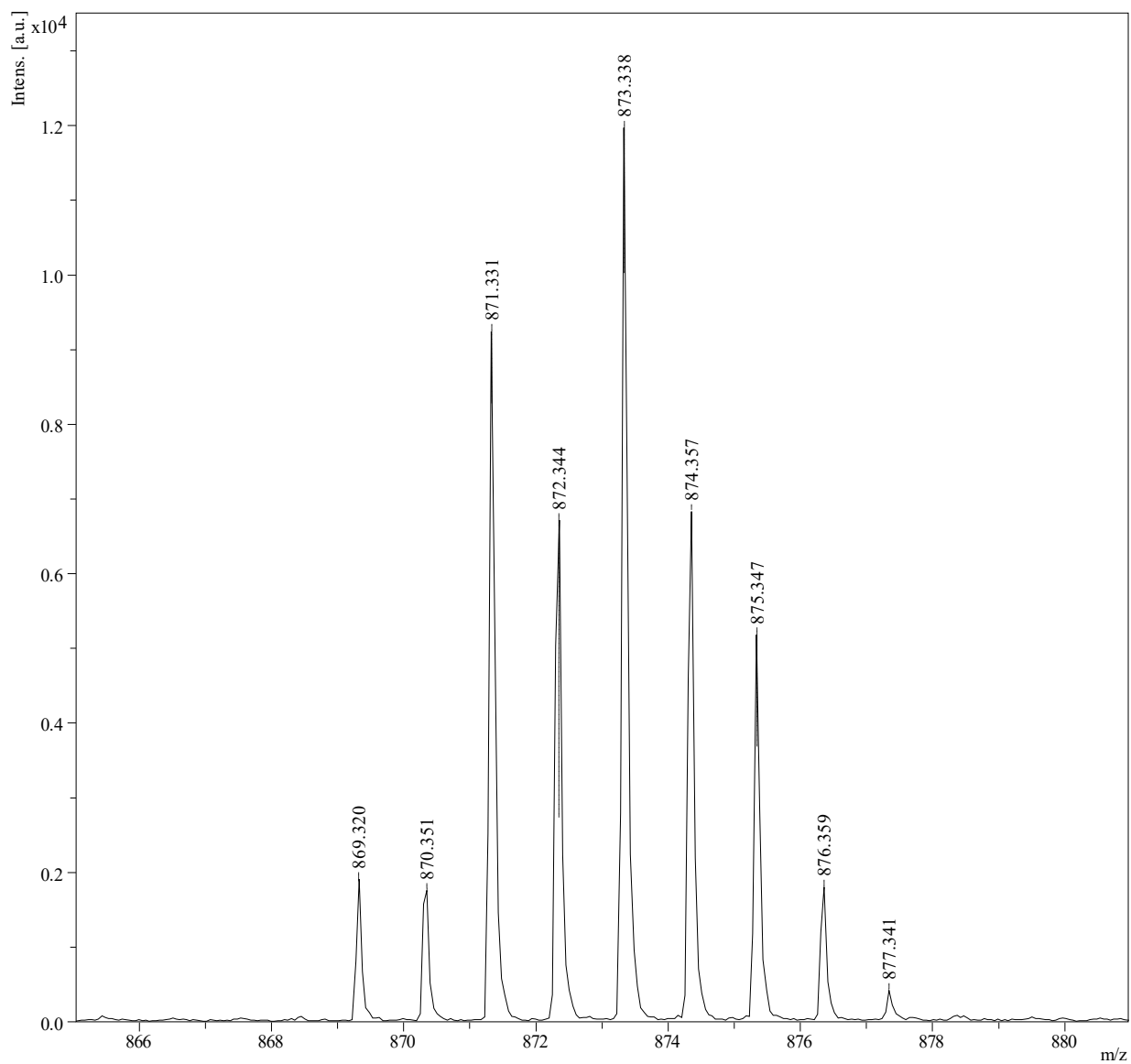
Figure A.32: MALDI spectra of DHDNDI prepared from a chloroform solution with DCTB matrix
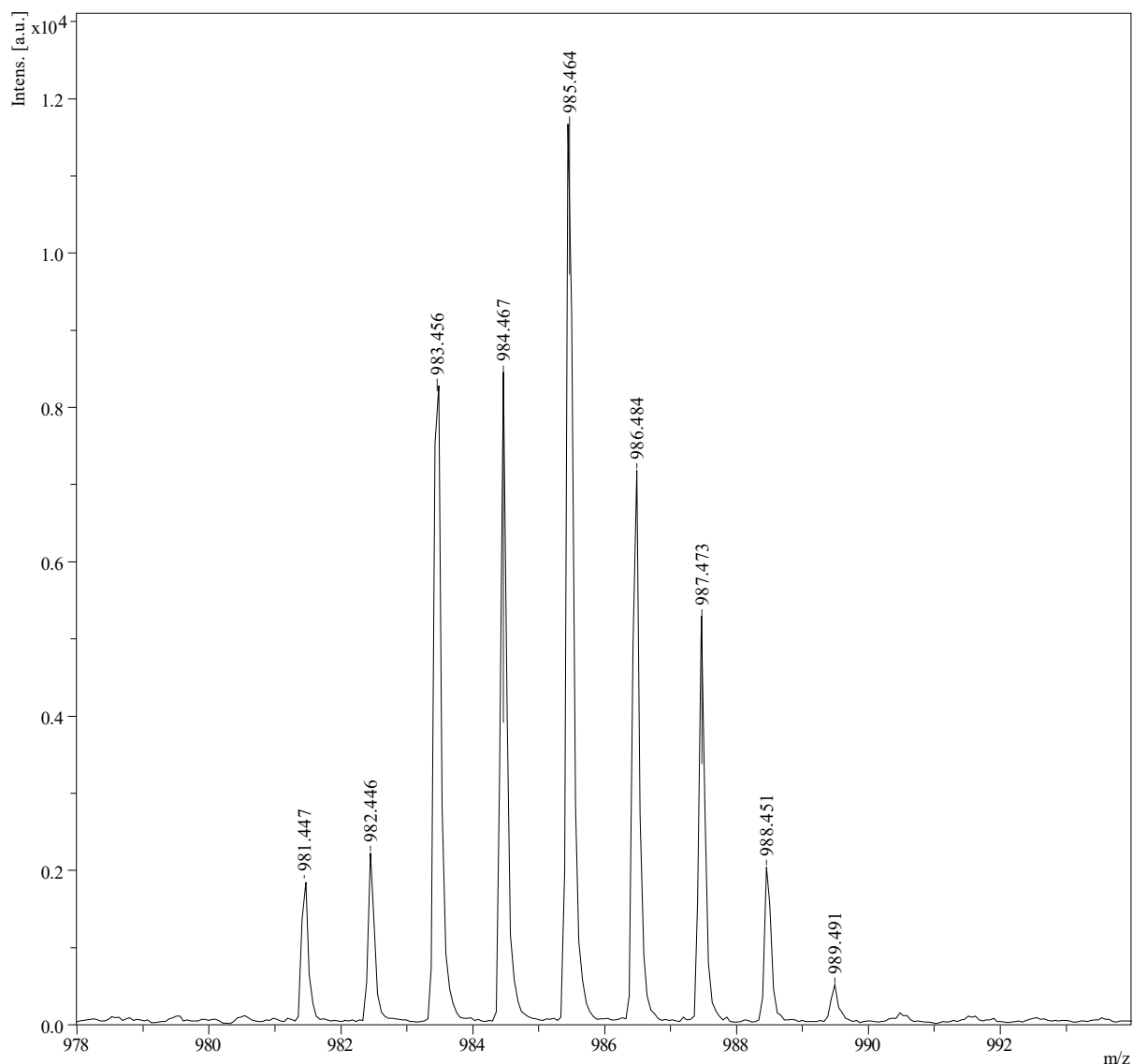
Figure A.33: MALDI spectra of DODNDI prepared from a chloroform solution with DCTB matrix

A.6.2 DSA-TOF

Direct sample analysis – time of flight (DSA-TOF) mass spectra was obtained on a AxION 2 TOF connected to a AxION DSA (Perkin Elmer). Samples were prepared by dissolving one small grain/crystal of each of the small molecules/monmers in 1 mL of chloroform, a further dilution was conducted by taking one drop of the solution and dissolving it in 1 mL of chloroform. 20 µL of the final solution was deposited on the aluminium mesh that acted as sample stage.
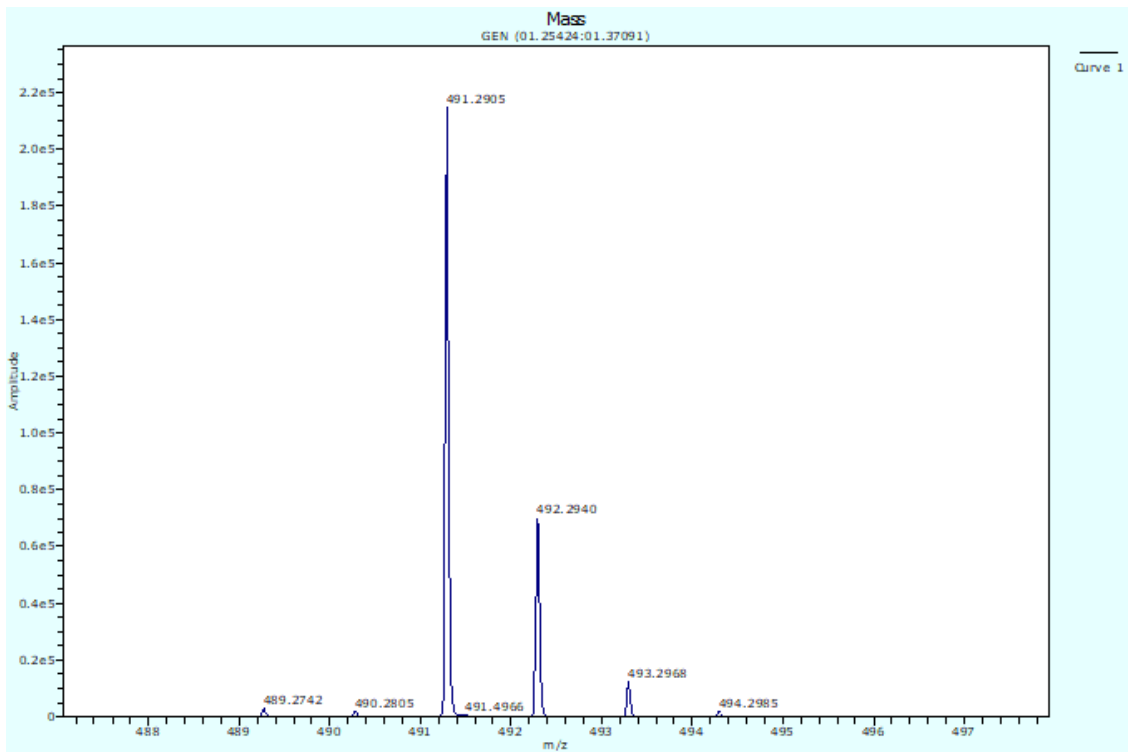
Figure A.34: DSA-TOF spectra of DEHNDI.
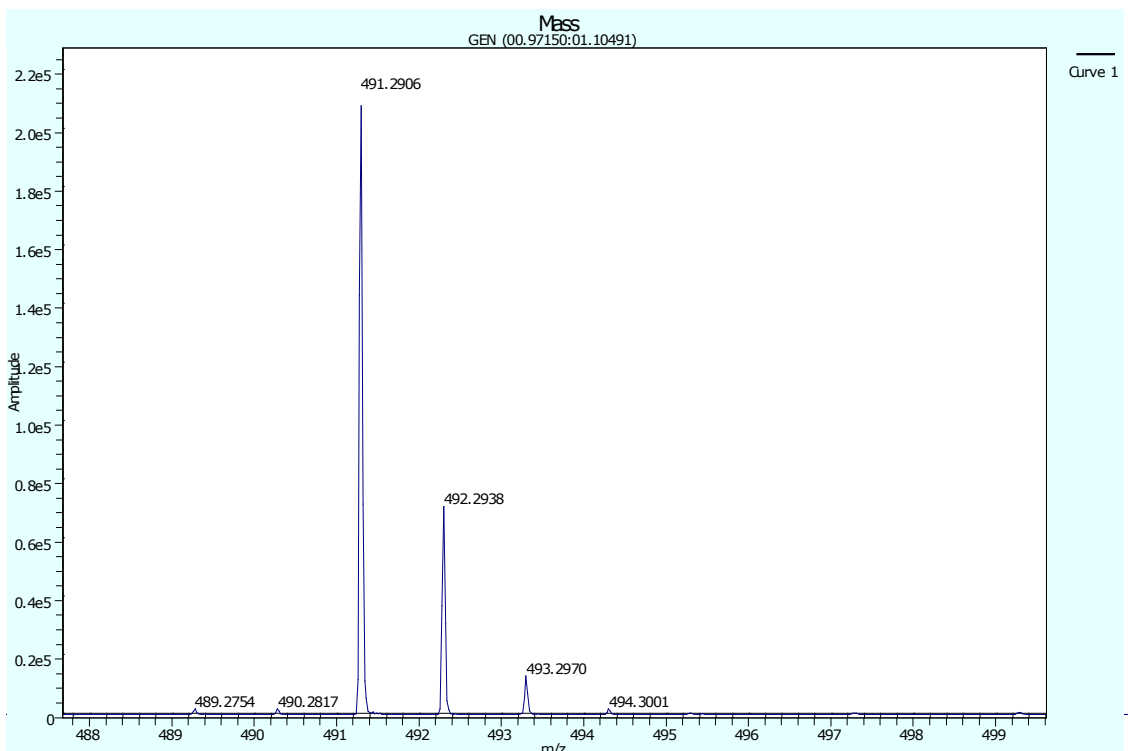
Figure A.35: DSA-TOF spectra of DONDI.
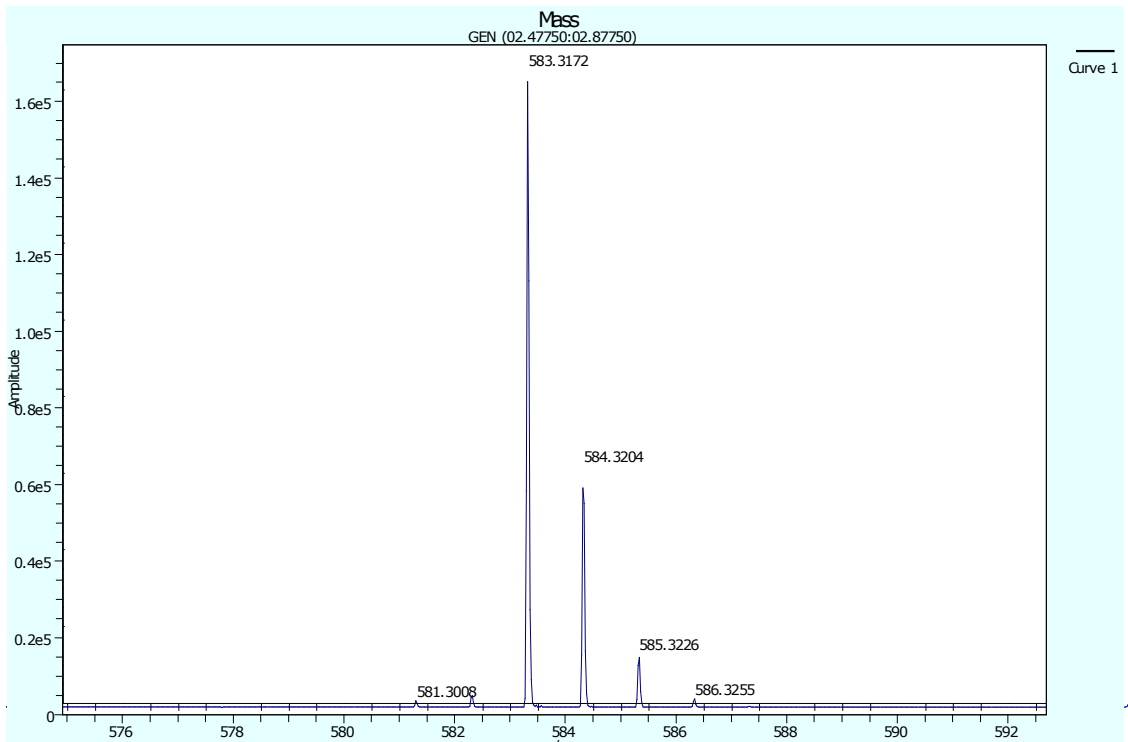
Figure A.36: DSA-TOF spectra of AsNDI.
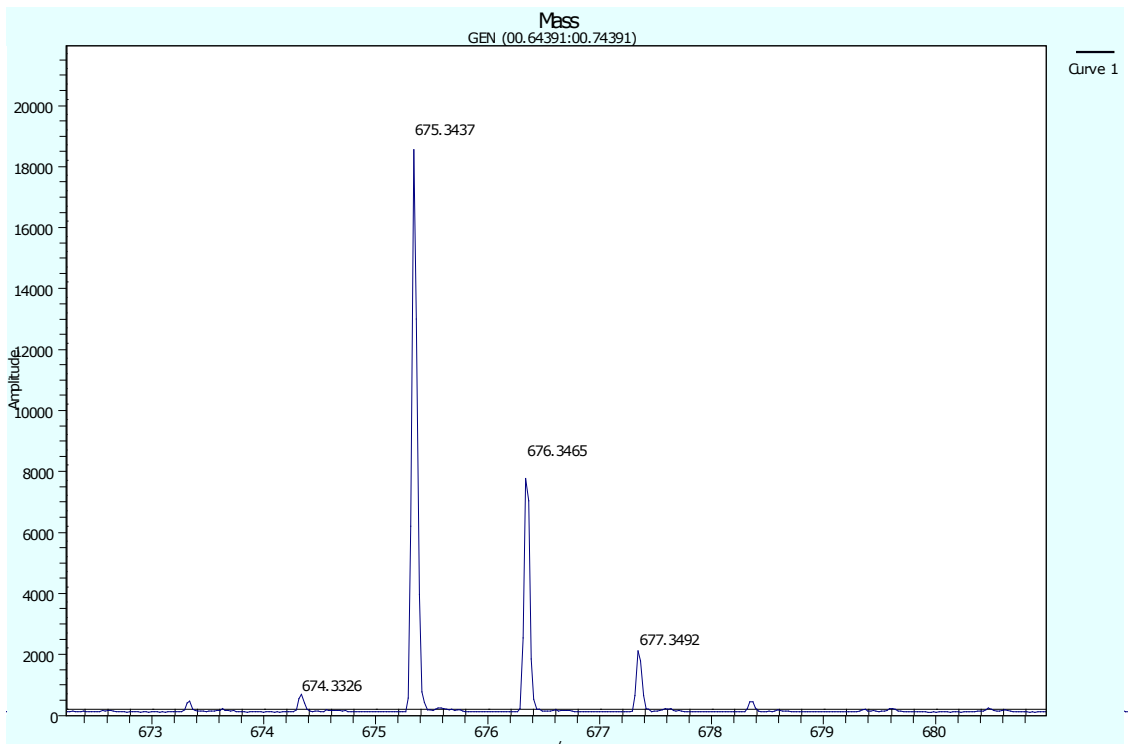
Figure A.37: DSA-TOF spectra of DOBNDI.
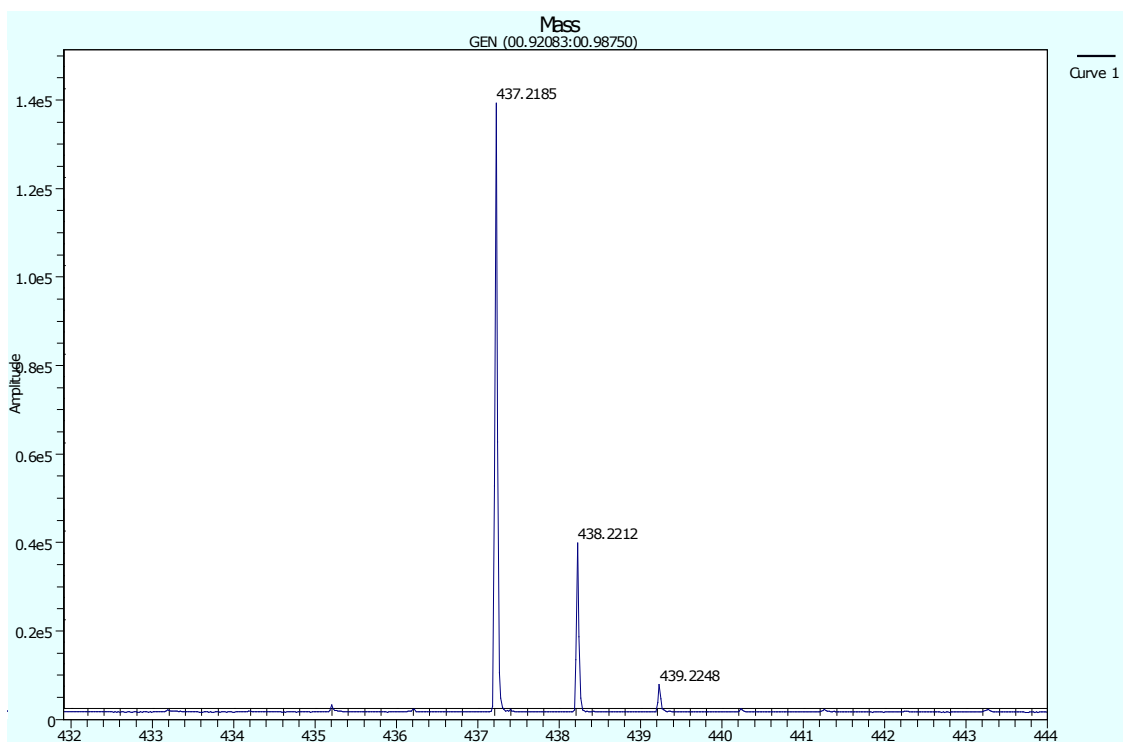
Figure A.38: DSA-TOF spectra of DANDI.
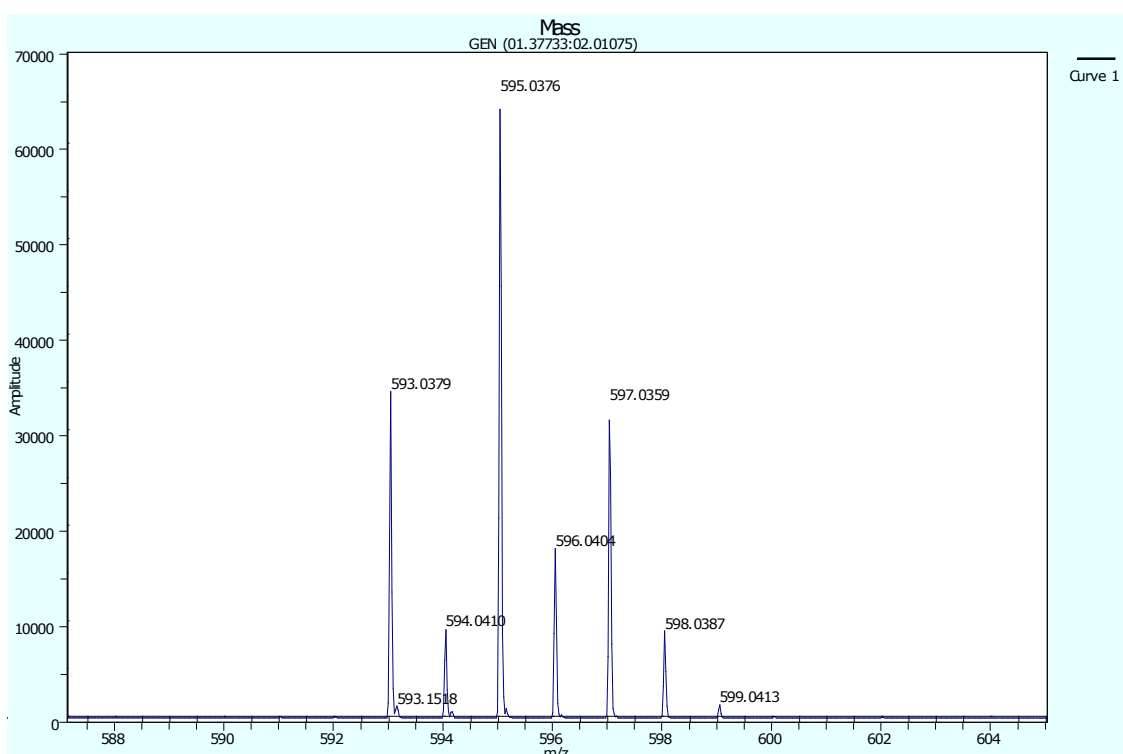
Figure A.39: DSA-TOF spectra of diBrDANDI.
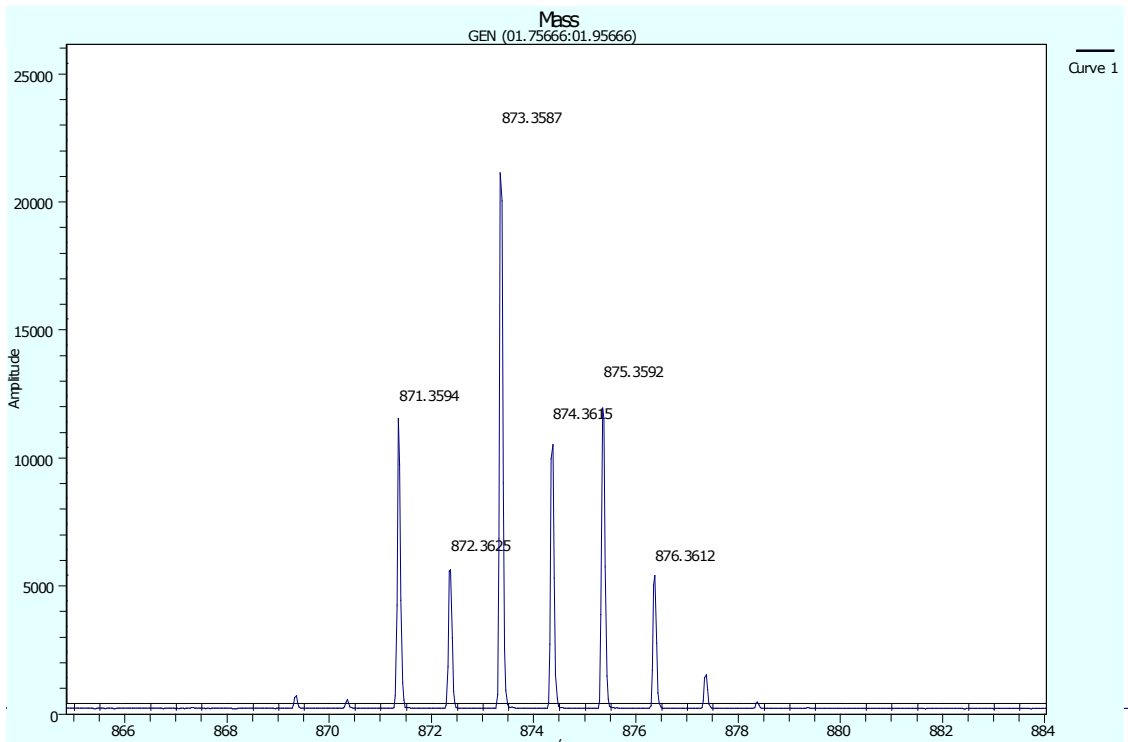
Figure A.40: DSA-TOF spectra of DHDNDI.
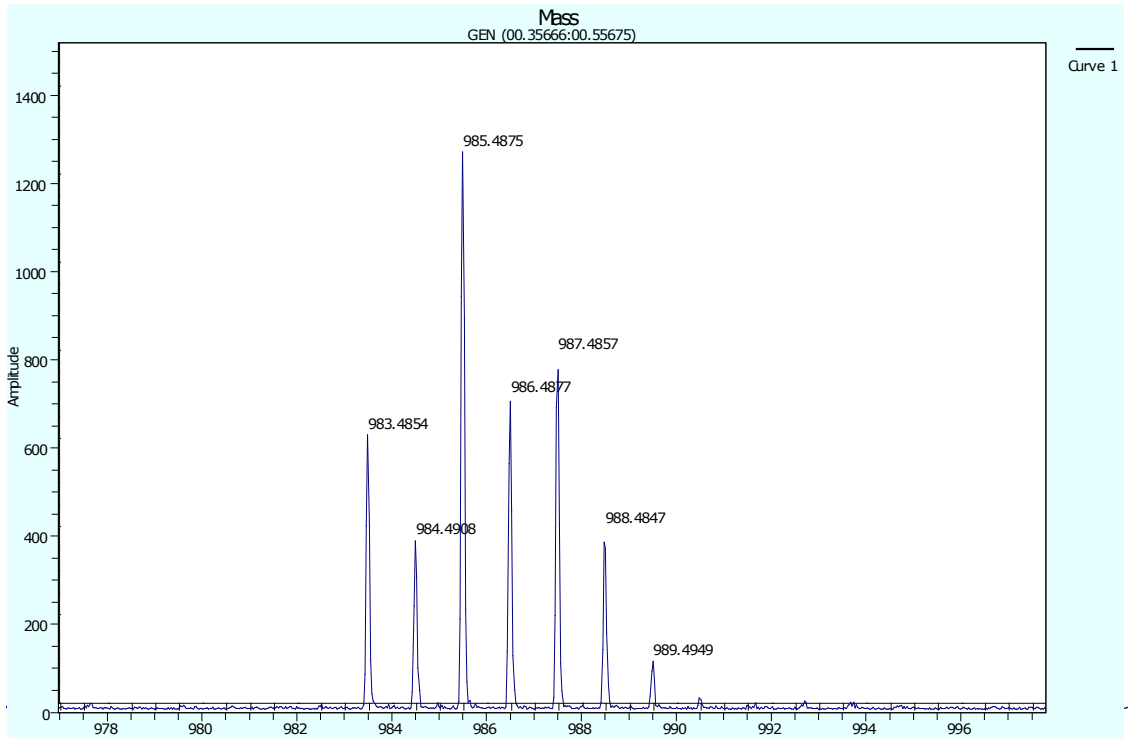
Figure A.41: DSA-TOF spectra of DODNDI.

A.7 References

(1)   Murto, P.; Genene, Z.; Benavides, C. M.; Xu, X.; Sharma, A.; Pan, X.; Schmidt, O.; Brabec, C. J.; Andersson, M. R.; Tedde, S. F.; Mammo, W.; Wang, E., High Performance All-Polymer Photodetector Comprising a Donor–Acceptor–Acceptor Structured Indacenodithiophene–Bithieno[3,4-c]Pyrroletetrone Copolymer. *ACS Macro Lett.* **2018**, 7, 395-400.

(2)   Li, Z.; Xu, X.; Zhang, W.; Meng, X.; Ma, W.; Yartsev, A.; Inganäs, O.; Andersson, M. R.; Janssen, R. A. J.; Wang, E., High Performance All-Polymer Solar Cells by Synergistic Effects of Fine-Tuned Crystallinity and Solvent Annealing. *J. Am. Chem. Soc.* **2016**, 138, 10935-10944.

(3)   Sharma, A.; Kroon, R.; Lewis, D. A.; Andersson, G. G.; Andersson, M. R., Poly(4-vinylpyridine): A New Interface Layer for Organic Solar Cells.   *ACS Appl. Mater. Interfaces* **2017**, 9, 10929-10936.